UNIVERSIDAD AUTÓNOMA DE QUERÉTARO

FACULTAD DE QUÍMICA

“EVALUACIÓN DEL RENDIMIENTO DE CELDAS SOLARES DE PEROVSKITAS BASE CALCOGENURO: ANÁLISIS DETALLADO DE $SrHfSe_3$ Y $BaZrS_3$ CON DIVERSAS CAPAS DE TRANSPORTE DE HUECOS Y PROPIEDADES SINTONIZADAS DE $ABSe_3$ (A = Ca, Ba; B = Zr, Hf) Y ALEACIONES DE Zr-$BaHfS_3$”

TESIS

QUE COMO PARTE DE LOS REQUISITOS PARA OBTENER EL

GRADO DE

DOCTORADO EN CIENCIAS DE LA ENERGÍA

PRESENTA

DHINESHKUMAR SRINIVASAN

DIRIGIDO POR

Dra. LATHA MARASAMY

SANTIAGO DE QUERÉTARO, QUERÉTARO, NOVIEMBRE 2025.

UNIVERSIDAD AUTÓNOMA DE QUERÉTARO

FACULTAD DE QUÍMICA

DOCTORADO EN CIENCIAS DE LA ENERGÍA

"EVALUACIÓN DEL RENDIMIENTO DE CELDAS SOLARES DE PEROVSKITAS BASE CALCOGENURO: ANÁLISIS DETALLADO DE $SrHfSe_3$ Y $BaZrS_3$ CON DIVERSAS CAPAS DE TRANSPORTE DE HUECOS Y PROPIEDADES SINTONIZADAS DE $ABSe_3$ (A = Ca, Ba; B = Zr, Hf) Y ALEACIONES DE Zr-$BaHfS_3$"

TESIS

QUE COMO PARTE DE LOS REQUISITOS PARA OBTENER EL
GRADO DE

PRESENTA

DHINESHKUMAR SRINIVASAN

DIRIGIDO POR

Dra. LATHA MARASAMY

SINODALES

Dra. Latha Marasamy
Presidente

Dr. José Santos Cruz
Secretario

Dr. Francisco Javier de Moure Flores
Vocal

Dra. Aruna Devi Rasu Chettiar
Suplente

Dr. José Álvaro Chávez Carvayar
Suplente

Centro Universitario, Querétaro, Qro.
noviembre, 2025
México

Contents

List of Figures

List of Tables

Resumen

Las perovskitas de haluro de plomo han alcanzado eficiencias fotovoltaicas de hasta 26.9 % en una década; no obstante, su comercialización se ve limitada por su toxicidad y su inestabilidad química. En este contexto, las perovskitas de calcogenuro (CP) emergen como una alternativa prometedora al combinar baja toxicidad, mayor estabilidad y propiedades optoelectrónicas favorables. En esta tesis se investiga el rendimiento de las celdas basadas en CP de $SrHfSe_3$ y $BaZrS_3$, empleando distintas capas transportadoras de huecos (HTL); y se analiza la capacidad de ajuste de ancho de banda prohibida en la familia $ABSe_3$ (A = Ca, Ba; B = Zr, Hf; X = Se) y en $BaHfS_3$ aleado con Zr. Mediante el ajuste sistemático del espesor de capas, la concentración de portadores y la densidad de defectos, se simularon 3043 dispositivos en SCAPS-1D. En la primera parte se evaluó la arquitectura FTO/$BaSnO_3$/$SrHfSe_3$/HTL/Au, examinando 41 HTL. La configuración con SnS alcanzó 27.87 % de eficiencia, atribuible a una alineación de bandas favorable, mayor resistencia a la recombinación y absorción extendida hacia el infrarrojo cercano. En la segunda parte se amplió el estudio a $ABSe_3$ (A = Ca, Ba; B = Zr, Hf); $CaZrSe_3$ y $BaZrSe_3$ superaron 30% de eficiencia, impulsadas por una banda prohibida más estrecha, absorción mejorada (53.60%), J_{SC} elevado (29 mA/cm^2) y una tasa de generación de 1.19×10^{22} $cm^{-2}s^{-1}$. En la tercera parte se exploró el $BaZrS_3$ aleado con Zr, obteniéndose eficiencias entre 14.26 % y el 21.94 % según la fracción de aleación; las mejoras se asociaron con un mayor potencial incorporado, incremento de la absorción (~51.05%) y reducción de la recombinación. En la cuarta parte se compararon los HTL tipo delafosita con el estándar Spiro-OMeTAD en dispositivos basados en $BaZrS_3$; los dispositivos con $CuFeO_2$ alcanzaron 28.34 % de eficiencia debido a un V_{OC} superior, favorecido por un mayor desdoblamiento de cuasi nivel de Fermi y por reforzamiento del campo electrostático interno. En conjunto, estos resultados delinean un marco de diseño y optimización para celdas solares CP estables, libres de plomo y de alto desempeño, y establecen lineamientos claros para la validación experimental futura.

Palabras clave: SCAPS-1D, perovskitas de calcogenuros, alineación de bandas de energía, tasa de recombinación, campo eléctrico

Abstract

Lead-halide perovskites have made significant advancements in solar cell efficiency, reaching up to 26.9% within a decade. However, their commercialization is hindered by concerns over toxicity and stability. In this context, chalcogenide perovskites (CPs) have emerged as a promising alternative, offering non-toxicity, enhanced stability, and remarkable optoelectronic properties. This thesis comprehensively investigates the performance of solar cells using $SrHfSe_3$ and $BaZrS_3$ CPs with different HTLs, as well as the tunable properties of $ABSe_3$ (A = Ca, Ba; B = Zr, Hf; X = Se) and Zr-alloyed $BaHfS_3$. By systematically tuning the layer thickness, carrier concentration, and defect density, we simulated 3,043 solar cells using SCAPS-1D, and the results are detailed in different sections. In the first part, we began with a device structure FTO/$BaSnO_3$/$SrHfSe_3$/HTL/Au, investigating the impact of 41 different HTLs on the solar cells' performance. Among them, SnS emerged as the best candidate, achieving a PCE of 27.87%, which is attributed to favorable band alignment, high recombination resistance, and extended near-infrared absorption. In the second part, we expanded our investigation to Se-substituted $ABSe_3$ (A = Ca, Ba; B = Zr, Hf) CPs. Detailed parameter analysis revealed that $CaZrSe_3$ and $BaZrSe_3$ achieved PCEs exceeding 30%. This performance is driven by their narrow bandgap, enhanced absorption (53.60%), high J_{SC} (29 mA/cm^2), and elevated generation rate of 1.19×10^{22} cm^{-2}s^{-1}. In the third part, we explored Zr-alloyed $BaZrS_3$, which yielded efficiencies ranging from 14.26% to 21.94% across various alloying compositions. These improvements stem from enhanced built-in potential, increased absorption (~51.05%) and stronger recombination resistance. In the fourth part, we evaluated the potential of $BaZrS_3$-based absorbers using a range of delafossite HTLs against the conventional Spiro-OMeTAD. Notably, devices based on $CuFeO_2$ achieved a PCE of 28.34%, attributed to significantly improved V_{OC} through enhanced quasi-Fermi level splitting and a strengthened internal electrostatic field. Overall, these four investigations provide a systematic framework for advancing stable, lead-free, and high-performance CPs solar cells, laying the groundwork for future experimental studies.

Keywords: SCAPS-1D, Chalcogenide Perovskite, Energy band alignment, Recombination rate, Electric filed

Student Statement of Responsibility

I declare that the data obtained in this research were generated during the development of my thesis work in an ethical manner, and I report the necessary details so that the results of this thesis can be reproduced in future research.

Finally, this thesis is an original work in which any collaboration or direct citation presented in the document has been properly declared and acknowledged.

Dhineshkumar Srinivasan

Dedication

This work is dedicated to all those who have been part of my journey, especially to my parents, my beloved brother and sister-in-law, my professor, my friends, and God, who have stood by me with unwavering support, love, and encouragement at every step of the way.

I thank my father, ***Mr. Srinivasan Kanthasamy****, for his silent strength and sacrifices. Though he could not always be present during significant moments, he taught me the value of patience, listening, and the importance of seeking answers through knowledge and self-reliance.*

I am deeply grateful to my mother, ***Mrs. Kaliswari Srinivasan****, whose love, understanding, and tireless dedication have been my greatest source of strength. Her encouragement and wisdom ignited my curiosity, inspired me to overcome obstacles, and guided me to embrace the pursuit of knowledge with humility and determination.*

To my brother, ***Dr. Vigneshwaran Srinivasan****, and my sister-in-law,* ***Mrs. Nithya Sree Rajamanikam****, thank you for walking beside me with love and belief. Your presence and support have been invaluable, and I carry the lessons I've learned from both of you with gratitude.*

I wish to express my deepest and most heartfelt gratitude to my thesis director, ***Dr. Latha Marasamy****, whose guidance, kindness, and unwavering support have been the foundation of my academic journey. From the very first day I nervously sat before* ***Dr. Marasamy*** *during my PhD interview, she looked beyond my fears, mistakes, and shortcomings. Rather than seeing only my weaknesses, she recognized the spark of determination within me to pursue a PhD. In that moment,* ***Dr. Marasamy*** *chose to believe in me, giving me a chance and opening the door to a future I had only dreamed of. Very few professors would extend such trust, and for that act of faith, I will remain forever indebted to her. Even during the most challenging times in* ***Dr. Marasamy's*** *life, when she faced personal health issues abroad, she never ceased to care for me like a family member. She guided and helped me through moments of struggle with delayed stipends, immigration procedures, housing arrangements, and the everyday challenges of living in a foreign land. When my financial situation became uncertain, she carried my burdens as though they were her own, ensuring I was never left stranded. In moments when I felt lost,* ***Dr. Marasamy*** *transformed from a mentor into an elder sister, holding my hand and helping me navigate both academic and personal pathways. At my weakest points, struggling with simulations, facing unfamiliar software, and disheartened by repeated rejections of my research articles,* ***Dr. Marasamy*** *never lost patience with me. Instead, she stood by my side,*

day and night, teaching and guiding me with the tenderness of a mother helping her child take their first steps. ***Dr. Marasamy*** *tirelessly corrected my work, no matter how many revisions it required, and inspired me to rise again every time I stumbled. Her sacrifices of time, health, and precious moments with her own family were given selflessly to help me grow. It was* ***Dr. Marasamy's*** *unshakable faith in me that provided the strength to publish my research and ultimately bring this thesis to completion. This thesis is not just a record of my academic endeavor; it is a testament to* ***Dr. Marasamy's*** *extraordinary mentorship, compassion, and dedication. While my parents gave me life, it is* ***Dr. Marasamy*** *who has profoundly shaped my future through her devotion, sacrifices, and love. No words can fully capture the depth of my gratitude, but my heart will carry the memory of her kindness and sacrifices for as long as I live. To this extraordinary professor, I owe not just this degree but also the strength and confidence to move forward in life. I am also grateful to all the teachers and professors who walked this path with me.*

Finally, I am grateful to my dear friends, ***Mohan Raj, Gokul Raj, Sudhakar, Gowtham, Swathi, Gayathri, Vairamuthu, Srikanth, Arshad, Logeshwaran, Naveen, Santhra, Kaviya Tracy, Eupsy Navis, Evangeline Linda, and Valentina Sneha*** *for their enduring friendship and support. Each of you played a special role in shaping this journey, and I carry your encouragement in my heart always.*

Acknowledgement

I am deeply grateful to the **National Council of Humanities, Science and Technology (CONAHCyT)** for the funding and support provided throughout the course of this research.

I would also like to extend my sincere thanks to the **Autonomous University of Querétaro (UAQ)** and the **Faculty of Chemistry** for providing the necessary infrastructure and support, both academic and personal, that have been essential throughout my journey.

I would like to express my sincere gratitude to my thesis director, **Dr. Latha Marasamy**. Her invaluable guidance, steadfast encouragement, and unwavering support have been instrumental throughout my doctoral research journey. **Dr. Marasamy's** profound knowledge and insightful advice have not only shaped this thesis but have also significantly influenced my personal and professional development. I am truly thankful for her tireless mentorship, which has made this achievement possible.

I am especially thankful to the members of my examination committee, **Dra. Aruna Devi Rasu Chettiar, Dr. José Álvaro Chávez Carvayar, Dr. Francisco de Moure Flores, Dr. José Santos Cruz,** and my mentor **Dra. Claudia Elena Pérez García**, for being an integral part of this project and for their valuable insights and contributions.

I extend my heartfelt gratitude to **C. Nathaly González Miranda**, **Lic. Arlette Torres López**, **Erika Vargas Mosqueira** and the **Faculty of Chemistry,** UAQ for their continual support and guidance during this journey. I'm grateful for your constant kindness and helpfulness.

Finally, I would like to express my sincere appreciation to **Prof. Marc Burgelman** from ELSI, University of Gent, Belgium, for providing access to the **SCAPS-1D** simulation software, which was vital to this research.

Publications of JCR-Indexed Journals During the PhD Period

1. **D. Srinivasan**, A.-D. Rasu Chettiar, K.T. Arockiadoss, L. Marasamy, "A new class of $SrHfSe_3$ chalcogenide perovskite solar cells with diverse HTMs: Theoretical modelling towards efficiency enhancement", ***Solar Energy Materials and Solar Cells*** 290 (2025) 113727. **https://doi.org/10.1016/j.solmat.2025.113727.**
2. **D. Srinivasan**, A.-D. Rasu Chettiar, E.N. Vincent Mercy, L. Marasamy, "Scrutinizing the untapped potential of emerging $ABSe_3$ (A = Ca, Ba; B = Zr, Hf) chalcogenide perovskites solar cells", ***Scientific Reports*** 15 (2025) 3454. **https://doi.org/10.1038/s41598-024-80473-4.**
3. **D. Srinivasan**, A.-D. Rasu Chettiar, L. Marasamy, "Engineering $BaHfS_3$ with Zr alloying to improve solar cell performance: Insights from SCAPS-1D simulations", ***Materials Science and Engineering: B*** 315 (2025) 118126. **https://doi.org/10.1016/j.mseb.2025.118126**.
4. **D. Srinivasan**, A.-D. Rasu Chettiar, S. Rajendran, H. Bencherif, P. Sasikumar, J. Ramanujam, L. Marasamy, "Boosting the efficiency of $BaZrS_3$ solar cells with inorganic delafossite HTLs: A promising alternative to Spiro-OMeTAD", ***Inorganic Chemistry Communications*** (2025) 114997. **https://doi.org/10.1016/j.mseb.2025.118126**.
5. E.N. Vincent Mercy, A.D Rasu Chettiar, **D. Srinivasan**, L. Marasamy, "Unlocking the Potential of Emerging $SrZrSe_3$ Solar Cells with Diverse Inorganic Metal Sulfide Hole Transport Layers", ***Energy Technology*** 13 (2025). **https://doi.org/10.1002/ente.202401459**.
6. E.N. Vincent Mercy, **D. Srinivasan**, L. Marasamy, "Emerging $BaZrS_3$ and $Ba(Zr,Ti)S_3$ Chalcogenide Perovskite Solar Cells: A Numerical Approach Toward Device Engineering and Unlocking Efficiency", ***ACS Omega*** 9 (2024) 4359–4376. **https://doi.org/10.1021/acsomega.3c06627.**
7. E. Linda, A.D Rasu Chettiar, V. S. George, R. Manisekaran, **D. Srinivasan**, A. B. Martínez, M. K. Hossain, Md. Ferdous Rahman, J. Á. Chávez Carvayar, S. A. Tomás, Á. Mantilla, L. Marasamy, "Exploring the physical properties of pristine γ-In_2S_3 and its influence on Ba doping for photocatalytic degradation of 2,4-D herbicide", ***Journal of Photochemistry and Photobiology A: Chemistry***, 456 (2024) 115831. **https://doi.org/10.1016/j.jphotochem.2024.115831.**

1. Introduction

1.1. Sustainable energy future

Renewable energy encompasses power generated from natural sources that are consistently replenished through ongoing environmental processes. These sources are considered practically infinite on a human timescale due to their constant availability. Examples of renewable energy include solar power, wind energy, hydropower, geothermal energy, biomass, and biogas. In contrast to fossil fuels, such as coal, oil, and natural gas, which take millions of years to form and release harmful greenhouse gases when burned, renewable energy is essential for a sustainable future [1]. As global energy consumption continues to escalate, driven by population growth and rapid industrialization, the negative environmental impacts of fossil fuel use, such as severe air pollution, water contamination, and the intensification of global warming, are raising serious concerns. These issues have prompted governments, industries, and environmental organizations around the world to prioritize a transition toward renewable energy solutions that are safer, more sustainable, and more environmentally friendly [2]. The advancement of renewable energy technologies not only reduces our reliance on finite natural resources but also helps combat environmental degradation by lowering the emissions of greenhouse gases and minimizing pollution.

1.2. Solar energy

Among the various types of renewable energy, solar energy stands out as one of the most promising and fastest-growing technologies. Its vast availability, inexhaustible supply, and relatively low environmental footprint make it a cornerstone of the transition to sustainable energy systems [3]. The Earth is continuously flooded with an enormous amount of energy from the sun; in fact, the solar energy received in just one hour could meet the entire global energy demand for a whole year. If this immense resource could be captured and utilized efficiently, even in small portions, it would be more than adequate to meet the increasing global energy needs [4]. Moreover, this would significantly reduce our reliance on fossil fuels and help lower carbon dioxide emissions that contribute to climate change.

In line with this global trend, Mexico has demonstrated remarkable growth in its solar energy sector over the past decade. With its favorable geographic location within the solar belt, Mexico receives one of the highest levels of solar irradiance in the world, averaging between 4.5 and 6.5 $kWh/m^2/day$, making it an ideal candidate for large-scale solar energy deployment. In recent years, solar power has become one of the most rapidly expanding sources of electricity

in the country, contributing significantly to the national grid and playing a vital role in Mexico's clean energy targets.

By the end of 2024, Mexico had installed over 9 GW of solar capacity, placing it among the top solar producers in Latin America. This progress aligns with global trends, as solar photovoltaic (PV) technology has consistently outpaced wind and fossil fuel sources in new capacity additions. However, compared to major solar adopters like China, the United States, or India, Mexico still holds untapped potential in fully capitalizing on its solar resources. Continued investment in PV technologies, infrastructure, and policy reforms could elevate Mexico's position as a regional leader in solar energy production, contributing not only to its own sustainability goals but also to the broader global efforts to decarbonize the energy sector.

1.3. Photovoltaic technology

One of the key advantages of solar energy is its wide accessibility, especially in remote or rural regions where conventional energy infrastructure is often limited, outdated, or economically unviable. In these regions, solar power can serve as a practical and cost-effective energy solution. PV technology enables the direct conversion of sunlight into electricity and has proven to be highly efficient and increasingly affordable [3]. The conversion process is straightforward and involves few mechanical components, which leads to reduced maintenance needs and greater reliability over time. Moreover, PV systems are highly flexible in their application, as they can be scaled to fit various energy demands ranging from small residential rooftop installations to large solar farms that power entire towns or industrial complexes [4]. This versatility makes solar energy an attractive option for a wide array of energy needs across diverse geographic and socioeconomic contexts [5,6].

1.4. Problem statement

In the past decade, significant advancements have been made in the development of PV materials, especially with the discovery and refinement of lead halide perovskites [LHPVs] [7–9].These materials, often represented by the general formula $APbX_3$ (where A can be methylammonium (MA), formamidinium (FA), or cesium (Cs), and X can be iodine (I), bromine (Br), or chlorine (Cl)), have dramatically changed the landscape of solar cell technology. They exhibit outstanding optoelectronic characteristics, including high absorption capabilities, long carrier diffusion lengths, and relatively low manufacturing costs [10,11]. The journey of perovskite solar cells started gaining attention in 2009 when an initial prototype achieved a power conversion efficiency (PCE) of just 3.8%, utilizing a liquid electrolyte-based

hole transport layer (HTL) [12]. This initial effort marked the beginning of a rapid period of innovation. By 2012, a solid-state HTL called spiro-OMeTAD replaced the liquid version, resulting in a significant increase in PCE to 9.7% [13]. The field continued to progress swiftly, and by 2023, [LHPVs] reached a certified PCE of 26.9% by 2025[14]. This extraordinary improvement ranks them among the most efficient PV materials currently under active development. Their impressive performance, coupled with low material and processing costs, has made LHPVs a focal point for research and development aimed at achieving high-efficiency, next-generation solar technologies [10,11]. Nevertheless, despite their promising attributes, several substantial challenges continue to hinder the commercial scale deployment of LHPVs. The most pressing issues include the inherent toxicity of lead (Pb) and the material's susceptibility to environmental degradation, particularly when exposed to moisture, high temperatures, or prolonged sunlight. These limitations pose significant safety and durability concerns, especially for large-scale applications or those requiring long-term stability [15–19].

To address challenges associated with traditional perovskite materials, scientists are investigating various lead-free alternatives that retain the beneficial properties of these compounds while minimizing their environmental and health impacts [20]. Among these alternatives, materials incorporating tin (Sn) and germanium (Ge) as substitutes for Pb have received considerable attention. Notable examples include compounds such as $MASnI_3$, $CsSnI_3$, $FASnI_3$, $CsGeI_3$, $MAGeI_3$, $FAGeI_3$ and $CsSn_{0.5}Ge_{0.5}I_3$. These materials are valued for their electronic configurations (s^2p^2), which closely resemble those of lead-based perovskites, as well as for their high carrier mobility and suitable bandgaps [21]. These features are essential for efficient light absorption and effective charge transport in solar cells. However, despite their potential, perovskites based on Sn and Ge encounter significant stability challenges. Both Sn^{2+} and Ge^{2+} ions are susceptible to oxidation in ambient conditions, leading to the formation of Sn^{4+} and Ge^{4+} states that considerably undermine the performance of the materials. Additionally, the relative scarcity and high cost of Ge pose further barriers to widespread adoption [22].

To explore more stable and less toxic alternatives, researchers have investigated perovskites that contain trivalent cations like bismuth (Bi^{3+}) and antimony (Sb^{3+}). These elements offer greater chemical stability and significantly lower toxicity compared to lead. Unfortunately, Bi and Sb based perovskites typically show reduced PCEs [20,23]. This limitation is mainly due to their low-dimensional crystal structures, which result in poor optoelectronic behavior, such as low charge carrier mobility and high exciton binding energies.

Consequently, while these materials are safer and more stable, their performance has not yet reached the levels necessary for competitive commercial applications [19,20,24].

To resolve these structural limitations, scientists have investigated a class of materials known as halide double perovskites (HDPs), characterized by the formula $A_2B^+B^{3+}X_6$. In this structure, two Pb^{2+} ions are replaced with a combination of one monovalent (B^+) and one trivalent (B^{3+}) cation, which preserves the overall charge balance and enables the formation of stable, three-dimensional crystal lattices [25]. This approach has led to the development of compounds like $Cs_2AgBiBr_6$, $Cs_2NaBiCl_6$, $(CH_3NH_3)_2AgBiBr_6$, and $(CH_3NH_3)_2KBiCl_6$. These double perovskites offer benefits in terms of environmental friendliness and structural stability [26]. However, their PV performance is still limited by challenges such as heavy effective masses for charge carriers, relatively wide band gaps exceeding 2 eV, and inadequate charge transport capabilities [27].

Given these challenges, research has increasingly focused on antimony-based perovskites, including compounds like $Cs_2SbCuCl_6$, $Cs_4SbCuCl_{12}$, $Cs_2SbAgCl_6$, Cs_2SbAgI_6, and $Cs_2SbAgBr_6$. These materials have gained interest for their thermal resilience and reasonable conductivity for charge carriers. Nevertheless, they continue to suffer from limitations like large bandgaps, elevated exciton binding energies, and bulky charge carrier masses, all of which hinder their ability to achieve high PCEs [26,27]. In addition to perovskite materials, scientists are examining other light-absorbing compounds as possible for future PV technologies. These include ternary II-IV-N_2 nitrides like $ZnSnN_2$, binary halides such as InI_3 and BiI_3, and chalcogenide containing elements such as Bi, Sb, Pb, and Ag, as well as hybrid organic-inorganic chalcogenides and complex multinary semiconductors like $Cu_2BaSnSe_4$ and Zn_3P_2. While these materials show promise in terms of potential properties, most have not yet achieved PCEs exceeding 8%, indicating that further research is needed to unlock their capabilities.

To sum up, LHPSCs have achieved high PCEs but face significant challenges due to Pb toxicity and poor environmental stability. Lead-free alternatives such as Sn and Ge offer similar optoelectronic properties but are prone to rapid degradation. Safer options incorporating Bi and Sb, and halide double perovskites provide greater stability but generally suffer from lower efficiencies. Other emerging materials remain underperforming. Balancing efficiency, stability, and safety continues to be the challenge in developing next-generation solar cells [19,20]. Therefore, researchers are investing in alternative materials that combine the excellent

optoelectronic properties of LHPSCs with the non-toxic nature of oxide perovskites while addressing current limitations. Recently, CPs have attracted attention as promising semiconductors due to their outstanding optoelectronic properties. These materials follow the general formula ABX_3, where A is a group II cation (e.g., Ba^{2+}, Ca^{2+}, Sr^{2+}), B is a group IV transition metal (e.g., Ti^{4+}, Zr^{4+}, Hf^{4+}), and X is a chalcogen (S, Se). CPs are composed of non-toxic, earth-abundant elements and exhibit high thermal and chemical stability [28,29]. However, CP materials are still in the early stages of development. Experimental research on them is time-consuming and costly, requiring advanced characterization techniques [29]. Therefore, theoretical modeling is essential for establishing a foundation and efficiently guiding experimental efforts. In this thesis, we investigate novel chalcogenide materials using SCAPS-1D simulation to explore their potential for PV applications [29].

1.5. Justification

In this thesis, we focus on sulfur-based CPs, specifically $BaZrS_3$ and $BaHfS_3$, as promising absorber materials for PV applications [28,30–33]. These materials are composed of non-toxic, earth-abundant elements displaying high stability, making them attractive for efficient solar energy absorption owing to their direct bandgaps, which range from ~1.7 eV to 1.95 eV. In addition, they possess exceptional optoelectronic properties such as high absorption coefficient exceeding 10^5 cm^{-1}, supreme charge carrier mobilities (~30 $cm^2/V.s$) and predominant p-type conductivity. Their remarkable stability under various environmental conditions, including moisture, prolonged light exposure, and thermal fluctuations further positions them as strong candidates for long term PV performance [34–42]. To enhance these desirable properties, we explore B-site alloying as an effective strategy for tuning the optoelectronic behavior of these materials. In particular, we investigated Zr-alloying in $BaHfS_3$ following the general formula $BaHf_{1-x}Zr_xS_3$ (where x = 0.25, 0.5, and 0.75). Experimental results indicate that these alloyed compounds enable fine-tuning of the bandgap, effectively broadening the absorption spectrum while retaining favorable charge transport characteristics [41,43,44]. Building on this compositional engineering approach, we further investigated chalcogen-site substitution by replacing sulfur (S) with selenium (Se). This modification is known to effectively reduce the bandgap and extend light absorption into the near-infrared region, a key attribute for next-generation solar cell technology [45,46]. In recent theoretical and experimental work, several selenium-based CPs, including $CaZrSe_3$, $BaZrSe_3$, $CaHfSe_3$, $BaHfSe_3$, and $SrHfSe_3$, have been studied [47–52]. These materials exhibit bandgaps ranging from 1.35 eV to 1.75 eV, closely matching the optimal range for single-junction solar cells.

They maintain high absorption coefficients, cost-effective to fabricate, and demonstrates strong resistance to environmental degradation, making them highly promising for real-world PV performance [47,51,52].

Optimizing the absorber layer is crucial, but the overall performance of a PV device relies significantly on the charge transport layers, namely the electron transport layer (ETL) and hole transport layer (HTL). The ETLs are responsible for efficiently extracting and transporting photogenerated electrons to the front electrode, while minimizing recombination losses. Conversely, the HTL aids in hole collection at the back contact by enhancing the formation of the electric field and reducing interfacial energy barriers. This process improves charge separation and collection [53–55]. In our research, we selected TiO_2 and $BaSnO_3$ as ETL materials because of their excellent electron mobility, chemical stability, and appropriate energy level alignment with our selected absorber materials [56–61]. For the HTL, we conducted an extensive study on a diverse set of 46 HTLs including inorganic semiconductors (MoS_2, Cu_2S, Sb_2S_3, CuO, SnS, $CuBiS_3$, Cu_2SnS_3, Cu_2SbS_2, Cu_2BaSnS_3, CIGS, CZTS, CZGS, CuS, CoO, WS_2, FeS_2, $CaFe_2O_4$, MoO_3, $YFeO_3$, VO_x, $BiVO_4$, SnS_2, Sb_2Se_3, Ce_2Se_3, Mg_2Si and NiO), polymers (P_3HT, P_3Cpent, CPE-K, P_2, P_3, P_1, PEDOT:PSS, PCPDT-T, PCPDT-2T, TFB, PTAA, PFS, g-C_3N_4, Spiro-OMeTAD), MXenes (Zr_2CO_2, Hf_2CO_2, Ti_2CO_2) and delafossite HTLs (e.g., $CuFeO_2$, $CuGaO_2$, $CuAlO_2$).

Each class of HTL offers distinct advantages: inorganic semiconductors and delafossites are recognized for their thermal and chemical robustness, as well as high hole mobility. Polymers enable flexible fabrication, tunable electronic properties, and good interfacial compatibility. Meanwhile, MXenes are notable for their intrinsic p-type conductivity and excellent optical transparency [62–70]. By evaluating these materials based on band alignment, charge transport properties, and interface compatibility with our CPs absorbers, we aim to identify the most suitable ETLs and HTLs for high-efficiency, stable solar cell architectures through theoretical studies.

Theoretical approaches in solar cell design are essential for understanding how they function, identifying suitable device configurations more efficiently and analyzing the impact of each layer on the overall device performance. Importantly, modelling solar cells before fabrication is crucial, as it saves time, resources, and effort. Various software tools are available for modeling solar cell performance, each with unique capabilities to study the relationship between structural parameters and efficiency. Popular options include SETFOS, SILVACO-

ATLAS, COMSOL, Wx-AMPS, and SCAPS-1D. In our research, we utilized SCAPS-1D (version 3.3.10), a program developed by Professor Marc Burgelman at Ghent University, Belgium. While other tools like SILVACO-ATLAS and COMSOL offer advanced multiphysics capabilities and complex three-dimensional device modeling, SCAPS-1D is notable for its accessibility, user-friendly design, and ability to simulate solar cell performance accurately. Additionally, SETFOS and GPVDM provide strong functionalities for optical and electrical modeling. However, SCAPS-1D specializes in detailed electro-optical analysis of multi-layered structures, making it an excellent choice for our research. Furthermore, SCAPS-1D is freely available, making it ideal for both academic and industrial researchers. The software enables detailed simulations of solar cell structures with up to seven layers and supports batch processing for efficient data analysis. Moreover, SCAPS-1D allows researchers to modify key material and device parameters, such as bandgap, carrier density, defect levels, electron affinity, and mobility, offering significant customization for diverse research objectives. It also supports simulations under various lighting conditions, including AM0, AM1.5G, and monochromatic sources, allowing for in-depth analysis of performance in different environments. The program uses fundamental semiconductor equations, including Poisson's equation, carrier continuity equations, and drift-diffusion equations, to model device behavior. These computational strengths make SCAPS-1D a reliable and versatile tool for studying PV devices and improving their efficiency [71–74].

We analyzed the material properties of each layer by varying key parameters, such as carrier concentration, defect density, and thickness. We also examined the influence of back contacts in all the simulated solar cells by tuning the metal work functions. To gain a deeper understanding of solar cell performance, we employed various analyses, including recombination profiles, electric field distribution, capacitance-voltage (C-V), capacitance-frequency (C-F), and quantum efficiency (QE). Additionally, we evaluated the impact of series resistance, shunt resistance, and working temperature on the performance of the high PCE solar cells. This research provides a pathway for developing novel, cost-effective, non-toxic, and highly stable solar cells based on CPs absorbers, featuring an efficient device configuration suitable for the PV industry.

2. Background (Antecedents)

2.1. Mechanism of Solar Cell

A solar cell, also known as a PV cell, functions by converting sunlight directly into electricity through the PV effect. The fundamental structure of a solar cell consists of several layers, each with a specific role in the conversion process. **Fig. 1**. Illustrates the schematic structure and working mechanism of a typical solar cell, include the following layers in a superstrate configuration: soda lime glass substrate (SLG), Fluorine-doped tin oxide (FTO), ETL, absorber layer, HTL, and a metal contact.

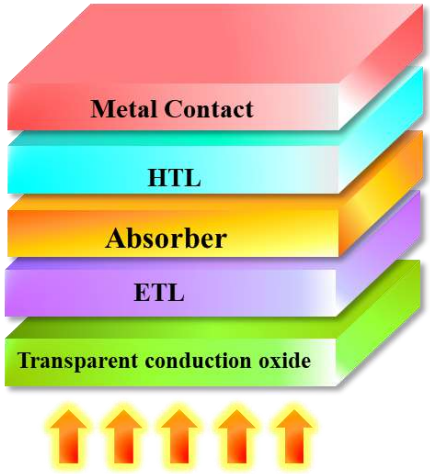

Fig. 1. Working Mechanism of Solar Cell

Light Absorption and Transmission

When sunlight hits the solar cell, it first passes through the SLG. This layer serves as a mechanical support and is transparent, allowing light to reach the absorber layers within the solar cell. SLG has the transparent conductive oxide (TCO) layer, usually composed of FTO. This layer functions as a front electrode, being both electrically conductive and transparent, which enables light to pass through it.

Charge Transport

After the light passes through the FTO layer, it reaches the n-type ETL. This layer facilitates the movement of electrons while blocking holes, ensuring selective charge transport. The ETL is crucial for transferring the photo-generated electrons from the absorber layer to the FTO contact.

Charge Generation

The absorber layer is the core component of the solar cell where the actual light absorption and conversion of electrical energy occur. When sunlight reaches this layer, photons are absorbed, exciting electrons and creating electron-hole pairs. This process is known as the PV effect.

Built-in-Electric Field Charge Separation

A built-in electric field is generated at the p-n junction, driving the separation of the electron-hole pairs. Electrons move toward the ETL layer, while holes are directed toward the HTL layer. The p-type HTL allows the movement of holes while blocking electrons, effectively transferring holes to the metal contact. This selective transport enhances efficiency by minimizing recombination losses.

Charge Collection and Electricity Generation

Once the charge carriers are separated, they are collected by their respective electrodes. Electrons travel from the absorber to the FTO and are extracted as current, while holes are collected by the metal contact through the HTL. This movement of electrons and holes through an external circuit generates an electric current, which can be harnessed as usable electric power.

In summary, the solar cell works by allowing sunlight to pass through a TCO layer, reaching an absorber layer that generates charge carriers. These carriers are separated by an internal electric field and are transported by the HTL and ETL layers before being collected at the contacts. The flow of these carriers through an external load generates the usable electrical energy produced by the solar cell [75,76].

2.2. Role of solar cells

2.2.1. Transparent Conductive Oxides (TCOs)

TCOs are critical components in solar cell architectures due to their dual functionality, providing both high optical transparency and excellent electrical conductivity. These materials facilitate the maximum transmission of visible light to the absorber layer while efficiently collecting and transporting photo-generated charge carriers to the external circuit. Commonly used TCOs include Indium Tin Oxide (ITO), FTO, and Aluminium-doped Zinc Oxide (AZO),

Among these, FTO is particularly attractive for PV applications due to its thermal stability, chemical durability, and cost-effectiveness.

FTO typically exhibits high transparency (>80%) in the visible range and possesses low series resistance, ranging from 10 to 15 Ω/sq, making it suitable for use in various solar technologies, including dye-sensitized and perovskite solar cells. Their ability to withstand high-temperature processing (>500°C) enables integration with manufacturing processes such as screen-printing and sintering, which are common in solar cell fabrication. Additionally, FTO exhibits good mechanical and environmental stability, making it suitable for long-term applications. These features make FTO a widely used and reliable TCO for enhancing the efficiency and longevity of solar cells [77,78].

2.2.2. Electron transport layer (ETL)

In a solar cell, the ETL plays a pivotal role in enhancing performance by effectively extracting and transporting electrons from the absorber layer to the external circuit while minimizing recombination losses. A well-designed ETL should possess several key features, including high electron mobility, excellent optical transparency, proper energy level alignment with the absorber material, and the ability to block holes to prevent recombination. To meet these requirements, materials such as TiO_2, SnO_2, ZnO, and PCBM are commonly employed for high-performance solar cells [79–81].

Among these materials, TiO_2 has emerged as the most extensively used ETL, owing to its long-standing application across various PV technologies, including dye-sensitized and perovskite solar cells. Its wide bandgap of ~3.2 eV allows for strong optical transparency, enabling most visible light to pass through the ETL. In addition, TiO_2 offers high electron mobility (~0.1 to 4 cm^2/V. s) and exhibits excellent chemical and thermal stability, making it suitable for stable, long-lifetime devices. Furthermore, it effectively blocks holes, reduces recombination, and aligns well with the energy levels of perovskite materials to ensure directional electron flow [60].

On the other hand, $BaSnO_3$ has recently gained considerable attention as an advanced ETL candidate for perovskite solar cells owing to its low lattice mismatch with perovskite materials. This structural compatibility leads to improved interface quality and reduced defect density, ultimately improving device performance. Moreover, $BaSnO_3$ exhibits exceptionally high electron mobility (~ 300 cm^2/V. s) and a wide bandgap (~ 3.1 eV), ensuring excellent electrical conductivity and transparency. Its remarkable thermal and environmental stability

further underlines the development of high-efficiency and long-term stable perovskite solar cells [57,58]. Therefore, the strategic selection and engineering of ETLs such as TiO_2 and $BaSnO_3$ are crucial for enhancing both the efficiency and durability of solar cell technologies.

2.2.3 Absorber layer

In solar cells, the absorber layer is one of the most critical components, as it is responsible for capturing sunlight and converting it into electrical energy. This layer performs several key functions: it absorbs light, generates charge carriers (electrons and holes), and enables the separation and transport of these carriers to the external circuit. The choice of absorber material directly influences how efficiently a solar cell can convert sunlight into electricity.

Over the years, a variety of absorber materials have been developed, including Silicon (Si), Gallium Arsenide (GaAs), Cadmium Telluride (CdTe) and Copper Indium Gallium Selenide (CIGS) [82,83]. GaAs has achieved the highest reported PCE of 27.6%, but its high-cost limits large-scale adoption. Si-based solar cells continue to dominate the market; however, their production requires thick absorbers, which makes them relatively expensive. On the other hand, CdTe and CIGS are widely used in commercial applications; however, their reliance on scarce elements raises concerns about long-term sustainability. Although earth-abundant alternatives such as CZTSSe have been investigated, their efficiencies remain lower than those of conventional absorbers. Interestingly, the rapid progress of perovskite solar cells (PSCs) has stirred excitement in the PV industry. Perovskites first entered the PV field in 2009, replacing dyes in dye-sensitized solar cells and achieved a modest PCE of 3.8% using a liquid electrolyte. A major breakthrough occurred in 2012, when researchers replaced the liquid electrolyte with a solid-state Spiro-OMeTAD HTL, resulting in a significant increase in PCE to 9%. Since then, continuous advancements in film deposition techniques, material composition, and surface/interface engineering have pushed perovskite efficiency to 26.9% by 2025 [84–86].

Despite the remarkable progress made in perovskite solar cell technology, challenges remain regarding long-term stability and toxicity, primarily due to the presence of Pb. As a result, researchers are actively searching for new materials that can match or exceed the desirable properties of lead-based perovskites while also offering improved environmental stability and cost-effectiveness [8,19]. In recent years, CPs have emerged as a promising alternative due to their non-toxic nature, stability, abundance on Earth, and excellent

optoelectronic characteristics. These materials adhere to the ABX_3 formula, where A represents a group II cation (e.g., Ba^{2+}, Ca^{2+}, Sr^{2+}), B is a group IV transition metal ion (e.g., Ti^{4+}, Zr^{4+}, Hf^{4+}), and X denotes chalcogen elements such as sulfur (S) or selenium (Se) [28–31]. In 2015, Sun et al. identified several ABX_3 CP candidates that showed potential as high-efficiency solar absorbers [87]. Among them, $BaZrS_3$ has gained significant attention due to its appealing optoelectronic properties. However, early synthesis methods required very high temperatures, around 900-1000°C, raising concerns about compatibility with other standard solar cell components such as substrates and ETLs. For example, Zhonghai Yu et al. synthesized $BaZrO_3$ films at 1050°C, converting them to $BaZrS_3$ through sulfurization at high temperatures between 650 and 1100°C. These extreme conditions posed challenges for the practical fabrication of devices [88]. Fortunately, recent research has made significant progress in reducing the synthesis temperature. Comparotto et al. demonstrated that $BaZrS_3$ thin films can be produced using a sputtering-sulfurization approach at temperatures below 600°C [89]. Yu et al. further improved this process, achieving synthesis at just 500°C by adjusting the reaction chemistry [90]. Additionally, Lorenza Ramagnoli et al. [41], proposed a straightforward low-temperature route, while Yang et al. [35] and Zilevu et al. [91] developed colloidal synthesis methods that operate at temperatures below 350°C, making them especially attractive for solution-based processing. These advancements represent a significant breakthrough by lowering synthesis temperatures to levels compatible with existing PV manufacturing processes, enhancing the practical viability of $BaZrS_3$ and opening the door for further development of high-performance solar cells. However, it is important to note that, to date, only one report has been published regarding the fabrication of $BaZrS_3$ solar cells, which achieved a PCE of merely 0.17% [92]. This indicates that, while the materials hold great promise, further research and development are crucial to fully realize their potential in PV applications.

Recent studies have identified S and Se-based CPs with the general formula ABX_3 (where A = Ba, Ca, Sr; B = Zr, Hf; X= S, Se), as highly promising absorber materials for next-generation PV. Among them, $BaZrS_3$ and $BaHfS_3$ have garnered attention due to their non-toxic, earth-abundant nature, direct bandgaps (~1.7 – 1.95 eV), and high absorption coefficient (>10^5 cm^{-1}) for photon energies >1.97 eV. These materials also exhibit notable p-type conductivity, stable charge carrier mobilities of ~30 cm^2/V. s, and excellent stability to moisture, light, and heat, making them suitable for long-term solar performance. To further optimize these properties, researchers have explored B-site alloying through $BaHf_{1-x}Zr_xS_3$ (where x = 0.25, 0.5, 0.75), enabling precise tuning of the bandgap and enhancing light absorption and charge transport

[28,41,42,44]. In addition, substituting chalcogens of S to Se has resulted in optimized bandgaps ranging from 1.35 to 1.75 eV, which is ideal for single-junction solar cells [48].

Based on these studies, $BaZrS_3$, $BaHf_{1-x}Zr_xS_3$, and $ABSe_3$ have emerged as promising absorber materials due to their strong light absorption, cost-effective synthesis, and excellent environmental stability, making them viable candidates for efficient, stable, and sustainable PV devices.

2.2.4. Hole transport layer (HTL)

HTLs play a vital role in solar cell architectures by efficiently collecting holes from the absorber layer, transporting them to the back contact, preventing charge recombination, and facilitating energy level matching at the interface. A well-optimized HTL significantly enhances the device performance by improving charge extraction and reducing energy losses. Commonly used HTLs include NiO, Cu_2O, MoO_3, and Spiro-OMeTAD, each of which contributes to effective charge transport and energy alignment [69,70]. To identify high-performing HTLs compatible with our CPs absorbers, we conducted a comprehensive investigation of 46 HTL materials from diverse material classes, including inorganic semiconductors, organic polymers, MXenes, and delafossites.

Inorganic HTLs such as MoS_2, Cu_2S, Sb_2S_3, CuO, SnS, $CuBiS_3$, Cu_2SnS_3, Cu_2SbS_2, Cu_2BaSnS_3, CIGS, CZTS, CZGS, CuS, CoO, WS_2, FeS_2, $CaFe_2O_4$, MoO_3, $YFeO_3$, VO_x, $BiVO_4$, SnS_2, Sb_2Se_3, Ce_2Se_3, Mg_2Si and NiO are known for their high thermal stability, strong chemical durability, and high hole mobility, making them attractive candidates for stable and efficient devices [69,70]. Polymers such as P_3HT, P_3Cpent, CPE-K, P_2, P_3, P_1, PEDOT:PSS, PCPDT-T, PCPDT-2T, TFB, PTAA, PFS, g-C_3N_4, Spiro-OMeTAD provide excellent processability, tunable energy levels, and compatibility with flexible substrates [65,66]. MXene-based HTLs (Zr_2CO_2, Hf_2CO_2, Ti_2CO_2) offer promising features such as intrinsic p-type conductivity and high optical transparency [67,68]. Additionally, delafossite oxides ($CuFeO_2$, $CuGaO_2$, $CuAlO_2$) exhibit good band alignment and chemical stability, positioning them as emerging HTLs for next-generation devices [62–64].

Each HTL material was analyzed based on critical criteria such as energy band alignment with the absorber, charge transport characteristics, and interfacial compatibility. These theoretical evaluations support the development of optimized solar cell structures with improved PCEs and long-term stability for CPs solar cells.

2.2.5. Metal contacts

Metal contacts are essential components in solar cell devices, significantly impacting charge extraction and the overall performance. Located at the terminal ends of the device structure, these contacts are responsible for collecting charges from the transport layers, completing the external high electrical circuit, and minimizing resistive losses. An ideal metal contact should possess high electrical conductivity and a suitable work function to enable selective charge extraction. Additionally, it must demonstrate chemical stability and strong compatibility with adjoining transport layers. Effective metal contacts also need to minimize carrier recombination at their interface to improve V_{OC} and FF. Traditionally, metals such as gold (Au), silver (Ag), and platinum (Pt) are preferred due to their excellent conductivity and inertness. However, their high cost and potential interfacial instability in certain architectures highlight the need for alternative materials.

Recent studies have examined various emerging metal contacts with tailored work functions to improve charge selectivity and interface energetics in thin-film and perovskite-based solar cells. These include Copper (4.6 eV), Silver (4.7 eV), Iron (4.8 eV), Copper-doped carbon (5.0 eV), gold (5.1 eV), Tungsten (5.22 eV), Nickel (5.5 eV), Palladium (5.6 eV), and Platinum (5.7 eV). Proper work function alignment between the metal contact and the adjacent HTL or ETL is critical for forming efficient ohmic or Schottky interfaces. For instance, metals with higher work functions ($\geq$ 5.0 eV) are preferable for hole-selective contacts, as they improve hole extraction and reduce contact resistance in devices that utilize wide-bandgap HTLs. Additionally, selecting metal contacts must take into account their thermal and chemical compatibility with both absorber and transport layers, especially under long-term operational conditions [93–95].

In our theoretical investigation, we conducted a systematic evaluation of these metal contacts in conjunction with various HTL and CP absorbers. The key criteria for evaluation included work function alignment, series resistance, interfacial recombination potential, and contact stability. Our results indicate that optimizing the metal contacts, along with the properties of the HTL and absorber, can significantly boost PCEs and device stability. This offers a clear pathway toward optimized and commercially viable PV architectures.

2.2.6. Interface layer

In the architecture of a solar cell, the interface layer serves as a crucial connection between different functional layers, particularly the absorber and the ETL or HTL. This

interface is more than just a structural transition zone; it plays a significant role in governing the flow and behavior of charge carriers. As a result, it can greatly influence the overall efficiency and stability of the solar device. Imperfections at these interfaces, such as mismatched crystal lattices, dangling bonds, or high defect densities, can create sites for trap-assisted recombination, ultimately reducing key performance metrics like the V_{OC} and FF.

This challenge is especially evident in CP solar cells, where polycrystalline films are often more prone to grain boundary defects and interfacial inconsistencies. To overcome these issues, researchers have employed various interface engineering strategies. These include the integration of ultra-thin interlayers, chemical surface treatments, and the use of novel 2D materials to smooth out energy barriers, reduce recombination, and better align energy levels between layers.

In the present study, meticulous interface optimization was a key focus. Parameters such as energy band offsets, recombination rates, and defect concentrations were carefully analyzed to enhance the interaction between the chalcogenide absorber and adjacent transport layers. Through these efforts, the interface layer was not only stabilized but also utilized to improve built-in potential, promote efficient carrier transport, and ensure the long-term operational reliability of the solar cell.

2.2.7. PV parameters

PV parameters are crucial metrics for assessing the performance and efficiency of solar cells. They provide quantitative insights into how effectively a solar device converts incident sunlight into electrical energy. A clear understanding of these parameters allows researchers to evaluate material quality, interface behavior, and energy conversion mechanisms, which in turn support the optimization of device architectures. The main PV parameters include open-circuit voltage (V_{OC}), short-circuit current density (J_{SC}), fill factor (FF), and power conversion efficiency (PCE).

1. **Open-Circuit Voltage (V_{OC})**

   The open-circuit voltage (V_{OC}) is defined as the maximum voltage output of a solar cell when the circuit is open, meaning there is no external load connected and hence, no current flows. V_{OC} is determined by the difference in quasi-Fermi levels of electrons and holes under illumination. It indicates the extent of charge separation that can be achieved within the cell and is highly sensitive to recombination losses. Mathematically, V_{OC} can be approximated using the diode **equation (1)**:

$$V_{OC} = \frac{nkT}{q} In \left[\frac{I_L}{I_o} + 1\right] \quad (1)$$

where n is the diode ideality factor, k is the Boltzmann constant, T is the absolute temperature, q is the elementary charge, I_L is the photocurrent, and I_o is the reverse saturation current. A higher V_{OC} generally indicates reduced recombination losses and better material quality.

2. Short-Circuit Current Density (J_{SC})

The short-circuit current density (J_{SC}) represents the current output per unit area when the terminals of the solar cell are shorted (voltage = 0). J_{SC} quantifies the number of charge carriers generated and successfully collected at the electrodes under standard illumination conditions, typically AM1.5G at 1000 W/m^2. It depends on the absorption efficiency, charge carrier mobility, and the strength of the internal electric field. J_{SC} can be expressed by the **equation (2)**:

$$Jsc = q \int_{\lambda} \phi(\lambda) \cdot EQE(\lambda)\, d\lambda \quad (2)$$

where $\phi(\lambda)$ is the incident photon flux at wavelength λ, and EQE(λ) is the external quantum efficiency. High J_{SC} values indicate effective photon absorption and charge carrier collection.

3. Fill Factor (FF)

The fill factor (FF) is a dimensionless parameter that reflects the quality of the solar cell's output characteristics. It is defined as the ratio of the maximum obtainable power (Pmax) to the theoretical power obtained from the product of V_{OC} and J_{SC}, expressed in **equation (3)**.

$$FF = \frac{V_{MP} \cdot J_{MP}}{V_{OC} \cdot Jsc} \quad (3)$$

Here, V_{MP} and J_{MP} are the voltage and current density at the maximum power point (M_{PP}). A higher FF indicates lower series resistance and better diode quality. Typical FF values for efficient solar cells range between 70% and 85%.

4. Power Conversion Efficiency (PCE)

Power conversion efficiency (PCE) is a critical parameter used to benchmark the overall performance of a solar cell. It is defined as the percentage of incident solar power that is converted into usable electrical energy under standard test conditions, as expressed in **equation (4)**.

$$PCE = \frac{V_{OC}.J_{SC}.FF}{P_{in}} \times 100 \quad (4)$$

where Pin is the incident light power density, typically 1000 W/m^2. All other PV parameters influence PCE and reflect the cumulative effectiveness of light absorption, charge carrier separation, and transport.

In this thesis, all PV parameters were derived through numerical simulation using SCAPS-1D. These parameters served as key indicators for evaluating the performance of various CP-based architectures, particularly in terms of absorber composition, transport layer selection, and interface engineering. The interactions between V_{OC}, J_{SC}, FF, and PCE were critically analyzed to identify optimal configurations that maximize efficiency while ensuring device stability and scalability for practical PV applications.

2.3. SCAPS-1D background

SCAPS-1D, developed by Mark Burgelman at the University of Ghent, has become an essential simulation tool for analyzing and optimizing thin-film solar cells. It plays a significant role in pre-experimental validation by providing valuable insights into the electrical behavior of various device architectures, including perovskite, chalcogenide, and heterojunction-based solar cells. The strength of SCAPS-1D lies in its ability to solve one-dimensional Poisson's and continuity equations, which allows for accurate modeling of J-V, C-V, QE, and transient responses of PV devices. Researchers have widely adopted SCAPS-1D to simulate emerging solar cell materials and it helps assess their PV potential and optimize key parameters like layer thickness, carrier concentration, defect density, and contact materials. Although SCAPS-1D is limited to one-dimensional geometries and requires external input for optical absorption, it remains a reliable and user-friendly platform for designing and refining next-generation solar cell devices, effectively bridging the gap between theoretical predictions and experimental implementations [96–100].

3. Hypothesis

Novel ABX_3 (where A = Ba, Sr, Ca; B = Hf, Zr; and X = S, Se) chalcogenide perovskites demonstrate potential as highly efficient photo-active materials due to their strong absorption coefficient and low effective masses contributing to high charge carrier mobility, which, when appropriately integrated with optimal hole transport layers could enhance energy level alignment, minimize interfacial recombination, and strengthen the built-in electric field, ultimately leading to improved solar cell performance.

4. Objectives

4.1. General objectives

To investigate the performance of eco-friendly and low-cost solar cells utilizing chalcogenide perovskite absorbers, specifically $SrHfSe_3$ and $BaZrS_3$ with various hole transport layers, as well as engineered properties of $ABSe_3$ (where A = Ca, Ba and B = Zr, Hf), and Zr-alloyed $BaHfS_3$, with the goal of gaining insights into the device physics and the fundamental mechanisms that affect the efficiency of these innovative devices.

4.2. Specific objectives

1. To investigate the performance of a new $SrHfSe_3$ chalcogenide perovskite solar cell with the structure FTO/$BaSnO_3$/$SrHfSe_3$/MoS_2 and analyze the influence of V_{OC}, J_{SC}, FF and PCE using SCAPS-1D theoretical simulations.
2. To evaluate the impact of 41 HTLs, including inorganic semiconductors, polymers, and MXenes, as well as 9 metal contacts, on the performance of $SrHfSe_3$ solar cells, through detailed analysis on energy band alignment and interfacial properties.
3. To study the performance of chalcogenide perovskite solar cells utilizing $CaZrSe_3$, $BaZrSe_3$, $CaHfSe_3$ and $BaHfSe_3$ absorbers and analyzing their absorption rate, carrier generation mechanisms, and J-V profiles to better understand absorber properties and enhance overall performance.
4. To analyze the role of Zr-alloying concentrations in $BaHfS_3$ solar cells and examine the impact of bandgap tuning, accumulation capacitance at the interfaces, energy band shifts and built-in potential to improve overall device performance.
5. To explore the suitability of inorganic delafossite HTLs as an alternative to Spiro-OMeTAD in $BaZrS_3$ solar cells by evaluating their influence on electric field behavior, carrier recombination dynamics, charge transfer resistance, and interface characteristics.

4.3. Overview of the Objectives

Objectives 1 and 2

A comprehensive investigation pertaining to objectives 1 and 2 is detailed in Sections 5.1 and 6.1. In this section, we have numerically designed a novel $SrHfSe_3$-based chalcogenide perovskite (CPs) solar cell with the configuration FTO/$BaSnO_3$/$SrHfSe_3$/MoS_2/Au, utilizing SCAPS-1D. This marks the first exploration of its suitability for photovoltaic (PV) applications. The performance of the solar cell was

enhanced through the optimization of critical parameters associated with the electron transport layer (ETL), absorber, hole transport layers (HTLs), and back metal work function (BMWF). Following this, we simulated 1,627 solar cell configurations by substituting MoS_2 with 40 different HTLs, encompassing inorganic semiconductors, polymers, and MXenes, while optimizing their material properties and BMWF. A thorough analysis was conducted to extract current density-voltage (J-V), capacitance-voltage (C-V), Mott–Schottky, capacitance-frequency, energy band alignment, and quantum efficiency (QE) characteristics, offering detailed insights into the function of each layer within the device. Our findings demonstrated that the novel $SrHfSe_3$ solar cells, in conjunction with the 41 HTLs, significantly improved efficiency, achieving a low energy deficit of approximately 0.4 V, a high short-circuit current density of around 26.22 mA/cm^2, and enhanced absorption of about 60.4%. Among all HTL categories, the highest power conversion efficiencies (PCEs) of 27.87%, 27.39%, and 26.30% were recorded with SnS, CPE-K, and Ti2CO2 for the inorganic semiconductor, polymer, and MXenes-based HTLs, respectively. This research has been published: **D. Srinivasan**, A.-D. Rasu Chettiar, K.T. Arockiadoss, L. Marasamy, "A new class of $SrHfSe_3$ chalcogenide perovskite solar cells with diverse HTMs: Theoretical modelling towards efficiency enhancement", ***Solar Energy Materials and Solar Cells*** 290 (2025) 113727. **https://doi.org/10.1016/j.solmat.2025.113727.**

Objective 3

An in-depth study aligned with objective 3 is presented in Sections 5.2 and 6.2. In this section, we introduce the $CaZrSe_3$, $BaZrSe_3$, $CaHfSe_3$, and $BaHfSe_3$ solar cells in a superstrate configuration, employing SCAPS-1D numerical simulation. Remarkably, initial power conversion efficiencies (PCEs) of 9.94%, 10.14%, 8.20%, and 13.04% are achieved for the innovative $CaZrSe_3$, $BaZrSe_3$, $CaHfSe_3$, and $BaHfSe_3$ solar cells, respectively. Subsequently, we analyze the material properties of each layer and enhance their performance through the optimization of key parameters and interface defects. Notably, adjusting the absorber thickness and carrier concentration increases light absorption by approximately 11.93% and boosts the conductivity and built-in potential of the solar cells, facilitating the efficient transfer of charge carriers. Additionally, optimizing the carrier concentration of the hole transport layer (HTL) enhances the PCE by about 5%, attributed to the elevated electric field at the absorber/HTL interface. Ultimately, after systematic optimization of each layer, we achieve maximum PCEs of 30.08%, 30.58%, 22.74%, and 27.60% for the $CaZrSe_3$, $BaZrSe_3$, $CaHfSe_3$, and $BaHfSe_3$ solar cells, respectively. Notably, the $CaZrSe_3$ and $BaZrSe_3$ solar cells exceed a PCE of 30%, owing to their narrow bandgap,

which leads to improved light absorption, the highest generation rates of charge carriers, and elevated J_{SC} values of approximately 29 mA/cm^2. This work has been published: **D. Srinivasan**, A.-D. Rasu Chettiar, E.N. Vincent Mercy, L. Marasamy, "Scrutinizing the untapped potential of emerging $ABSe_3$ (A = Ca, Ba; B = Zr, Hf) chalcogenide perovskites solar cells", ***Scientific Reports*** 15 (2025) 3454. **https://doi.org/10.1038/s41598-024-80473-4.**

Objective 4

To comprehensively address objective 4, **Sections 5.3** and **6.3**, introduce novel CPs absorbers, specifically $BaHfS_3$, $BaHf_{0.75}Zr_{0.25}S_{cs}$, $BaHf_{0.5}Zr_{0.5}S_3$, and $BaHf_{0.25}Zr_{0.75}S_3$, aimed at evaluating their potential and suitability for PV applications using SCAPS-1D. We achieved base PCEs of 3.42%, 4.31%, 5.05%, and 5.92% for the $BaHfS_3$, $BaHf_{0.75}Zr_{0.25}S_3$, $BaHf_{0.5}Zr_{0.5}S_3$, and $BaHf_{0.25}Zr_{0.75}S_3$ solar cells, respectively. The material properties of each layer were then analyzed, and performance was further optimized by fine-tuning key parameters of each layer, their interface defects, and metal work function behaviors. Notably, tuning the absorber's acceptor density altered the energy band positions, suppressed barriers, and intensified the electric field. Moreover, increasing the absorber thickness to 1000 nm enhanced light absorption by approximately 25% across all absorbers, leading to increased carrier generation in solar cells. By optimizing the HTL electron affinity, we achieved appropriate CBO and VBO of ~1.15 eV and ~0.13 eV, respectively, at all absorber/HTL interfaces. Ultimately, the optimized devices of $BaHfS_3$, $BaHf_{0.75}Zr_{0.25}S_3$, $BaHf_{0.5}Zr_{0.5}S_3$, and $BaHf_{0.25}Zr_{0.75}S_3$ achieved PCEs of 14.26%, 16.75%, 19.28%, and 21.94%, respectively, due to a high built-in potential (~1.5 V), high diffusion length (~0.4 μm), high absorption rate (~51.05%), and strong resistance to recombination. The highest PCE exceeding 20% was obtained for the FTO/TiO_2/$BaHf_{0.25}Zr_{0.75}S_3$/NiO/Ni device. This work has been published: **D. Srinivasan**, A.-D. Rasu Chettiar, L. Marasamy, "Engineering $BaHfS_3$ with Zr alloying to improve solar cell performance: Insights from SCAPS-1D simulations", ***Materials Science and Engineering: B*** 315 (2025) 118126. **https://doi.org/10.1016/j.mseb.2025.118126**.

Objective 5

An extensive study focusing on objective 5 is detailed in Sections 5.4 and 6.4. This section presents our design of innovative $BaZrS_3$ solar cells utilizing inorganic delafossite hole transport layers (HTLs), specifically $CuFeO_2$, $CuGaO_2$, and $CuAlO_2$, through SCAPS-1D numerical simulations. We then compare their performance to that of the conventional

HTL, Spiro-OMeTAD. Initial power conversion efficiencies (PCEs) of 8.25%, 10.35%, 7.42%, and 9.86% were achieved for the $CuFeO_2$, $CuGaO_2$, $CuAlO_2$, and Spiro-OMeTAD-based solar cells, respectively. Notably, adjusting the carrier concentration in the absorber facilitates changes in energy band positions, reducing interface barriers, and enhancing the PCE by approximately 3% across all solar cells. Additionally, optimizing the affinity of the HTL contributes to an ideal conduction band offset (CBO) and valence band offset (VBO), which further improves solar cell performance. Ultimately, maximum PCEs of 28.35%, 27.83%, 25.05%, and 27.80% were attained for the $CuFeO_2$, $CuGaO_2$, $CuAlO_2$, and Spiro-OMeTAD-based solar cells, respectively. Our findings reveal that the increased PCE results from favorable band alignment, enhanced absorption, a rise in charge carrier generation, and improved built-in potential, demonstrating the potential of delafossite HTLs as a viable alternative to the conventional Spiro-OMeTAD for novel $BaZrS_3$ solar cells. This research has been published: **D. Srinivasan**, A.-D. Rasu Chettiar, S. Rajendran, H. Bencherif, P. Sasikumar, J. Ramanujam, L. Marasamy, "Boosting the efficiency of $BaZrS_3$ solar cells with inorganic delafossite HTLs: A promising alternative to Spiro-OMeTAD", ***Inorganic Chemistry Communications*** (2025) 114997. **https://doi.org/10.1016/j.mseb.2025.118126**.

5. Methodology

SCAPS-1D is a simulation software developed by Mark Burgelmann at the University of Ghent in Belgium. It is designed to predict the performance of solar cells based on the properties of each layer and their interfaces. The software solves three key equations: the Poisson equation (5) hole and electron continuity equations, (6) and (7) and carrier transport equations (8) and (9) for its analysis.

$$\frac{\partial^2 \varphi(x)}{\partial x^2} = \frac{q}{\varepsilon}\left(n(x) - p(x) - N_D^+(x) + N_A^-(x) - p_t(x) + N_t(x)\right) \quad (5)$$

Where q represents the elemental charge, ε is the dielectric constant, φ is the electrostatic potential, N_D^+ is the donor carrier concentration, N_A^- is the acceptor carrier concentration, p is hole concentration, n is the electron concentration.

$$\frac{\partial n}{\partial t} = \frac{1}{q}\frac{\partial J_n}{\partial x} + (G_n - R_n) \quad (6)$$

$$\frac{\partial p}{\partial t} = -\frac{1}{q}\frac{\partial J_p}{\partial x} + \left(G_p - R_p\right) \quad (7)$$

Here, R_n, R_p, G_n, G_p, J_n, and J_p are the electron recombination rate, hole recombination rate, the generation rate of electrons, the generation rate of holes, hole current density, and electron current density, respectively.

$$J_n = qD_n\frac{\partial n}{\partial x} - q\mu_n n\frac{\partial \varphi}{\partial x} \quad (8)$$

$$J_p = qD_p\frac{\partial p}{\partial x} - q\mu_p p\frac{\partial \varphi}{\partial x} \quad (9)$$

The D_n signifies the electron diffusion coefficient, D_p is the hole diffusion coefficient, μ_n and μ_p are the electron and hole mobility, respectively [97,98].

5.1. Approach of $SrHfSe_3$ Solar Cells: Influence of 41 HTLs and Back Contacts

A detailed simulation related to **objectives 1** and **2** is presented in this section**.** This work describes the numerical design of a novel solar cell made of $SrHfSe_3$ CPs absorber. The solar cell has the initial device structure of FTO/$BaSnO_3$/$SrHfSe_3$/MoS_2/Au, as shown in **Fig. 2**. In this structure, FTO acts as a transparent conductive oxide, $BaSnO_3$ serves as the ETL, $SrHfSe_3$ functions as the CP absorber, MoS_2 works as the HTL, and Au is the back contact. Each layer's input parameters are taken from the literature and are listed in **Table 1**. The thermal velocity of electrons and holes in each layer is 1×10^7 cm/s. The simulations are carried out under AM 1.5G (100mW/cm^2, one sun) spectral irradiance, with a working temperature of 300 K. During the optimization process, the series resistance, shunt resistance are not considered, and the flat band potential is set at the front contact. **Fig. 3** demonstrates the process of SCAPS-1D simulation and the optimization details. [52] The study focuses on investigating the properties of each layer by varying parameters such as electron affinity, carrier concentration, defect density, and thickness. This allows us to obtain corresponding solar cell parameters such as V_{OC}, J_{SC}, FF, and PCE. Once the initial solar cell is optimized, the study proceeds to investigate the influence of the properties of HTLs. In total, 41 HTLs are examined, including inorganic semiconductors, polymers, and MXenes. Like the initial solar cell, each HTL is optimized by modifying its material parameters. In addition, the impact of the back contact is analyzed by tuning the metal work function from 4.5 eV to 5.7 eV. The solar cell performances are elucidated using C-V, QE, Nyquist plots, energy bands, recombination profiles, and electric field distribution, all extracted from SCAPS-1D. Finally, the study investigates the impact of

series resistance, shunt resistance, and working temperature on the performance of high PCE solar cells under each category of HTLs.

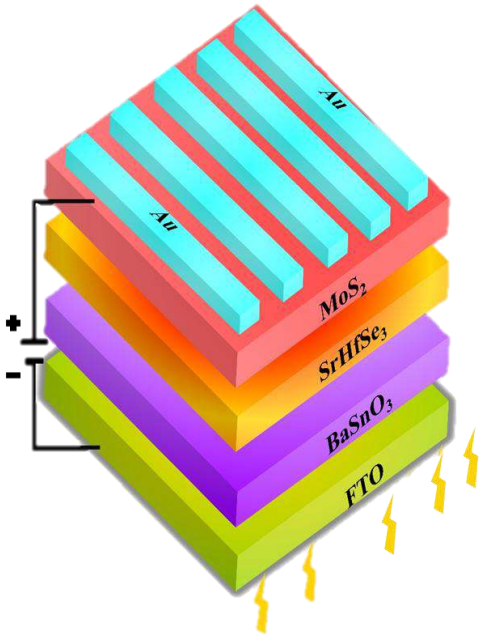

Fig. 2. Initial solar cell structure of $SrHfSe_3$ solar cell [52].

Table 1. SCAPS-1D input parameters of FTO, $BaSnO_3$, $SrHfSe_3$ and MoS_2 [52].

Parameter	**FTO**	**$BaSnO_3$**	**$SrHfSe_3$**	**MoS_2**
Thickness (µm)	100	50	400	70
E_g (eV)	3.5	3.12	1.75	1.29
χ (eV)	4.0	4.4	4.1	3.6
ε_r	9.0	17.0	9.6	30.600
N_C (cm^{-3})	2.2E+18	1.2E+19	5.4E+17	2.2E+18
N_V (cm^{-3})	1.8E+19	1.8E+19	8.5E+18	1.8E+19
μ_m (cm^2/Vs)	2E+1	2E+2	1.130E+1	1E+2
μ_h (cm^2/Vs)	1E+1	2.5E+1	5.580E+0	2.5E+1
N_D (cm^{-3})	1E+18	1E+19	0	0
N_A (cm^{-3})	0	0	1E+18	1E+18
N_t (cm^{-3})	1E+15	1E+15	1E+16	1E+16
Defect type	SA	SA	SD	SD
Abbreviation: SA-Single acceptor; SD- Single Donor				
References	[39]	[57,58]	[87]	[101,102]

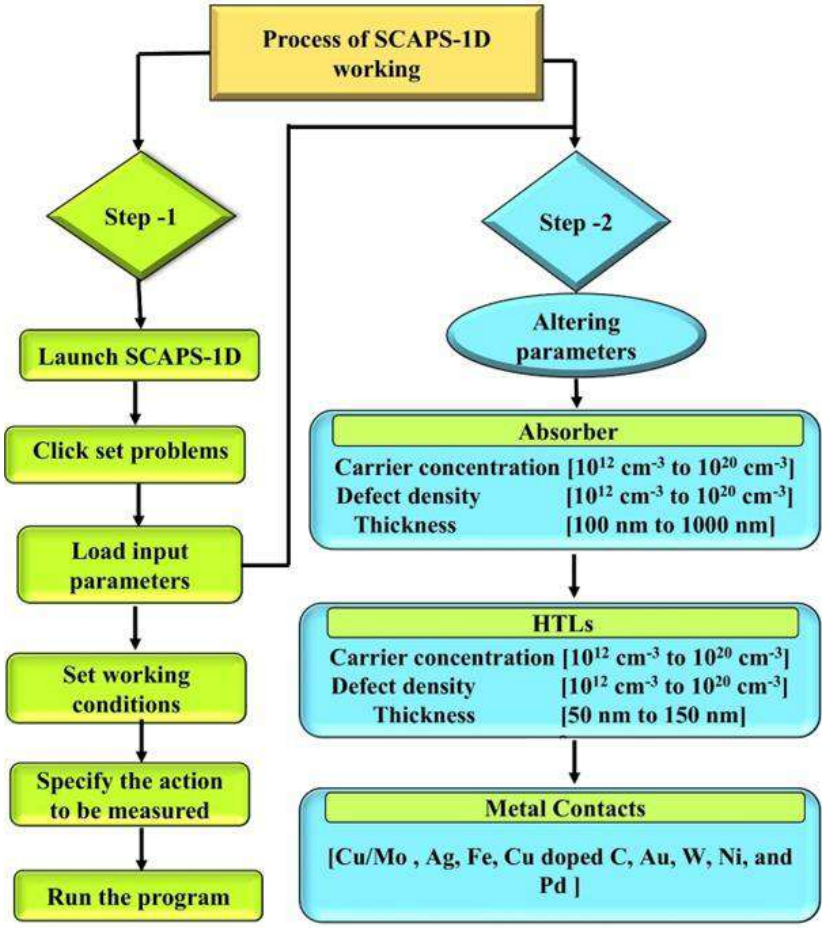

Fig. 3. Flowchart representation of SCAPS-1D process and optimization parameters of $SeHfSe_3$ CPs solar cells [52].

5.2. Methods of $ABSe_3$ (A=Ca, Ba; B=Zr, Hf) CPs Solar Cells

This section describes the simulation methodology employed to address **objective 3**. In this work, we conducted a detailed investigation into the performance of novel chalcogenide solar cells using the SCAPS-1D. The solar cells featured innovative CPs absorbers: $CaZrSe_3$, $BaZrSe_3$, $CaHfSe_3$, and $BaHfSe_3$. We employed a superstrate device configuration, structured as follows: FTO/TiO_2/A (Ca, Ba) B (Zr, Hf) Se_3/NiO/Au, as illustrated in **Fig. 4** and a flow chart of the simulation in **Fig. 5**. The parameters for each layer were set based on existing literature, detailed comprehensively in **Table 2.** The simulations were conducted at 300 K under AM 1.5G solar spectrum irradiance. The work functions were -4.07 eV for FTO and -5.1 eV for Au. Additionally, the surface recombination velocities for both electrons and holes were set at 1×10^7, as indicated in **Table 3**. To simulate realistic solar cell conditions, we introduced neutral defects at the Absorber/HTL and ETL/Absorber interfaces, as detailed in **Table 3**.

Initially, the study concentrated on designing solar cells using the parameters outlined in **Tables 2** and **3.** Subsequently, we explicitly investigated the effects of varying the thickness (ranging from 50 nm to 150 nm), carrier concentration (from 10^{12} cm^{-3} to 10^{20} cm^{-3}), and defect density (also from 10^{12} cm^{-3} to 10^{20} cm^{-3}) of the ETL. Moreover, we assessed the potential of CP absorbers such as $CaZrSe_3$, $BaZrSe_3$, $CaHfSe_3$, and $BaHfSe_3$ by altering their thickness (between 100 nm and 1500 nm), carrier concentration, and defect density within the same ranges mentioned above. Furthermore, we explored the role of HTL by optimizing its thickness (from 50 nm to 150 nm), carrier concentration (from 10^{12} cm^{-3} to 10^{20} cm^{-3}), and defect density (from 10^{12} cm^{-3} to 10^{20} cm^{-3}). The impact of defects at both the ETL/Absorber and Absorber/HTL interfaces was also examined. Overall, the findings were supported by various measurements, including J-V, C-F, electric field distribution, recombination profiles, generation rate, energy band diagram and QE. The series resistance, shunt resistance, and operating temperature were varied from 1 to 10 Ω cm^2, 1000 to 5000, and 300 to 480K, respectively, for $CaZrSe_3$, $BaZrSe_3$, $CaHfSe_3$, and $BaHfSe_3$ solar cells [47].

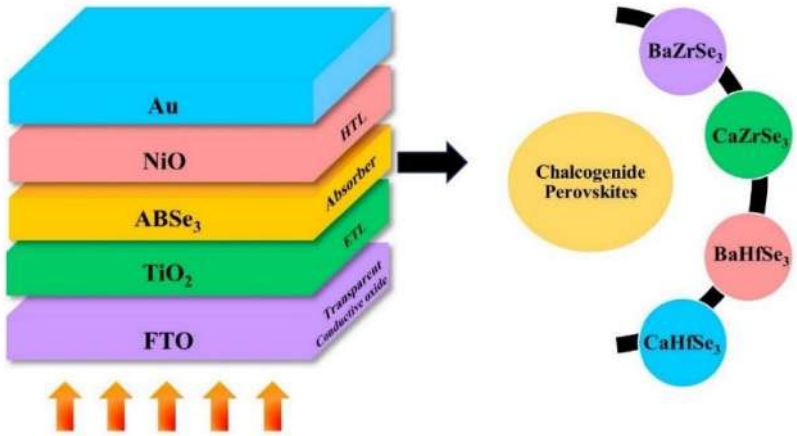

Fig. 4. Schematic representation of novel CP solar cells [47].

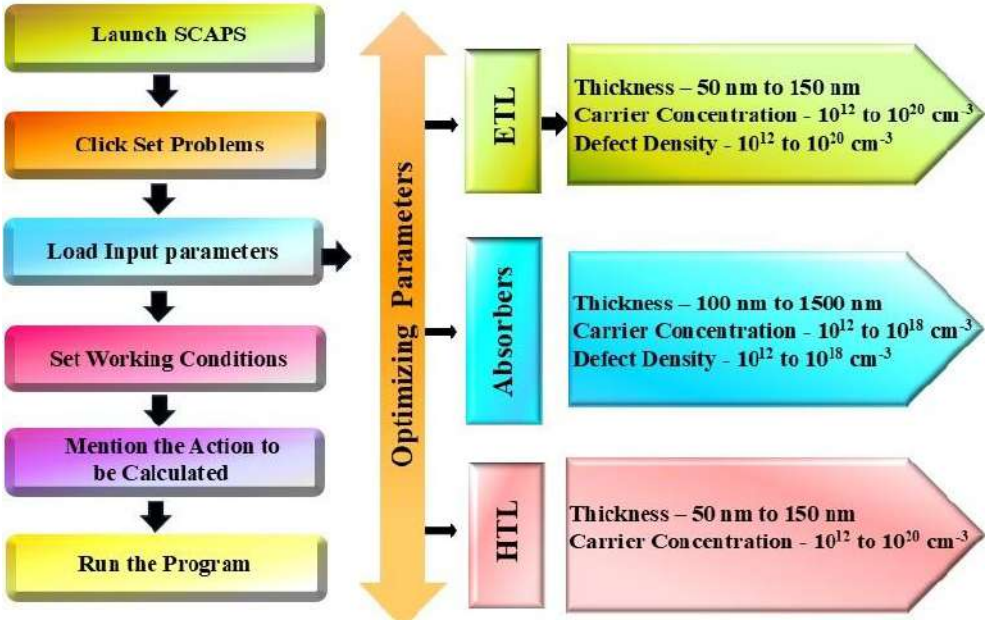

Fig. 5. Flowchart representation of the simulation process and optimization parameters of novel CP solar cells [47].

Table 2. SCAPS input parameters for initial CP solar cells [47].

Parameter	FTO	TiO_2	$CaZrSe_3$	$BaZrSe_3$	$CaHfSe_3$	$BaHfSe_3$	NiO
Thickness (μm)	200	50	500	500	500	500	80
E_g (eV)	3.5	3.2	1.4	1.35	1.65	1.5	3.25
χ (eV)	4.0	4.0	3.8	3.8	3.7	3.8	1.8
ε_r	9.0	9.0	11.0	11.0	11.0	11.0	11.75
N_C (cm^{-3})	2.2E+18	2.2E+18	2.2E+18	2.2E+18	2.2E+18	2.2E+18	2.0E+18
N_V (cm^{-3})	1.8E+19	1.8E+19	1.8E+19	1.8E+19	1.8E+19	1.8E+19	1.8E+19
μ_m (cm^2/Vs)	2E+1	2E+2	2.8E-2	2.8E-2	7.6E-2	9.4E-2	8E+0
μ_h (cm^2/Vs)	1E+1	1E+1	5.9E-2	8.2E-2	3.4E-2	3.5E-2	2E+0
N_D (cm^{-3})	1E+20	1E+17	0	0	0	0	0
N_A (cm^{-3})	0	0	1E+18	1E+18	1E+18	1E+18	1E+16
N_t (cm^{-3})	1E+15	1E+15	1E+15	1E+15	1E+15	1E+15	1E+15
References	[39]	[39]	[87]	[87]	[87]	[87]	[103,104]

Table 3. Parameters for front and back contact, as well as interface defects, in novel CP solar cells [47].

Front and back contact parameters		
Contacts	**Back metal contact properties (Au)**	**Front metal contact Properties (FTO)**
Metal work function (eV)	5.10	4.07
Surface recombination velocity of electron (cm/s)	1.000×10^7	1.000×10^7
Surface recombination velocity of hole (cm/s)	1.000×10^7	1.000×10^7
Interface defect parameter		
Parameters (unit)	**A (Ca, Ba) B (Zr, Hf) Se_3/TiO_2 interface**	**A (Ca, Ba) B (Zr, Hf) Se_3/NiO interface**
Defect density (cm^{-3})	1.0×10^{12} cm^{-2}	1.0×10^{12} cm^{-2}
Defect type	neutral	neutral
Capture cross section for electrons (cm^2)	1.0×10^{-19} cm^2	1.0×10^{-19} cm^2
Capture cross section for holes (cm^2)	1.0×10^{-19} cm^2	1.0×10^{-19} cm^2
Energetic distribution	single	single
Reference for defect energy level E_t	Above the highest valence band	Above the highest valence band
Energy level with respect to valence band maximum (eV)	0.6 eV	0.6 eV

5.3. Strategy of Zr-alloying $BaHfS_3$ CPs Solar Cells

The simulation framework and setup for **objective 4** are presented in this section. This research meticulously analyzed the performance of novel chalcogenide solar cells using SCAPS-1D, focusing on $BaHfS_3$, $BaHf_{0.75}Zr_{0.25}S_3$, $BaHf_{0.5}Zr_{0.5}S_3$, and $BaHf_{0.25}Zr_{0.75}S_3$ CP absorbers. The solar cell were designed with a superstrate configuration, as shown in **Fig. 6**a and the energy band diagram, as displayed in **Fig. 6**b. TiO_2 was employed as the ETL and NiO as the HTL due to their excellent charge carrier dynamics. Au was chosen as the back metal contact because of its high electrical conductivity, approximately 4.1×10^7 S/m. This elevated conductivity minimizes resistance at the contact interface, reduces energy losses, and enhances the overall PCE of the solar cells. Another notable advantage of Au is its high work function, around 5.1 eV, which aligns well with the energy levels of many absorber materials, ensuring long-term stability and reliability for solar cells. The parameters for each layer were initially established based on existing literature, which is comprehensively listed in **Table 4.** These parameters include critical aspects such as carrier concentrations (N_A), and defect densities (N_t)

and thickness (nm). Simulations were carried out at 300K under AM 1.5G solar spectrum irradiance, considering flat band conditions for the front contact while excluding R_{Sh} and R_S. Realistic solar cell conditions were implemented by introducing neutral defects at the ETL/absorber and absorber/HTL interfaces, as detailed in **Table 5.** The research initially focused on designing the initial solar cells presented in **Table 4**. Subsequent investigations explicitly examined the thickness (50 nm to 150 nm) and carrier concentration (10^{12} cm^{-3} to 10^{20} cm^{-3}) of the ETL. Moreover, the study examined the potential of $BaHfS_3$, $BaHf_{0.75}Zr_{0.25}S_3$, $BaHf_{0.5}Zr_{0.5}S_3$, and $BaHf_{0.25}Zr_{0.75}S_3$ CPs absorbers by altering the carrier concentration, defect density and thickness from 10^{12} cm^{-3} to 10^{20} cm^{-3}, 10^{12} cm^{-3} to 10^{20} cm^{-3} and 100 nm to 2000 nm, respectively. Additionally, the impact of HTL was explored by optimizing the thickness (50 nm to 150 nm), carrier concentration (10^{12} cm^{-3} to 10^{20} cm^{-3}), and defect density (10^{12} cm^{-3} to 10^{20} cm^{-3}). The study evaluated the effects of these parameter variations through a series of measurements, including J-V, C-V, Mott-Schottky, C-F, electric field distribution, recombination profiles, and QE. Furthermore, we investigated the influence of R_S, R_{Sh}, and working temperature for $BaHfS_3$, $BaHf_{0.75}Zr_{0.25}S_3$, $BaHf_{0.5}Zr_{0.5}S_3$ and $BaHf_{0.25}Zr_{0.75}S_3$ solar cells [44].

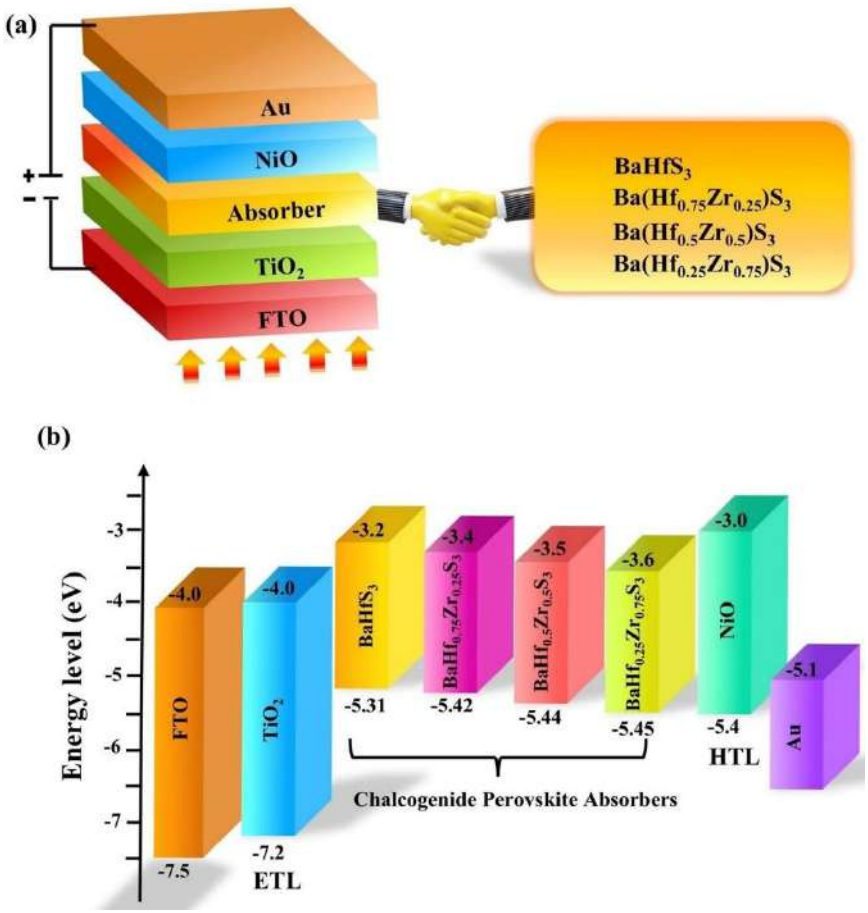

Fig. 6. (a) Schematic representation of the novel CP solar cell structure and (b) energy band diagram of the solar cell [44].

Table 4. SCAPS input parameters for $BaHf_{1-x}Zr_xS_3$ base CPs solar cells [44].

Parameter	**FTO**	**TiO_2**	**$BaHfS_3$**	**$BaHf_{0.75}Zr_{0.25}S_3$**	**$BaHf_{0.5}Zr_{0.5}S_3$**	**$BaHf_{0.25}Zr_{0.75}S_3$**	**NiO**
Thickness (nm)	200	50	500	500	500	500	80
E_g (eV)	3.5	3.2	2.11 (exp)	2.02 (exp)	1.94 (exp)	1.85 (exp)	3.6
χ (eV)	4.0	4.0	3.20	3.40	3.50	3.60	1.8
ε_r	9.0	9.0	8	8.4	8.6	9.8	11.75
N_C (cm^{-3})	2.2E+18	2.2E+18	4.0E+18	3.5E+18	3.3E+18	3.0E+18	2.5E+20
N_V (cm^{-3})	1.8E+19	1.8E+19	3.2E+19	2.7E+19	2.4E+19	2.1E+19	2.5E+20
μ_n (cm^2/Vs)	2E+1	2E+1	1.40E-2	1.30E-2	1.20E-2	1.10E-2	2.8E+0
μ_h (cm^2/Vs)	1E+1	1E+1	3.6E-2	3.7E-2	3.8E-2	3.9E-2	2.8E+0
N_D (cm^{-3})	1E+20	1E+17	0	0	0	0	0
N_A (cm^{-3})	0	0	1E+18 (variable)	1E+18 (variable)	1E+18 (variable)	1E+18 (variable)	1E+16 (variable)
N_t (cm^{-3})	1E+15	1E+15	1E+15 (variable)	1E+15 (variable)	1E+15 (variable)	1E+15 (variable)	1E+15 (variable)
References	[39]	[39]	[41,43,90, 105]	[41,43,90, 105]	[41,43,90, 105]	[41,43,90, 105]	[103,104]

Table 5. Interface defect parameters for novel CP solar cells [44].

Parameters (unit)	**$BaHf_{1-x}Zr_xS_3/TiO_2$ interface**	**$BaHf_{1-x}Zr_xS_3/NiO$ interface**
Defect density (cm^{-3})	1.0×10^{12} cm^{-3}	1.0×10^{12} cm^{-3}
Defect type	neutral	neutral
Capture cross section for electrons (cm^2)	1E-19 cm^2	1E-19 cm^2
Capture cross section for holes (cm^2)	1E-19 cm^2	1E-19 cm^2
Energetic distribution	single	single
Reference for defect energy level Et	Above the highest valence band	Above the highest valence band
Energy level with respect to valence band maximum (eV)	0.6 eV	0.6 eV

5.4. Process of $BaZrS_3$-based CPs Solar Cells with Delafossite and Spiro-OMeTAD HTLs

This section details the simulation approach used to investigate **objective 5**. This study focuses on the efficiency of $BaZrS_3$ PV devices that incorporate delafossite HTLs, namely $CuFeO_2$, $CuGaO_2$, and $CuAlO_2$, and compares their performances with the conventional Spiro-OMeTAD. This analysis is conducted utilizing SCAPS-1D simulation. The device configuration consists of a superstrate structure: FTO/TiO_2/$BaZrS_3$/delafossite HTL/Au, as illustrated in **Fig. 7**. As shown in **Table 6**, the initial settings for each layer are sourced from existing studies. The table lists essential parameters, such as the bandgap (E_g), electron affinity (χ), and dielectric permittivity (ε_r). It further outlines the effective density of states in both the conduction band (N_C) and the valence band (N_V), as well as electron mobility (μ_n) and hole mobility (μ_p). Moreover, it includes details on donor density (N_D), acceptor density (N_A), and defect density (N_t). In the simulations, thermal velocities of electrons and holes are set at 10^7 $cm.s^{-1}$ throughout all layers. FTO serves as the front contact, while Au acts as a back contact. The simulations are conducted at a temperature of 300 K, utilizing AM 1.5G spectral irradiance. To accurately represent the operational environment of the PV devices, fixed defects are introduced at the ETL/$BaZrS_3$ and $BaZrS_3$/HTL interfaces, as outlined in **Table 7**. Initially, a solar cell is designed based on the parameters outlined in **Table 6**. Following this, a detailed analysis is conducted to assess the impact of varying carrier concentrations (from 10^{12} cm^{-3} to 10^{20} cm^{-3}) and defect densities (ranging from 10^{12} cm^{-3} to 10^{20} cm^{-3}). Additionally, the effect of defects at the interfaces of ETL/$BaZrS_3$ and $BaZrS_3$/HTL is assessed, with defect levels varying from 10^{12} cm^{-3} to 10^{20} cm^{-3}.

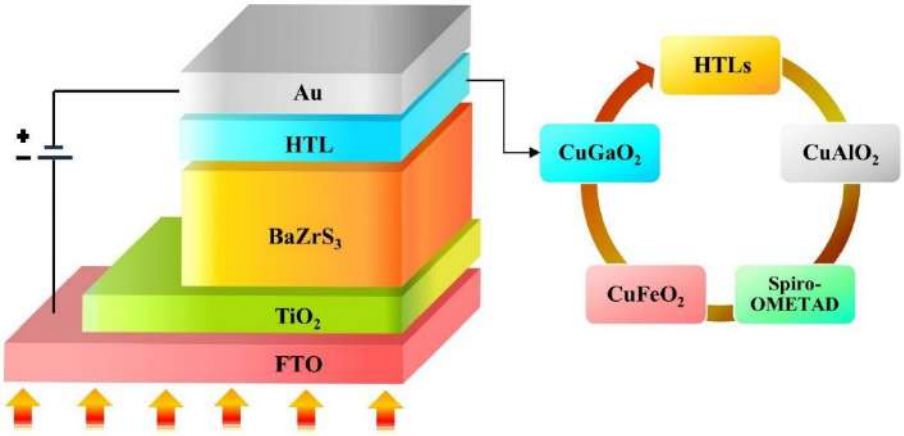

Fig. 7. Depiction of the $BaZrS_3$ solar cell device with different HTLs [260].

Table 6. SCAPS simulation inputs for the baseline configuration [260].

Parameter	**FTO**	**TiO_2**	**$BaZrS_3$**	**$CuFeO_2$**	**$CuGaO_2$**	**$CuAlO_2$**	**Spiro-OMeTAD**
Thickness (nm)	0.200	0.50	0.500	0.50	0.50	0.50	0.50
E_g (eV)	3.50	3.2	1.7	2.45	2.51	2.65	3.2
χ (eV)	4.00	3.8	4.1	2.7	3.0	2.4	2.1
ε_r	9.0	9.0	9.6	11.75	11.75	11.75	3.0
N_C (cm^{-3})	2.2×10^{18}	2.2×10^{18}	2.2×10^{18}	2.0×10^{18}	2.0×10^{18}	2.0×10^{18}	2.2×10^{18}
N_V (cm^{-3})	1.8×10^{19}	1.8×10^{19}	1.8×10^{19}	1.8×10^{19}	1.8×10^{19}	1.8×10^{19}	1.0×10^{19}
μ_n (cm^2/Vs)	2.0×10^{1}	2.0×10^{1}	3.4×10^{-2}	8.0×10^{1}	8.0×10^{1}	8.0×10^{1}	1.0×10^{-4}
μ_h (cm^2/Vs)	1.0×10^{1}	1.0×10^{1}	7.6×10^{-2}	2.0×10^{1}	2.0×10^{1}	2.0×10^{1}	2.0×10^{-4}
N_D (cm^{-3})	1.0×10^{20}	1×10^{20}	0	0	0	0	0
N_A (cm^{-3})	0	0	1×10^{18}	1×10^{17}	1×10^{17}	1×10^{17}	1×10^{18}
N_t (cm^{-3})	1.0×10^{15}	1×10^{16}	1×10^{15}	1×10^{16}	1×10^{16}	1×10^{16}	1×10^{16}
References	[39]	[39]	[39]	[106]	[106]	[106]	[107]

Table 7. Interface defect characteristics for the $BaZrS_3$ devices [260].

Parameters (unit)	**$BaZrS_3$/ETL interface**	**$BaZrS_3$/HTL interface**
Defect density (cm^{-3})	1.0×10^{12} cm^{-3}	1.0×10^{12} cm^{-3}
Defect type	neutral	neutral
Capture cross section for electrons (cm^2)	1E-19 cm^2	1E-19 cm^2
Capture cross section for holes (cm^2)	1E-19 cm^2	1E-19 cm^2
Energetic distribution	single	single
Reference for defect energy level Et	Above the highest valence band	Above the highest valence band
Energy level with respect to valence band maximum (eV)	0.6 eV	0.6 eV

6. Result and Discussions

6.1. Performance of $SrHfSe_3$ Solar Cells: Influence of HTLs and Back Contacts

This section outlines the detailed simulation results related to **objectives 1** and **2**. **Section 6.1.1** presents the initial solar cell performance. **Sections 6.1.2** to **6.1.5** analyze the performance of the $SrHfSe_3$ absorber layer**. Sections 6.1.6** to **6.1.8** evaluate the performance of the MoS_2 HTL, while **Section 6.1.9** examines the metal contact properties. **Section 6.1.10** focuses on the design and analysis of 40 different HTLs. **Sections 6.1.11** to **6.1.16** investigate the influence of high-efficiency HTLs, and **Section 6.1.17** discusses experimental strategies for achieving optimal power conversion efficiency (PCE).

6.1.1 Initial Solar Cell Performance of $SrHfSe_3$ Solar Cells

The initial simulations were conducted based on the parameters listed in **Table 1**, using the solar cell structure FTO/$BaSnO_3$/$SrHfSe_3$/MoS_2/Au, as illustrated in **Fig. 2**. The corresponding current density-voltage (J-V) characteristics, shown in **Fig. 8**, revealed an initial V_{OC} of 1.00 V, J_{SC} of 14.08 mA/cm^2, FF of 80.81%, and PCE of 11.42%. Further improvement was achieved by optimizing key parameters of each layer, including electron affinity, carrier concentration, defect density, and thickness, as discussed in the following sections.

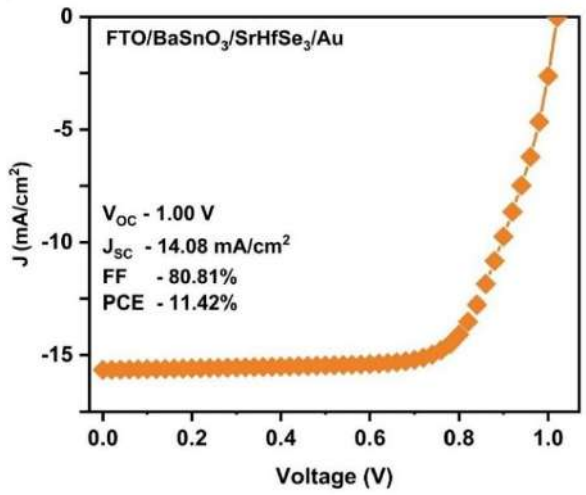

Fig. 8. Initial J-V of $SrHfSe_3$ solar cell [52].

6.1.2. Optimization of $SrHfSe_3$ Absorber Parameters

Optimizing the absorber is key to boosting solar cell performance. To understand its effect, we varied the carrier concentration, defect density, and thickness from 10^{12} cm^{-3} to 10^{18}

cm^{-3}, 10^{12} cm^{-3} to 10^{20} cm^{-3}, and 100 nm to 1000 nm, respectively. The results of optimizing $SrHfSe_3$ are discussed in the following sections.

6.1.3. Impact of $SrHfSe_3$ Absorber's Carrier Concentration

The absorber's carrier concentration determines solar cells' charge transport and stability [29]. Finding the optimal carrier concentration of the absorber is key to maximizing solar cell efficiency. In this work, $SrHfSe_3$'s carrier concentration was adjusted between 10^{12} cm^{-3} and 10^{18} cm^{-3}, and its impact on J-V characteristics, V_{OC}, J_{SC}, FF, and PCE is illustrated in **Fig. 9**(a-c). The results indicate that V_{OC} and FF remain stable up to 10^{15} cm^{-3} but show a significant increase beyond this level. Specifically, as the carrier concentration rises from 10^{12} cm^{-3} to 10^{18} cm^{-3}, V_{OC} improves from 0.94 V to 1.18 V, while FF increases from 44.43% to 88.77%, ultimately boosting PCE from 9.17% to 11.67%. The increase in V_{OC} is attributed to the enhanced built-in potential (Vb) of the solar cells, resulting from the improved carrier concentration, as illustrated in Mott-Schottky plots (**Fig. 9**d). To explain this, Mott-Schottky ($1/C^2$) plots for $SrHfSe_3$ were generated from C-V data using SCAPS-1D simulation software. The built-in potential (V_b) was then determined from the intercept of these plots, as shown in **Fig. 9**d, where V_B increases from 1.02 V to 1.05 V for the variation in carrier concentration from 10^{12} cm^{-3} to 10^{18} cm^{-3}. This enriches the transportation of charge carriers and aids in their successful collection at the corresponding contacts without recombination, resulting in improved FF [108]. Additionally, the rise in carrier concentration causes an upward shift in both the conduction band (E_C) and valence band (E_V), as shown in **Fig. 9**(e). This shift moves the valence band of $SrHfSe_3$ closer to the quasi-Fermi level of holes (F_P), enhancing conductivity and improving charge carrier transport within the solar cell. Furthermore, these also reveals a splitting of quasi-fermi levels, i.e., F_P and F_N (electron quasi-fermi level), increase along the absorber region for 10^{18} cm^{-3}, which explicitly improves V_{OC}, leading to an overall improvement in solar cell performance. Additionally, a higher carrier concentration strengthens the electric field at the $SrHfSe_3/MoS_2$ interface, as seen in **Fig. 9**(f). This helps drive more holes from the absorber to the HTL while preventing electron leakage, ultimately improving hole collection at the back contact and enhancing overall performance [109]. On the contrary, J_{SC} is unaltered till 10^{17} cm^{-3} and sharply decreases for 10^{18} cm^{-3}. At higher carrier concentrations, most of the depletion region moves into the ETL, leaving a much thinner depletion layer in the absorber [110]. Eventually, the absorption in the solar cell declines since the majority of photon absorption occurs along the absorber region. This reduces the charge carrier generation rate, leading to a drop in J_{SC}. However, the overall solar cell efficiency originates from the increment

in V_{OC} and FF while it is independent of J_{SC}. Overall, increasing the carrier concentration of SrHfSe3 significantly impacts the energy band positions, enhances quai-Fermi level splitting, strengthens the V_B, and improves the internal electric field, all contributing to higher PCE. Based on these findings, a carrier concentration of 10^{18} cm^{-3} is identified as the optimal value for further simulations.

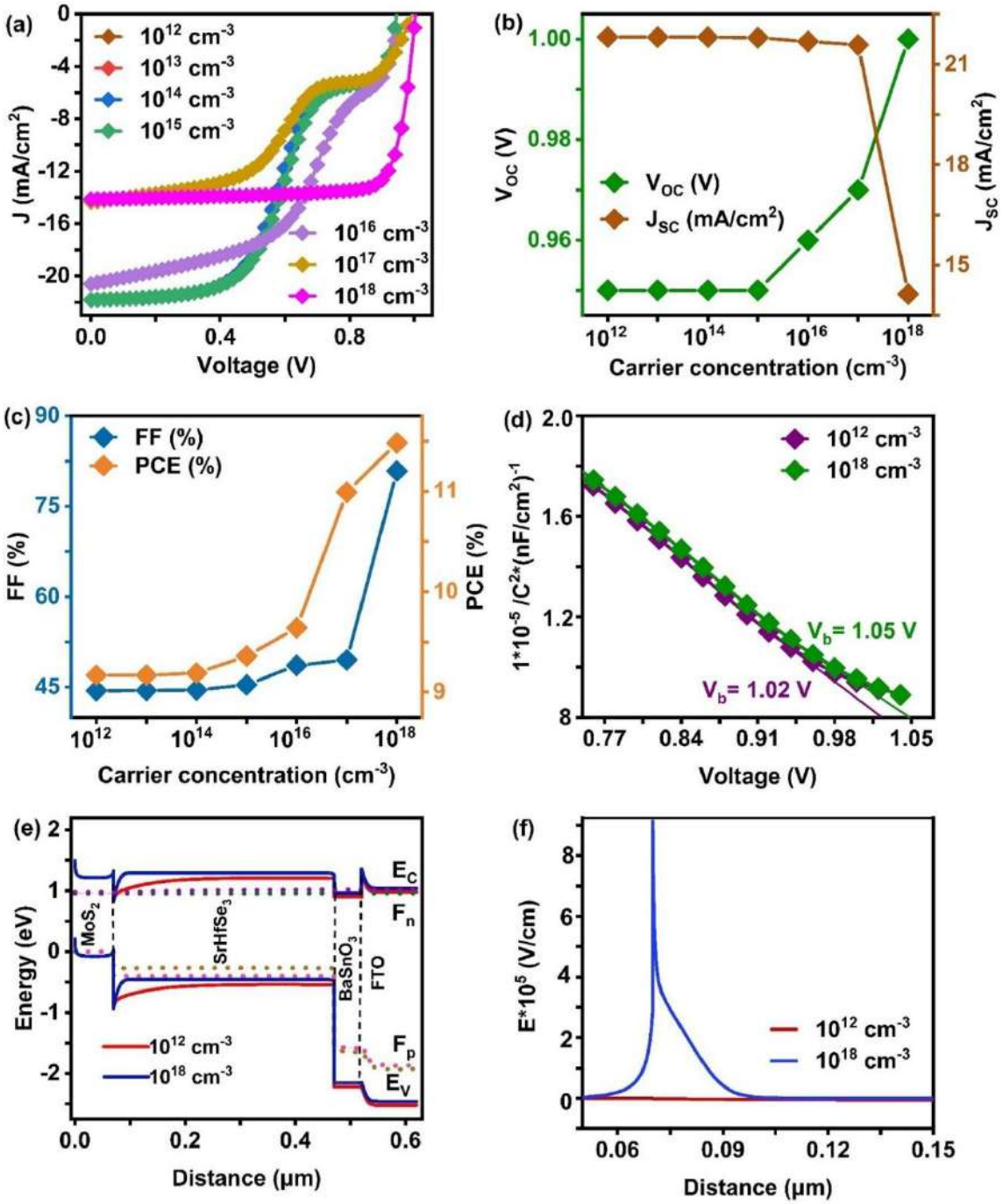

Fig. 9. Changes in (a) J-V (b) V_{OC}, J_{SC} (c) FF, PCE (d) Mott-Schottky (e) energy band alignment and (f) electric field (E) corresponding to $SrHfSe_3$'s carrier concentration [52].

6.1.4. Impact of $SrHfSe_3$ Absorber's Defect Density

The presence of defects in the absorber layer plays a crucial role in shaping the overall performance of a solar cell. It is usually formed due to structural imperfections, non-stoichiometry, impurities, fabrication methods, etc [111,112]. Thus, it is essential to control the absorber defects to attain the best solar cell performance. In this work, we adjusted the defect density of $SrHfSe_3$, ranging from 10^{12} cm^{-3} to 10^{20} cm^{-3}, to thoroughly analyze its influence. **Fig. 10**(a-c) shows the variation in J-V, V_{OC}, J_{SC}, FF, and PCE with respect to the defect density of $SrHfSe_3$. The V_{OC} remains unchanged up to a defect density of 10^{16} cm^{-3}, then rises at a defect density of 10^{18} cm^{-3}, and decreases as the defect density continues to increase. The reason for the observed fluctuation is unknown. On the other hand, the J_{SC}, FF, and PCE stay steady up to a defect density of 10^{15} cm^{-3} and drop sharply beyond this threshold. In particular, J_{SC}, FF, and PCE drop from 16.79 mA/cm^2 to 2.12 mA/cm^2, 83.33% to 64.12%, and 14.07% to 1.43%, respectively, when the defect density is raised from 10^{12} cm^{-3} to 10^{20} cm^{-3}. This happens because the defects trap the photogenerated charge carriers on their way to the contacts, reducing their diffusion length and lifetime [113]. This trend is also evident in **Fig. 10**(d), where the minority carrier diffusion length reduces from 54 μm to 0.054 μm while their lifetime decreases from 10^5 to 10^{-3} ns, when the defect density of $SrHfSe_3$ rises from 10^{12} cm^{-3} to 10^{20} cm^{-3}, the charge carrier recombination rate increases significantly (**Fig. 10** (e)), impeding their collection at the corresponding contacts [39,114]. **Fig. 10**(f) illustrates the changes in the electric field for the defect density 10^{12} cm^{-3} and 10^{20} cm^{-3}. As the defect density increases, the electric field at the absorber/HTL interface decreases. This consequently diminishes the separation and collection of holes from the absorber to the back contact, negatively impacting the performance of solar cell. In our study, we found that maintaining a defect density of 10^{14} cm^{-3} in the absorber layer significantly improves PCE. Since the $SrHfSe_3$ materials are still under development, we have proposed strategies inspired by previous research on similar $BaZrS_3$ CPs to enhance solar cell performance. Meng et al. reported that synthesizing CPs films under sulfur-rich and zirconium-poor conditions leads to strong p-type behavior and a lower defect density. This improvement is linked to the increased formation energy of deep-level defects, which reduces their occurrence. Controlling elemental composition during synthesis is therefore essential for achieving optimal carrier concentration and minimizing deep-level defects [115]. Hwang et al. experimentally showed that post-heat treatment of absorber materials can lower defect densities to 10^{13} cm^{-3}, contributing to high PCE [116]. Moreover, Yanping et al. explored bromine (Br) doping in perovskite absorbers,

achieving a defect density of approximately 10^{14} cm^{-3} [117]. Taking these findings into account, we selected 10^{14} cm^{-3} as the optimal defect density for $SrHfSe_3$-based solar cells to balance defect reduction and solar cell performance improvement.

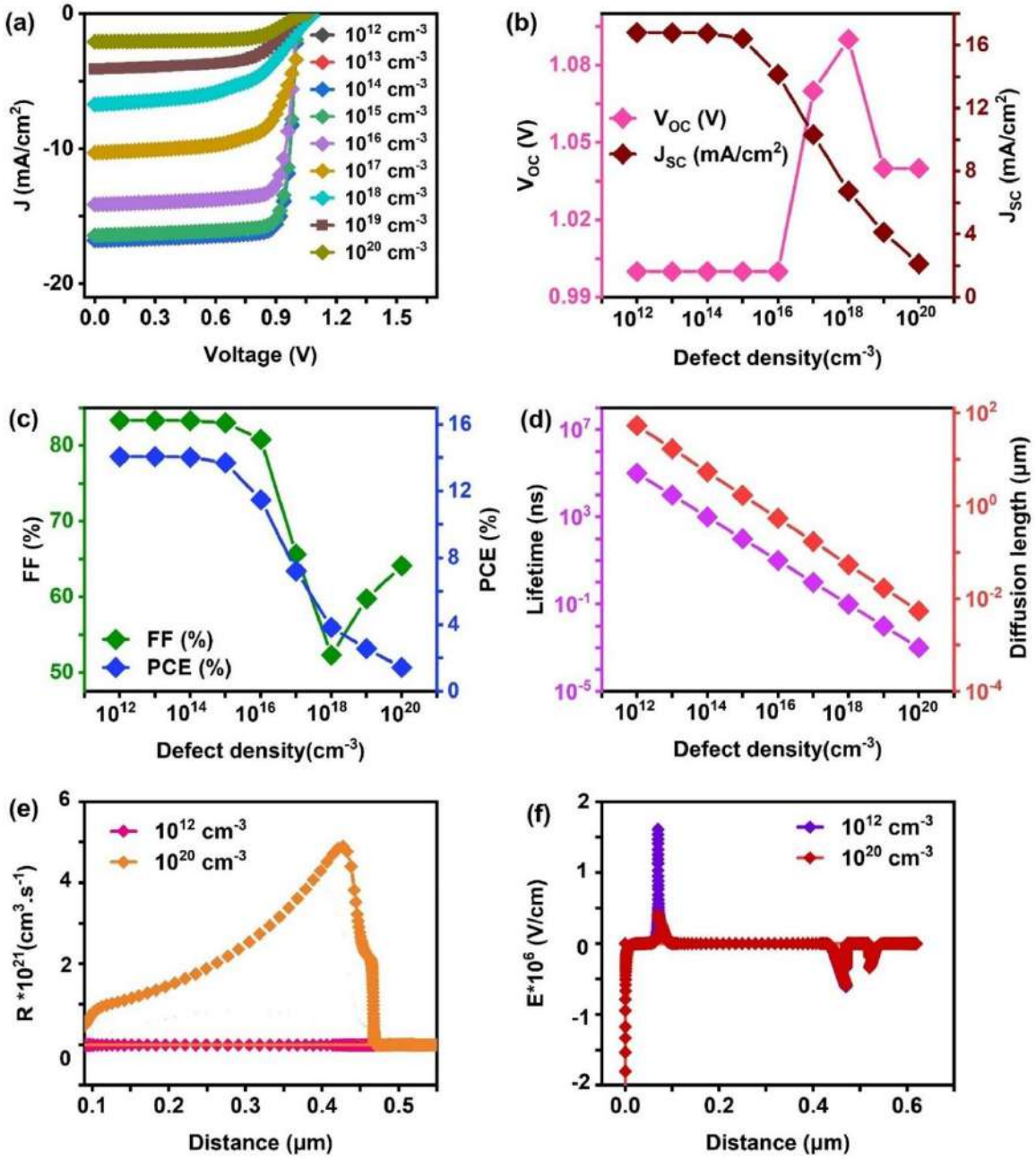

Fig. 10. Changes in (a) J-V (b) V_{OC}, J_{SC} (c) FF, PCE (d) lifetime and diffusion length of charge carriers (e) recombination rate and (f) electric field corresponding to $SrHfSe_3$'s defect density [52].

6.1.5. Impact of $SrHfSe_3$ Absorber's Thickness

The absorber's thickness influences the solar cell performance to a great extent. A thin absorber partly absorbs the photons and transmits the majority of light, reducing the charge

carrier generation, although a thick absorber can decline the solar cell performance due to the limitation in diffusion length of charge carriers [118]. Thus, optimizing the absorber thickness to achieve maximum PCE is crucial. Therefore, the $SrHfSe_3$ absorber thickness is altering from 100 nm to 1000 nm, as shown in **Fig. 11**(a–c). It can be noticed that all the solar cell parameters increase with the increasing absorber's thickness. That is, when the thickness is enhanced from 100 nm to 1000 nm, the V_{OC}, J_{SC}, FF, and PCE rise from 0.98 V to 1.02 V, 15.47 mA/cm^2 to 18.30 mA/cm^2, 77.84% to 84.95% and 11.82 % to 15.97% respectively. Nevertheless, we could see that the increment in PCE is around 1.29 times, as the thickness is extended from 100 nm to 700 nm, whereas it is just 1.04 times when it is further increased to 1000 nm. This occurs because the photon absorption in $SrHfSe_3$ drastically improves with its thickness, resulting in the effective charge carrier generation [118]. However, when the absorber is too thick, the diffusion length and lifetime of photogenerated charge carriers will be inadequate to reach the required metal contacts. Consequently, Shockley–Read–Hall recombination also enhances along with larger charge carrier generation in $SrHfSe_3$, which eventually saturates the performance of the solar cell [119]. This behavior is evidenced in QE of varying thickness **Fig. 11(**d), where the absorption increases by 1.26 times when it is increased from 100 nm to 700 nm while improving by just 1.01 times on further increment to 1000 nm. Recent research on CPs solar cells has shown that increasing the absorber layer thickness from 600 nm to 1000 nm enhances the built-in electric field, which in turn improves carrier extraction and boosts PCE. Sun et al. studied the optoelectronic properties of $CaTiS_3$, $BaZrS_3$, $CaZrS_3$, and $CaHfS_3$ using density functional theory (DFT). Their findings suggest that strong light absorption and efficient carrier transport can be achieved with absorber layers thinner than 1000 nm, providing flexibility in device design [87]. Similarly, Nishigaki et al. synthesized various chalcogenide compounds, including $BaZrS_3$, $Ba(Zr,Ti)S_3$, and $BaZr(S,Se)_3$, and highlighted the importance of absorber layer thickness. Their results indicate that an optimal thickness of around 700 nm is ideal for maximizing light absorption, a key factor in achieving high-efficiency solar cells [120]. Eupsy et al. also explored the performance of $BaZrS_3$ using SCAPS-1D simulations and found that a 700 nm thick absorber layer can Pb to impressive PCE, reinforcing its potential for practical use [39]. Further supporting this, Swarnkar et al. synthesized materials such as $BaZrS_3$, $SrZrS_3$, and the layered perovskite $Ba_3Zr_2S_7$. Their study suggested that an absorber thickness of approximately 600 nm could enhance PCE, aligning with the general consensus that the optimal range lies between 600 nm and 1000 nm [121]. In conclusion, multiple studies agree that absorber layer thickness plays a crucial role in optimizing the efficiency of CPs solar cells. Considering the evidence from these studies, an absorber thickness of 700 nm has been

chosen for $SrHfSe_3$-based solar cells, as it aligns with established best practices in solar cell design.

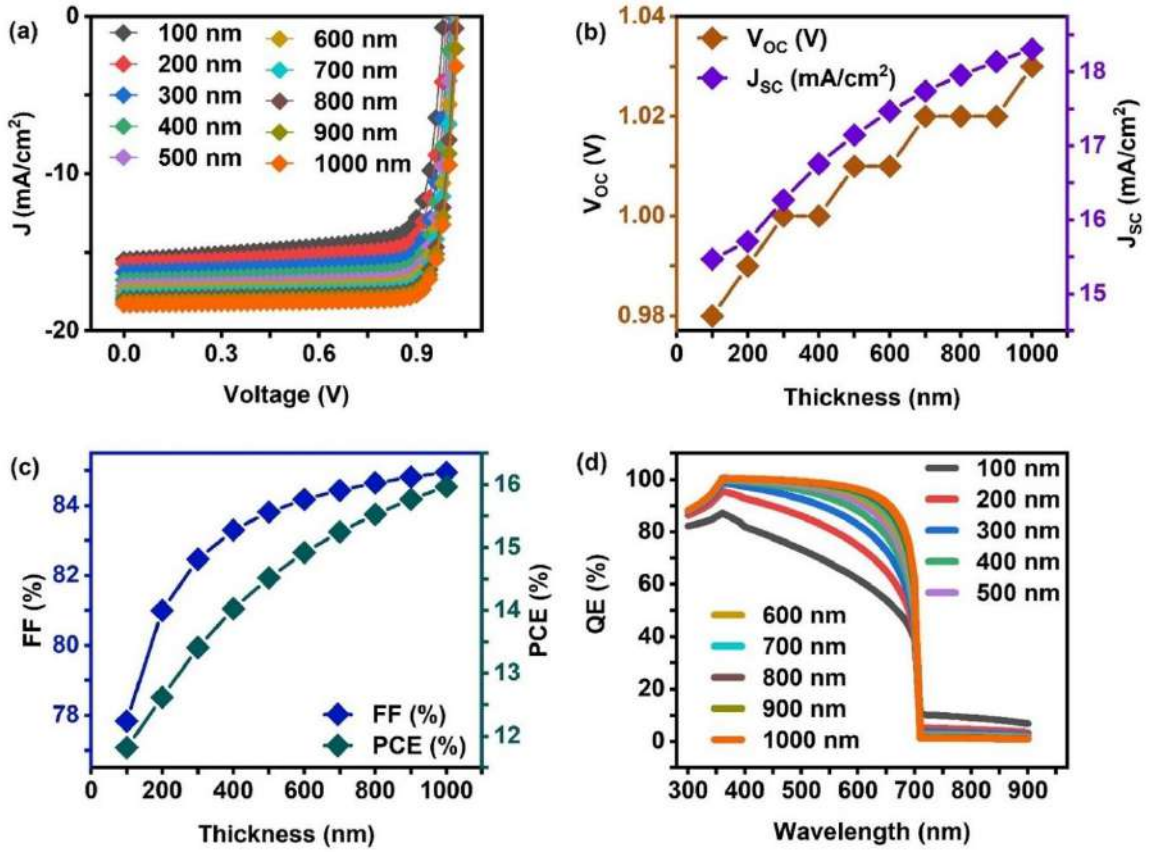

Fig. 11. Changes in (a) J-V (b) V_{OC}, J_{SC} (c) FF, PCE (d) QE corresponding to $SrHfSe_3$'s thickness [52].

6.1.6. Optimization of MoS_2 HTL Parameters

The insertion of HTL between the absorber and back contact diminishes the large barrier for photogenerated holes and results in efficient transportation to the back contact [122]. Therefore, it is crucial to study the material properties of MoS_2 to enhance solar cell performance. In this context, electron affinity, carrier concentration, defect density, and thickness are altered from 3.5 eV to 3.8 eV, 10^{17} cm^{-3} to 10^{20} cm^{-3}, 10^{14} cm^{-3} to 10^{20} cm^{-3}, and 60 nm to 150 nm, respectively to understand its influence on device performance.

6.1.7. Impact of MoS_2's Electron Affinity and Carrier Concentration

The conduction band offset (CBO) and valence band offset (VBO) at the absorber/HTL interface are directly determined by the electron affinity of HTL [109]. Thus, optimization of HTL's electron affinity is important in solar cells to mitigate the formation of energy barriers. Therefore, we altered the electron affinity of MoS_2 from 3.5 eV to 3.8 eV to detect the optimum

value for the enhanced transportation of holes. The corresponding variation in J-V, V_{OC}, J_{SC}, FF, and PCE is shown in **Fig. 12**(a-c). It is evident that the V_{OC} and FF display an upward trend while J_{SC} and PCE show a downward trend with increasing affinity values. Generally, a high CBO and low VBO are required at the absorber/HTL interface indicating a large barrier for electrons and less barrier for holes. This will restrict the electron flow and enhance the transport of holes through HTL. Therefore, CBO and VBO for each affinity value are calculated using **eqn** (10) and **eqn** (11) [123,124], and the corresponding values are listed in **Table 8**.

$$CBO = \chi_{ABS} - \chi_{HTL} \quad (10)$$

$$VBO = \chi_{HTL} + E_{G,HTL} - (\chi_{ABS} + E_{G,ABS}) \quad (11)$$

Where χ_{ABS} is the affinity of absorber, χ_{HTL} is the affinity of HTL while $E_{G,ABS}$ and $E_{G,HTL}$ are the absorber bandgaps and HTL respectively.

According to **Table 8**, it can be noticed that the VBO decreases and thus the barrier for holes decreases with increasing electron affinity. On the other hand, CBO also declines, representing a simultaneous reduction in the barrier for electrons. Thus, the optimum VBO and CBO must be identified to enhance solar cell performance. On comparing **Fig. 12**(a-c) with offset values, it can be observed that PCE decreases from 18.61 % to 14.47% when VBO (CBO) shrinks from -1.06 eV to -0.76 eV (0.6 eV to 0.3 eV). This strongly reveals that though the barrier for holes is reduced by decreasing VBO, the decrement in CBO intensely decreases the barrier height for electrons at the absorber/HTL interface, allowing the majority of photogenerated electrons to be collected by HTL instead of ETL, negatively impacting the performance of solar cell. This consequently leads to high recombination as can be seen in **Fig. 12(**d). Thus, an electron affinity of 3.5 eV is the optimum value to enhance the solar cell performance.

Table 8. Variation in CBO and VBO concerning electron affinity of MoS_2 HTL.

χ (eV)	3.5	3.6	3.7	3.8
CBO (eV)	0.6	0.5	0.4	0.3
VBO (eV)	-1.06	-0.96	-0.86	-0.76

After that, the effect of MoS_2's carrier concentration was examined by altering it from 10^{17} cm^{-3} to 10^{20} cm^{-3}. **Fig. 12**(e-g) presents the change in J-V, V_{OC}, J_{SC}, FF, and PCE with changes in MoS_2's carrier concentration. It evidenced that all the PV parameters increase when the carrier concentration is enhanced from 10^{17} cm^{-3} to 10^{20} cm^{-3} i.e., V_{OC} from 0.97 V to 1.09

V_{OC}, J_{SC} from 20.92 mA/cm^2 to 23.05 mA/cm^2 and FF from 83.93% to 86.81%. This V_{OC}, J_{SC}, and FF improvement has enhanced PCE from 17.11% to 21.91%. The observed elevation in performance can be explained by extracting the energy band diagram with respect to MoS_2's carrier concentration **Fig. 12(**h). It can be noticed that when MoS_2's carrier concentration is improved from 10^{17} cm^{-3} to 10^{20} cm^{-3}, the E_C and E_V slightly shift upwards such that the latter moves towards the F_P. As a result, a strong built-in electric field is developed at the $SrHfSe_3/MoS_2$ interface. The enhancement in the electric field within the HTL region for increasing carrier concentration can be seen in **Fig. 12**(i). The presence of an intense electric field at the interface elevates the hole transportation from $SrHfSe_3$ to the back contact through MoS_2 [125]. Moreover, the obtained results reveal a solution for the case where the optimal CBO and VBO cannot be achieved experimentally at the absorber/HTL interface. Increasing the HTL's carrier concentration can diminish the barrier for holes and boost the barrier for electrons by shifting the respective bands upwards. Overall, it can be seen that that MoS_2's carrier concentration of 10^{20} cm^{-3} is needed to acquire high performance of solar cell and thus it is fixed for further simulations.

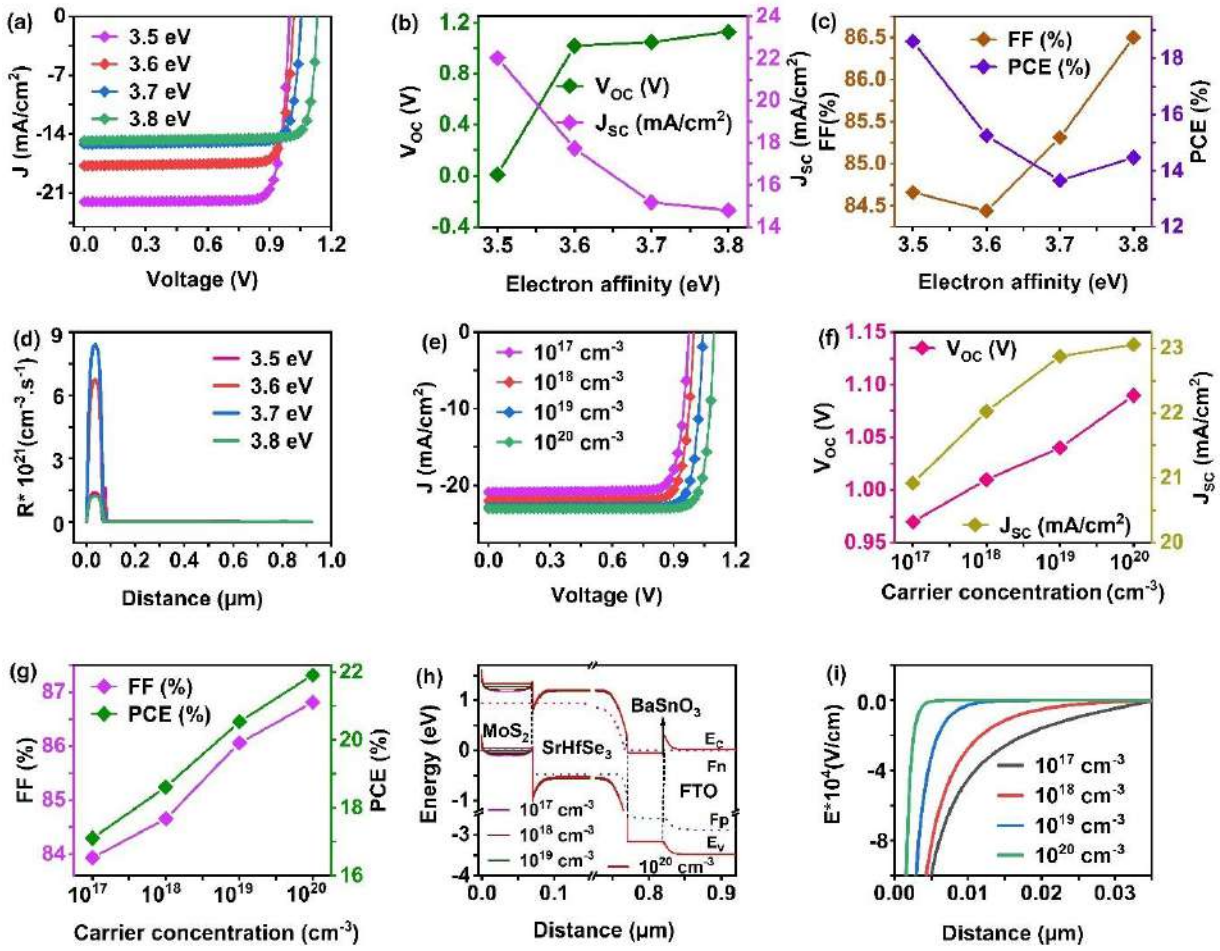

Fig. 12. Changes in (a) J-V b) V_{OC}, J_{SC} (c) FF, PCE, and (d) recombination rate corresponding to MoS_2's electron affinity. Variations in (e) J-V (f) V_{OC}, J_{SC} (g) FF, PCE (h) energy band alignment, and (i) electric field corresponding to MoS_2's carrier concentration [52].

6.1.8. Impact of MoS_2's Defect Density and Thickness

Fig. 13(a–c) depicts the influence of MoS_2's defect density on the J-V, V_{OC}, J_{SC}, FF, and PCE of solar cells for the defect density range from 10^{14} cm^{-3} to 10^{20} cm^{-3}. It is evidenced, when the defect density is increased from 10^{14} cm^{-3} to 10^{20} cm^{-3}, the V_{OC}, J_{SC}, and PCE are reduced from 1.19 V to 0.95 V, 23.12 mA/cm^2 to 16.28 mA/cm^2 and 23.02% to 13.01% respectively while a discrepancy is observed in the behavior of FF. The significant drop in performance of solar cell is largely attributed to an increased number of recombination centers at the interface between at the interface between $SrHfSe_3/MoS_2$ with increasing defect density which acts as a trap for the photogenerated carriers, thereby boosting the recombination rate [126]. This can also be witnessed in **Fig. 13(**d) where the recombination rate dramatically increases with defect density, deteriorating the PCE. Therefore, a defect density of 10^{14} cm^{-3} is optimized to attain high performance of the solar cell.

The thickness of HTL is a key to improving the performance of the solar cell and reducing the direct contact between the $SrHfSe_3$ absorber and back contact [127]. For analysis, the thickness of MoS_2 is altered from 60 nm to 150 nm with a fixed $SrHfSe_3$ thickness of 700 nm, as shown in **Fig. 13(**e-g). It can be noticed that PCE drastically rose from 22.48% to 26.55% which stems from the significant improvement in J_{SC} from 19.33 mA/cm^2 to 24.54 mA/cm^2 with increasing thickness of MoS_2. The enhancement in J_{SC} is directly related to the improved light absorption in solar cells with increasing MoS_2 thickness which can be witnessed in QE measurements **Fig. 13(**h). When the thickness is 60 nm, the QE is above 95% in the UV-Vis region (300-700 nm) due to high light absorption in $SrHfSe_3$, resulting in large photoinduced carrier generation. It is important to mention that photons with energy below the active layer's bandgap are unable to be absorber and pass through to the HTL [128]. Thus, QE drops to 25% at 708 nm as the bandgap of $SrHfSe_3$ is 1.75 eV. In addition, QE is maintained at 25% in the NIR region (708-960 nm) and falls to zero at 960 nm indicating a minute light absorption in MoS_2. Interestingly, when the thickness raised from 60 to 150 nm, QE in the NIR region improves from 25% to 45%. It strongly reveals that photocarrier generation in MoS_2 enhanced with its thickness. Specifically, as the bandgap of MoS_2 is 1.29 eV, it absorbs the low-energy photons transmitted from $SrHfSe_3$ and enhances the absorption to a larger wavelength. Thus, the outcomes indicate that MoS_2 performs dual action of light absorption and transportation of holes, resulting in high performance of the solar cell.

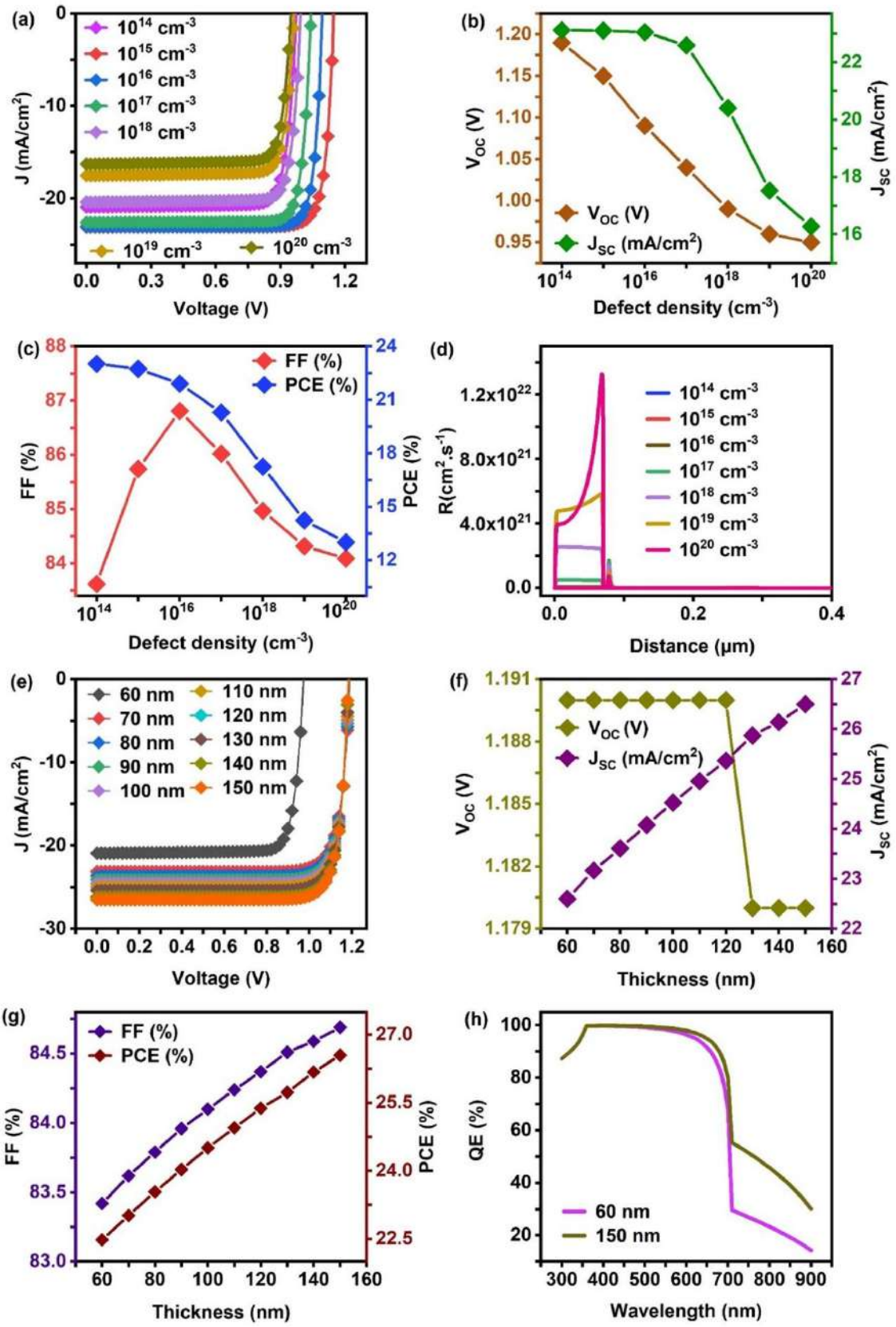

Fig. 13. Changes in (a) J-V (b) V_{OC}, J_{SC} (c) FF, PCE, and (d) recombination rate corresponding to MoS_2's defect density. Changes in (e) J-V (f) V_{OC}, J_{SC} (g) FF, PCE, and (h) QE corresponding to MoS_2's thickness [52].

6.1.9. Impact of Back Metal Work Function

The work function of back contacts is important to provide ohmic contact for potential transportation of hole and to increase the V_b in solar cells. Thus, metals such as Cu/Mo, Ag, Fe, Cu doped C, Au, W, Ni, and Pd with work functions 4.6, 4.7, 4.8, 5.0, 5.1, 5.22, 5.5, and 5.6 eV respectively are used in the proposed structure of solar cell to identify suitable back metal contact. The J-V, V_{OC}, J_{SC}, FF, and PCE as changes of metalwork function are displayed in **Fig. 14**(a-c). It can be noticed that all the PV parameters increased with the metal work function till 5.22 eV and became constant. This behavior can be illustrated with the schematic diagram given in **Fig. 14(**d). A low work function causes the metal's Fermi level to be situated close to the E_C of the HTL. Thus, it generates a huge barrier (Schottky) for holes, hindering its transfer from HTL to metal contact [129]. Moreover, as the barrier for electrons is very low, it can quickly transfer from the E_C of HTL to metal contact or vice versa leading to high recombination in solar cells. On the other hand, if the work function is high, the fermi level is near the E_V of HTL which reduces the barrier for holes, resulting in the efficient hole transfer to the metal contact [129]. Hence, it is evident that enhancement in performance of solar cell with escalating work function occurs due to the movement of the metal's fermi level towards the E_V of HTL [130]. The maximum PCE of 26.21% is obtained for Ni as it forms ohmic contact at the MoS_2/Ni interface to efficiently flow holes while displaying the Schottky barrier towards electrons. It can also be noticed that the PV parameters become saturated beyond 5.22 eV, happening due to the increasing ohmic resistance at the HTL/metal interface [130,131].

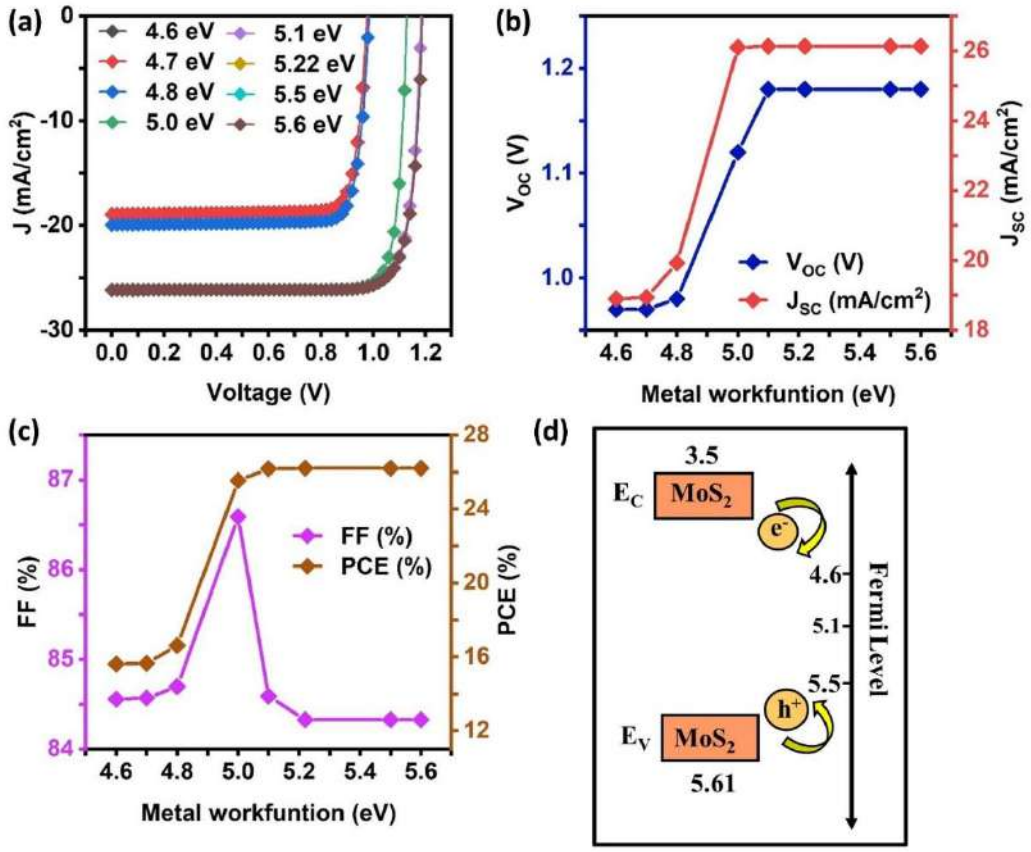

Fig. 14. (a) Variation in (a) J-V (b) V_{OC}, J_{SC} (c) FF, PCE as a function metal work function. (d) Schematic representation of the movement of metal's fermi level concerning the work function [52].

6.1.10. Design of 41 Solar Cells

After the optimization of $SrHfSe_3$, MoS_2, and back contact with the initial solar cell structure, the V_{OC}, J_{SC}, FF, and PCE increased from 1.00 V to 1.18 V, 14.08 mA/cm^2 to 26.14 mA/cm^2, 80.81% to 84.59% and 11.42% to 26.21% respectively. It can be illustrated from the results that PCE increases by 1.72 times after the optimisation of MoS_2 revealing that the impact of HTL on the performance of solar cell is considerably high. Thus, to investigate its properties comprehensively as well as to identify the suitable device configuration, MoS_2 was replaced by 40 HTLs including inorganic semiconductors (MoS_2, Cu_2S, Sb_2S_3, CuO, SnS, $CuBiS_3$, Cu_2SnS_3, Cu_2SbS_2, Cu_2BaSnS_3, CIGS, CZTS, CZGS, CuS, CoO, WS_2, FeS_2, $CaFe_2O_4$, MoO_3, $YFeO_3$, VO_x, $BiVO_4$, SnS_2, Sb_2Se_3, Ce_2Se_3, Mg_2Si), polymers (P_3HT, P_3Cpent, CPE-K, P_2, P_3, P_1, PEDOT: PSS, PCPDT-T, PCPDT-2T, TFB, PTAA, PFS, g-C_3N_4), and MXenes (Zr_2CO_2, Hf_2CO_2, Ti_2CO_2) and parameters such as χ, N_A, N_t and thickness are optimized for all HTLs by keeping the other layers parameters constant. Furthermore, their back metal work functions are also optimized. As a result, 1627 solar cells were designed involving 1033 solar cells with

inorganic semiconductors, 117 with polymers, and 477 using MXenes as HTLs. The parameters are employed in the simulation of different HTL-based solar cells. **Fig. 15** displays the bar diagram where the number of solar cells that exhibited PCE above 20% is plotted for each category of HTLs. In the case of inorganic semiconductors, among 1033 solar cells, 429 devices displayed PCE >20%, and 240 devices demonstrated PCE>25% wherein the highest PCE of 27.87% was achieved for SnS-based solar cell with structure FTO/$BaSnO_3$/$SrHfSe_3$/SnS/Ni. Similarly, nearly 10 out of 117 solar cells exhibited PCE above 25% in polymer-based solar cells and the FTO/$BaSnO_3$/$SrHfSe_3$/CPE-K/Ni device structure has presented the best PCE of 27.39%. Considering MXenes-based solar cells, the highest PCE of 26.30% is delivered for FTO/$BaSnO_3$/$SrHfSe_3$/Ti_2CO_2/Ni device structure where more than 420 and 160 solar cells portrayed PCE >20% and >25% respectively. Among the 1627 simulated solar cells, 888 devices achieved PCE above 20% while 410 devices achieved PCE above 25%, demonstrating the high potential of the novel $SrHfSe_3$ absorber for achieving high performance. The solar cell parameters before and after optimization of each HTL along with their corresponding optimized metal contacts are provided in **Table 9.** It is evident that the results of the different HTL-based solar cells after the optimization of HTL's material parameters and metal contacts are different. This occurs due to the variation in their energy band positions and the consequent modification in the band alignment of each HTL with $SrHfSe_3$ and corresponding metal contacts as displayed in **Fig. 16**. Overall, the best PCE is attained for SnS, CPE-K, and Ti_2CO_2 HTLs under the category of inorganic semiconductors, polymers, and MXenes-based solar cells respectively. Here, studying their properties elaborately to understand why they have high PCE among the other solar cells is crucial. However, comparing its properties and variations in PV performance with all 41 HTLs may become an intense work. Therefore, their superiority over the other HTLs is broadly elucidated by comparing their optical, electrical, and material properties with the HTLs that presented low PCEs. According to **Table 9,** Mg_2Si, PEDOT: PSS, and Hf_2CO_2-based solar cells have shown the least PCEs among inorganic semiconductors, polymers, and MXenes-based solar cells respectively. Thus, the above-mentioned solar cells are selected for comparison with SnS, CPE-K, and Ti_2CO_2-based solar cells to gain deep insights into their dominance over other devices. In the comparative study performed in the following sections, the low PCE devices denote Mg_2Si, PEDOT: PSS, and Hf_2CO_2-based solar cells and the high PCE devices represent the SnS, CPE-K, and Ti_2CO_2-based solar cells.

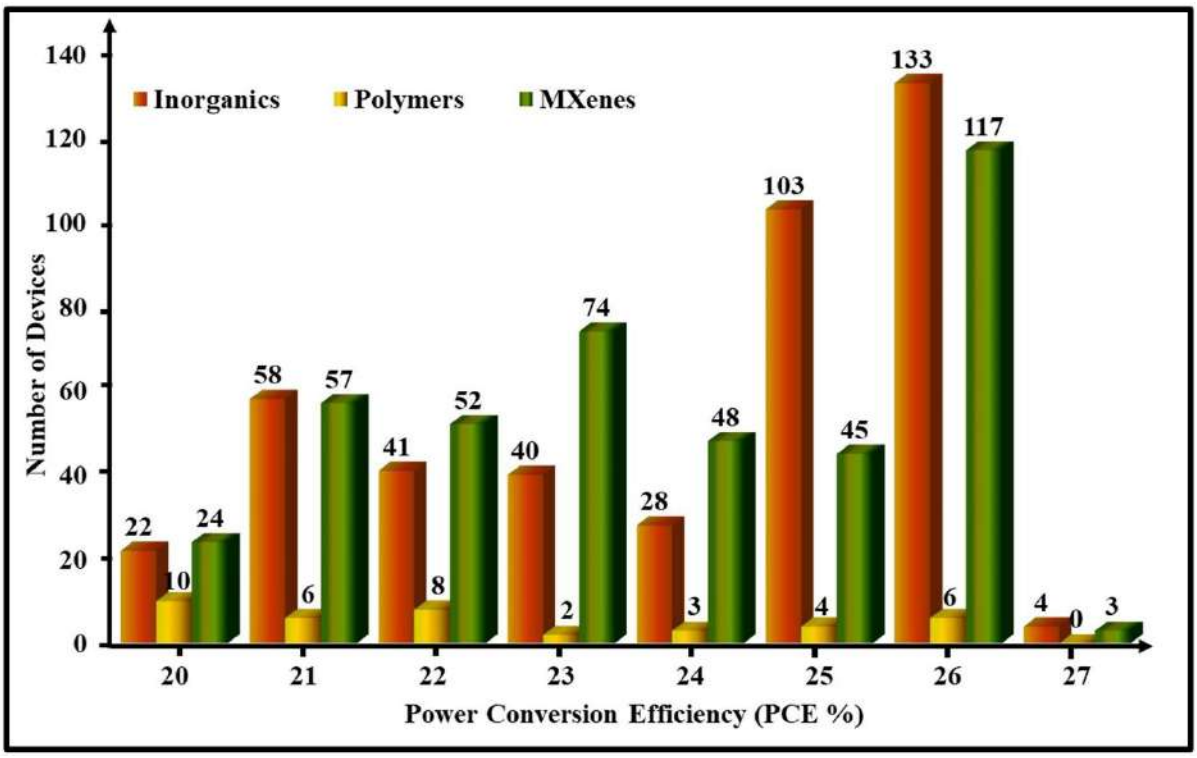

Fig. 15. Bar diagram of inorganic semiconductors, polymers, and MXene-based solar cells that demonstrated PCE above 20% [52].

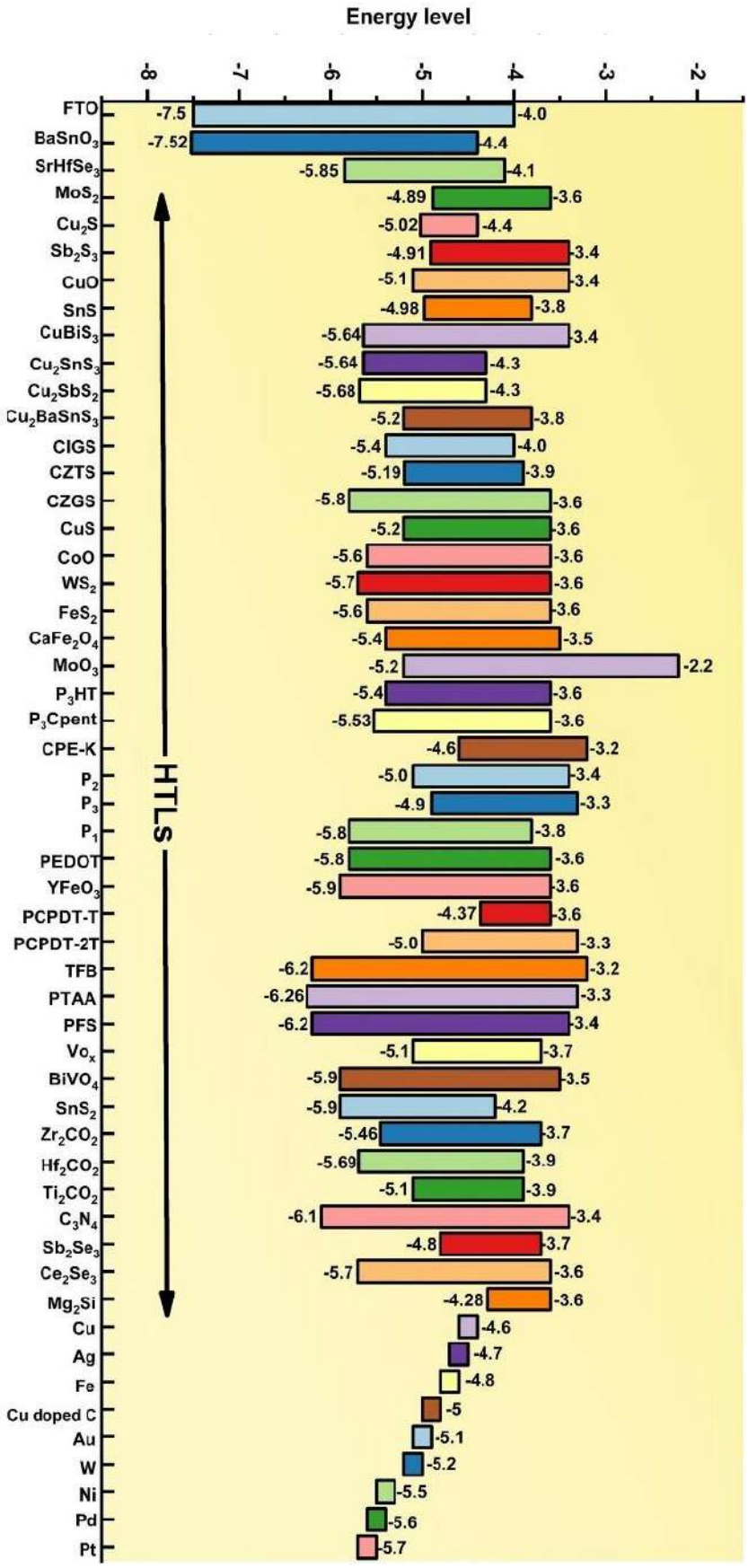

Fig. 16. Schematic representation of energy band alignment of 41 HTLs with $SrHfSe_3$ and back contacts [52].

Table 9. Solar cell parameters before and after the optimization of HTLs including inorganic semiconductors, polymers and MXenes with their optimized back contacts [52].

Number of SCs	Different HTL	Before Optimization with Au Back Contact				After Optimization				Optimized Back contact
		V_{OC} (V)	J_{SC} (mA/cm^2)	FF (%)	PCE (%)	V_{OC} (V)	J_{SC} (mA/cm^2)	FF (%)	PCE (%)	
Inorganic semiconductor										
1	MoS_2	1.00	14.08	80.81	11.42	1.18	26.14	84.33	26.21	Ni
2	Cu_2S	1.24	14.80	87.05	16.02	1.34	14.83	87.48	17.41	Ni
3	Sb_2S_3	1.39	14.84	87.69	18.12	1.43	20.61	86.79	25.61	W
4	CuO	1.19	14.79	86.83	15.38	1.20	21.82	85.19	22.37	Ni
*** 5**	**SnS**	**1.25**	**14.80**	**87.12**	**16.16**	**1.21**	**26.22**	**87.72**	**27.87**	**Ni**
6	$CuBiS_3$	1.31	14.82	87.35	16.97	1.34	21.20	85.55	24.48	Ni
7	Cu_2SnS_3	1.29	14.81	87.30	16.80	1.42	14.85	87.80	18.56	Ni
8	Cu_2SbS_2	1.36	14.90	87.64	17.86	1.43	14.90	87.87	18.73	Pt
9	Cu_2BaSnS_3	1.35	14.87	87.57	17.64	1.43	14.88	87.86	18.71	Au
10	CIGS	1.25	14.80	87.11	16.13	1.38	14.84	87.65	18.01	Au
11	CZTS	1.25	14.81	87.11	16.24	1.43	14.89	87.87	18.73	Au
12	CZGS	1.25	14.87	86.68	16.23	1.43	14.94	87.89	18.79	Pt
13	CuS	0.88	17.25	85.96	13.18	1.52	18.94	91.39	26.47	Pt
14	CoO	1.54	18.92	88.90	25.97	1.54	18.91	90.91	26.50	Pt
15	WS_2	1.14	14.78	86.52	14.61	1.54	18.95	91.05	26.64	Au
16	FeS_2	1.18	16.14	87.56	16.73	1.42	14.85	87.80	18.56	Au
17	$CaFe_2O_4$	1.03	14.86	85.95	13.20	1.54	18.94	91.05	26.60	Pt
18	MoO_3	1.54	18.91	88.32	25.79	1.54	18.92	88.61	25.87	Pt
19	$YFeO_3$	1.47	16.91	88.14	21.92	1.54	18.98	87.92	25.73	Ni
20	Vox	1.16	14.84	86.37	14.90	1.24	20.25	87.24	21.94	Ni
21	$BiVO_4$	0.97	15.20	85.69	12.70	1.52	18.92	91.30	26.28	Ni
22	SnS_2	0.92	14.83	85.15	11.72	1.43	15.50	88.29	19.66	Ni
23	Sb_2Se_3	1.04	14.75	85.99	13.30	1.31	14.82	87.38	17.08	Au
24	Ce_2Se_3	1.54	18.87	90.57	26.36	1.54	18.95	91.01	26.63	Pt
25	Mg_2Si	1.19	14.77	86.40	14.28	1.18	14.79	86.80	15.26	Au

Number of SCs	Different HTL	Before Optimization with Au Back Contact				After Optimization				Optimized Back contact
		V_{OC} (V)	J_{SC} (mA/cm^2)	FF (%)	PCE (%)	V_{OC} (V)	J_{SC} (mA/cm^2)	FF (%)	PCE (%)	
Polymers										
26	P_3HT	1.25	14.90	87.18	16.37	1.52	19.09	91.10	26.52	Au
27	P_3Cpent	1.54	18.92	87.06	25.43	1.54	18.94	87.80	25.67	Ni
***28**	**CPE-K**	**1.16**	**16.83**	**85.35**	**16.69**	**1.29**	**24.25**	**87.11**	**27.39**	**Ni**
29	P_2	1.42	14.89	87.86	18.71	1.47	19.00	88.14	24.78	Ni
30	P_3	1.30	15.09	86.14	16.92	1.45	19.51	86.71	24.60	Ni
31	P_1	0.87	14.82	84.67	10.97	1.52	18.93	91.38	26.41	Pt
32	PEDOT: PSS	1.27	18.53	86.11	20.32	1.31	19.39	87.72	22.33	Ni
33	PCPDT-T	1.41	16.00	86.59	19.67	1.50	19.01	89.10	25.50	Ni
34	PCPDT-2T	1.33	16.09	85.62	18.37	1.41	19.21	88.05	23.94	Ni
35	TFB	1.54	18.92	90.29	26.37	1.54	18.92	91.04	26.59	Au
36	PTAA	1.54	18.92	90.94	26.55	1.54	18.92	91.05	26.60	Ni
37	PFS	1.54	18.91	86.60	25.29	1.54	18.92	91.05	26.59	Ni
38	g-C_3N_4	1.54	18.92	90.92	26.55	1.54	18.92	91.04	26.59	Au
MXenes										
39	Zr_2CO_2	1.29	14.91	87.36	16.89	1.45	17.19	89.49	22.49	Pt
40	Hf_2CO_2	0.92	14.84	85.17	11.74	1.44	16.45	88.98	21.16	Ni
***41**	**Ti_2CO_2**	**1.04**	**17.82**	**84.51**	**15.73**	**1.13**	**26.66**	**86.97**	**26.30**	**Ni**

6.1.11. Energy Band Diagram

The critical factor that rules the solar cell performance is the appropriate alignment of energy bands between each layer [132,133]. Thus, to investigate the impact of simulated solar cells as a changes of band alignment, the energy band diagram of the low and high PCE solar cells under each category of HTLs, i.e., inorganic semiconductors, polymers, and MXenes are extracted from SCAPS-1D **Fig. 17**(a-f). It can be seen that the alignment of E_C and E_V at the absorber/ETL and ETL/FTO interface is almost the same in all 6 solar cells due to the presence of the same absorber and ETL. Hence, it is evident that the difference in their PCE arises from the changes in band alignment between absorber and HTL. On comparing the Mg_2Si and SnS-based solar cells **Fig. 17(**a) and (b), the alignment of E_V is almost similar in both cases at the

interface of absorber/HTL, demonstrating that the barrier for holes is the same. Whereas, a cliff-like barrier is observed for electrons at the E_C of $SrHfSe_3$/Mg_2Si interface, which results in electrons flowing through Mg_2Si instead of $BaSnO_3$ leading to high recombination of charge carriers [134]. On the other hand, a spike-like barrier is observed at the $SrHfSe_3$/SnS interface, which restricts the collection of electrons via SnS; thus, reducing the recombination rate and elevating the performance of solar cell. In the case of polymers and MXenes-based solar cells, the primary difference between low and high PCE solar cells begins from the alignment of the HTL's energy bands with the fermi level of back contacts. Considering their low PCE solar cells, the Schottky barrier is formed at the interface of HTL/back contact. This blocks the collection of holes at the back contact, raising their accumulation in the HTL which adversely deteriorates the solar cell performance [129,130]. Contrarily, ohmic contact is observed for high PCE polymers and MXenes-based solar cells at the interface of HTL/back contact where a compelling collection of holes occurs, boosting their PCE. Overall, it is clear that the proper energy band alignment at absorber/HTL and HTL/back contact interface gave rise to the best PCEs in SnS, CPE-K, and Ti_2CO_2-based solar cells.

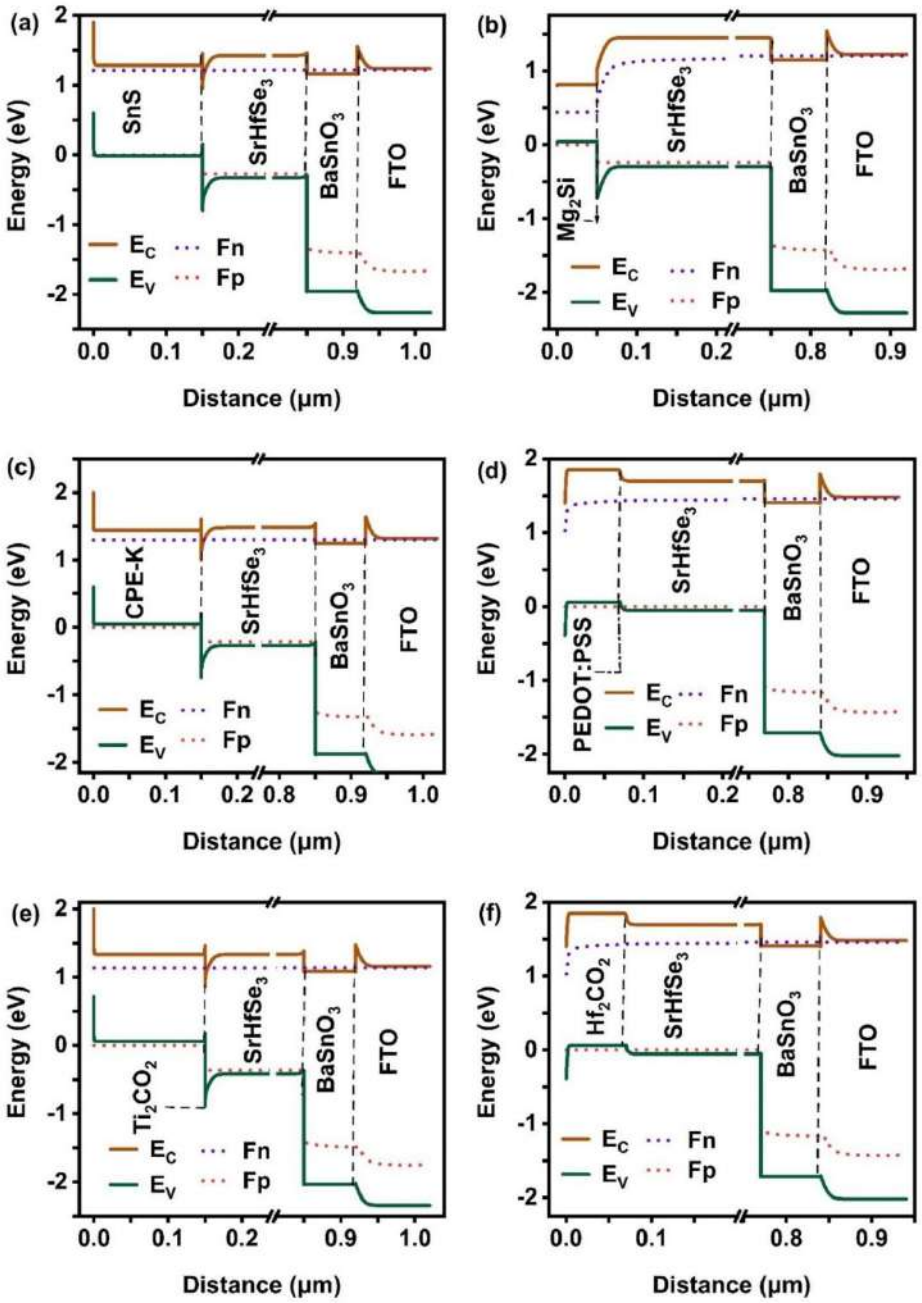

Fig. 17. Energy band diagram of low and high PCE solar cells with (a,b) inorganic semiconductors (c,d) polymers, and (e,f) MXenes HTLs [52].

6.1.12. Nyquist Plot

Impedance spectroscopy has been utilized to characterize solar cells and understand the movement of charge carriers, offering valuable insights into their operational mechanisms [135]. Hence, the Nyquist plot of low and high PCE inorganic semiconductors, polymers, and MXenes-based solar cells are plotted from C-F measurements (**Fig. 18**(a-c)). All the solar cells display semi-circular plot which strongly reveals the superiority of the depletion regions in the

solar cells. The Nyquist plots of solar cells generally consist of two semicircles in different frequency regions. The low-frequency semicircle corresponds to the recombination resistance (R_{rec}) while the one at the high frequency represents the charge transfer resistance (R_{CT}) of the solar cells [136]. In our case, a single semicircle has been observed in the entire frequency region, indicating the R_{rec} of the solar cells. In addition, the semicircle of high PCE solar cells is larger than their counterparts, disclosing that R_{rec} is vast in high PCE solar cells while it is small in low PCE solar cells. Thus, due to large R_{rec}, the photogenerated charge carriers in high PCE solar cells can be effectively separated and collected at the respective contacts without recombination, attributing to their surpassing PCE. In contrast, the less R_{rec} in low PCE solar cells boosts the carrier's recombination, ascribing to their poor performance of solar cell. This is also witnessed in the energy band diagram **Fig. 17**(a–f)) where the possibility of recombination is high in low PCE solar cells due to the improper alignment of energy bands at the absorber/HTL and HTL/back contact interface.

6.1.13. J-V and QE

Fig. 18(d-f) demonstrates the J-V characteristics of low and high PCE devices and their corresponding PV parameters in **Table 9.** For MXenes-based solar cells, the V_{OC} and FF of Ti_2CO_2 are less than Hf_2CO_2-based devices whereas its J_{SC} is comparatively large. Thus, it is obvious that the high PCE of Ti_2CO_2-based solar cells mainly comes from their towering J_{SC} values. In the case of inorganic semiconductor and polymer-based solar cells, the V_{OC} and FF are approximately similar for both high and low-PCE solar cells. Notably, there is a massive difference in their J_{SC}. Specifically, the J_{SC} of SnS is 26.22 mA/cm^2 and CPE-K is 24.25 mA/cm^2 which is 1.77 and 1.25 times higher than Mg_2Si and PEDOT: PSS respectively. Overall, the results precisely demonstrate that the best PCE achieved in SnS, CPE-K, and Ti_2CO_2-based solar cells originates from their drastically high J_{SC} values while the V_{OC} and FF do not contribute to their performance. It is worth noting that the J_{SC} of the high PCE devices is also larger than the other HTL-based solar cells, exhibiting their superiority over all the simulated devices.

QE is an important technique that gives the maximum amount of current produced when the solar cell is irradiated by photon flux [137]. Therefore, QE for low and high PCE solar cells are plotted to understand the reason behind the difference in their J_{SC} values. In all the low PCE solar cells, the absorption terminates at 708 nm, indicating the absorption edge of $SrHfSe_3$ with the bandgap 1.75 eV. Whereas it extends till 960 nm, 850 nm, and 970 nm for SnS, CPE-K, and Ti_2CO_2-based solar cells respectively, occurring due to the additional absorption in the

HTL region due to their low bandgap than the absorber as discussed in section 3.3.2 (**Fig. 18 (**g–i)). In addition, we could notice that the QE is 100% in the visible region (400-700 nm) in all high PCE solar cells. This denotes that $SrHfSe_3$ absorbs all possible photons of wavelength 400-700 nm, generating the colossal amount of charge carriers collected at the respective contacts owing to the proper alignment of energy bands in high PCE solar cells. Conversely, in the visible region, the QE is <80% in Mg_2Si and Hf_2CO_2-based solar cells and it reduces from 100% to <95% at 595 nm in PEDOT: PSS-based solar cells, arising from the poor band alignment of HTLs with the absorber and back contact which terminates the carrier generation in these solar cells due to high minority carrier recombination. Thus, the J_{SC} holds greater values in high PCE devices owing to overall absorption of 58.22%, 56.67%, and 60.48% in SnS, CPE-K, and Ti_2CO_2-based solar cells respectively which is 1.51, 1.18, and 1.44 times larger than Mg_2Si, PEDOT: PSS and Hf_2CO_2 based solar cells respectively.

Overall, among the 41 HTLs, SnS, CPE-K, and Ti_2CO_2 portrayed exceptional solar cell performance under the category of inorganic semiconductors, polymers, and MXenes respectively due to their favorable band alignment at absorber/HTL and HTL/back contact interface, large $R_{rec,}$ and high light absorption. Thus, these high PCE solar cells are selected further to the impact of series resistance, shunt resistance, and working temperature on their achievement which are elaborated in the following sections.

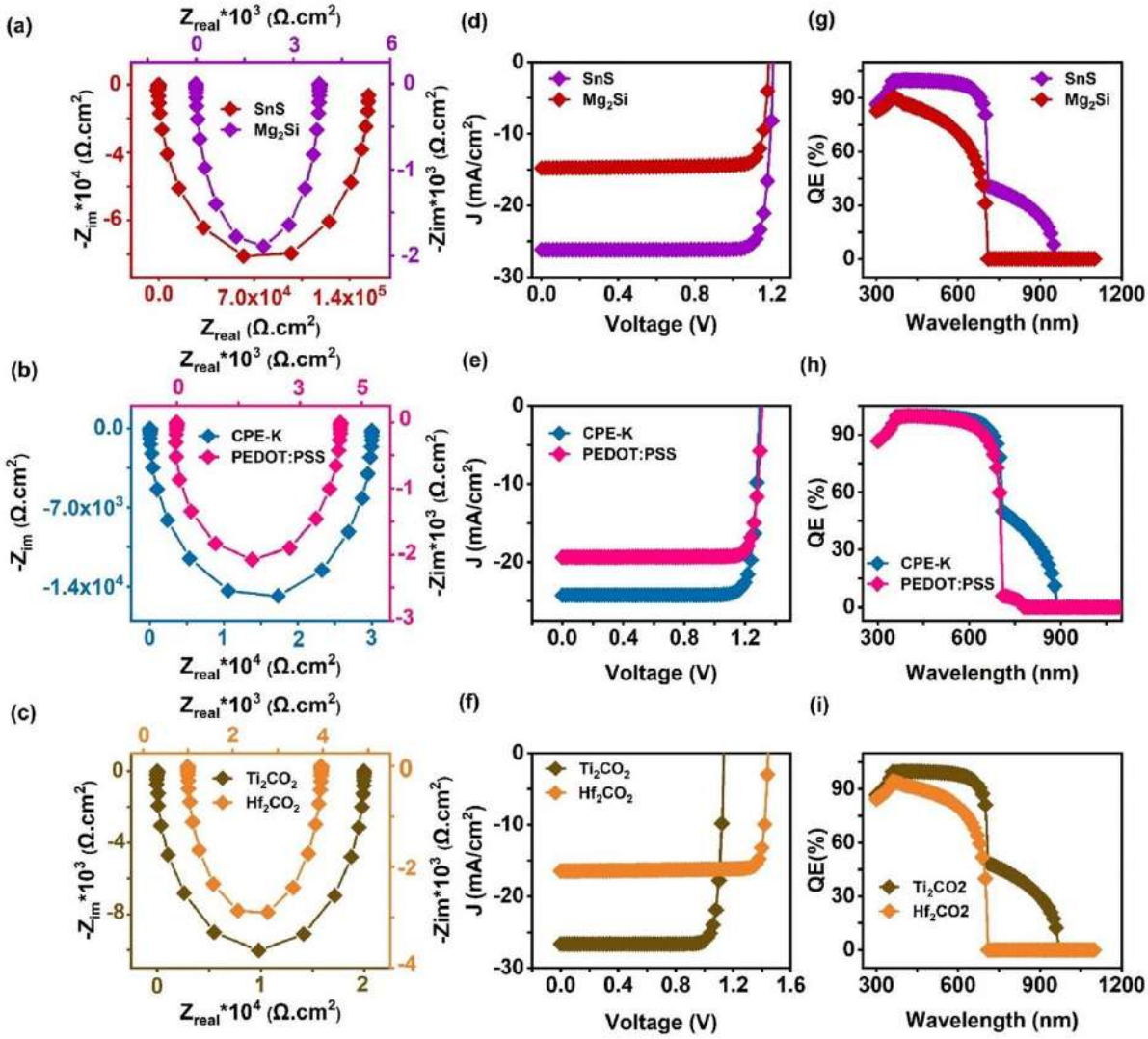

Fig. 18. (a-c) Nyquist plot (e-f) J-V and (g-i) QE of high and low PCE solar cells [52].

6.1.14. Effect of Series and Shunt Resistance

Series resistance and Shunt resistance, called parasitic resistances, have an immense effect on the behaviour of solar cells [138]. In general, the resistance between metal contacts (front and back) and transport layers as well as the resistance of the absorber outside the space charge region improved the series resistance in devices. On the other hand, R_{Shunt} mainly stems from the reverse saturation current in devices [138]. Thus, we investigated their effect on the behaviour of high-PCE solar cells. Firstly, the series resistance of all the solar cells is optimized from 1 to 10 Ω cm^2. V_{OC}, J_{SC} FF, and PCE corresponding to series resistance are displayed in **Fig. 19**(a–d). In all the solar cells, it can be noticed that V_{OC} and J_{SC} remain unaltered. On the contrary, FF drastically reduces from 85.67% to 67.78%, 85.36% to 70.07%, and 84.75% to 65.51% in SnS, CPE-K, and Ti_2CO_2-based solar cells respectively. This is due to the vast power loss (P_{loss}) in the solar cells for large series resistance, as seen in the following **eqn** (12) [139].

$$P_{loss} = I_{sc}^2 R_{series} \quad (12)$$

As power loss (P_{loss}) is directly proportional to series resistance, a rise in series resistance will increase P_{loss} in the solar cells, affecting FF. It eventually reduces the PCE of SnS, CPE-K, and Ti_2CO_2-based solar cells to 21.55%, 22.05%, and 19.83% respectively. Thus, a low R_{Series} of 1 Ω cm^2 is required for the potential solar cell operation. Secondly, we altered shunt resistance from 500 to 5000 Ω cm^2 to explore their effect on the behaviour of all solar cells (**Fig. 20**(a–d)). The results demonstrated that J_{SC} and V_{OC} of both solar cells remains constant while FF and PCE are enhanced with rising shunt resistance. However, the difference in the PCE between 500 Ω cm^2 and 5000 Ω cm^2 is small, i.e., 2.16%, 2.47%, and 1.87% for SnS, CPE-K, and Ti_2CO_2-based devices respectively. It highlighted that the effect of R_{Shunt} on solar cell behaviour is negligible compared to series resistance.

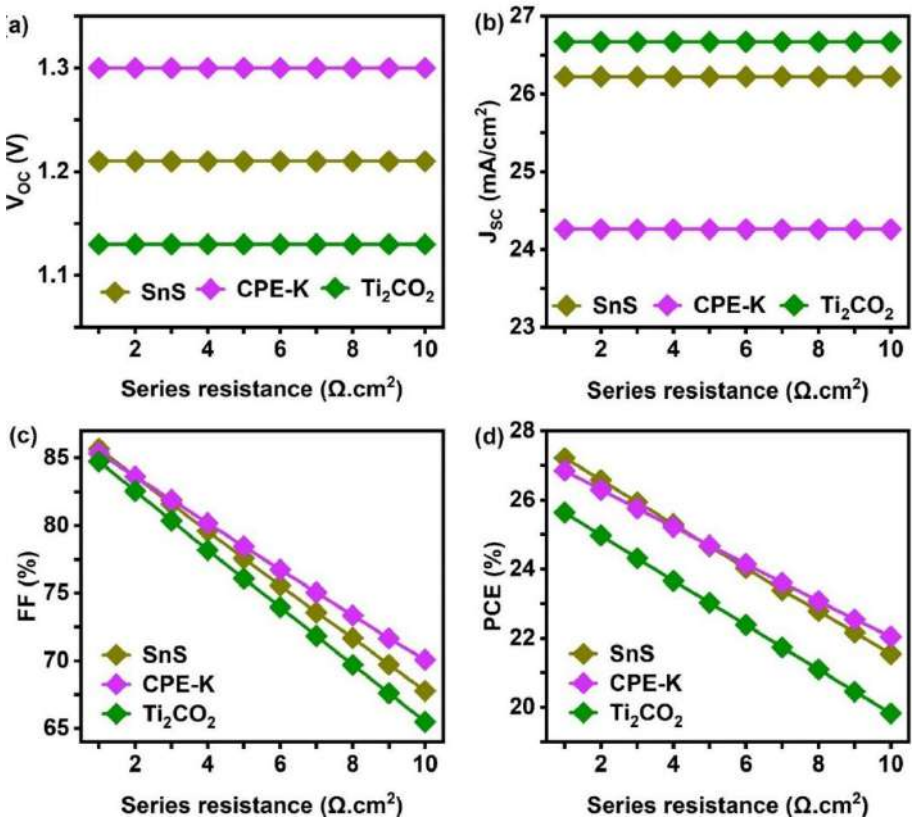

Fig. 19. Changes in (a) V_{OC} (b) J_{SC} (c) FF and (d) PCE of high PCE solar cells concerning the series resistance [52].

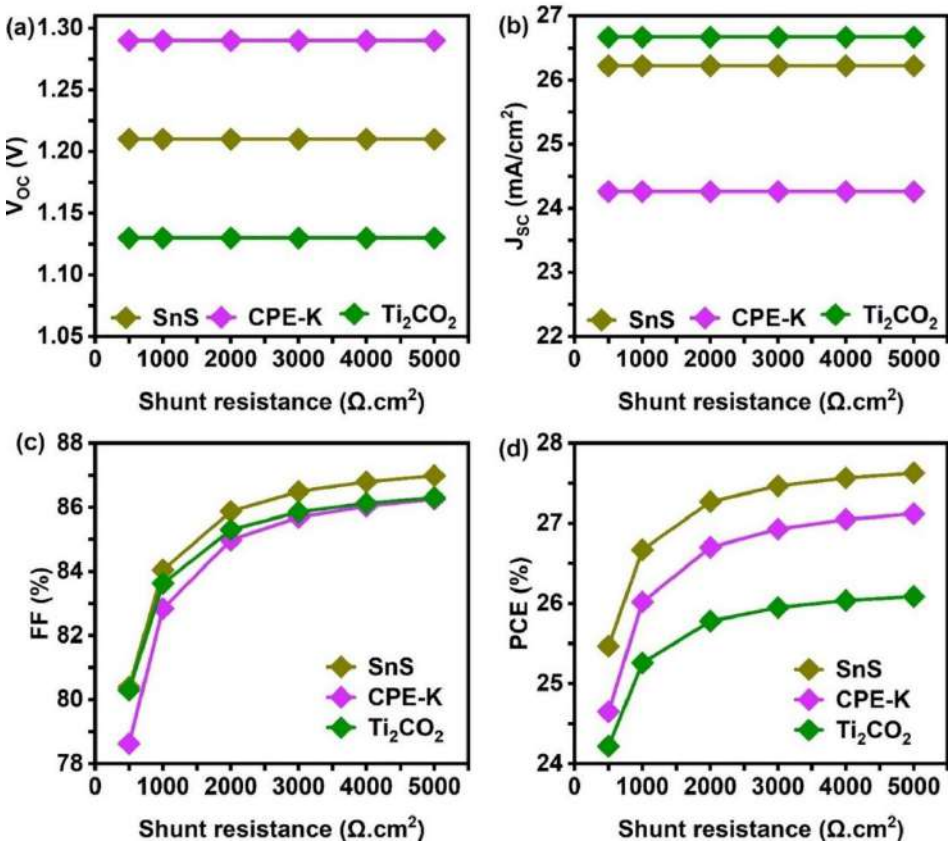

Fig. 20. Changes in (a) V_{OC} (b) J_{SC} (c) FF and (d) PCE of high PCE solar cells concerning the shunt resistance [52].

6.1.15. Effect of Working Temperature

As the solar panels are installed in an open atmosphere, the working temperature plays a significant role in the solar cell performance [140]. Thus, its influence on SnS, CPE-K, and Ti_2CO_2-based solar is investigated by varying it from 300 to 480 K. **Fig. 21(**a–d) shows the changes in V_{OC}, J_{SC}, FF, and PCE as a function of temperature. All the PV parameters decrease with the increasing temperature. Specifically, PCE deteriorated from 27.87% to 17.92%, 27.39% to 21.10%, and 26.30% to 14.47% in SnS, CPE-K, and Ti_2CO_2-based solar cells respectively. This behiours is attributed to increase in temperature, parameters such as carrier concentration, bandgap of absorber, mobility of charge carriers, etc of solar cells are adversely affected, deteriorating the solar cell performance [141]. Additionally, the connection between V_{OC} and temperature can be described using the following **eqn** (13) [142]:

$$V_{OC} = \frac{Ea}{q}\ \frac{MkT}{q}\ In\ \frac{j00}{jPD} - (13)$$

where T represents temperature, M is the ideality factor, E_a is the activation energy for recombination, q is the elementary charge, k is the Boltzmann constant, J_{00} is a prefactor, and

J_{PD} is the photocurrent density. Assuming that M, J_{00}, and J_{PD} do not vary with temperature, plotting V_{OC} against T should produce a straight line. By extending this line to absolute zero (0 K), the activation energy E_a can be determined. If E_a is lower than the bandgap of the absorber, it suggests that interface-induced recombination is the dominant loss mechanism, typically occurring at the interfaces between the absorber and either the ETL or HTL. On the other hand, if E_a is close to or equal to the absorber bandgap, recombination within the space charge or neutral region of the absorber mainly through the Shockley–Read–Hall (SRH) process becomes the primary loss mechanism [143,144]. This indicates that improper energy level alignment and interface defects contribute significantly to V_{OC} losses in these devices. Notably, E_a of CPE-K HTL is higher than the other HTLs which signifies that it has better energy level alignment and lower recombination losses than its counterparts. The observed E_a rise may also include additional contributions, such as the effective density of states and the temperature-dependent thermal velocity [145]. This reveals that CPE-K HTL has higher thermal stability than SnS and Ti_2CO_2-based solar cells leading to comparatively less degradation in PCE with increasing temperature. Furthermore, it evidenced that the degradation in PCE is less in CPE-K-based devices, indicating that it is comparatively stable towards temperature than SnS and Ti_2CO_2-based solar cells.

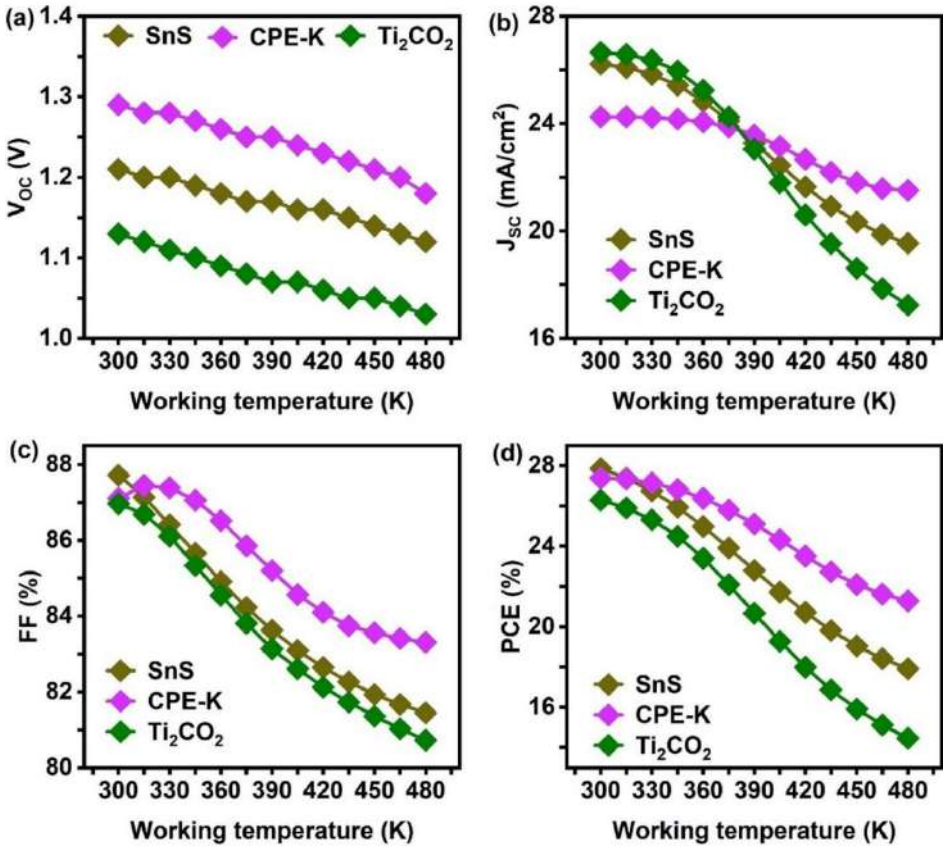

Fig. 21. Changes in (a) V_{OC} (b) J_{SC} (c) FF and (d) PCE of high PCE solar cells concerning the working temperature [52].

6.1.16. Comparison of SCAPS-1D Results with Previous Works in the Literature

As mentioned in the introduction, the applicability of CPs as an absorber in solar cells has not been studied via experiments. However, theoretical reports focusing on the potential of CPs in solar cells have fledged recently. **Table 10** compares the present simulation work with the SCAPS-1D results of other CPs-based solar cells. To date, only Zr-based CPs are investigated in the literature. In particular, $BaZr(S/Se)_3$ is the widely studied CPs; the highest PCE reported is 25.84%. Recently, Chawki et al. have demonstrated PCE of 25.97% using $SrZrS_3$ CPs absorber. Remarkably, for the first time, we have designed a Hf-based CPs solar cell using $SrHfSe_3$ absorber and simulated 1627 solar cells to identify suitable configurations. Notably, we have achieved PCEs of 27.87%, 27.39%, and 26.30% for SnS, CPE-K, and Ti_2CO_2-based solar cells which is the highest among the reported works. This reveals the potential of $SrHfSe_3$ as an alternative emerging absorber to LHPSCs. Therefore, we believe that our comprehensive work on the properties of novel $SrHfSe_3$ and its device structure engineering kindles the research community's interest in fabricating novel $SrHfSe_3$ PSCs with efficient solar cell configuration.

Table 10. Comparison between SCAPS-1D results of CPs-based solar cells [52].

Device structure	V_{OC} (V)	J_{SC} (mA/cm^2)	FF (%)	PCE (%)	Ref
FTO/TiO_2/$BaZrS_3$/Spiro-OMeTAD/Au	0.70	22.00	79.40	12.12	[146]
FTO/TiO_2 /$BaZrS_3$/Cu_2O /Au	1.16	12.24	87.13	12.42	[29]
FTO/ TiO_2 /$BaZrS_3$/$CuSbS_2$/W	1.00	22.57	73.7	17.13	[147]
AZO/i-ZnO/CdS/ $BaZrS_3$/ a-Si	1.31	19.08	78.88	19.72	[137]
FTO/TiO_2/$BaZrSe_3$/Spiro-OMeTAD/Au	0.72	46.65	77.32	25.84	[147]
FTO/ZnO /$SrZrS_3$/NiO/Ni	1.18	26.13	84.29	25.97	[148]
FTO/$BaSnO_3$/$SrHfSe_3$/SnS/Ni	1.21	26.22	87.72	27.87	*
FTO/$BaSnO_3$/$SrHfSe_3$/CPE-K/Ni	1.29	24.25	87.11	27.39	*
FTO/$BaSnO_3$/$SrHfSe_3$/Ti_2CO_2/Ni	1.13	26.66	86.97	26.30	*
The * indicates the results of the present work.					

6.1.17. Experimental Suggestions to Enhance Solar Cell Performance in Practice Based on Simulation Results

The performed simulation provides a comprehensive theoretical investigation of the device engineering of $SrHfSe_3$ based solar cells. Wherein, the highest PCE of 27.87%, 27.39%, and 26.30% has been demonstrated for the champion device structures FTO/$BaSnO_3$/$SrHfSe_3$/SnS/Ni, FTO/$BaSnO_3$/$SrHfSe_3$/CPE-K/Ni and FTO/$BaSnO_3$/$SrHfSe_3$/Ti_2Co_2/Ni respectively. Since there are no reports available on the fabrication of these novel solar cells, it is indeed important to offer effective guidelines for experimentalists to attain the best PCEs practically. SCAPS-1D is a commonly used tool for simulating PV devices, offering valuable insights into their electrical and optical properties. However, there are some limitations to the software that might affect this study. For example, it doesn't take into account reflection losses at intermediate interfaces or lattice mismatches. To account for these effects, future work could consider the wavelength-dependent complex refractive index (n-k values) of each $BaHf_{1-x}Zr_xS_3$ material, which is important for accurately modeling light absorption and propagation in multi-layer solar cells. Including these factors would improve simulations and allow for a more detailed evaluation of new materials and device structures. Therefore, we have proposed several strategies from the literature to prepare each layer by overcoming the experimental challenges and fabricating an efficient solar cell.

$BaSnO_3$ has been applied as an ETL in the present work due to its wide bandgap, high chemical stability, and carrier kinetics [149–151]. It has been reported to be easily synthesized

using chemical methods, molecular beam epitaxy, pulsed layer deposition, and solid-state reaction method [152–157]. Moreover, its thickness can be tuned by changing the substrate temperature, growth rate, deposition time, pressure, etc [158–161]. Also, several ways have been demonstrated in literature for controlling its defects and carrier concentration. Zhang et al. varied the stochiometric ratio of Ba:Sn in $BaSnO_3$ to improve its carrier concentration and mobility [159,161]. In addition, Liu and his co-authors have proposed that the modulation of oxygen vacancies is an effective path to tune the carrier concentration. They performed heat treatment of $BaSnO_3$ under a nitrogen atmosphere to improve its oxygen vacancies and crystallinity. Afterward, they cooled it in the oxygen gas to passivate the defects [162,163]. Similarly, vacuum annealing of $BaSnO_3$ can effectively enhance the carrier concentration and control the defects [164]. Apart from these, external doping of elements such as La, Sb, Gd, and Ta is another method for elevating their carrier concentration [165–168].

So far, chalcogenide PSCs have not been fabricated due to the requirement of high temperature (>900ºC) for preparing CPs films, according to the earlier reports [169]. Recent studies on low-temperature synthesis are increasing, which opens doors for their fabrication. For instance, Vincent et al. prepared high-quality $BaZrS_3$ films at around 500-575ºC using a solution method followed by sulfurization [170]. Also, Comparotto et al. synthesized CPs thin film by sputter-sulfurization approach at <600ºC while Nag et al. prepared $BaZrS_3$ nanopowders at 600º C and coated films using the ink formulation [171]. Similarly, Yang et al. and Zilevu et al. demonstrated the colloidal synthesis of $BaZrS_3$ at temperatures much below 350º C, highlighting the promise of CP's solution-based approaches [41,172,173]. Thus, it is evident that $SrHfSe_3$ can also be prepared at low temperatures <600º C following similar approaches. Also, its carrier concentration and defect densities can be controlled by tuning its stoichiometric ratio [173,174].

Thin films for all HTLs can be deposited using various techniques such as chemical vapor deposition (CVD), thermal evaporation, solution processing, and sputtering. The required deposition temperatures vary depending on the type of HTL. For example, inorganic material-based HTLs typically require temperatures in the range of approximately 300–500°C. Polymer-based HTLs are processed at lower temperatures, ranging from room temperature to approximately 80°C and MXenes-based HTLs require deposition temperatures in the range of 400–500°C. Furthermore, among the 25 inorganic HTLs, the highest PCE was obtained for SnS-based solar cells. SnS is an earth-abundant material that already finds potential application in PVs as an absorber and HTL [175]. It can be easily synthesized using precipitation, chemical bath deposition, hot injection, hydrothermal, solvothermal, etc. However, the formation of

secondary phases such as Sn_2S_3 and SnS_2 is a critical problem during the synthesis [176–180]. Therefore, various steps have been undertaken to overcome the aforementioned issue. Steinmann et al. found that annealing SnS for one hour under vacuum conditions (15 mTorr) at 500°C, or in an Ar or H_2 gas atmosphere at room temperature, helps prevent the formation of impurity phases [175]. Additionally, incorporating an excess of Sn ($Sn_{1.05}S$) during the synthesis significantly reduces the formation of Sn_2S_3, eliminating the need for extra thermal processing [175]. In addition to the inorganic, organic semiconductor of CPE-K HTL demonstrated the best PCE of 27.39%. However, the main drawback limiting the usage of organic HTLs is their stability [181]. To be specific, the prominently used PEDOT:PSS has an acidic nature that corrodes the electrodes due to its decomposition with perovskite film, deteriorating the stability of solar cells [182]. Surprisingly, CPEs have a neutral pH and thus possess comparatively greater stability than PEDOT:PSS but still lower than inorganic HTL [183]. they also have large hydrophilicity and wettability to perovskites, leading to their potential usage in PSCs. Zhang et al. incorporated K^+ cations into CPE (termed as CPE-K) and utilized it as HTL in PSC wherein CPE-K demonstrated high hole selectivity, passivated the defects, and elevated the stability of PSCs [184]. Nevertheless, CPEs are reported to have aggregation effects, which may degrade the solar cell performance. Jian et al. illustrated that adding ionic liquids to CPEs in different mass ratios inhibited the intermolecular aggregation of CPEs and elevated their HTL properties. Similarly, the maximum PCE of 26.30% was accomplished for Ti_2CO_2 amidst the three Mxenes-based HTLs. Ti_2CO_2 MXenes have tuneable work functions, high stability, large surface area, and high conductivity, making them a potential candidate for HTLs in solar cells [185]. It has been functionalized with groups such as -F, -OH, and -O, where Ti_2CO_2 is prominently studied due to its superior properties. It is widely investigated as electrodes in supercapacitors, photocatalysis, sensors, and field effect transistors. Whereas its applicability in PVs has not yet been explored as the utilization of MXenes in PVs has recently begun from the last quarter of 2018. Interestingly, Ti_3C_2O with similar properties is the broadly evaluated MXene in PVs [186–188]. It is successfully applied as additives, electrodes, and HTLs in solar cells, indicating that Ti_2CO_2 could also exhibit extraordinary performance [189]. It has been demonstrated that using MXenes as HTL could passivate the surface defects in perovskite film, improving its quality and morphology [190]. Also, its work function can be varied by introducing strain, ultraviolet-ozone treatments, N_2H_4 treatments, etc [189]. Despite these properties, several limitations need to be addressed concerning the prospects of MXenes in the PV industry, which are as follows. Firstly, more viable and safe synthesis methods must be explored, which could be done by avoiding

hydrofluoric acid during their synthesis. Similarly, their stability must be improved. Though they have displayed higher stability than their organic counterparts, exposure to the environment for a long duration degrades their performance, which occurs due to oxidation. The high defective states in MXenes are the main reason for their instability. This could be overcome by implementing surface passivation techniques such as inserting MXene films with suitable polymer coating, edge capping with negatively charged ligands, and synthesizing polymer assisted Mxenes. Also, more MXenes must be explored via theoretical simulations and experiments to expand their application in the future. From the above discussion on the champion HTLs, we can infer that SnS could be the best candidate for the successful fabrication of $SrHfSe_3$ solar cells owing to its low cost, stability, and numerous reports available in the literature. By addressing their experimental challenges, CPE-K and Ti_2CO_2 can also be applied as HTLs. Overall, we believe the aforementioned methodologies could help the experimental scientist efficiently fabricate novel $SrHfSe_3$ solar cells with the best PCE in the proposed device structures.

6.2. Optimizations of $ABSe_3$ (A=Ca, Ba; B=Zr, Hf) CPs Solar Cells

This section presents the detailed simulation results related to **objective 3**. Section **6.2.1** provides the initial performance metrics of $CaZrSe_3$, $BaZrSe_3$, $CaHfSe_3$, and $BaHfSe_3$ solar cells. **Sections 6.2.2** and **6.2.3** analyze the effects of ETL and absorber layer properties, including thickness, carrier concentration, and defect density. **Section 6.2.4** investigates the influence of HTL thickness and carrier concentration. **Section 6.2.5** examines interface defect densities at the ETL/absorber and absorber/HTL junctions. **Section 6.2.6** compares the overall performance of the four novel absorbers. **Section 6.2.7** evaluates the effects of series/shunt resistance and working temperature. Finally, **Section 6.2.8** compares the simulation outcomes with existing literature.

6.2.1. Initial device performance

The initial solar cell was designed with the structure of FTO/TiO_2/ A (Ca, Ba) B (Zr, Hf) Se_3/ NiO/ Au, as shown in **Fig. 4**. Simulations were carried out using the parameters listed in **Table 2** and **Table 3**. The initial PV parameters for the novel solar cells, specifically $CaZrSe_3$, $BaZrSe_3$, $CaHfSe_3$, and $BaHfSe_3$, are presented in **Table. 11**. Notably, these novel CPs solar cells achieved PCEs of 9.94% for $CaZrSe_3$, 10.14% for $BaZrSe_3$, 8.20% for $CaHfSe_3$, and 13.04% for $BaHfSe_3$ absorbers. The performance of the solar cells is further improved through

careful optimization of the ETL, absorber, and HTL material parameters. Detailed insights into these optimization processes are discussed in the following sections.

Table 11. Initial PV parameters of novel CPs solar cells [47]

Solar cell configuration	V_{OC} (V)	J_{SC} (mA/cm^2)	FF (%)	PCE (%)
FTO/ TiO_2/$CaZrSe_3$/NiO/Au	1.03	12.17	79.06	9.94
FTO/ TiO_2/$BaZrSe_3$/NiO/Au	0.98	13.04	78.85	10.14
FTO/ TiO_2/$CaHfSe_3$/NiO/Au	1.17	8.73	80.08	8.20
FTO/ TiO_2/$BaHfSe_3$/NiO/Au	1.13	13.88	82.57	13.04

6.2.2. Impact of ETL's thickness, carrier concentration, and defect density

The thickness of the ETL plays a critical role in the transportation of electrons, enhancing light transmission, and preventing recombination within solar cells [39]. In this context, the ETL thickness varied from 50 nm to 150 nm, and its impact on PV parameters is illustrated in **Fig. 22**(a-d). Notably, the V_{OC} remains unchanged across this range, while the FF increases from 79.06%, 78.85%, 80.08%, and 82.57% to 81.22%, 80.88%, 82.50%, and 84.08% for $CaZrSe_3$, $BaZrSe_3$, $CaHfSe_3$, and $BaZrSe_3$ based solar cells respectively. This improvement can be attributed to the reduced R_S and recombination rates at the Absorber/ETL interface. Consequently, there is a slight increase in the PCE, rising from 9.84% to 10.01%, 10.14% to 10.20%, 8.20% to 8.28%, and 13.04% to 13.11% for $CaZrSe_3$, $BaZrSe_3$, $CaHfSe_3$, and $BaZrSe_3$-based solar cells, respectively. However, a slight decrease in Jsc is observed as the thickness increases from 50 nm to 150 nm. This decline is primarily attributed to the transparent properties of the ETL. Typically, it is preferable to keep the n-type layer thinner than the p-type layer. This approach allows photons to reach the upper layers without being absorbed, which prevents them from being converted into electron-hole pairs that are then separated by built-in potential. Furthermore, a thicker ETL tends to absorb some light, thereby slowing down charge generation and collection. This results in absorption losses and reduced transmittance. The relationship between ETL thickness and transmittance is described by **Eqn**. (14) [114].

$$\alpha_e = \frac{1}{d_e}\ln\frac{1}{T_e} \quad (14)$$

Here, d_e, T_e, and α_e represent the thickness, transmittance, and absorption coefficient, respectively. Based on observations and experimental challenges, an ideal thickness of 50 nm is chosen for $CaZrSe_3$, $BaZrSe_3$, $CaHfSe_3$, and $BaZrSe_3$-based solar cells.

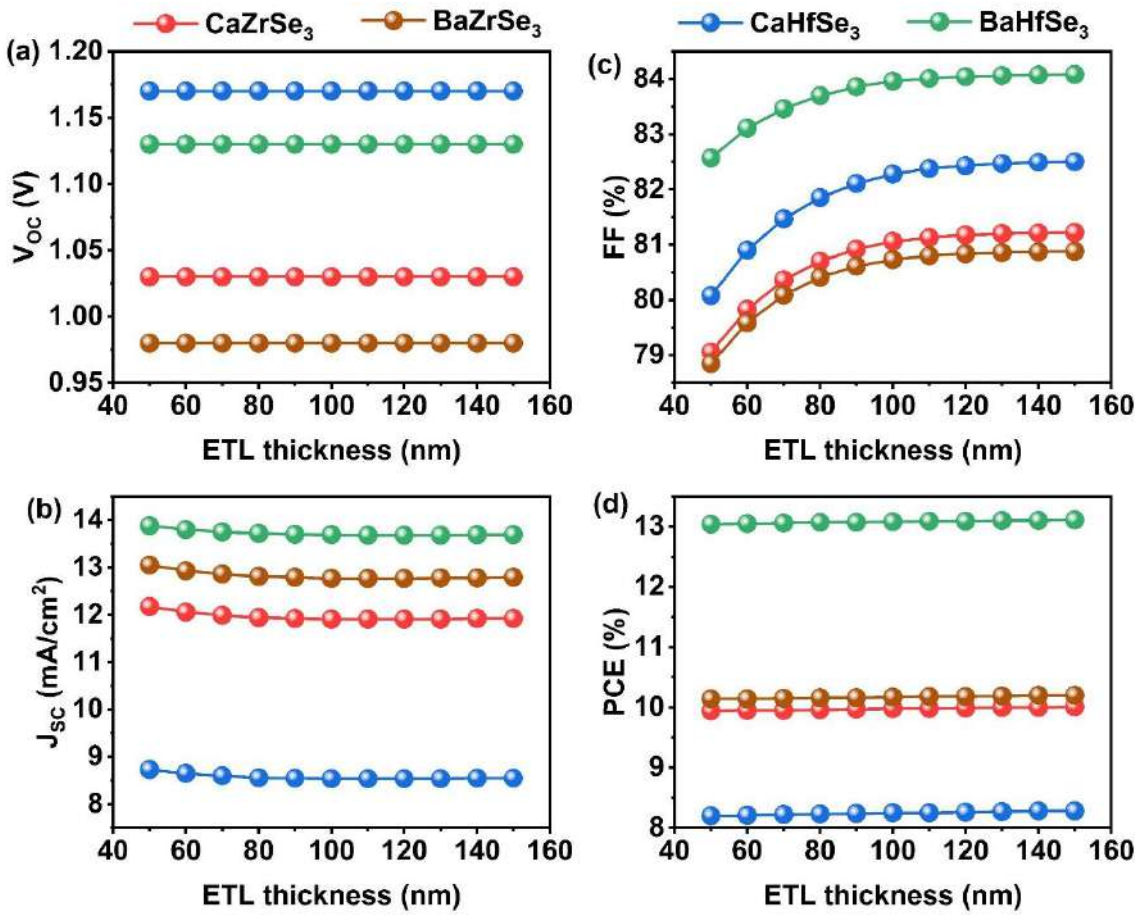

Fig. 22. Changes in (a) V_{OC} (b) J_{SC} (c) FF and (d) PCE as a function of ETL's thickness [47].

The carrier concentration of the ETL is varied from 10^{12} cm^{-3} to 10^{20} cm^{-3} to investigate its influence on the PV parameters, as shown in **Fig. 23**(a-d). The Voc remained relatively constant at 1.03 V, 0.99 V, 1.18 V, and 1.13 V for the $CaZrSe_3$, $BaZrSe_3$, $CaHfSe_3$, and $BaHfSe_3$-based solar cells, respectively, until the carrier concentration reached 10^{16} cm^{-3}. Beyond this point, V_{OC} began to decline. This decrease indicates a reduction in quasi-Fermi level splitting as the carrier concentration increases [191]. Similarly, the FF remained constant across all solar cells up to 10^{16} cm^{-3}, followed by a slight decrease at higher concentrations. Interestingly, when the carrier concentration exceeded 10^{16} cm^{-3}, there was a gradual increase in Jsc, which ultimately led to an improvement in PCE. The PCE increased from 9.91% to 11.73% for $CaZrSe_3$, from 10.11% to 11.99% for $BaZrSe_3$, from 8.18% to 10.03% for $CaHfSe_3$, and from 13.08% to 14.49% for $BaHfSe_3$. This enhancement is attributed to the increase in built-in potential and conductivity in the solar cells with higher carrier concentrations [192]. Generally, at lower carrier concentrations, the holes mainly occupy the interface states, which act as traps for electrons, thereby impeding the flow of photogenerated charge carriers. Conversely, an increase in carrier concentration lowers the barrier height at the ETL/Absorber interface [193–

195]. Xu et al. demonstrated that a higher carrier concentration generates deep energy levels at the interfaces, which reduces non-radiative recombination and enhances solar cell performance. As shown in **Fig. 23**(e-h), when the carrier concentration is high (at 10^{20} cm^{-3}), all the solar cells exhibit lower recombination rates compared to those with low carrier concentration (10^{12} cm^{-3}). Therefore, an optimal carrier concentration is crucial for ensuring proper band alignment, generating a substantial electric field that facilitates efficient charge carrier transport, reducing interface recombination rates, and consequently improving solar cell performance [196]. As a result, an ideal carrier concentration of 10^{20} cm^{-3} is selected for all the solar cells.

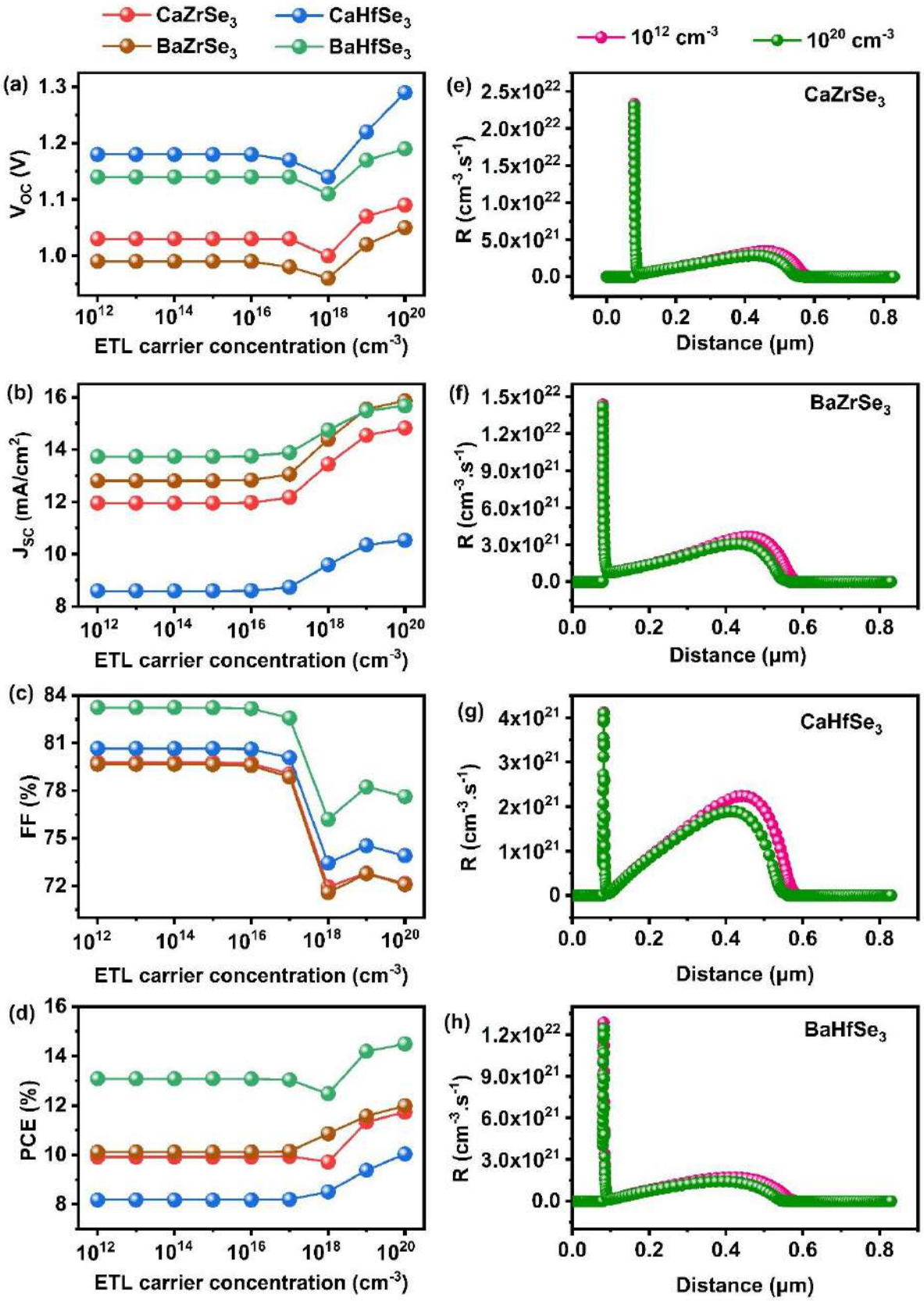

Fig. 23. Changes in (a) V_{OC} (b) J_{SC} (c) FF (d) PCE and (e-h) Recombination rates as a function of ETL's carrier concentration [47].

Defects in materials create additional pathways for non-radiative recombination, converting light into heat instead of electricity. Specifically, these recombination centers trap photogenerated carriers, preventing them from reaching the terminals and thereby reducing their lifespan. Consequently, minimizing defects is essential for improving device performance. To investigate their impact, we varied the defect density from 10^{12} cm^{-3} to 10^{20} cm^{-3}, as shown in **Fig. 24**(a-d). Across all solar cells, the PV parameters remained stable within the range of 10^{12} cm^{-3} to 10^{16} cm^{-3}, but exhibited a slight decline as defect density increased further. Specifically, the PCE decreased from 11.73% to 11.57% for $CaZrSe_3$, from 11.99% to 11.84% for $BaZrSe_3$, from 10.03% to 9.84% for $CaHfSe_3$, and from 14.49% to 14.32% for $BaHfSe_3$ solar cells. This drop in performance is attributed to the rising number of defect states, which act as barriers for charge carriers, thereby enhancing recombination within the solar cells [197]. Nevertheless, it is important to note that the reduction in performance is minimal specifically, 0.16%, 0.15%, 0.19%, and 0.17% for $CaZrSe_3$, $BaZrSe_3$, $CaHfSe_3$, and $BaHfSe_3$-based solar cells, respectively. This indicates that the influence of ETL defect density on solar cell performance is negligible. Therefore, an optimal defect density of 10^{16} cm^{-3} is chosen for the subsequent simulations.

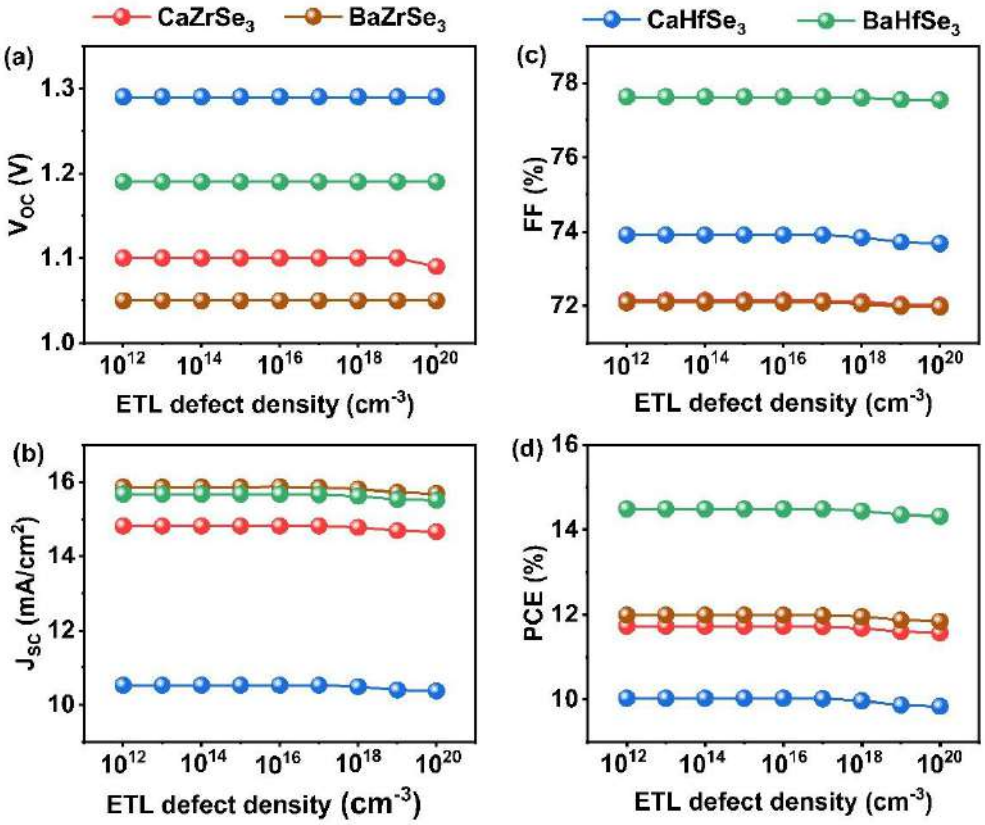

Fig. 24. Changes in (a) V_{OC} (b) J_{SC} (c) FF and (d) PCE as a function of ETL's defect density [47].

6.2.3. Impact of absorber's thickness, carrier concentration and defect density

The thickness of the absorber has a significant impact on the performance of solar cells [29]. To determine the optimal thickness, we varied it from 100 nm to 1500 nm for all absorbers, as illustrated in **Fig. 25**(a-d). As the thickness increases from 100 nm to 500 nm, the J_{SC} shows a substantial increase from ~6 mA/cm^2 to 15 mA/cm^2 across all solar cells. This leads to a rise in the PCE from 8.89% to 11.75% for $CaZrSe_3$, from 10.14% to 12.01% for $BaZrSe_3$, from 5.96% to 10.06% for $CaHfSe_3$, and from 7.64% to 14.72% for $BaHfSe_3$. The improvement in performance occurs because thinner absorbers are unable to effectively absorb photons with longer wavelengths, resulting in lower photon absorption and insufficient generation of charge carriers [118]. As the thickness increases, the ability to absorb photons improves, leading to enhanced charge carrier generation and a marked boost in solar cell performance. However, an interesting trend is observed in the PCE once the thickness exceeds 500 nm, where the improvements become marginal, only increasing by about 0.03% across all solar cells. Initially, the increase in thickness from 100 nm to 500 nm results in substantial gains in PCE: 2.84% for $CaZrSe_3$, 1.85% for $BaZrSe_3$, 4.07% for $CaHfSe_3$, and 6.85% for $BaHfSe_3$. When the thickness goes beyond 500 nm, the distance that charge carriers must travel to reach their respective contacts becomes significant. Consequently, many of these carriers recombine due to their limited diffusion lengths compared to the thickness of the absorber, leading to a saturation in solar cell performance [119]. This phenomenon is further supported by QE measurements (**Fig. 25**(e-h)), which show that the increase in absorption is 5.83%, 4.77%, 7.3%, and 11.93% for $CaZrSe_3$, $BaZrSe_3$, $CaHfSe_3$, and $BaHfSe_3$ solar cells, respectively, within the thickness range of 100 nm to 500 nm. Beyond this, the absorption only increases by about 0.4% with additional thickness. On the other hand, the V_{OC} improves up to 300 nm, after which it stabilizes for all solar cells. This initial enhancement is attributed to increased quasi-Fermi level splitting from greater charge carrier generation, while the later stabilization is a result of higher dark saturation currents and recombination rates associated with greater thickness [118,148]. The FF shows a similar trend, increasing until 300 nm before stabilizing across all solar cells due to increased R_S in thicker absorbers. Recent studies on CPs solar cells indicate that when the absorber layer thickness exceeds 500 nm, there is a notable decrease in the built-in electric field. This reduction adversely affects effective carrier extraction, ultimately lowering the device's PCE.

Research by Sun et al. examined the optoelectronic properties of $CaTiS_3$, $BaZrS_3$, $CaZrS_3$ and $CaHfS_3$ CPs materials through DFT. Their findings suggested that light absorption

and carrier dynamics are achievable with absorber layer thicknesses significantly below 1000 nm, providing greater flexibility in design decisions. A pivotal study conducted by Nishigaki et al. involved the synthesis of several chalcogenide compounds, such as $BaZrS_3$, $Ba(Zr,Ti)S_3$, and $BaZr(S,Se)_3$. This research emphasized the significance of absorber layer thickness, revealing that an optimal thickness of approximately 500 nm is essential for maximizing light absorption, a critical factor for developing high-efficiency solar cells [120]. Additionally, Himanshu et al. utilized SCAPS-1D theoretical simulations to evaluate the performance of $BaZrS_3$ as an absorber layer. Their results demonstrated that a layer thickness of 500 nm can Pb to impressive PCE, highlighting the material's potential for practical applications [198]. Another significant contribution came from Swarnkar et al., who successfully synthesized various compounds, including $BaZrS_3$, $SrZrS_3$, and the layered perovskite $Ba_3Zr_2S_7$ [121]. They suggested that an absorber layer thickness of around 550 nm could maximize the PCE of solar cells, indicating a general consensus on the optimal thickness range. In summary, several reports advocate for absorber thicknesses between 500 nm and 1000 nm for CPs solar cells to achieve high PCE. Based on a thorough review of the collective evidence from these studies, an optimal thickness of 500 nm has been selected for $CaZrSe_3$, $BaZrSe_3$, $CaHfSe_3$, and $BaHfSe_3$-based solar cells, aligning well with the established best practices in the field.

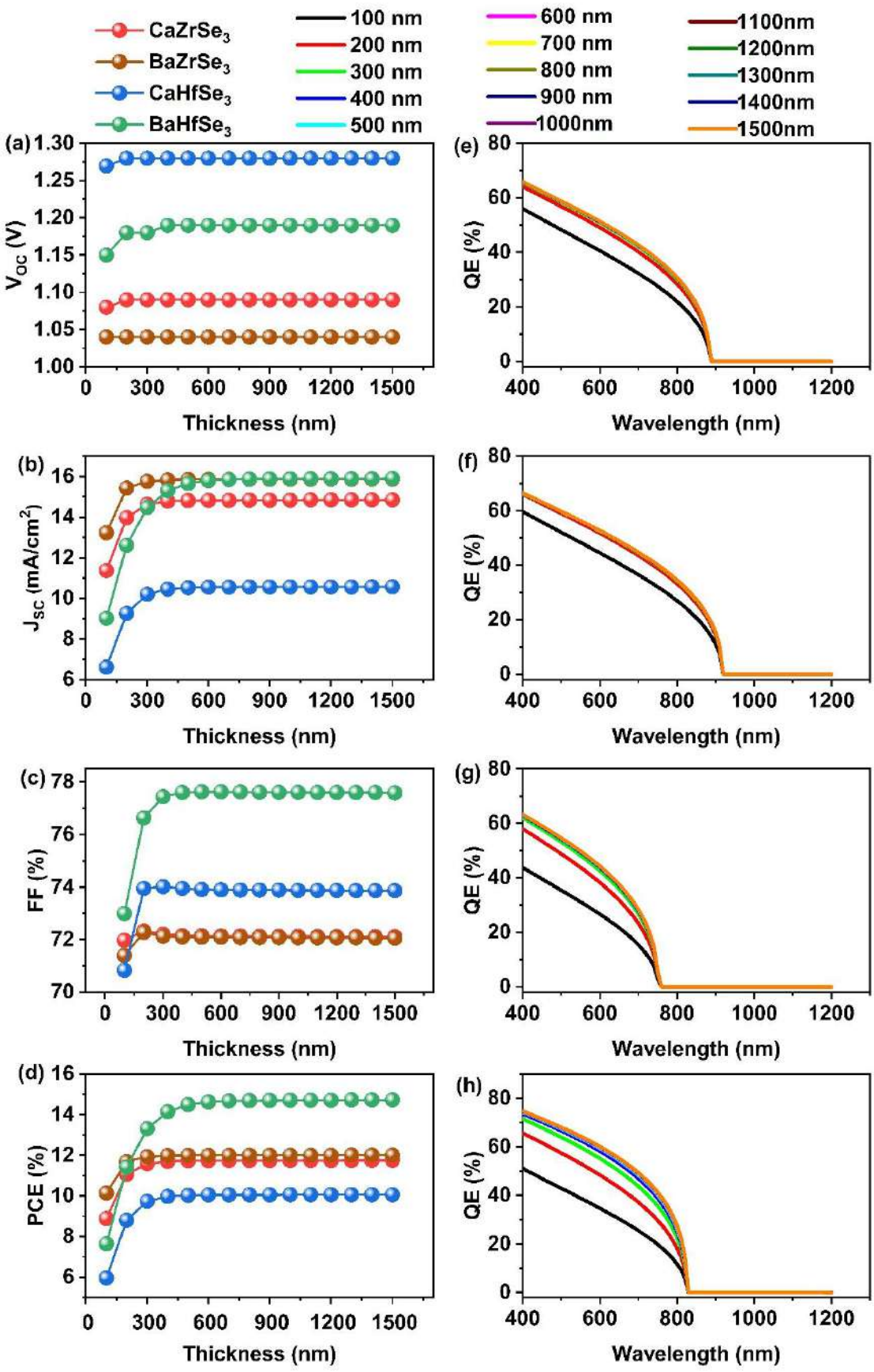

Fig. 25. Changes in (a) V_{OC} (b) J_{SC} (c) FF (d) PCE and (e-h) QE as a function of absorber's thickness [47].

The carrier concentration in the absorber layer is crucial for governing both charge transport and the overall stability of solar cells. Therefore, determining the optimal carrier concentration is essential to achieve high-performance solar cells. While a higher carrier concentration can enhance certain properties, it also increases the risk of Auger recombination, which can hinder hole movement by causing significant recombination and impurity scattering within the absorber layer [199,200]. Consequently, optimizing the carrier concentration is vital for improving solar cell efficiency.

In our study, we varied the carrier concentration of $CaZrSe_3$, $BaZrSe_3$, $CaHfSe_3$ and $BaHfSe_3$ based absorbers from 10^{12} cm^{-3} to 10^{18} cm^{-3}, as shown in **Fig. 26**(a-d). We observed that the PCE remained stable up to 10^{14} cm^{-3}, followed by a sharp increase until 10^{16} cm^{-3}; however, it declined with further increases in carrier concentration across all solar cells. Additionally, the V_{OC} and FF remained constant up to 10^{14} cm^{-3} but showed significant improvement beyond that point. This enhancement can be attributed to the increased intrinsic capacity of the device, which allows for more efficient carrier extraction and accumulation at the contacts while minimizing recombination. Moreover, varying the carrier concentration from 10^{12} cm^{-3} to 10^{18} cm^{-3} affects the energy band alignment and elevates the quasi-Fermi level splitting, resulting in higher V_{OC} and improved overall performance. To further investigate these effects, we extracted energy band diagrams from SCAPS-1D for carrier concentration ranging from 10^{12} cm^{-3} to 10^{18} cm^{-3}, as depicted in **Fig. 26**(e-h). As the carrier concentration rises from 10^{12} cm^{-3} to 10^{18} cm^{-3}, the energy bands of all layers shift upwards, bringing the valence band of the absorber closer to the hole quasi-Fermi level. This facilitates hole transport from the absorber to the HTL while simultaneously limiting electron transport and enhancing hole collection at the back contact [192,197].

Additionally, the electric field at the absorber/HTL interface intensifies with increased carrier concentration. However, we observed that the J_{SC} decreases when the carrier concentration exceeds 10^{16} cm^{-3}. This decline can be attributed to the higher recombination rates caused by excessive carrier concentration, as demonstrated in **Fig. 27**(a-d). Significant recombination is evident beyond 10^{16} cm^{-3}. Another factor contributing to the reduced J_{SC} at higher carrier concentration 10^{16} cm^{-3} is the shift of the depletion region at the ETL/absorber junction into the ETL, resulting in a narrower depletion width within the absorber. As a result, carriers with short-diffusion lengths and lifetimes are more likely to recombine, thereby lowering the J_{SC}. We obtained Nyquist plots to analyze the transport properties of charge carriers in all the solar cells, as illustrated in **Fig. 27**(e-h). Typically, Nyquist plots exhibit two semicircles: one representing recombination resistance at low frequencies and the other

representing charge transfer resistance at high frequencies. However, in our case, we observed a single semicircle across the entire frequency range, indicating that charge transfer resistance predominates in all the devices. The smaller semicircle at 10^{16} cm^{-3} corresponds to high conductivity and efficient charge transfer. In contrast, higher carrier concentrates hinder charge transfer and degrade solar cell performance. Additionally, Meng et al. reported that CPs films synthesized under S-rich/Zr-poor conditions exhibit strong p-type behavior with an optimal carrier concentration of 10^{15} cm^{-3}. Conversely, films synthesized under S-poor/Zr-rich conditions display n-type behavior with high carrier concentrations exceeding 10^{17} cm^{-3}, making them unsuitable as absorbers [115]. To achieve high PCE, it is recommended that the carrier concentration for CPs solar cell materials stay below 10^{17} cm^{-3} [51,114,193,201,202]. After considering all relevant factors, we selected an optimal carrier concentration of 10^{16} cm^{-3} for $CaZrSe_3$, $BaZrSe_3$, $CaHfSe_3$, and $BaHfSe_3$-based solar cells, which falls within the suggested range.

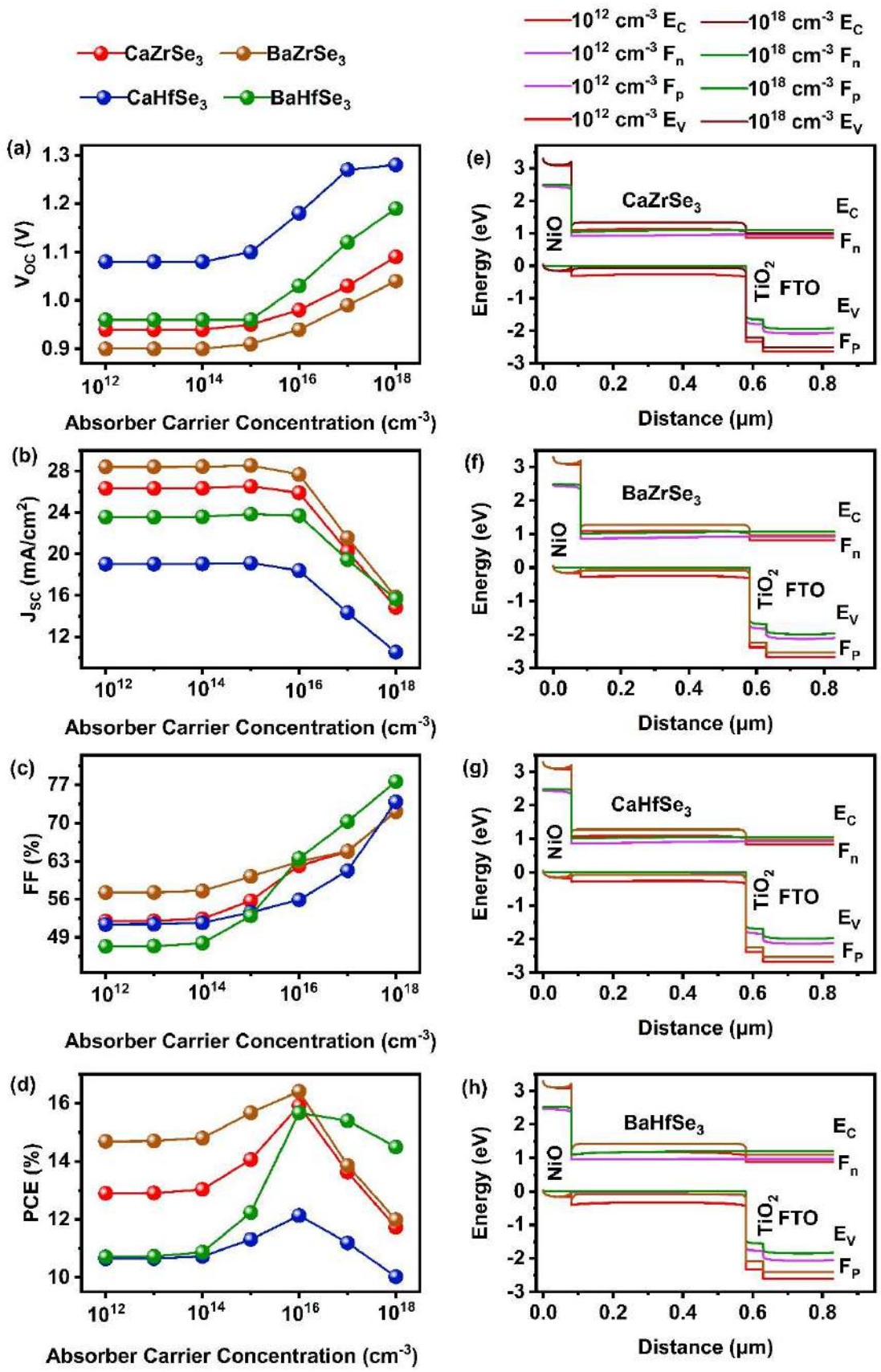

Fig. 26. Changes in (a) V_{OC} (b) J_{SC} (c) FF (d) PCE and (e-h) Energy band alignment as a function of absorber's carrier concentration [47].

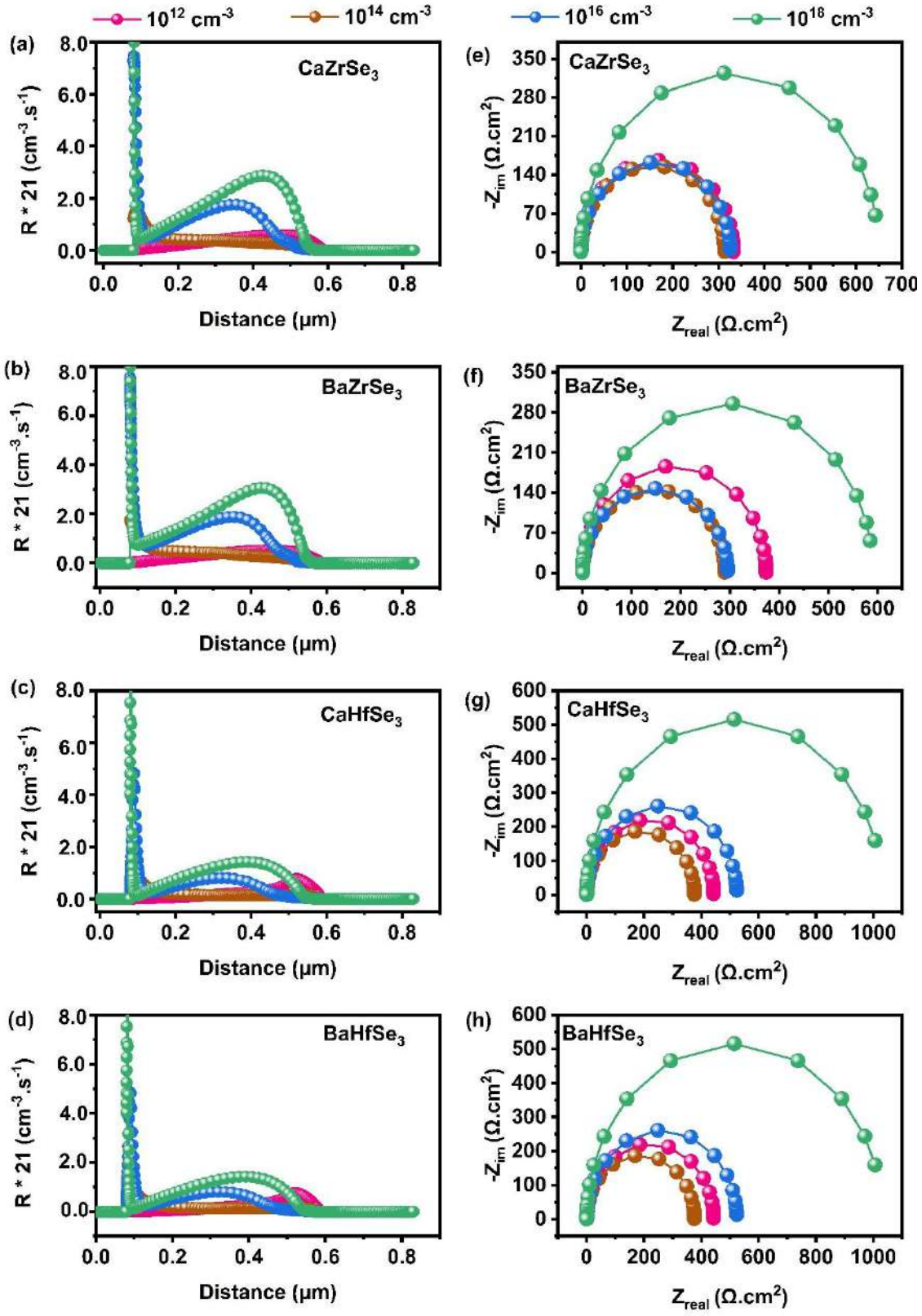

Fig. 27. Changes in (a-d) Recombination rate and (e-h) Nyquist plot as a function of absorber's carrier concentration [47].

Defects in solar cell absorbers typically arise from structural irregularities, non-stoichiometry, impurities, and fabrication technique [203]. Managing these absorber defects is crucial for achieving high efficiency in solar cells. To study the impact of absorber defect density on PV performance, we varied the defect density from 10^{12} cm^{-3} to 10^{18} cm^{-3} for $CaZrSe_3$, $BaZrSe_3$, $CaHfSe_3$ and $BaHfSe_3$ based solar cells. **Fig. 28**(a-d) illustrates how the V_{OC}, J_{SC}, FF, and PCE respond to changes in the absorber's defect density. Notably, all PV parameters significantly decrease as defect density increases. Specifically, V_{OC} and FF remain stable up to a defect density of 10^{13} cm^{-3}, but they drop sharply beyond this threshold. Additionally, increasing defect density disrupts the energy band alignment and lowers the quasi-Fermi level splitting, resulting in reduced V_{OC} and negatively impacting solar cell performance. As defect density increases from 10^{12} cm^{-3} to 10^{18} cm^{-3}, the energy bands of all layer's shift downward at higher defect densities. This shift lowers the barrier at the ETL/absorber interface and reduces the quasi-Fermi level splitting, further degrading the V_{OC} of all solar cell [204,205]. For instance, when the defect density rises from 10^{12} cm^{-3} to 10^{18} cm^{-3}, the PCE declines dramatically from 25.17% to 0.96%, 27.35% to 1.08%, 17.47% to 0.96% and 22.63% to 0.99% for $CaZrSe_3$, $BaZrSe_3$, $CaHfSe_3$ and $BaHfSe_3$ based solar cell respectively. This significant decrease in performance is primarily due to the increased recombination sites for photogenerated charge carriers, which reduces both their diffusion length and lifetime. **Fig. 29(**a-d) illustrates the recombination rate as a function of increasing defect density across all solar cells. As defect density increases, the recombination rate surges in the absorber region, particularly near the absorber/ETL junction, leading to a decline in overall performance. Interestingly, recombination at the absorber/NiO interface decreases with higher defect density. This reduction occurs because the increased recombination within the absorber region significantly lowers the density of photogenerated carriers throughout the bulk of the absorber and in the regions near the interface. As a result, fewer charge carriers reach the electrodes, thereby reducing the recombination rate at the absorber/NiO interface [206]. Moreover, **Fig. 29**(e-h) demonstrates that the electric field at the absorber/ETL interface weakens as defect density increases. This reduction in the electric field hampers the effective separation and collection of charge carriers, leading to further degradation in the overall performance of the solar cells. The decline in minority carrier density, along with the weakening of the built-in electric field at the p-n junction, significantly affects the overall performance of the solar cells. Despite these challenges, CPs are considered defect-tolerant due to their high formation energy, which makes them less susceptible to deep-level defect. Furthermore, Meng et al. reported that CPs films synthesized under S-rich/Zr-poor conditions

exhibit strong p-type behavior, while this composition also helps reduce defect density. This reduction occurs because of the higher formation energy associated with deep-level defects, resulting in fewer defects overall. It is crucial to adjust the elemental composition during the synthesis of CPs films to achieve optimal carrier concentration and minimize the formation of deep-level defects. Similarly, Carmen Baiano et al. controlled defect formation by optimizing stoichiometry and annealing in an oxygen-rich environment. For achieving high PCE, the literature recommends a defect density of 10^{10} to 10^{12} cm^{-3} for CPs solar cell materials. After evaluating all relevant factors, an optimal defect density of 10^{12} cm^{-3} has been selected for $CaZrSe_3$, $BaZrSe_3$, $CaHfSe_3$, and $BaHfSe_3$-based solar cells, which falls within the suggested range.

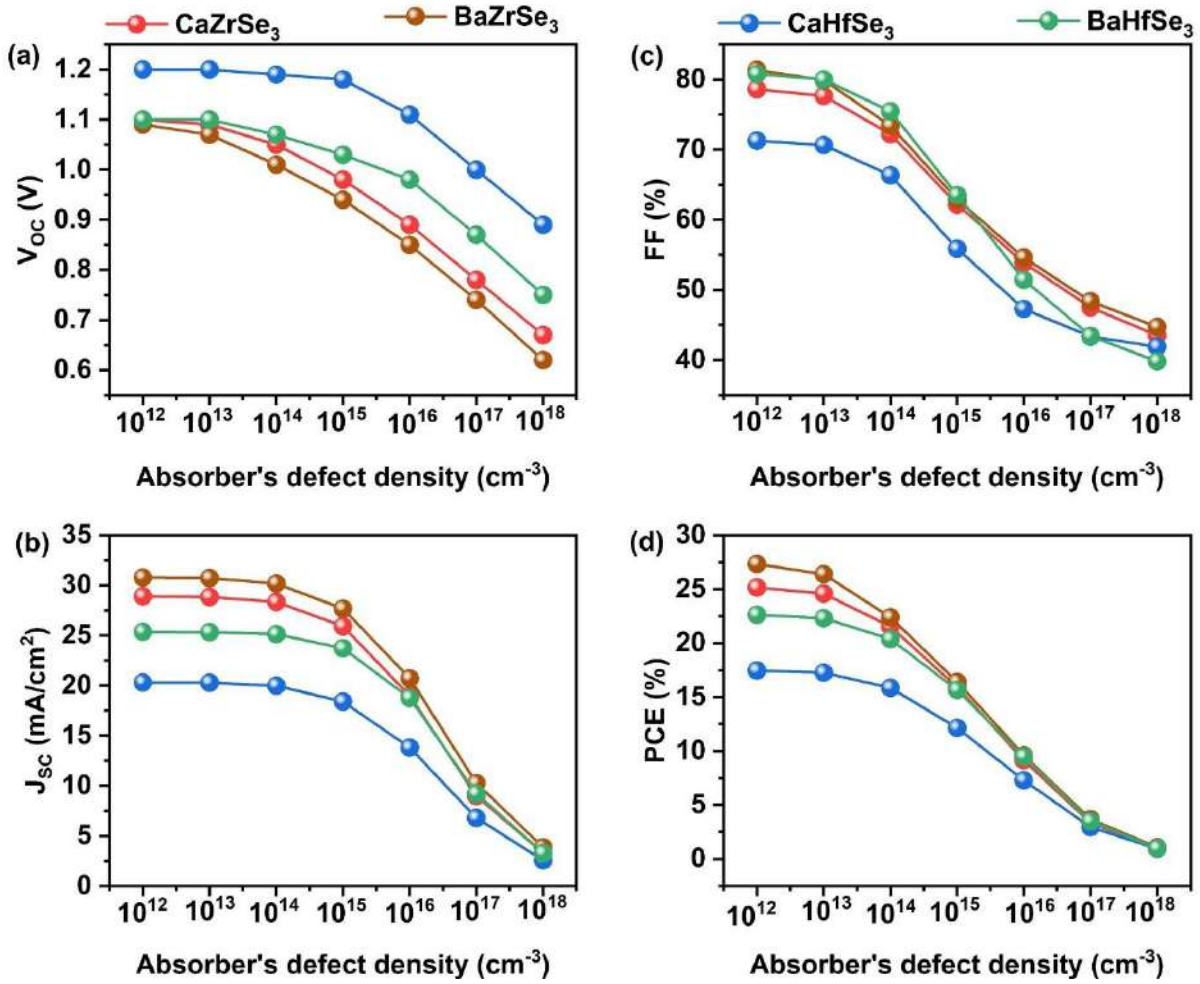

Fig. 28. Changes in (a) V_{OC} (b) J_{SC} (c) FF (d) PCE as a function of absorber's defect density [47].

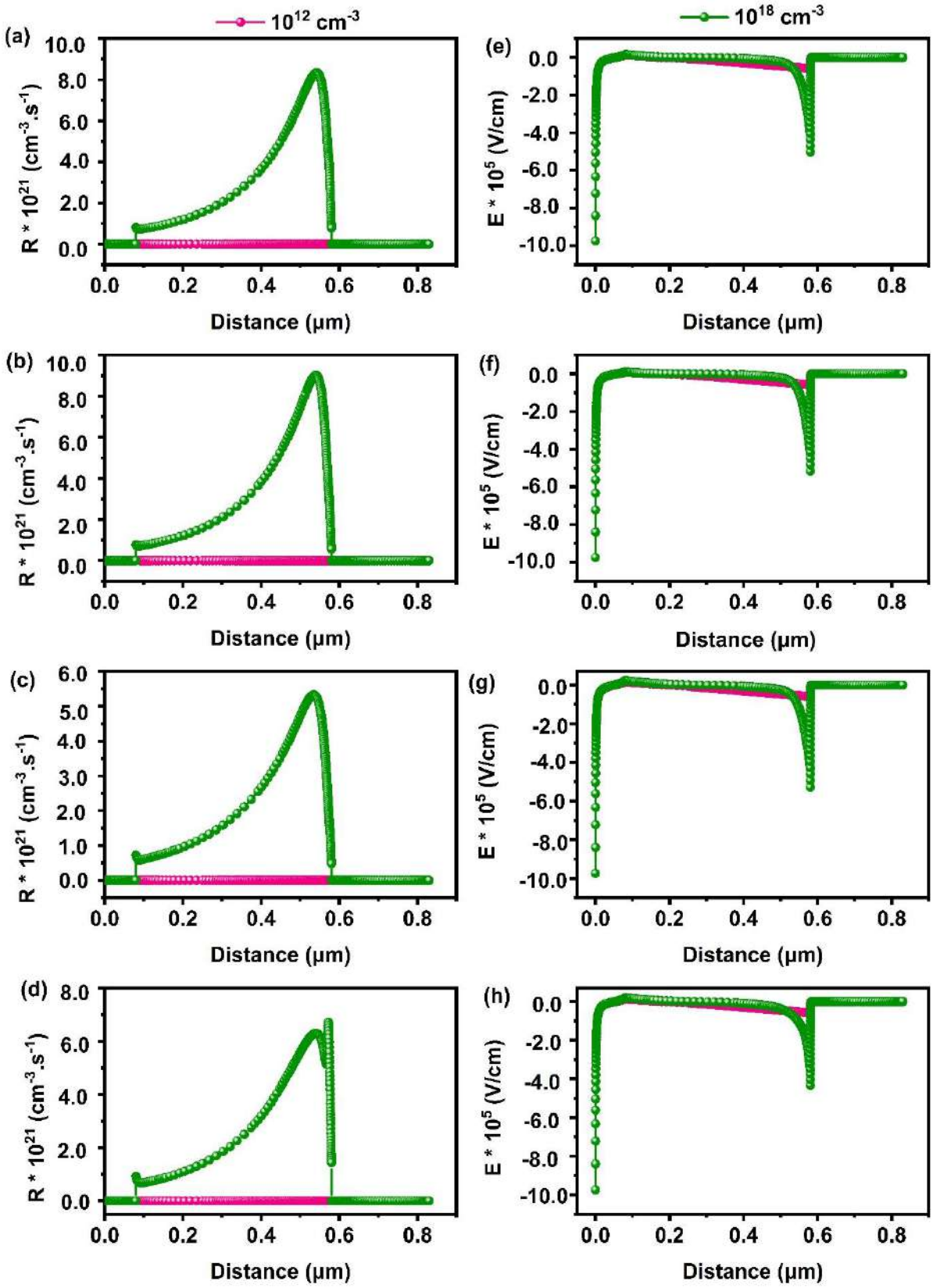

Fig. 29. Changes in (a-d) Electric field and (e-h) Recombination rates as a function of absorbers defect densities [47].

6.2.4. Impact of HTL thickness and carrier concentration

The HTL at the interface between the absorber and the back contact reduces the barrier for hole collection at the back contact, thereby decreasing interfacial recombination at the Absorber/HTL junction [207]. To investigate the impact of HTL thickness on solar cell performance, we varied the thickness from 50 nm to 150 nm across all solar cells (see **Fig. 30**(a-d)). Our observations indicate that changes in V_{OC}, J_{SC}, FF, and PCE relative to the HTL thickness are minimal, suggesting that the thickness has a limited effect on enhancing solar cell performance. As a result, considering material costs and experimental factors, we selected an HTL thickness of 100 nm as the ideal thickness for subsequent simulations.

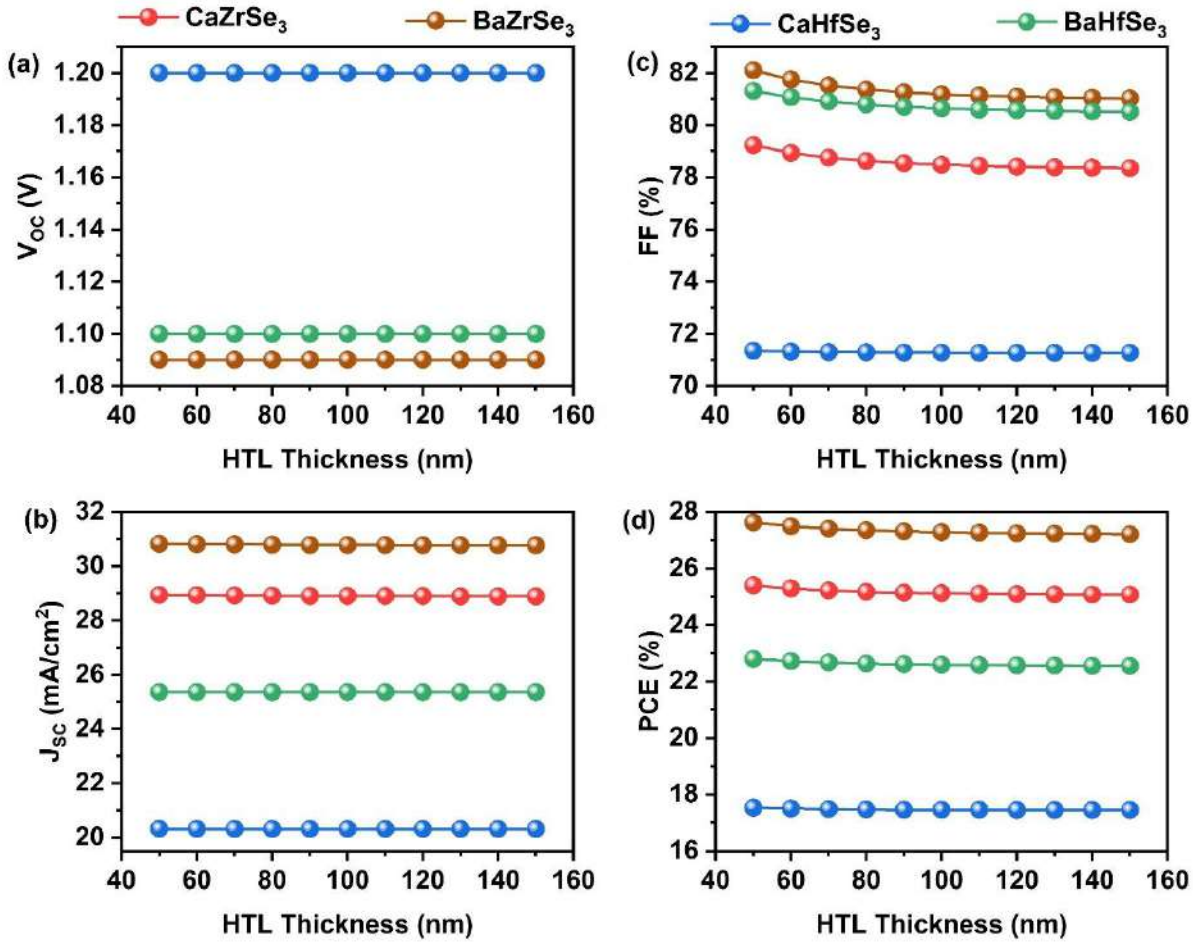

Fig. 30. Changes in (a) V_{OC} (b) J_{SC} (c) FF and (d) PCE as a function of HTL thickness [47].

The impact of the HTL's carrier concentration was studied by varying it from 10^{12} cm^{-3} to 10^{20} cm^{-3} for $CaZrSe_3$, $BaZrSe_3$, $CaHfSe_3$, and $BaHfSe_3$-based solar cells, respectively. **Fig. 31**(a-d) illustrates how the PV parameters change with the HTL carrier concentration. Notably, the V_{OC} of all solar cells remains stable up to 10^{16} cm^{-3} and shows slight improvement beyond this threshold, while the J_{SC} remains unchanged throughout the entire range. The observed

changes in V_{OC} are linked to an increase in quasi-Fermi level splitting as the carrier concentration of the HTL increases. In contrast, the FF values increase beyond 10^{16} cm^{-3}, leading to an overall enhancement in PCE. This effect arises from the relationship between the carrier concentration of the HTL and the absorber. When the carrier concentration of the HTL is lower than that of the absorber, the energy bands remain unaffected, and therefore, the performance of the solar cells does not change until the threshold of 10^{16} cm^{-3} is reached. Additionally, barriers at the Absorber/HTL interface and in the back contact act as recombination centers, hindering the smooth flow of charge carriers towards their respective contacts, which further impacts the solar cell performance. Conversely, when the carrier concentration of the HTL exceeds that of the absorber, shifts in the energy bands occur, reducing the barriers at both interfaces. Moreover, the recombination rate at the Absorber/HTL interface decreases significantly with an increase in carrier concentration for all solar cells, as shown in **Fig. 31**(e-h). This improvement leads to increased transport efficiency, conductivity, and built-in potential within the solar cells. Ultimately, the highest PCEs achieved were 30.08% for $CaZrSe_3$, 30.58% for $BaZrSe_3$, 22.53% for $CaHfSe_3$, and 27.60% for $BaHfSe_3$-based solar cells. In summary, these findings underscore the critical importance of HTL carrier concentration in enhancing solar cell performance.

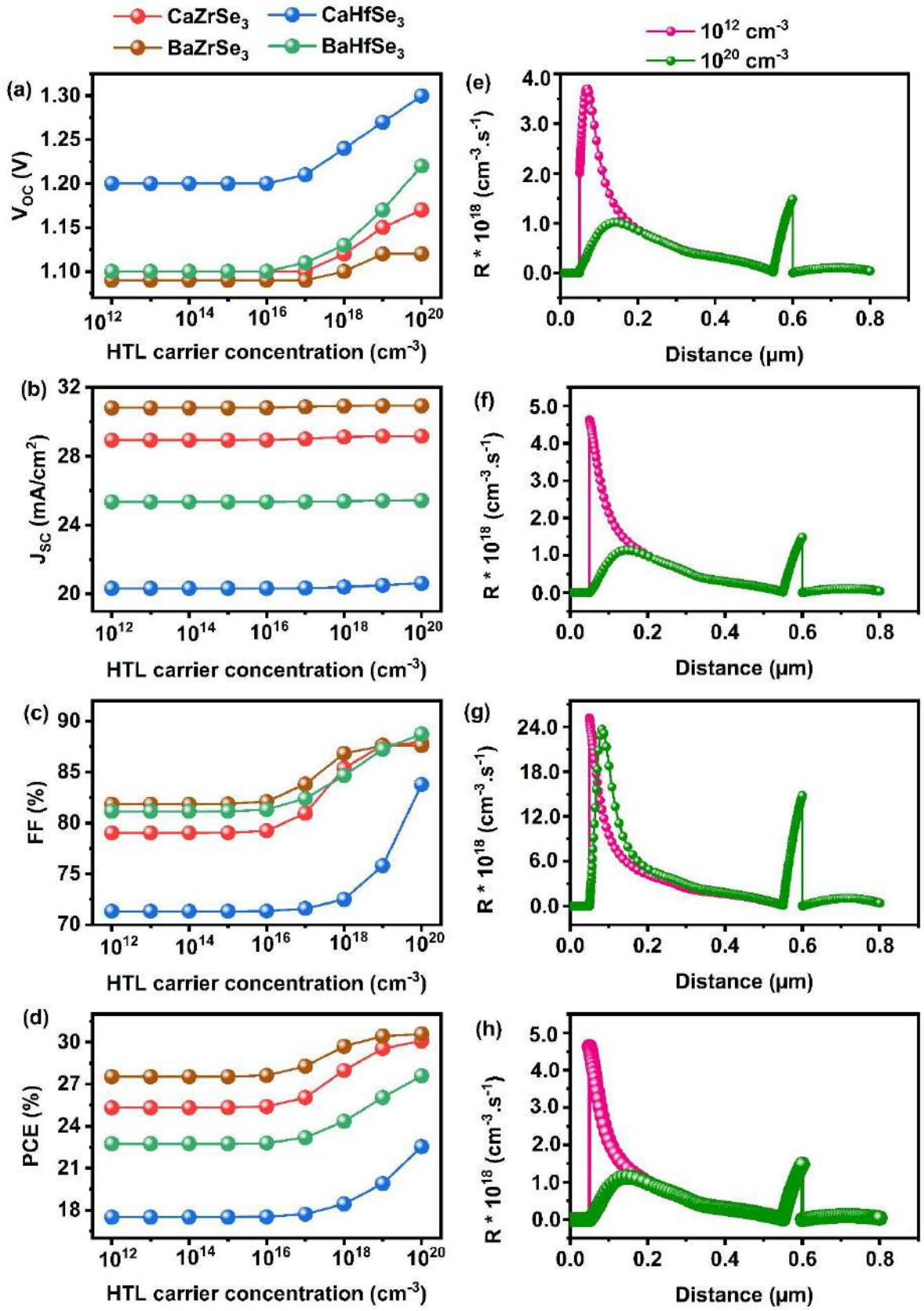

Fig. 31. Changes in (a) V_{OC} (b) J_{SC} (c) FF (d) PCE and (e-h) Recombination rates as a function of HTL carrier concentration [47].

6.2.5. Impact of interface defect density on ETL/Absorber and Absorber/HTL

Interface defects are a common occurrence during the fabrication of solar cells due to structural imperfections [208]. These defects significantly enhance the recombination of charge carriers at the interface, adversely affecting solar cell performance. This highlights the importance of analyzing their influence and determining an optimal defect density for experimental fabrication. In this work, all simulations were based on a neutral interface defect density of 10^{12} cm^{-3} at the ETL/Absorber and Absorber/HTL interfaces for all solar cells. To investigate the impact on PV parameters, we varied the interface defect density from 10^{12} cm^{-3} to 10^{20} cm^{-3} for the ETL/Absorber interface and from 10^{9} cm^{-3} to 10^{20} cm^{-3} for the Absorber/HTL interface.

As shown in **Fig. 32**(a-d), the V_{OC} declines significantly with an increase in interface defects from 10^{12} cm^{-3} to 10^{20} cm^{-3}. Meanwhile, the J_{SC} remains stable up to 10^{14} cm^{-3} before decreasing. Conversely, a marked drop in FF is observed, with values ranging from 87.88%, 87.61%, 83.78%, and 88.24% down to 82.19%, 81.68%, 80.63%, and 82.24% for $CaZrSe_3$, $BaZrSe_3$, $CaHfSe_3$ and $BaHfSe_3$-based solar cells, respectively. This leads to a significant reduction in PCE, indicating that FF plays a crucial role in determining solar cell performance at the ETL/Absorber interface. The decrease in PCE is approximately 7.01%, 7.94%, 4.31%, and 5.16% for $CaZrSe_3$, $BaZrSe_3$, $CaHfSe_3$ and $BaHfSe_3$-based solar cells, respectively, due to increased trap-assisted recombination at the ETL/Absorber interfaces, which impedes electron flow toward the front contact [209]. Given these results, an ideal defect density of 10^{12} cm^{-3} is recommended for the optimal performance of $CaZrSe_3$, $BaZrSe_3$, $CaHfSe_3$, and $BaHfSe_3$-based solar cells. Next, we assessed the Absorber/HTL interface defect density by varying it from 10^{9} cm^{-3} to 10^{20} cm^{-3}, as illustrated in **Fig. 32**(e-h). Here, all solar cell parameters remain relatively stable up to 10^{12} cm^{-3} but decline beyond this threshold. Notably, PCE experiences a drastic drop from 30.16%, 30.59%, 22.53%, and 27.60% to 25.04%, 26.57%, 18.31%, and 21.64% for $CaZrSe_3$, $BaZrSe_3$, $CaHfSe_3$ and $BaHfSe_3$-based solar cells, respectively. This decline in performance can be attributed to an increased likelihood of hole trapping at the Absorber/HTL interface due to defects. These findings strongly emphasize the necessity of maintaining a defect density below 10^{12} cm^{-3} at the Absorber/HTL interface to achieve high solar cell efficiency.

Currently, there are no experimental reports on the fabrication of solar cells using the materials $CaZrSe_3$, $BaZrSe_3$, $CaHfSe_3$, and $BaHfSe_3$. The only documented solar cell made from CPs is based on the $BaZrS_3$ absorber, which has recently achieved a reported PCE of just

0.17%. However, critical issues such as interface defects in the fabricated solar cell and methods to control these defects have not been investigated. This indicates a significant gap in the existing literature regarding effective strategies to mitigate interface defects specific to CPs solar cells. Given this situation, it may be helpful to explore techniques from other types of solar cells that could be adapted to address interface defects in these CPs. Methods like interface engineering and additive engineering are commonly used during solar cell fabrication to minimize recombination losses and defects at ETL/Absorber and HTL/Absorber interfaces. For example, a study by Wang et al. demonstrated that etching $Sb_2(S,Se)_3$ with a potassium fluoride solution before depositing the HTL could significantly reduce defects at the HTL/Absorber interface, thereby improving charge carrier transportation [210]. Similarly, research by Hwang et al. highlighted that post-heat treatment of the $Cu_2ZnSn(S,Se)_4$ absorber led to a reduction in interfacial recombination at the ETL/absorber interface, ultimately enhancing the solar cell's PCE [116]. Moreover, Tian et al. investigated the insertion of interfacial layers on either side of the $CsPbI_2Br$ perovskite absorber, which was found to passivate defects at both the ETL/Absorber and HTL/Absorber interfaces [139]. In a related study, Yanping and colleagues experimented with doping the perovskite absorber with bromine (Br) to further mitigate interface defects [211]. Overall, drawing from these insights and techniques employed in the fabrication of various types of solar cells, it is plausible that similar methods could effectively address the interface defect issues in solar cells based on $CaZrSe_3$, $BaZrSe_3$, $CaHfSe_3$, and $BaHfSe_3$. However, confirmation of suitable techniques for these specific solar cells can only be established following their actual fabrication and subsequent experimental evaluation.

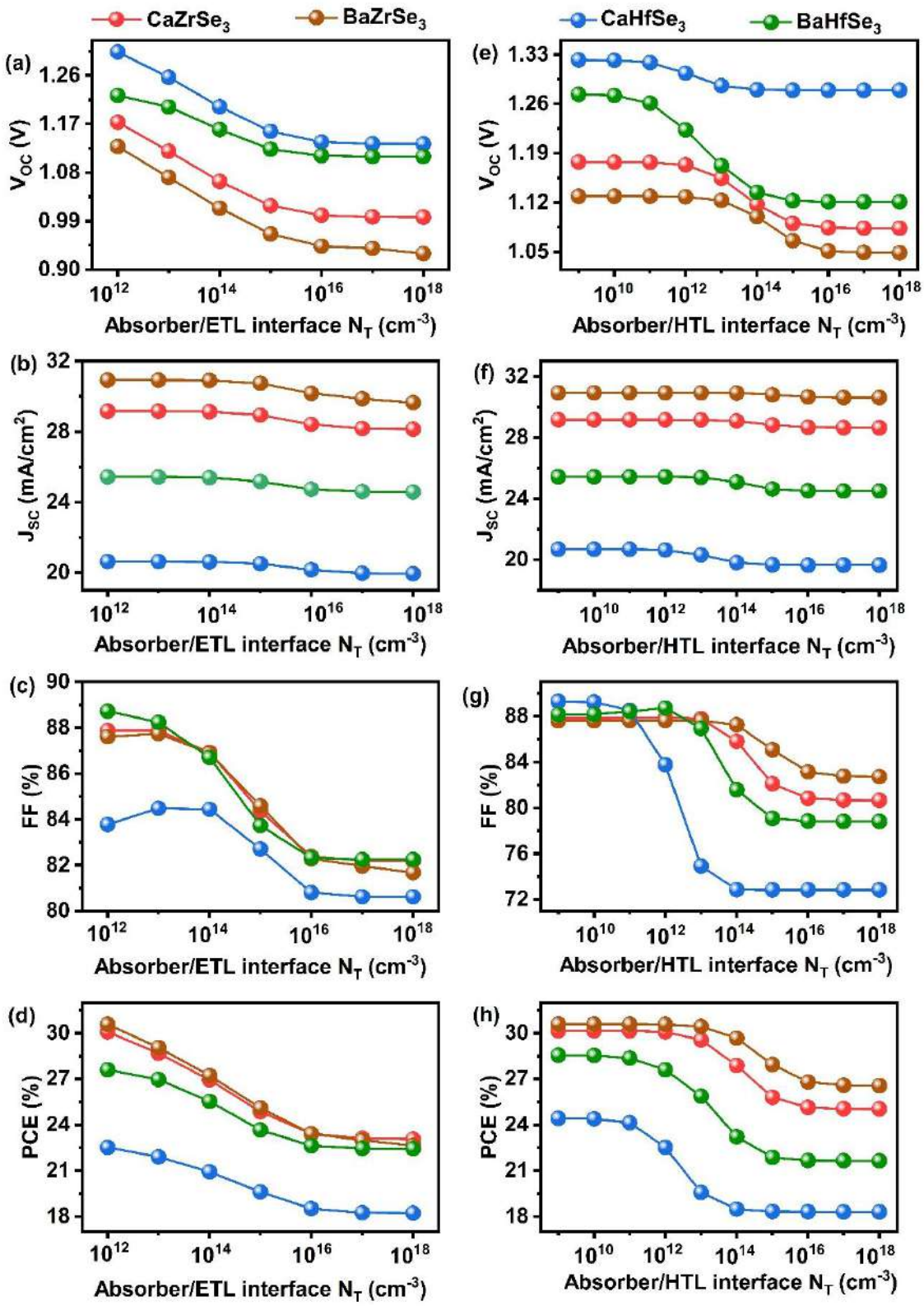

Fig. 32. Changes in V_{OC}, J_{SC}, FF, and PCE as a function of (a-d) ETL/Absorber and (e-h) Absorber/HTL interface defects [47].

6.2.6. Comparison of all absorbers

This study investigates the solar cell performance of novel CPs: $CaZrSe_3$, $BaZrSe_3$, $CaHfSe_3$, and $BaHfSe_3$. Notably, we achieved impressive final PCEs of 30.08%, 30.58%, 22.53%, and 27.60% for $CaZrSe_3$, $BaZrSe_3$, $CaHfSe_3$, and $BaHfSe_3$-based solar cells, respectively. The increase in PCE is primarily attributed to the enhancement in J_{SC}, as shown in **Fig. 33**(a) and (b). Specifically, the J_{SC} rises from 12.17 mA/cm^2, 13.04 mA/cm^2, 8.73 mA/cm^2 and 13.88 mA/cm^2 to 29.16 mA/cm^2, 30.93 mA/cm^2, 20.62 mA/cm^2 and 25.43 mA/cm^2 for $CaZrSe_3$, $BaZrSe_3$, $CaHfSe_3$ and $BaHfSe_3$-based solar cells, respectively. This underscores the significant role of J_{SC}, which largely depends on light absorption and charge carrier generation. Furthermore, the QE measurements and generation rates of the proposed solar cells were extracted from SCAPS-1D, as illustrated in **Fig. 33**(c) and (d). The $CaZrSe_3$, $BaZrSe_3$, $CaHfSe_3$, and $BaHfSe_3$ solar cells exhibited QEs of 57.78%, 61.10%, 43.94%, and 51.57%, respectively, with the highest generation rates of 1.22×10^{22} cm^{-3}s^{-1}, 1.35×10^{22} cm^{-3}s^{-1}, 7.77×10^{21} cm^{-3}s^{-1} and 1.02×10^{22} cm^{-3}s^{-1} at the Absorber/ETL interface (0.54 μm). Notably, $BaZrSe_3$ solar cells achieved a high QE and generation rate, which can be attributed to their lower bandgap compared to the other materials, leading to superior performance. Overall, this work demonstrates that all solar cells achieved PCEs greater than 20%, with $BaZrSe_3$ and $CaZrSe_3$ exceeding 30%. Our findings are likely to inspire material scientists to explore the fabrication of novel $CaZrSe_3$, $BaZrSe_3$, $CaHfSe_3$, and $BaHfSe_3$ solar cells.

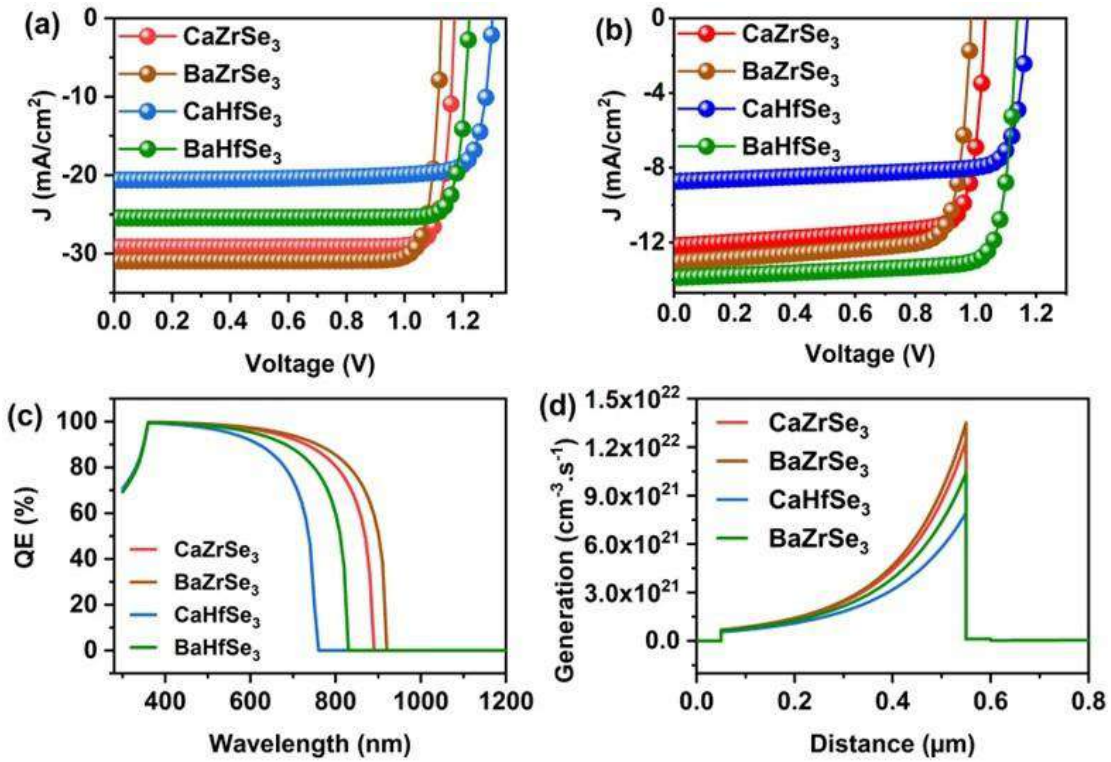

Fig. 33. Comparison of J-V characteristics (a) Initial, (b) Final, (c) QE, and (d) Recombination rate for novel CPs solar cells [47].

6.2.7. Impact of series, shunt resistance, and working temperature for $CaZrSe_3$, $BaZrSe_3$, $CaHfSe_3$, and $BaHfSe_3$ solar cells

The performance of solar cells is significantly affected by two key factors R_S and R_{SH}. R_S refers to the resistance encountered at metal contacts, transport layers, and the absorber's resistance outside the space charge region. An increase in R_S can Pb to a reduction in the overall PCE of solar cells, as it causes some of the current to dissipate as heat instead of being converted into usable electrical energy. To investigate the impact of R_S, we examined solar cells based on $CaZrSe_3$, $BaZrSe_3$, $CaHfSe_3$, and $BaHfSe_3$. We varied R_S from 1 to 10 Ω cm², as illustrated in **Fig. 34**(a-d). It was observed that the V_{OC} and J_{SC} remained largely unchanged across this range. However, the FF decreased significantly, dropping from 85.51%, 85.00%, 82.43%, and 86.74% for $CaZrSe_3$, $BaZrSe_3$, $CaHfSe_3$, and $BaHfSe_3$-based solar cells, respectively, to 64.98%, 62.52%, 70.63%, and 69.41%. This decline is attributed to substantial power loss (P_{loss}) within the solar cells at higher R_S values, as shown in **Eqn. (15)** [51,192].

$$P_{loss} = I_{sc}^2 R_S \quad (15)$$

The equation above illustrates that P_{loss} is directly proportional to R_S. This means that an increase in R_S results in a higher P_{loss}, which in turn reduces the PCE from 29.28% to 22.97%, 29.08% to 21.85%, 22.17% to 18.96%, and 26.99% to 21.60% in the solar cells based on $CaZrSe_3$, $BaZrSe_3$, $CaHfSe_3$ and $BaHfSe_3$, respectively. Therefore, an optimal R_S of 1 Ω cm² is recommended for the efficient operation of solar cells. On the other hand, the R_{SH} primarily results from factors such as interface barriers, charge-collecting interlayers, metal-based electrodes, and defects or impurities. These issues Pb to reverse saturation current in solar cells. Additionally, leakage pathways, like pinholes in the absorber and recombination losses, contribute to R_{SH}. The Shockley equation, as represented in **Eqn. (16)** and **Eqn. (17)**, describes the expected behavior of the J-V characteristics of a solar cell under ideal one-sun illumination conditions [144].

$$J_{SC} = J_{PH} - J_0 \left[\exp\left(\frac{q_e (V - JR_S)}{nkT_e}\right) - 1\right] - \frac{V - JR_S}{R_{Sh}} \quad (16)$$

$$V_{OC} = \left(\frac{nkT_e}{q_e}\right) \ln\left\{\frac{J_{PH}}{J_0}\left(1 - \frac{V_{OC}}{R_{Sh} J_{PH}}\right)\right\} \quad (17)$$

Where q_e, J_{PH}, J_0, R_S, R_{SH}, n, k, T_e represents the elementary charge, photocurrent density, density of the reverse bias saturation current, series resistance, shunt resistance, diode ideality factor, Boltzmann constant and ambient temperature, respectively [212]. Thus, R_{SH} is altered from 500 to 5000 Ω cm^2 to investigate its impact on the performance of solar cells. From **Fig. 34**(e-h), it can be noticed that J_{SC} and V_{OC} remain constant while FF and PCE enhance with an increase in R_{SH}. In particular, the FF and PCE rise around ~7.5% and 2.3%, respectively, for all the solar cells. Therefore, elevated R_{SH} values result in improved solar cell performance.

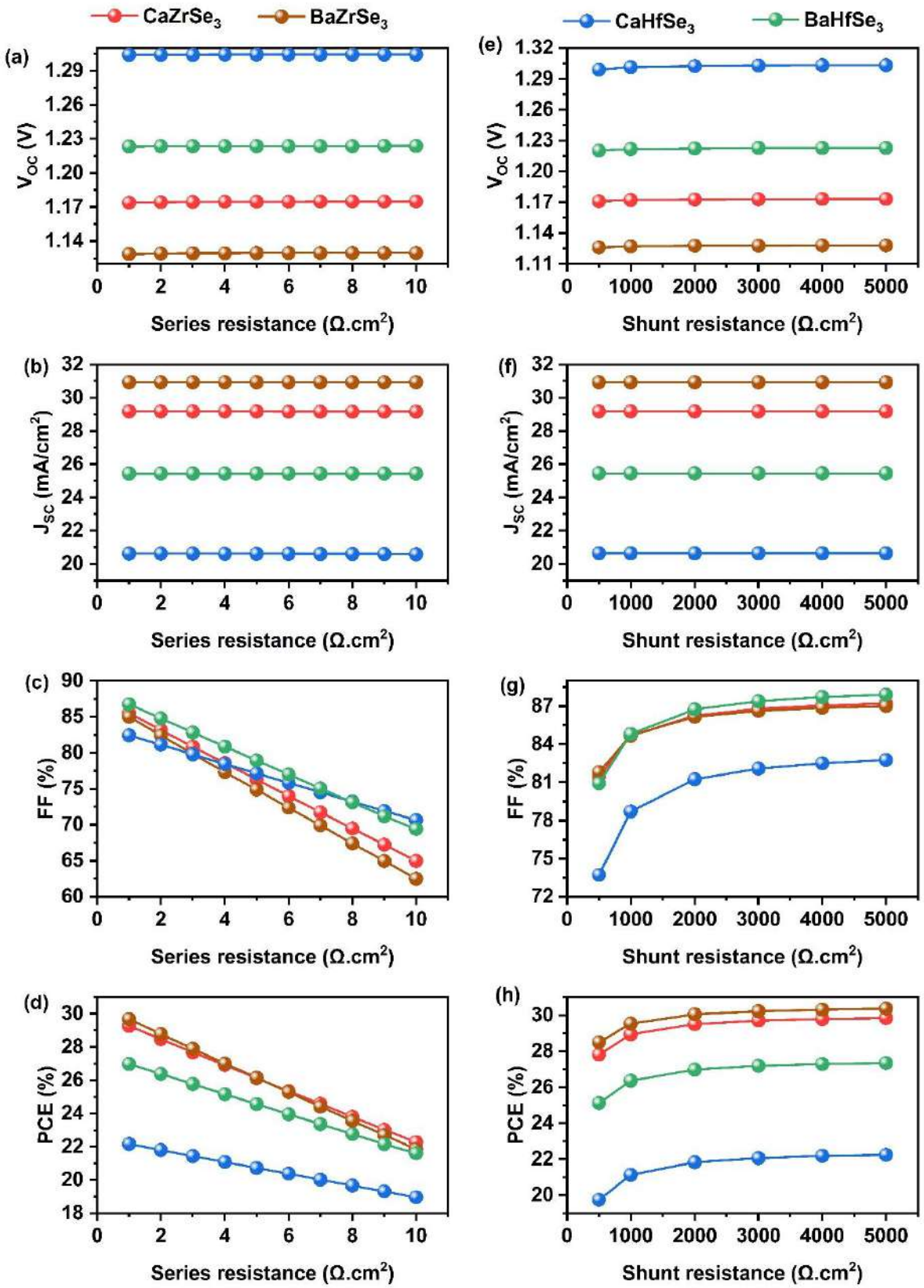

Fig. 34. Influence of V_{OC}, J_{SC}, FF, and PCE as a function of (a-d) series resistance and (e-h) shunt resistance [47].

The performance of solar cells often shows instability due to layer deformation at high temperatures. To investigate the relationship between temperature and PV parameters, we varied the temperature from 300K to 480K, as shown in **Fig. 35**(a-d). The results indicate that as the temperature increases, the V_{OC}, FF, and PCE decrease, while the J_{SC} remains relatively constant. The decline in V_{OC} is attributed to the increased vibration of thermally generated electrons at higher temperatures. This heightened vibration makes the electrons less stable and more prone to recombination with holes, leading to an increase in the reverse saturation current (J_0). This inverse relationship between V_{OC} and J_0 is clearly illustrated in **Eqn. (18)**.

$$V_{OC} = \frac{nKT}{q}\left(ln\left(1 + \frac{J_{SC}}{J_o}\right)\right) \quad (18)$$

Where $\frac{KT}{q}$ signifies the thermal voltage. Increasing the temperature negatively impacts several physical parameters, including carrier concentration, absorber bandgap, and the mobility of charge carriers. These changes directly affect the efficiency of charge carrier transport, ultimately leading to a reduction in the FF. As a result, the decline in V_{OC} and FF causes the PCE to drop significantly. For instance, PCE decreases from 30.08% to 2.62%, from 30.58% to 24.87%, from 22.53% to 21.36%, and from 27.60% to 23.17% in solar cells based on $CaZrSe_3$, $BaZrSe_3$, $CaHfSe_3$ and $BaHfSe_3$, respectively.

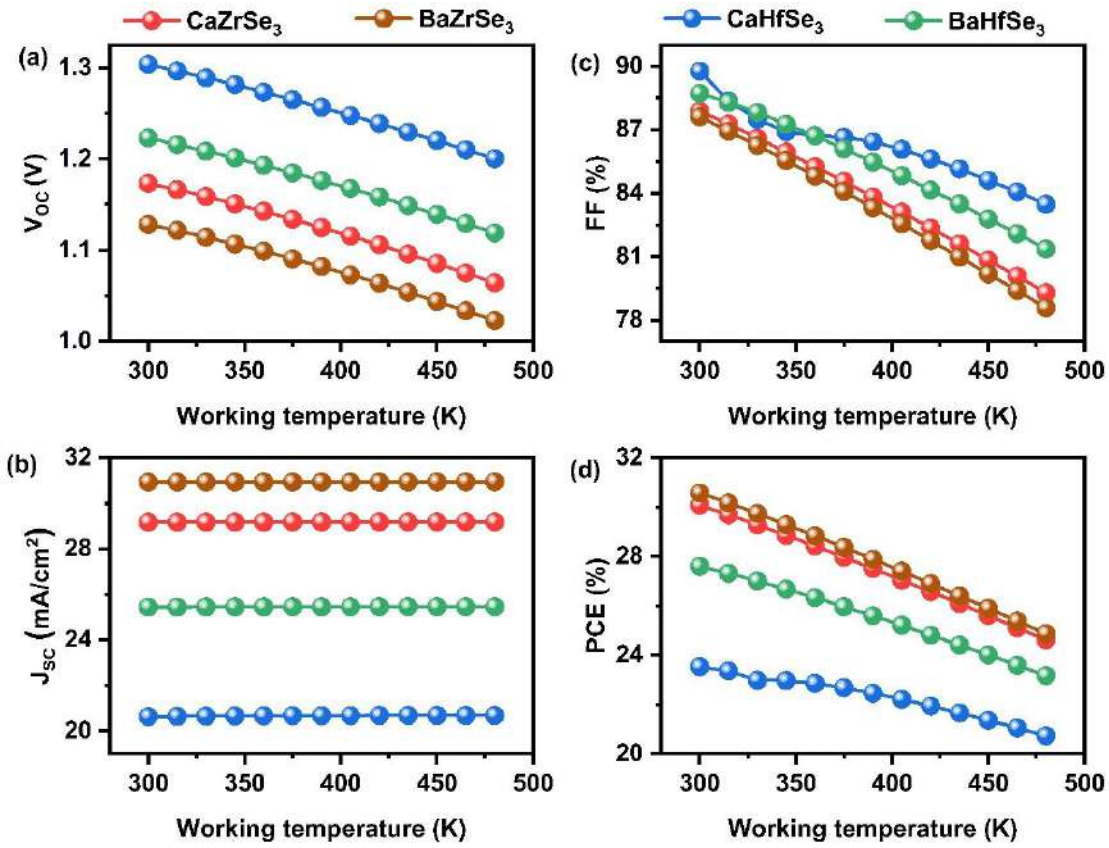

Fig. 35. Influence of V_{OC}, J_{SC}, FF, and PCE as a function of working temperature [47].

6.2.8. Comparison of SCAPS-1D outcomes with previous studies in the literature

Table 12 presents the outcomes of various theoretical studies on CPs solar cells using SCAPS-1D. Notably, extensive research has been conducted on $BaZrS_3$ CPs, achieving a maximum PCE of 28.17%. However, there is a need for further exploration of other potential CPs, highlighting a significant gap in research. Interestingly, we have successfully developed the first-ever $CaZrSe_3$, $BaZrSe_3$, $CaHfSe_3$, and $BaHfSe_3$ solar cells by employing TiO_2, NiO, and Au as the ETL, HTL, and metal contact, respectively. Remarkably, these new absorbers yielded unprecedented PCEs of 30.08% for $CaZrSe_3$, 30.58% for $BaZrSe_3$, 22.74% for $CaHfSe_3$, and 27.60% for $BaHfSe_3$. This underscores the potential of these emerging absorbers, comparable to that of $BaZrS_3$. Thus, our findings are expected to generate interest within the scientific community and contribute to a deeper understanding of the roposed c CPs , providing a framework for developing highly efficient CPs.

Table 12. Comparison between findings of novel CPs solar cells with previous studies in the literature [47].

Device structure	**V_{OC} (V)**	**J_{SC} (mA/cm^2)**	**FF (%)**	**PCE (%)**	**Ref**
FTO/TiO_2/$BaZrS_3$/Spiro-OMeTAD/Au	1.21	16.54	86.26	17.29	[213]
FTO/TiO_2 /$BaZrS_3$/Cu_2O/Au	1.16	12.24	87.13	12.42	[29]
FTO/TiO_2/$BaZrS_3$/Spiro-OMeTAD/Au	0.70	22.00	79.40	12.12	[49]
AZO/i-ZnO/CdS/ $BaZrS_3$/a-Si	1.31	19.08	78.88	19.72	[137]
FTO/TiO_2/$BaZrSe_3$/Spiro-OMeTAD/Au	0.72	46.65	77.32	25.84	[49]
FTO/TiO_2/$BaZrSe_3$/Spiro-OMeTAD/Au	0.69	33.05	81.39	19.76	[49]
FTO/ZrS_2/$BaZrS_3$/SnS/Pt	1.18	29.74	80.15	28.17	[39]
FTO/ZnO /$SrZrS_3$/NiO/Ni	1.18	26.13	84.29	25.97	[213]
FTO/ SnO_2/$SrZrS_3$/Cu-MOF/Ni	1.17	29.54	88.40	30.60	[197]
FTO/ TiO_2/$CaZrSe_3$/NiO/Au	1.17	29.16	87.88	30.08	*
FTO/ TiO_2/$BaZrSe_3$/NiO/Au	1.12	30.93	87.61	30.58	*
FTO/ TiO_2/$CaHfSe_3$/NiO/Au	1.30	20.62	83.78	22.53	*
FTO/ TiO_2/$BaHfSe_3$/NiO/Au	1.22	25.43	88.72	27.60	*
The * represents the findings of the present work					

6.3. Optimization of $BaHf_{1-x}Zr_xS_3$ CPs Solar Cells

This section presents detailed simulation results supporting **objective 4**, which focus on optimizing and enhancing the performance of $BaHf_{1-x}Zr_xS_3$-based solar cells. **Section 6.3.1** begins with the base device performance. **Sections 6.3.2** and **6.3.3** evaluate how variations in absorber layer thickness, acceptor density, and defect density affect device efficiency. **Section 6.3.4** investigates the role of the TiO_2 ETL layer across all absorbers, considering its donor concentration, defect levels, affinity, and thickness. **Section 6.3.5** examines different $BaHf_{1-x}Zr_xS_3$ compositions and their absorber properties. **Section 6.3.6** explores the impact of NiO HTL parameters, while **Section 6.3.7** addresses the effect of back metal work function. **Section 6.3.8** analyzes interface defect densities at both ETL/absorber and absorber/HTL junctions. **Section 6.3.9** studies the influence of series and shunt resistances and operational temperature. **Section 6.3.10** compares base and optimized devices using electrical and optical characteristics. **Section 6.3.11** contrasts simulation results with

6.3.1 Base device performance

The study utilized a solar cell base device constructed with FTO/TiO_2/$BaHf_{1-x}Zr_xS_3$/NiO/Au configuration, as depicted in **Fig. 5**. The base device's performance was assessed through simulations that incorporated the parameter outlined in **Table 4** and **Table 5**. The PV parameters for the $BaHfS_3$, $BaHf_{0.75}Zr_{0.5}S_3$, $BaHf_{0.5}Zr_{0.5}S_3$, and $BaHf_{0.25}Zr_{0.75}S_3$ solar cells are provided in **Table 13**. In our work in **Table 13**, Zr-substituted $BaHfS_3$ absorbers, despite their lower bandgap than pure $BaHfS_3$, presented larger V_{OC}. The observed discrepancy occurs due to various reasons. Typically, in addition to quasi-Fermi level splitting, V_{OC} is also significantly influenced by factors such as recombination dynamics and the built-in potential (V_B) of the device [214]. Hence, recombination rates and V_B of the diverse simulated absorbers were obtained from SCAPS-1D (**Fig. 36**a). In the figure, the recombination rate of charge carriers in pure $BaHfS_3$ solar cells is comparatively larger than its counterparts along the absorber region and at the absorber/HTL interface. Also, the V_B of all devices was estimated from the intercept of Mott-Schottky ($1/C^2$) plots shown in **Fig. 36**b. The V_B of Zr-substituted $BaHfS_3$ solar cells is >1.25 V, while it is about 1.16 V in pure $BaHfS_3$ solar cells. In light of the outcomes, it is apparent that although the bandgap of pure $BaHfS_3$ is large, it suffers from increased recombination losses and lower V_B than Zr-substituted $BaHfS_3$ solar cells, leading to its lower V_{OC}. Similarly, Zr-substituted $BaHfS_3$ has high J_{SC} and FF compared to pure $BaHfS_3$ due to enhanced charge carriers with low recombination. Finally, PCEs of 3.42% for $BaHfS_3$, 4.31% for $BaHf_{0.75}Zr_{0.25}S_3$, 5.05% for $BaHf_{0.5}Zr_{0.5}S_3$ and 5.92% for $BaHf_{0.25}Zr_{0.75}S_3$ absorbers are achieved. To improve the device's performance, extensive optimization of ETL, absorbers, and HTL material parameters was conducted. A comprehensive understanding of these optimizations' procedures can be obtained by referring to the subsequent sections.

Table 13. Photovoltaic parameters of the base device with different $BaHf_{1-x}Zr_xS_3$ absorbers [44].

Base device configuration	V_{OC} (V)	J_{SC} (mA/cm^2)	FF (%)	PCE (%)
FTO/TiO_2/$BaHfS_3$/NiO/Au	1.05	4.06	79.65	3.42
FTO/TiO_2/$BaHf_{0.75}Zr_{0.25}S_3$/NiO/Au	1.21	4.44	79.55	4.31
FTO/TiO_2/$BaHf_{0.5}Zr_{0.5}S_3$/NiO/Au	1.24	5.13	79.16	5.05
FTO/TiO_2/$BaHf_{0.25}Zr_{0.75}S_3$/NiO/Au	1.25	5.98	78.81	5.92

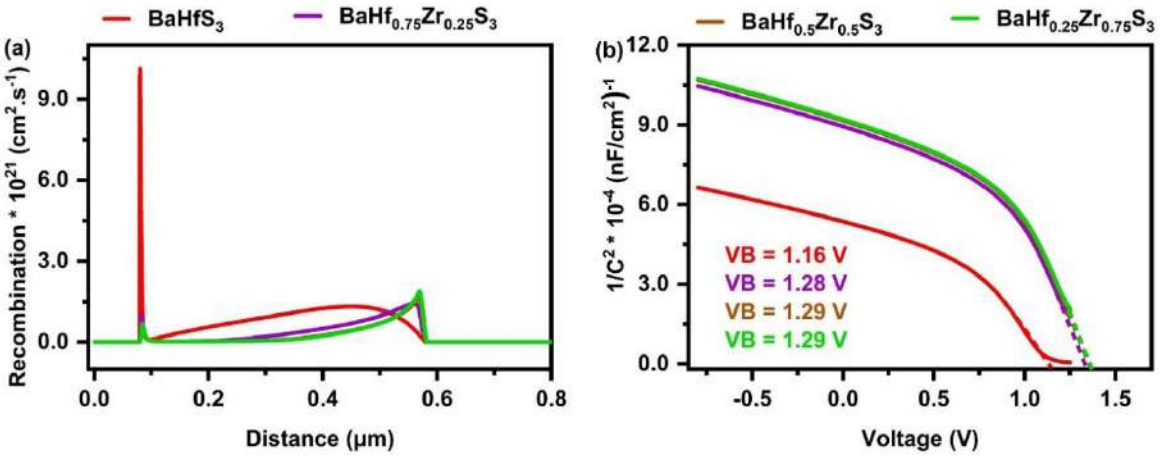

Fig. 36. Performance of $BaHf_{1-x}Zr_xS_3$ (a) recombination rate and (b) built-in potential [44].

6.3.2 Impact of varying absorber acceptor density with absorber layer thickness on the solar cell performance

The present study examines the effect of acceptor density on the performance of absorbers with different thicknesses in $BaHfS_3$, $BaHf_{0.75}Zr_{0.25}S_3$, $BaHf_{0.5}Zr_{0.5}S_3$, and $BaHf_{0.25}Zr_{0.75}S_3$-based solar cells. Contour plot mapping was used to evaluate their performance. The goal is to determine the optimal absorber thickness and acceptor density for effective light absorption and enhanced V_B in solar cells. The acceptor density varied from 10^{12} cm^{-3} and 10^{20} cm^{-3}, and the thickness ranged from 200 nm to 2000 nm, as shown in **Fig. 37**(a-d). The results revealed maximum V_{OC} values of 1.13 V, 1.31 V, 1.33 V, and 1.34 V for $BaHfS_3$, $BaHf_{0.75}Zr_{0.25}S_3$, $BaHf_{0.5}Zr_{0.5}S_3$, and $BaHf_{0.25}Zr_{0.75}S_3$-based absorbers, respectively. For the $BaHfS_3$ absorber, V_{OC} remained constant up to 10^{18} cm^{-3} and increased thereafter across the range of thickness and acceptor density. In contrast, the other absorbers showed a notable increase in V_{OC} with increased thickness, regardless of acceptor density, particularly significant for carrier concentrations between 10^{16} cm^{-3} and 10^{20} cm^{-3}. This trend is attributed to the increased splitting of the quasi-Fermi level for higher acceptor density, leading to larger V_{OC} values. Additionally, it enhances charge carrier separation by improving the V_B, thus raising V_{OC} [215]. **Fig. 37**(e-h) demonstrates the variations in the J_{SC} as a function of the absorber's thickness and acceptor density. The results clearly show that increasing the thickness from 100 nm to 1400 nm and the acceptor density from 10^{12} cm^{-3} to 10^{16} cm^{-3} leads to a rise in J_{SC} values. However, beyond 1400 nm in thickness and 10^{16} cm^{-3} in acceptor density, the J_{SC} values decline. This initial increase in J_{SC} is due to the thicker absorber generating more electron-hole pairs, thereby enhancing solar cell performance. Nonetheless, when the absorber's thickness surpasses a certain limit, charge carrier recombination increases because the diffusion lengths become shorter relative to the absorber thickness, resulting in decreased solar cell performance

[119]. Additionally, higher acceptor density increases carrier recombination within the absorber, which lowers the J_{SC} values [114]. Therefore, the optimal J_{SC} is achieved at an acceptor density of 10^{16} cm^{-3} for all absorber thicknesses. **Fig. *38***(a-d) illustrates the variation in FF for all absorbers as a factor of absorber thickness and acceptor density. Notably, all solar cells exhibited similar FF patterns when the absorber thickness and acceptor density were varied. The contour plot analysis revealed that when the acceptor density exceeded 10^{16} cm^{-3}, the FF significantly increased with changes in thickness across all absorbers. Conversely, the FF decreased with an increase in absorber thickness. Specifically, a notable drop in FF occurred with increasing thickness when the acceptor density ranged between 10^{11} cm^{-3} and 10^{15} cm^{-3}. The improvement in FF at higher acceptor density can be assigned to the high V_B at the absorber/ETL junction, which promotes efficient transport of photogenerated charge carriers [215]. However, the deterioration of FF with increasing absorber thickness may result from enhanced recombination rates of photogenerated carriers and significant power losses in thicker absorbers [216]. Overall, the results suggest that the optimum FF can be achieved at an acceptor density above 10^{16} cm^{-3} and a thickness below 600 nm. The effect of absorber thickness and carrier density on the effectiveness of PCE is analyzed through contour plots in **Fig. 38**(e-h). It is noteworthy that the acceptor density below and above 10^{16} cm^{-3} reduces the PCE of pure $BaHfS_3$, regardless of its thickness. For Zr-substituted $BaHfS_3$, the PCE increases significantly up to 10^{16} cm^{-3}, while only a negligible change is observed for acceptor densities beyond this threshold. Typically, variation in the acceptor density of the absorber alters the energy band offsets at the interfaces, affecting the transportation and collection of charge carriers [192]. Maximum solar cell performance is achieved at optimum acceptor densities where appropriate barriers are generated with charge carriers effectively reaching the respective contacts without recombination. Since QE provides insights into the photon absorption and charge carrier collection in solar cells, we extracted QE measurements from SCAPS-1D to evaluate the variations as a function of acceptor density **(Fig. 39)**. In pure $BaHfS_3$, QE% significantly improves up to 10^{16} cm^{-3}, while a drastic decrement is observed beyond that. This reveals that absorption losses and high recombination occur in $BaHfS_3$ owing to improper band alignment at the interfaces for acceptor densities greater or lesser than 10^{16} cm^{-3}. On the other hand, in Zr alloyed $BaHfS_3$, QE steadily elevates from ~22% to 38% for the range 10^{12} cm^{-3} to 10^{16} cm^{-3} while minutely improving to 39% on further improvement to 10^{20} cm^{-3}. This strongly discloses that maximum charge carriers can be collected for acceptor densities $\geq 10^{16}$ cm^{-3}. Overall, from the above discussion, the maximum PCE values of approximately 4.31%, 4.75%, 5.43%, and 6.18% can be achieved with absorber optimum thicknesses ranging from 600 to 1400 nm and

optimum carrier densities of 10^{16} cm^{-3} for $BaHfS_3$ and $\geq 10^{16}$ cm^{-3} for $BaHf_{0.75}Zr_{0.25}S_3$, $BaHf_{0.5}Zr_{0.5}S_3$ and $BaHf_{0.25}Zr_{0.75}S_3$-based solar cells.

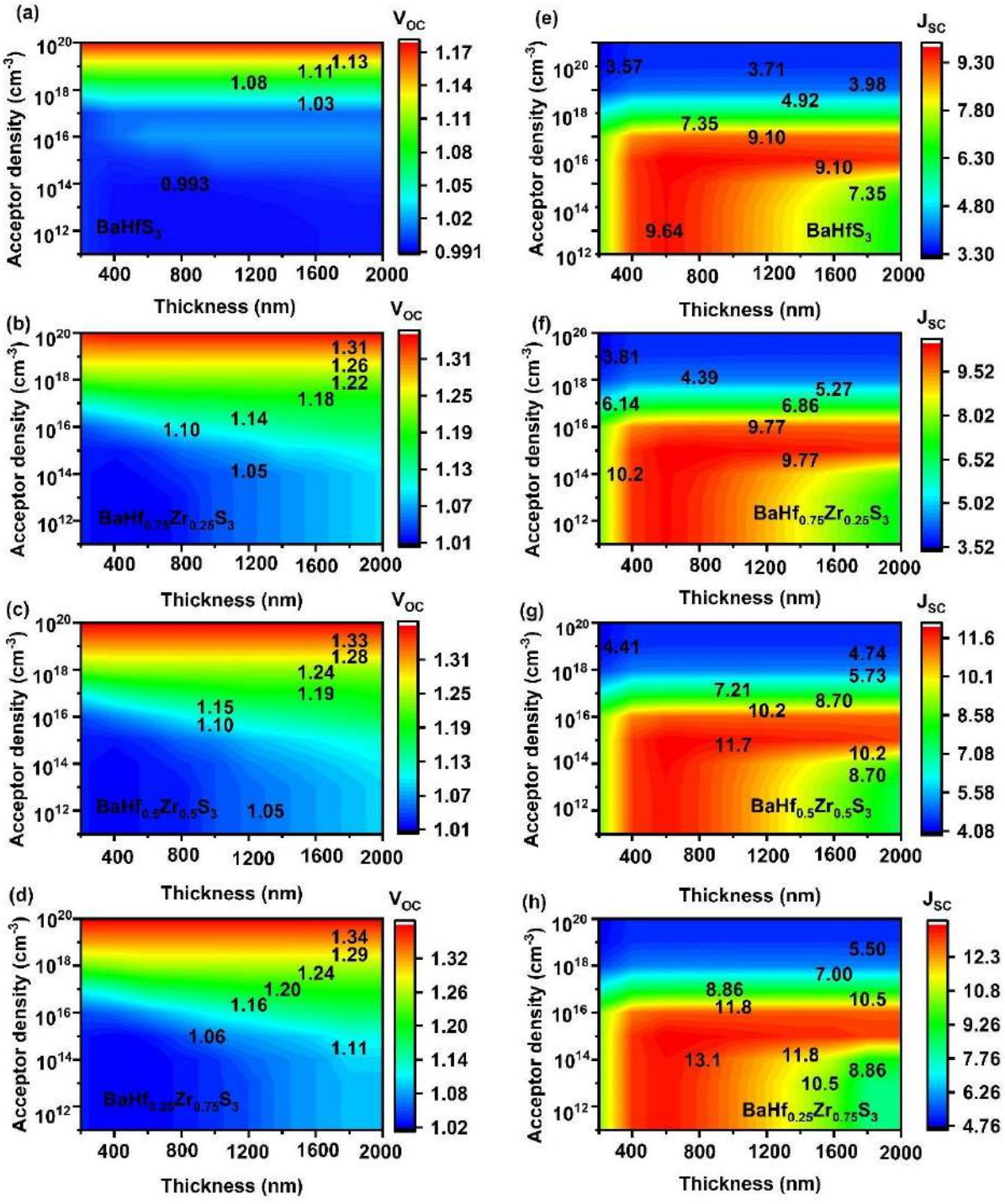

Fig. 37. Contour plots illustrating the effect of variation in absorber's thickness with acceptor density on the (a-d) V_{OC} (V) (e-h) J_{SC} (mA/cm^2) [44].

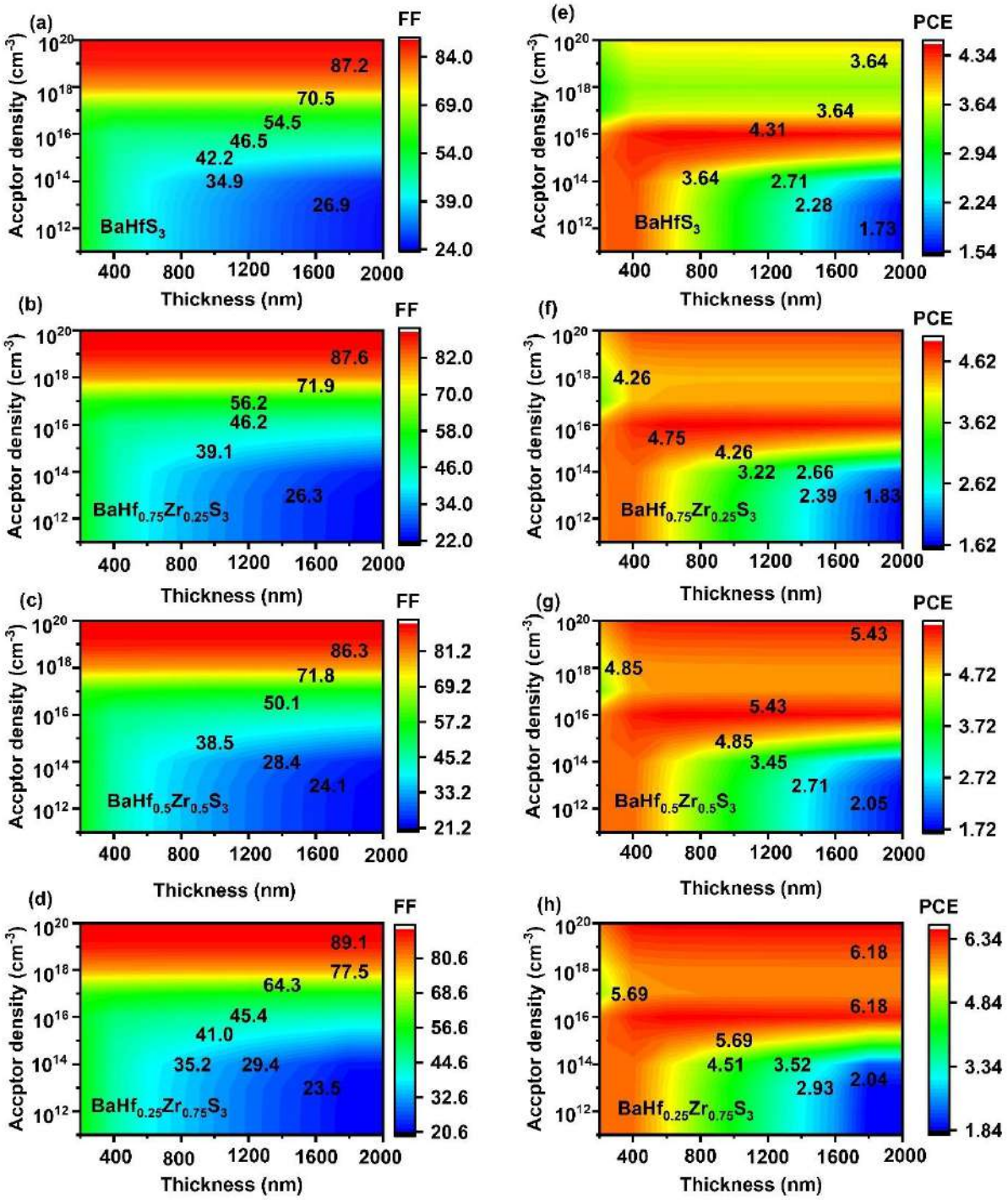

Fig. 38. Contour plots illustrating the effect of variation in absorber's thickness with acceptor density on the (a-d) FF (%) (e-h) PCE (%) [44].

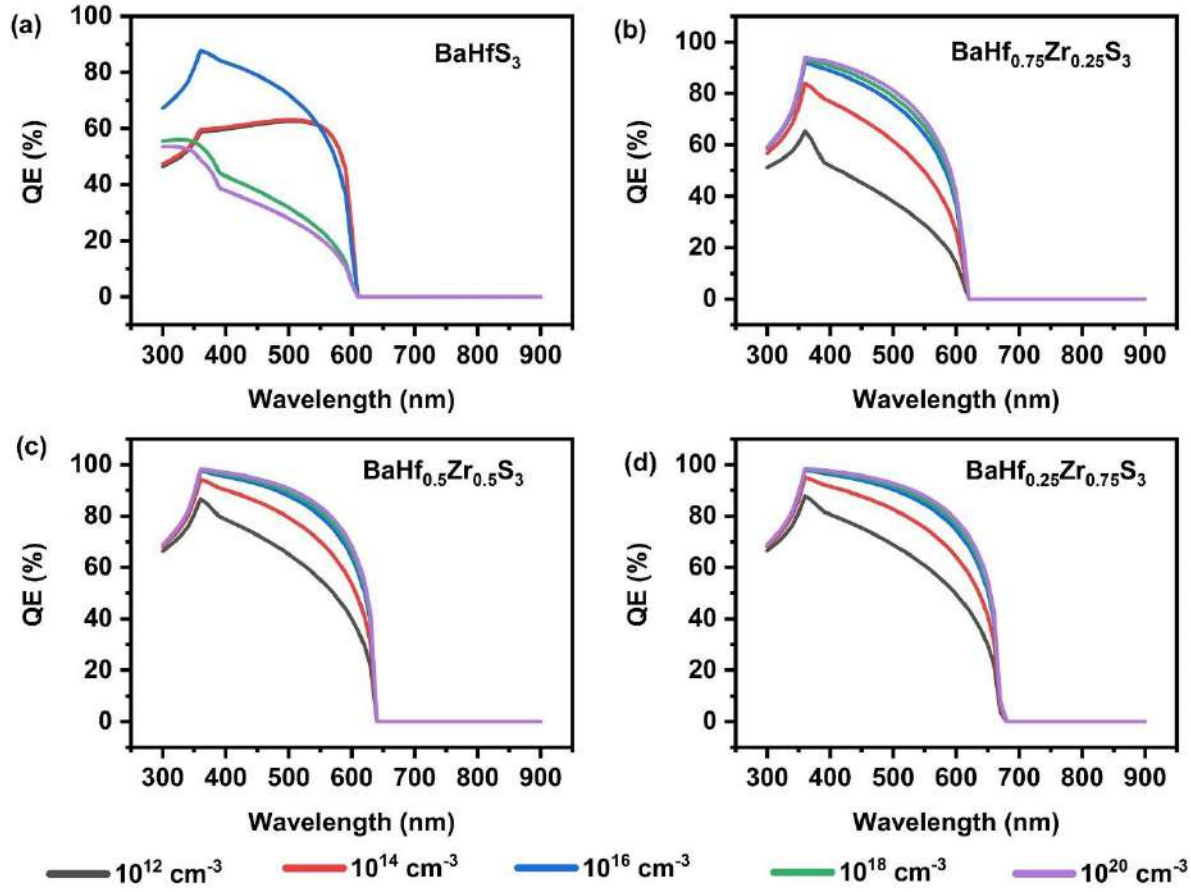

Fig. 39. Performance of QE measurements for absorber defect density (a) $BaHfS_3$ (b) $BaHf_{0.75}Zr_{0.25}S_3$ (c) $BaHf_{0.5}Zr_{0.5}S_3$ and (d) $BaHf_{0.25}Zr_{0.75}S_3$ [44].

6.3.3 Impact of varying defect density with absorber layer thickness on the solar cell performance

The thickness and defect density of the absorber influences the effectiveness of solar cells. To investigate the impact of these parameters on the performance of various absorber $BaHfS_3$, $BaHf_{0.75}Zr_{0.25}S_3$, $BaHf_{0.5}Zr_{0.5}S_3$, and $BaHf_{0.25}Zr_{0.75}S_3$-based solar cells, a study was conducted by simultaneously altering the absorber's thickness from 200 nm to 2000 nm and defect density from 10^{11} cm^{-3} to 10^{20} cm^{-3} using contour plots. **Fig. 40**(a-d) displays the changes in V_{OC} as a function of absorber thickness and defect density. When the thickness is increased from 200 nm to 2000 nm, the V_{OC} remained almost constant with negligible improvement across all defect density ranges of 10^{12} cm^{-3} and 10^{20} cm^{-3}. Since V_{OC} mainly depends on quasi-Fermi level splitting, its unaltered behavior discloses that the variation in absorber thickness does not change the positions of quasi-fermi levels in pure $BaHfS_3$ and Zr-substituted $BaHfS_3$. This is also witnessed in **Fig. 42**, where the electron and hole fermi levels (F_n and F_p) are extracted as a function of absorber thickness (200 to 2000 nm) at the defect density of 10^{13} cm^{-}

^{3} for all absorber-based solar cells. It can be seen that, as the thickness of $BaHfS_3$ and Zr-substituted $BaHfS_3$ absorbers is increased from 200 to 2000 nm, the F_n and F_p almost remain in the same position without significant change, confirming the minimal changes in V_{OC}. Similarly, the J_{SC} in relation to the thickness and defect density of the absorber is shown in **Fig. 40**(e-h). The highest J_{SC} is attained when the absorber's thickness surpasses 800 nm and the defect density is below 10^{13} cm^{-3}. All the solar cells exhibit their maximum J_{SC} when the thickness is less than 1500 nm, with defect densities ranging from 10^{11} cm^{-3} to 10^{13} cm^{-3}. The enhancement of charge carrier generation due to increased light absorption for larger absorber thicknesses contributes to the rise in J_{SC}. On the other hand, the decrease in J_{SC} can be attributed to the elevated charge carrier recombination resulting from higher defects in the absorber [118]. In addition, the results for the FF relation to the absorber's thickness and defect density can be seen in **Fig. 41**(a-d). It is evident that when the defect density is under 10^{15} cm^{-3}, the FF remains steady across the varying absorber thickness range. The decrease in FF within the range of 10^{15} cm^{-3} to 10^{18} cm^{-3} can be attributed to the reduced lifetime and diffusion length of photogenerated charge carriers, which leads to an increased recombination rate, negatively impacting the solar cell performance [192,217]. As defect density increases, additional recombination centers within the material are introduced, increasing the likelihood of carrier recombination. In some cases, transportation of charge carriers may enhance defects through tunneling or hopping conduction of charge carriers. In the former, the charge carriers travel defects to defects via quantum mechanical exchange, while they may travel from the trap level to the respective energy bands in the latter. Thus, the improvement in FF at defect densities above 10^{18} cm^{-3} may be associated with these enhanced trap-assisted charge transport properties. However, these improvements are overshadowed by the detrimental effects of increased recombination, which dominate at such high defect densities [218]. As a result, the overall PCE decreases despite the marginal improvement in FF observed above 10^{18} cm^{-3}. In summary, while FF may improve at defect densities exceeding 10^{18} cm^{-3}, the simultaneous increase in recombination losses leads to reductions in V_{OC} and J_{SC} and results in a decline in the PCE of the solar cells. The critical issue lies in the adverse impact of defects on carrier recombination, emphasizing the need to minimize defect density to achieve optimal device efficiency. Additionally, the maximum PCE is achieved with an absorber thickness greater than 800 nm. Moreover, PCE holds the maximum value for the defect density between 10^{11} cm^{-3} and 10^{13} cm^{-3} due to absorbers' defect tolerance within the range. Beyond this, the PCE decreases significantly, as evidenced in **Fig. 41**(e-h) for $BaHfS_3$, $BaHf_{0.75}Zr_{0.25}S_3$, $BaHf_{0.5}Zr_{0.5}S_3$ and $BaHf_{0.25}Zr_{0.75}S_3$-based solar cells. The defects in solar cells significantly

affect the diffusion length and lifetime. Therefore, we have extracted the diffusion length and lifetime behaviors using SCAPS-1D, as shown in **Fig. 43**. It can be seen that when the defect density is raised from 10^{12} cm^{-3} to 10^{20} cm^{-3}, the lifetime considerably decreases from 10^{6} ns to 10^{-3} ns, and their diffusion length is drastically reduced from 8.5 μm to 0.00027 μm. On comparing the obtained solar cell parameters with **Fig. 41**(e-h), it can be observed that the PCE almost remains unaffected till a lifetime of 10^{4} ns and diffusion length of 0.85 μm, revealing that the photogenerated charge carrier with these values gets effectively collected at the contact without recombination. On the other hand, diffusion length and lifetime firmly fall for defects $>10^{13}$ cm^{-3}, leading to high recombination of charge carriers which in turn adversely declines the PCE [51,192]. This underscores the importance of maintaining defect densities below 10^{13} cm^{-3} and absorber thicknesses above 800 nm to optimize PCE across all solar cell absorbers.

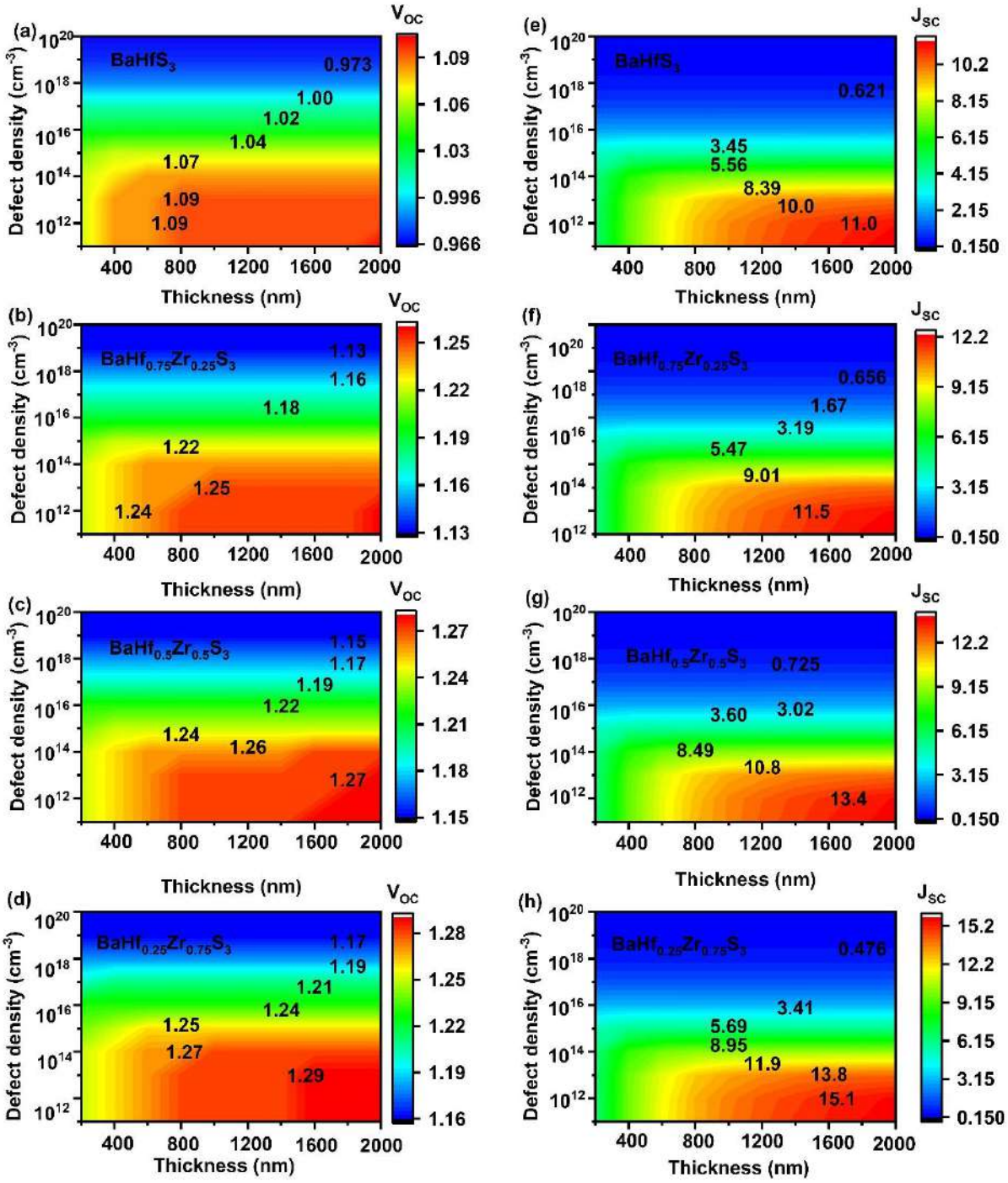

Fig. 40. Contour plots illustrating the effect of variation in absorber's thickness with defect density on the (a-d) V_{OC} (V) (e-h) J_{SC} (mA/cm^2) [44].

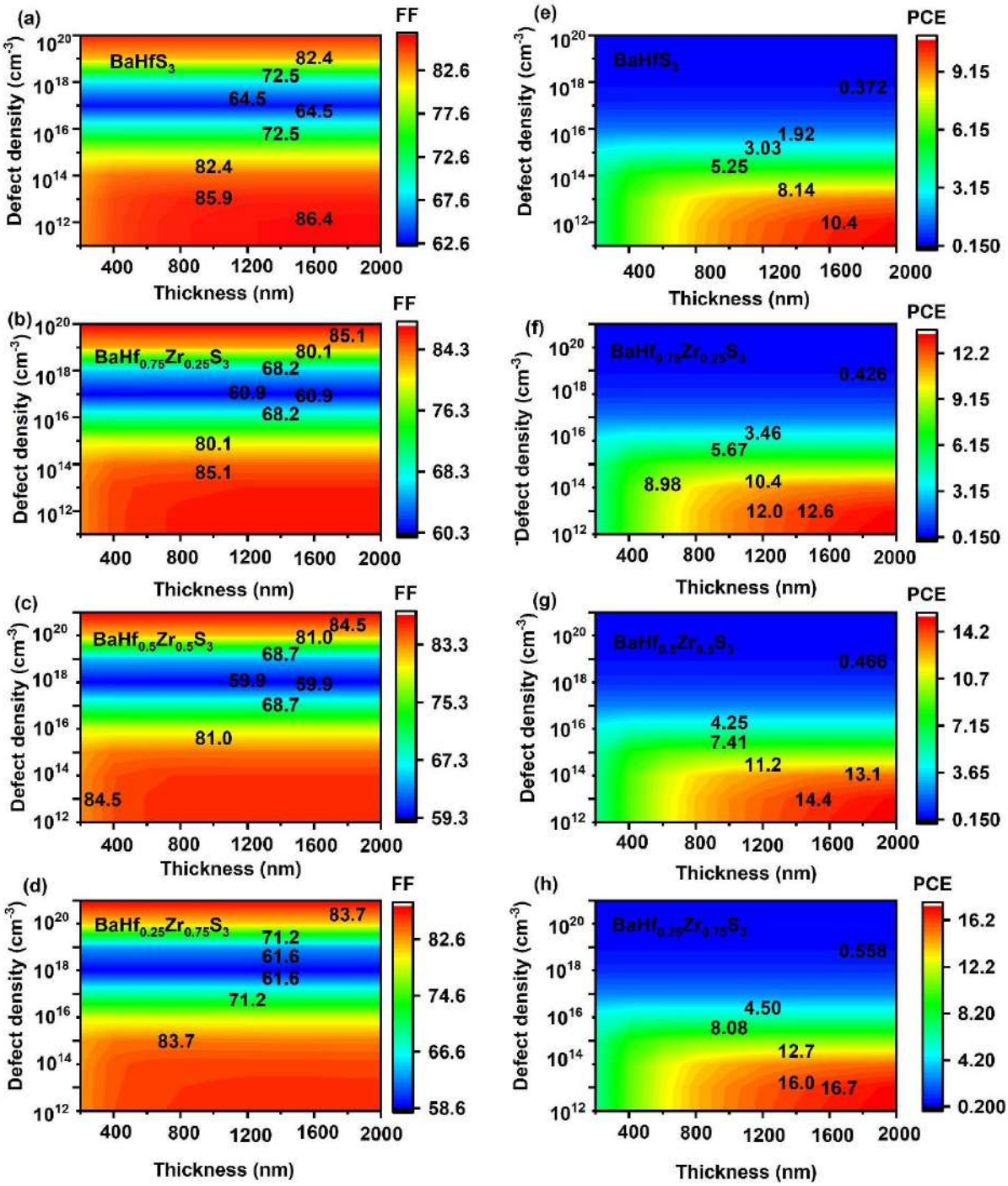

Fig. 41. Contour plots illustrating the effect of variation in absorber's thickness with defect density on the (a-d) FF (%) (e-h) PCE (%) [44].

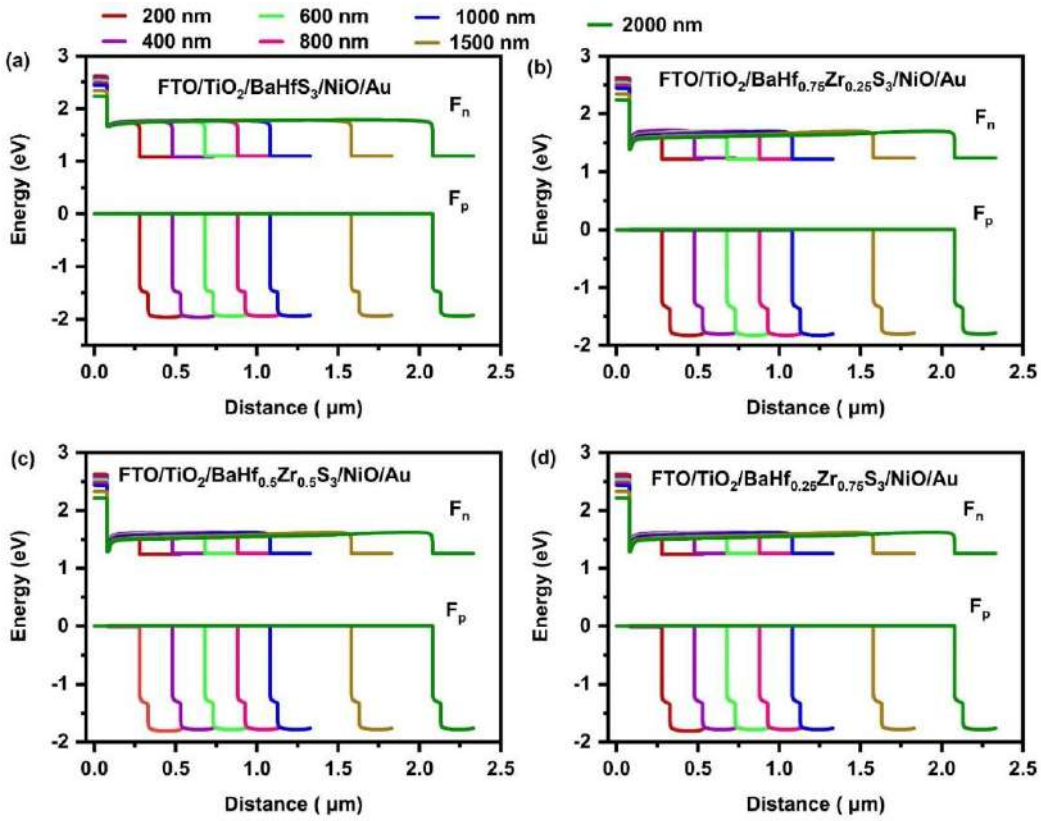

Fig. 42. Energy band diagram of thickness with defect density at 10^{13} cm^{-3} [44].

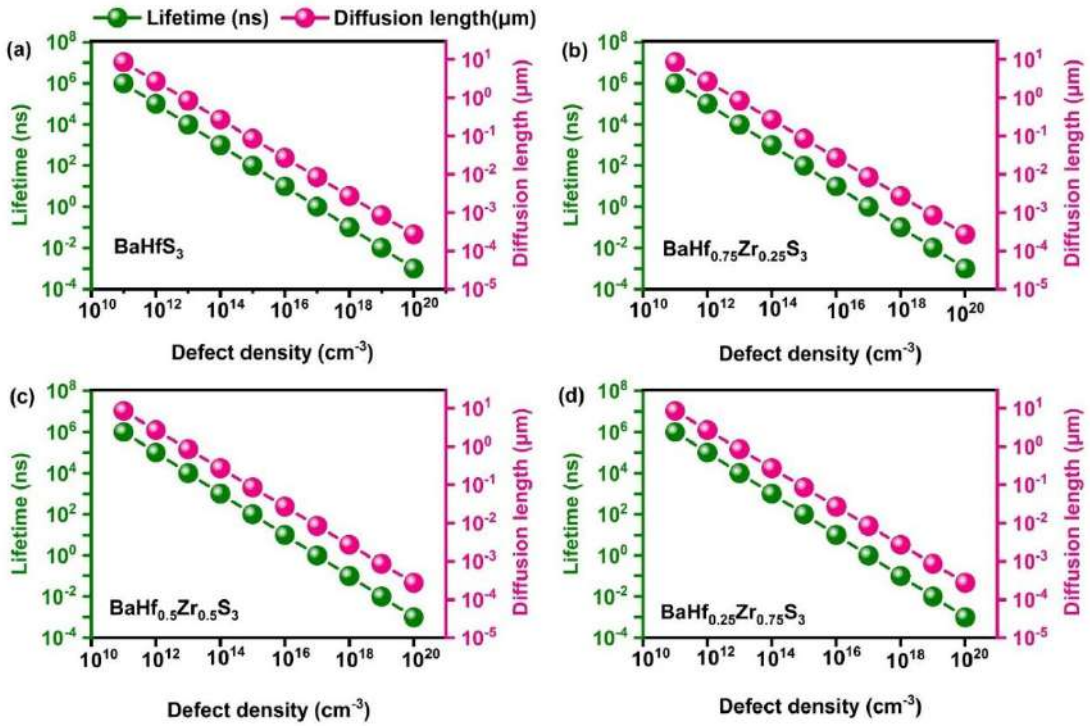

Fig. 43. Performance of lifetime and diffusion length for absorbers defect density (a) $BaHfS_3$ (b) $BaHf_{0.75}Zr_{0.25}S_3$ (c) $BaHf_{0.5}Zr_{0.5}S_3$ and (d) $BaHf_{0.25}Zr_{0.75}S_3$ [44].

6.3.4 Influence of ETL TiO_2 with all absorbers

6.3.4.1 Impact of ETL donor density and defect density

Examining the ETL donor density is essential as it affects the band alignment and interface properties between the layers. The donor density of the TiO_2 ETL is altered from 10^{12} cm^{-3} to 10^{20} cm^{-3} for $BaHfS_3$, $BaHf_{0.75}Zr_{0.25}S_3$, $BaHf_{0.5}Zr_{0.5}S_3$ and $BaHf_{0.25}Zr_{0.75}S_3$ solar cells, as illustrated in **Fig. 44**(a-d). The V_{OC} across the solar cells remains unchanged at 1.06 V, 1.22 V, 1.25 V, and 1.26 V until the concentration of 10^{16} cm^{-3} for $BaHfS_3$, $BaHf_{0.75}Zr_{0.25}S_3$, $BaHf_{0.5}Zr_{0.5}S_3$, and $BaHf_{0.25}Zr_{0.75}S_3$ based solar cells. After this value, there is a minimal decline, followed by a significant increase. This increase indicates an increase in quasi-Fermi level splitting with an increment in donor density [219]. Similarly, the FF remains constant across all solar cells up to 10^{16} cm^{-3}, after which a decrease is observed. Notably, an increase in donor concentration above 10^{16} cm^{-3} leads to a gradual improvement in J_{SC}, resulting in an increase in PCE from 3.42% to 4.35%, 4.29% to 5.37%, 5.02% to 6.28% and 5.89% to 7.35% for $BaHfS_3$, $BaHf_{0.75}Zr_{0.25}S_3$, $BaHf_{0.5}Zr_{0.5}S_3$ and $BaHf_{0.25}Zr_{0.75}S_3$ based absorber's, respectively. The upsurge is attributed to increased V_B and solar cell conductivity with a higher carrier concentration. In general, a lower carrier concentration results in holes primarily occupying the interface states, functioning as electron traps that impede the flow of photogenerated charge carriers. On the other hand, an increase in donor density lowers the barrier height at the ETL/absorber interface [220]. According to Xu et al., an increase in carrier concentration results in the formation of deep energy levels at interfaces, which leads to a reduction in non-radiative recombination and an improvement in solar cell performance [220]. The carrier density's deviation from the optimal value will impede the alignment of bands at the interfaces, as mentioned above, which hinders the separation and collection of electrons at the front contact, thereby impacting the performance of solar cells. Furthermore, considerable electron-electron scattering occurs for ETL donor densities that are more significant than the optimal value, which negatively affects the performance of solar cells and reduces their PCE [220]. Hence, an optimal carrier concentration ensures proper band alignment, generates a substantial electric field that facilitates efficient charge carrier transportation, reduces interface recombination rates, and enhances solar cell performance. Consequently, an optimal carrier concentration of 10^{20} cm^{-3} is chosen for all solar cells. Then defects in materials can create additional paths for non-radiative recombination, which results in the conversion of light into heat instead of electricity. The primary function of these recombination centers is to capture photogenerated carriers, thus limiting their ability to reach the terminals and consequently

reducing the carrier's lifespan. Hence, reducing defects is essential for improving device performance. To examine its influence, we modified the defects from 10^{12} cm^{-3} to 10^{20} cm^{-3}, as depicted in **Fig. 44**(e-h). All of the parameters related to the PV system remain within a specific range (10^{12} cm^{-3} to 10^{16} cm^{-3}) across all solar cells, but they show a slight decline as the presence of the defects increases further. Specifically, the PCE of $BaHfS_3$, $BaHf_{0.75}Zr_{0.25}S_3$, $BaHf_{0.5}Zr_{0.5}S_3$, and $BaHf_{0.25}Zr_{0.75}S_3$ based solar cells decreased from 4.35% to 4.18%, 5.37% to 5.18%, 6.28% to 6.08% and 7.35% to 7.15% respectively. The decrement in performance is attributed to the rise in defect states, which hinder the movement of charge carriers and foster recombination within solar cells [114]. Nonetheless, it is essential to recognize that the decrease in performance is negligible, specifically 0.17%, 0.19%, 0.20%, and 0.20% for $BaHfS_3$, $BaHf_{0.75}Zr_{0.25}S_3$, $BaHf_{0.5}Zr_{0.5}S_3$, and $BaHf_{0.25}Zr_{0.75}S_3$-based solar cells, respectively. Based on the analysis, the effect of defect density in the ETL on device performance appears to be insignificant. As a result, a defect density of 10^{16} cm^{-3} has been chosen for subsequent simulations, as it represents an ideal level.

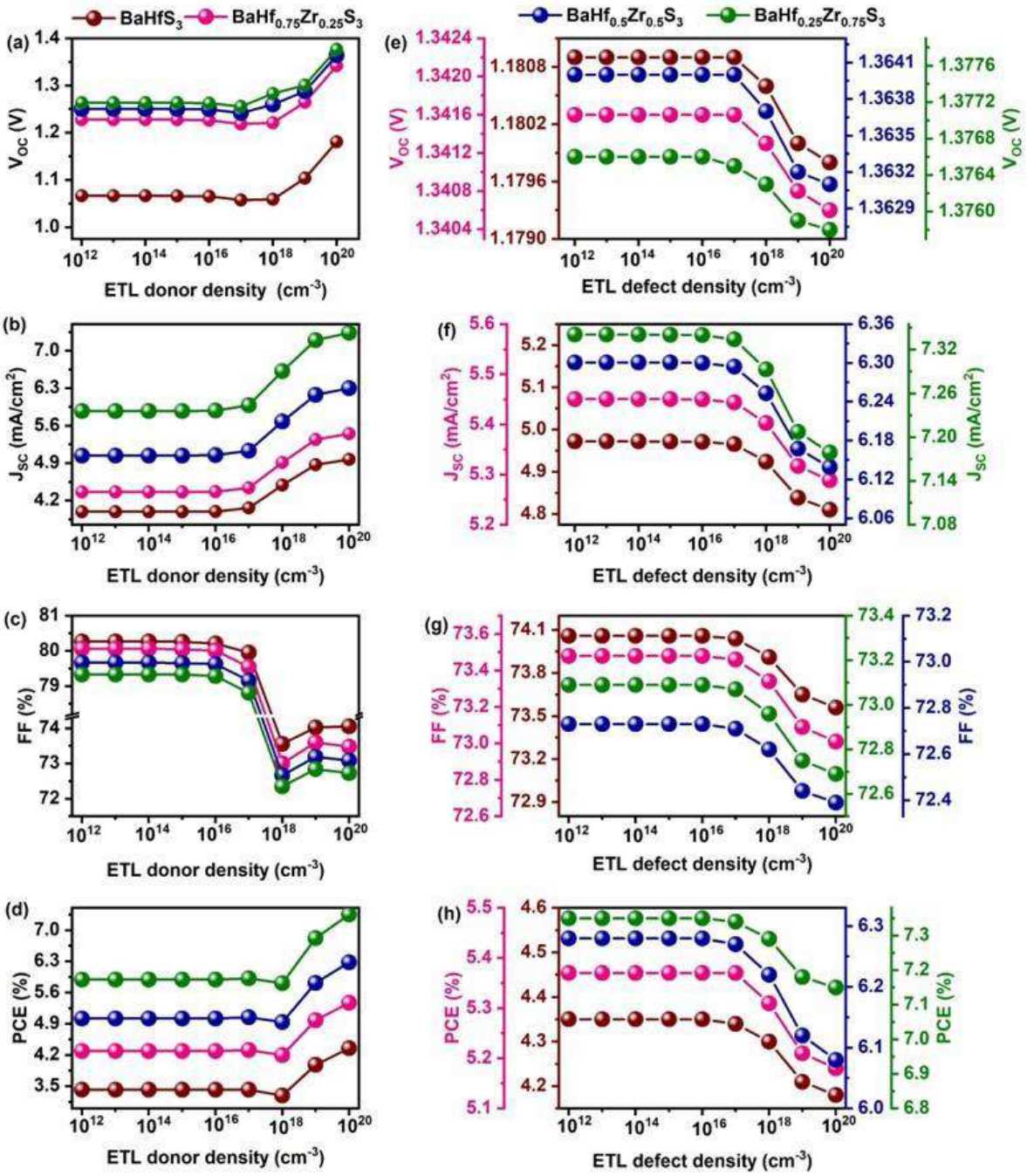

Fig. 44. (a-d) Impact of the ETL donor density on all absorbers, and (e-h) impact of the ETL defect density on all absorbers. The y-axis of (e-h) represents the following: wine for $BaHfS_3$, Pink for $BaHf_{0.75}Zr_{0.25}S_3$, Royal blue for $BaHf_{0.5}Zr_{0.5}S_3$ and Olive for $BaHf_{0.25}Zr_{0.75}S_3$ [44].

6.3.4.2 Impact of TiO_2 ETL affinity and TiO_2 ETL thickness

Modifying the energy band offsets at the ETL/absorber interface is essential for preventing energy barriers and enhancing charge collection in solar cells. To achieve this, we adjusted the electron affinity of TiO_2 from 3.7 eV to 4.1 eV to identify the optimal value for improved electron transport. **Fig. 45**(a-d) illustrates the effect of electron affinity on the PV

parameters. As the results show, V_{OC}, J_{SC}, and PCE decrease with increasing affinity, while FF slightly increases. However, when the affinity exceeds 3.7 eV, PV output deteriorates. It is vital to have a low conduction band offset (CBO) and a high valence band offset (VBO) at the absorbers/TiO_2 interface to capture electrons at the front contact efficiently. Therefore, the CBO and VBO for each affinity value were calculated using **Eqn (19)** and **(20)**, respectively [114,192].

$$CBO = \chi_{ABS} - \chi_{ETL} \quad (19)$$

$$VBO = \chi_{ETL} + E_{G,ETL} - (\chi_{ABS} + E_{G,ABS}) \quad (20)$$

Where χ_{ABS} is the affinity of the absorber, χ_{ETL} is the affinity of ETL, while $E_{G,ABS}$ and $E_{G,ETL}$ are the bandgaps of absorber and ETL, respectively.

Generally, when the absorber's electron affinity is lower than that of the ETL, a negative CBO results, indicating cliff formation. Conversely, a positive CBO is observed when the affinity is larger than the ETL's, resulting in spike formation at the interface. For a considerable period, it has been widely believed that the cliff-like barrier at the absorber/ETL interface is advantageous for fabricated devices. This is because cliffs facilitate the extraction and accumulation of charge carriers without limitations, whereas spikes create barriers that restrict charge movement. However, recent discoveries indicate that, in certain instances, a significant cliff-like barrier can Pb to a buildup of charge carriers at the interface due to a weak potential barrier. This buildup enhances interfacial recombination, ultimately impacting the performance. The essential barrier (either spike or cliff) at the absorber/ETL interface vary significantly depending on the specific material system used, as illustrated in various studies [114]. Based on the data presented in **Table 14**, the optimal CBO values for $BaHfS_3$, $BaHf_{0.75}Zr_{0.25}S_3$, $BaHf_{0.5}Zr_{0.5}S_3$, and $BaHf_{0.25}Zr_{0.75}S_3$ solar cells are -0.7 eV, -0.6 eV, -0.5 eV, and -0.4 eV, respectively. Additionally, the optimal VBO values for these materials are 1.84 eV, 1.78 eV, 1.76 eV, and 1.75 eV, respectively. Therefore, based on these results, an electron affinity value of 3.7 eV is appropriate for further studies.

Table 14. The electron affinity of TiO_2, with corresponding CBO and VBO at various $BaHf_{1-x}Zr_xS_3$ absorbers. Optimum values are denoted in [bold] [44].

TiO_2 affinity (eV)	$BaHfS_3$		$BaHf_{0.75}Zr_{0.25}S_3$		$BaHf_{0.5}Zr_{0.5}S_3$		$BaHf_{0.25}Zr_{0.75}S_3$	
	CBO (eV)	VBO (eV)	CBO (eV)	VBO (eV)	CBO (eV)	VBO (eV)	CBO (eV)	VBO (eV)
3.7	**-0.7**	**1.84**	**-0.6**	**1.78**	**-0.5**	**1.76**	**-0.4**	**1.75**
3.8	-0.8	1.94	-0.7	1.88	-0.6	1.86	RR	1.85
3.9	-0.9	2.04	-0.8	1.98	-0.7	1.96	-0.6	1.95
4.0	-1	2.14	-0.9	2.08	-0.8	2.06	-0.7	2.05
4.1	-1.1	2.24	-1	2.18	-0.9	2.16	-0.8	2.15

The thickness of the ETL is crucial for effective electron transport, enhanced light transmission, and prevention of recombination within the solar cell. To investigate this, we varied the ETL thickness from 10 nm to 150 nm and analyzed its impact on PVparameters, as shown in **Fig. 45**(e-h). The results indicate a slight increase in all PVparameters for all four absorbers. Generally, maintaining a thinner n-type layer compared to the p-type layer is prematurely preventing them from being converted into electro-hole pairs and separated by the V_B. Additionally, a thicker ETL can partially absorb light, slowing down charge generation and collection, which leads to absorption loss and reduced transmittance [39,192]. Therefore, for further studies, an optimal ETL thickness of 30 nm is chosen for $BaHfS_3$, $BaHf_{0.75}Zr_{0.25}S_3$, $BaHf_{0.5}Zr_{0.5}S_3$, $BaHf_{0.25}Zr_{0.75}S_3$.

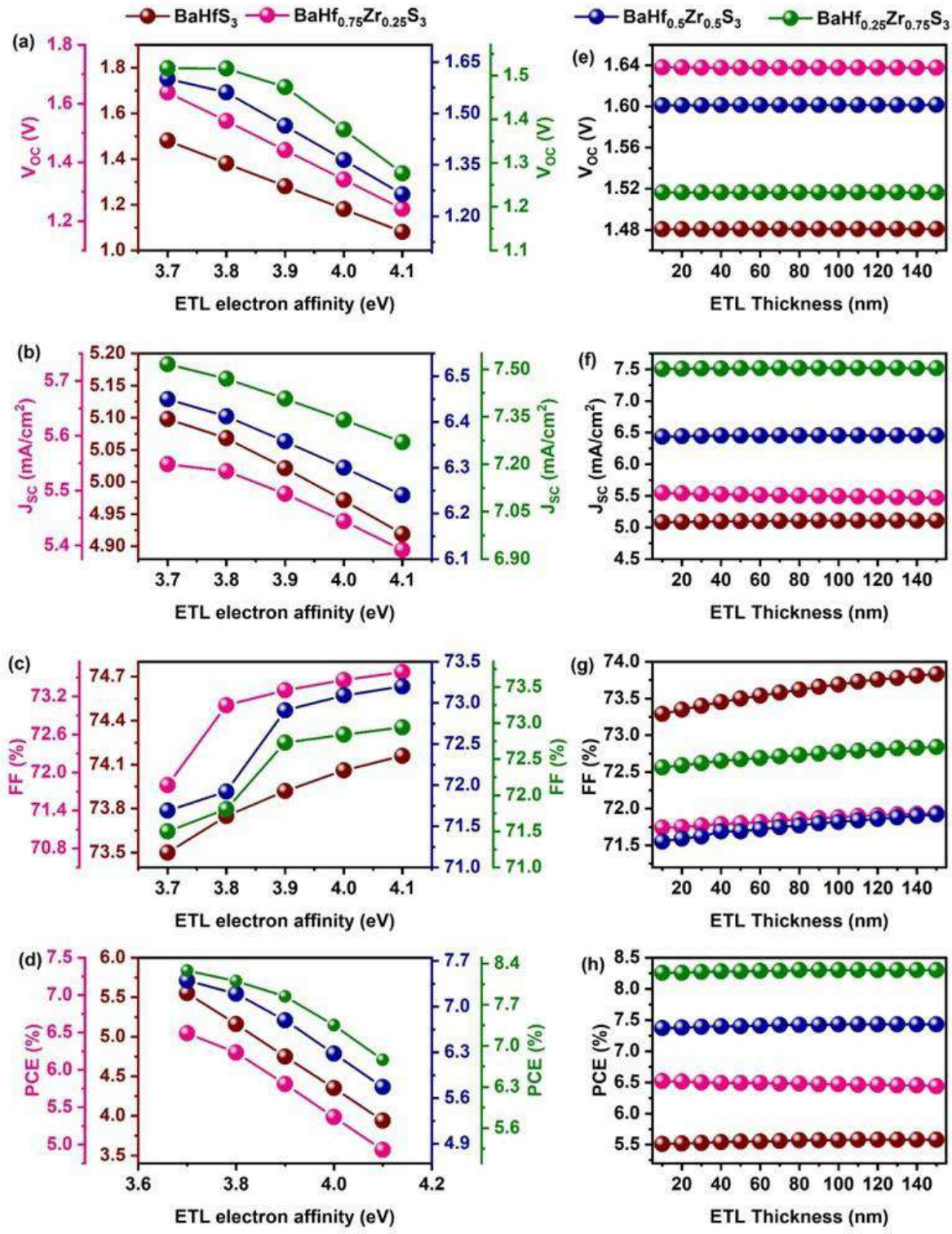

Fig. 45. Performance of TiO_2 (a-d) affinity varied with different $BaHf_{1-x}Zr_xS_3$ absorbers and (e-h) thickness varied with different $BaHf_{1-x}Zr_xS_3$ absorbers [44].

6.3.5 Influence of different $BaHf_{1-x}Zr_xS_3$ absorbers with TiO_2 ETL and NiO HTL

6.3.5.1 Impact of absorber's acceptor density and absorber's defect density

The acceptor density of the absorber is a crucial factor in determining the charge transport and stability of solar cells [221]. An increased acceptor density can result in a higher risk of auger recombination, which may hinder the movement of holes by causing significant recombination and impurity scattering within the absorber. Therefore, optimizing the acceptor density of the absorber is essential to attain enhanced performance in solar cells [114]. In our research, we modified the acceptor density of $BaHfS_3$, $BaHf_{0.75}Zr_{0.25}S_3$, $BaHf_{0.5}Zr_{0.5}S_3$, and $BaHf_{0.25}Zr_{0.75}S_3$ based absorbers from 10^{12} cm^{-3} to 10^{18} cm^{-3}, as illustrated in **Fig. 47**(a-d). It can be observed that the V_{OC} and FF remain the same up to 10^{14} cm^{-3} and then significantly increase afterward. The advancement can be attributed to the enhanced intrinsic capacity, which allows for efficient extraction and accumulation of the produced carriers at the contacts without reuniting with one another. Increasing the acceptor density in the absorber affects the energy band alignments and raises the quasi-Fermi level splitting, which leads to a higher V_{OC} and improved overall performance. To investigate these effects, energy band diagrams were generated using SCAPS-1D for acceptor densities ranging from 10^{12} cm^{-3} to 10^{18} cm^{-3} (**Fig. 47**(e-h). As the acceptor density increases, the energy bands of all layers shift upward, bringing the valence band of the absorber closer to the hole quasi-Fermi level [113]. Additionally, the electric field at the absorber/HTL interface becomes stronger as the acceptor density increases [114]. However, it is noteworthy that the J_{SC} decreases when the acceptor density exceeds 10^{16} cm^{-3}. This decline occurs because, at carrier concentrations higher than an optimal range, recombination rates increase, leading to lower J_{SC} values. This trend is illustrated in **Fig. 47**(i-l), which shows significant recombination occurring when carrier concentration exceeds 10^{16} cm^{-3}. The results show that the increase in acceptor density of $BaHf_{1-x}Zr_xS_3$ significantly affects the position of the energy bands and enhances the V_B and electric field, ultimately resulting in an improvement in the PCE values. Specifically, the PCE values increased from 5.53% to 7.93%, 6.50% to 8.60%, 7.39% to 9.80%, and 8.27% to 10.71% for $BaHfS_3$, $BaHf_{0.75}Zr_{0.25}S_3$, $BaHf_{0.5}Zr_{0.5}S_3$, and $BaHf_{0.25}Zr_{0.75}S_3$ based solar cells, respectively. These findings suggest that an acceptor density of 10^{16} cm^{-3} is the ideal value for further simulations.

Structural irregularities, non-stoichiometry, impurities, and fabrication techniques are common sources of defects in solar cells [51]. Therefore, managing these absorber defects is essential for achieving high efficiency. To investigate their impact, we altered the absorber's defect density from the range of 10^{12} cm^{-3} to 10^{20} cm^{-3} in all solar cells. **Fig. 48**(a-d) illustrates

how PV parameters change with respect to the defect density of the absorber. It is important to note that all PV parameter values significantly decrease as defect density increases. Specifically, when the defect density rises from 10^{12} cm^{-3} to 10^{20} cm^{-3}, solar cell performance declines sharply. The PCE drops from 11.41%, 12.07%, 13.63%, and 14.81% to just 0.11%, 0.08%, 0.23%, and 0.09% for the compositions of $BaHfS_3$, $BaHf_{0.75}Zr_{0.25}S_3$, $BaHf_{0.5}Zr_{0.5}S_3$, and $BaHf_{0.25}Zr_{0.75}S_3$, respectively. In parallel, their respective FF decreases from 89.09%, 88.65%, 88.54%, and 88.72% to 84.43%, 84.25%, 84.02%, and 83.95%. This dramatic decrease in performance is attributed to the increased number of recombination centers, as shown in **Fig. 48**(e-h), which ultimately leads to a reduction in both the diffusion length and the lifetime of the solar cells [114]. Additionally, as defect density rises, the electric field at the absorber/HTL interface decreases [39]. This reduction hinders the separation and collection of holes from the absorber to the back contact, adversely affecting solar cell performance. Therefore, for further simulations, a defect density of 10^{12} cm^{-3} has been chosen as the optimal level for all solar cells.

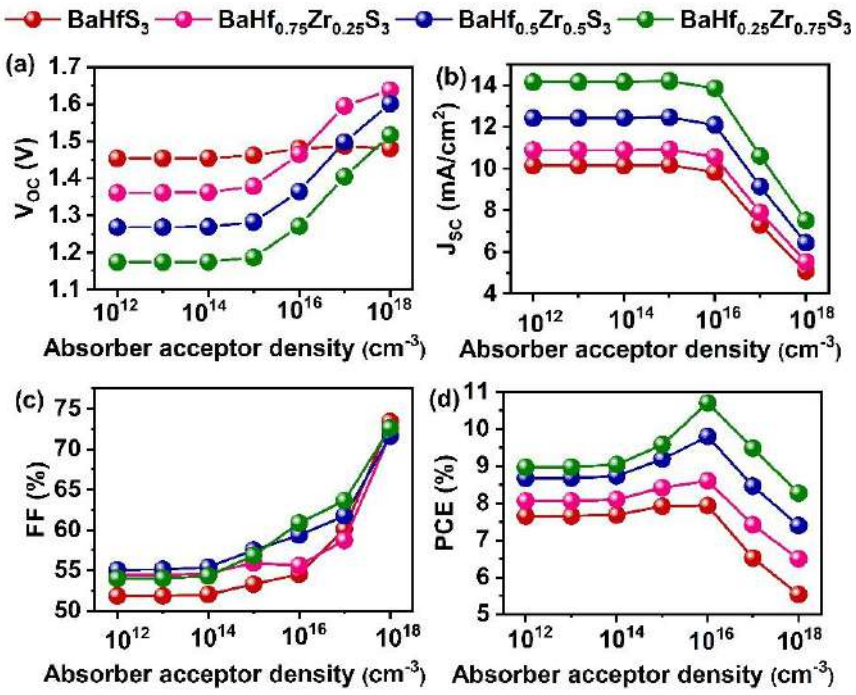

Fig. 46. Effect of absorber acceptor density on (a-d) photovoltaic performance

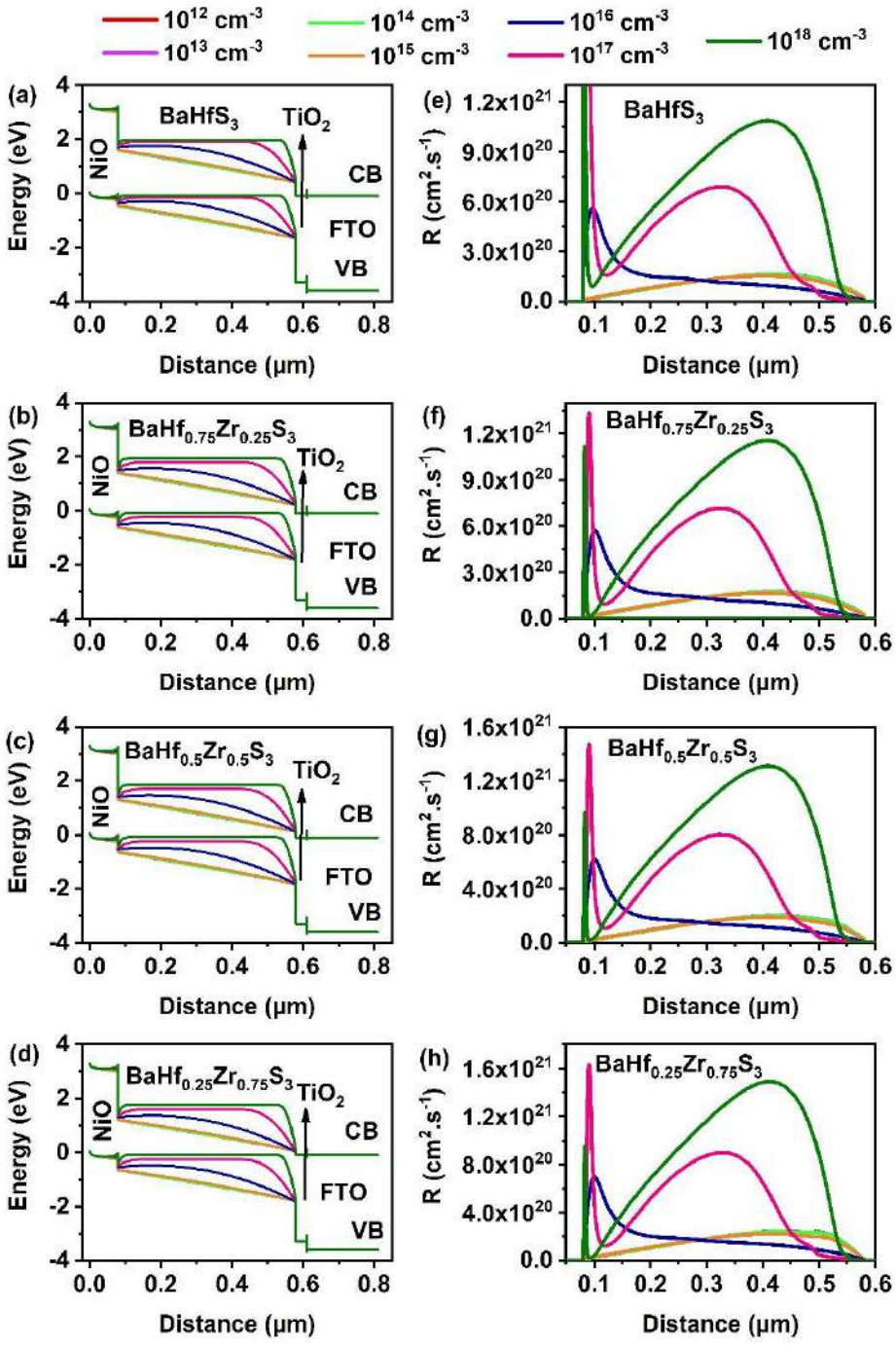

Fig. 47. Effect of absorber acceptor density on (a-d) photovoltaic performance (e-h) energy band alignment and (i-l) recombination rate [44].

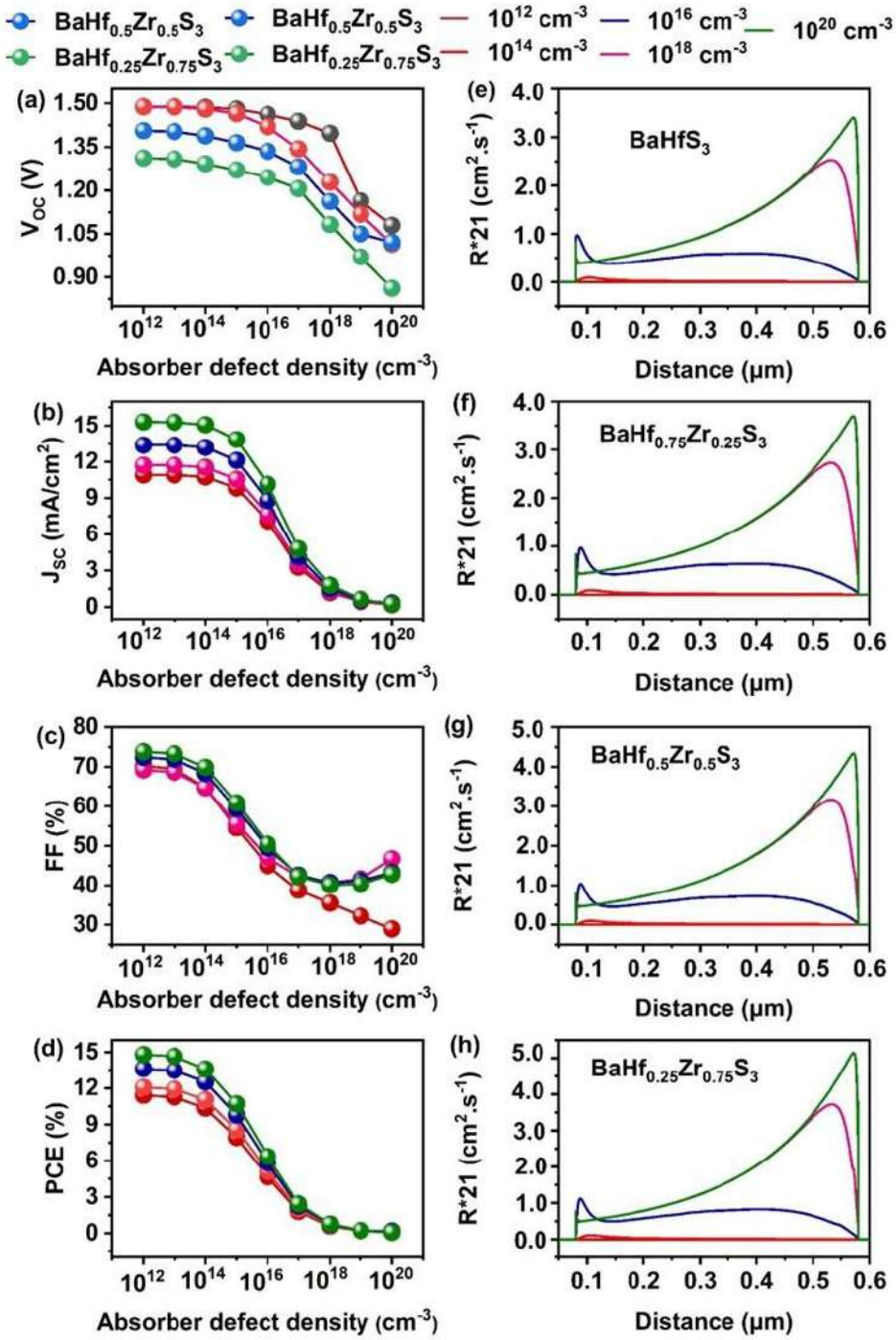

Fig. 48. Effect of absorber defect density on (a-d) photovoltaic performance and (e-h) recombination rate [44].

6.3.5.2 Impact of absorber's thickness

The absorber's thickness plays a crucial role in the solar cell performance [39,114]. To determine the optimal thickness for $BaHfS_3$, $BaHf_{0.75}Zr_{0.25}S_3$, $BaHf_{0.5}Zr_{0.5}S_3$, and $BaHf_{0.25}Zr_{0.75}S_3$-based absorbers, it was altered from 100 nm to 2000 nm. **Fig. 49**(a-d) illustrates the changes in PV parameters with respect to the thickness of the absorber. As the

thickness of the absorber increases from 100 nm to 2000 nm, J_{SC} shows a significant increase from 4.68 mA/cm^2, 5.02 mA/cm^2, 5.86 mA/cm^2, and 6.85 mA/cm^2 to 12.83 mA/cm^2, 13.85 mA/cm^2, 15.50 mA/cm^2, and 17.52 mA/cm^2 for $BaHfS_3$, $BaHf_{0.75}Zr_{0.25}S_3$, $BaHf_{0.5}Zr_{0.5}S_3$, and $BaHf_{0.25}Zr_{0.75}S_3$-based absorbers, respectively. This increase in J_{SC} enhances the spectral response at longer wavelengths, leading to a rise in PCE from 5.46% to 14.67%, 6.13% to 16.43%, 7.27% to 18.62%, and 8.56% to 20.59% for the respective absorbers. The data presented in **Fig. 49**(e-h) also indicate that the absorption rate is directly related to the thickness of the solar cells [222]. Specifically, the absorption rate increases by 23.8%, 26.1%, 27.8%, and 30.3% for $BaHfS_3$, $BaHf_{0.75}Zr_{0.25}S_3$, $BaHf_{0.5}Zr_{0.5}S_3$, and $BaHf_{0.25}Zr_{0.75}S_3$-based absorbers, respectively, when the solar cell thickness is raised from 100 nm to 2000 nm. These findings imply that increasing the thickness of the solar cells leads to a significant improvement in their absorption rates [223]. A thin absorber layer absorbs less light, transmitting a significant portion, which results in substantial absorption near the HTL. This elevates the accumulation and recombination of charge carriers, leading to suboptimal generation of charge carriers [223]. As the absorber thickness increases, the rate of photon absorption improves, resulting in increased charge carrier generation and lower accumulation. Consequently, the overall performance improves significantly. However, beyond a specific thickness, PCE saturation occurs. Specifically, increasing the thickness from 100 nm to 800 nm, 100 nm to 1200 nm, 100 nm to 1300 nm, and 100 nm to 1200 nm results in PCE increase of approximately 8.59%, 9.88%, 10.96%, and 12.03% for $BaHfS_3$, $BaHf_{0.75}Zr_{0.25}S_3$, $BaHf_{0.5}Zr_{0.5}S_3$, and $BaHf_{0.25}Zr_{0.75}S_3$-based solar cells, respectively. However, further increasing the thickness to 1500 nm only yields an approximately 0.5% increase in PCE. Solar cell performance is affected by absorber thickness exceeding a certain threshold leads to charge carrier recombination due to insufficient diffusion lengths, resulting in saturated performance [224,225]. The V_{OC} for all solar cells improves up to 400 nm and then stabilizes, attributed to enhanced quasi-Fermi level splitting and an increased number of charge carriers. However, V_{OC} saturation is due to the increased rate of recombination and dark saturation current with rising thickness [226]. Additionally, FF decreases with increasing thickness due to improved R_S in thicker absorbers. Considering charge carrier generation and overall manufacturing costs, optimal absorber thicknesses for $BaHfS_3$, $BaHf_{0.75}Zr_{0.25}S_3$, $BaHf_{0.5}Zr_{0.5}S_3$, and $BaHf_{0.25}Zr_{0.75}S_3$ in this simulation are determined to be 800 nm, 1200 nm, 1300 nm, and 1200 nm, respectively.

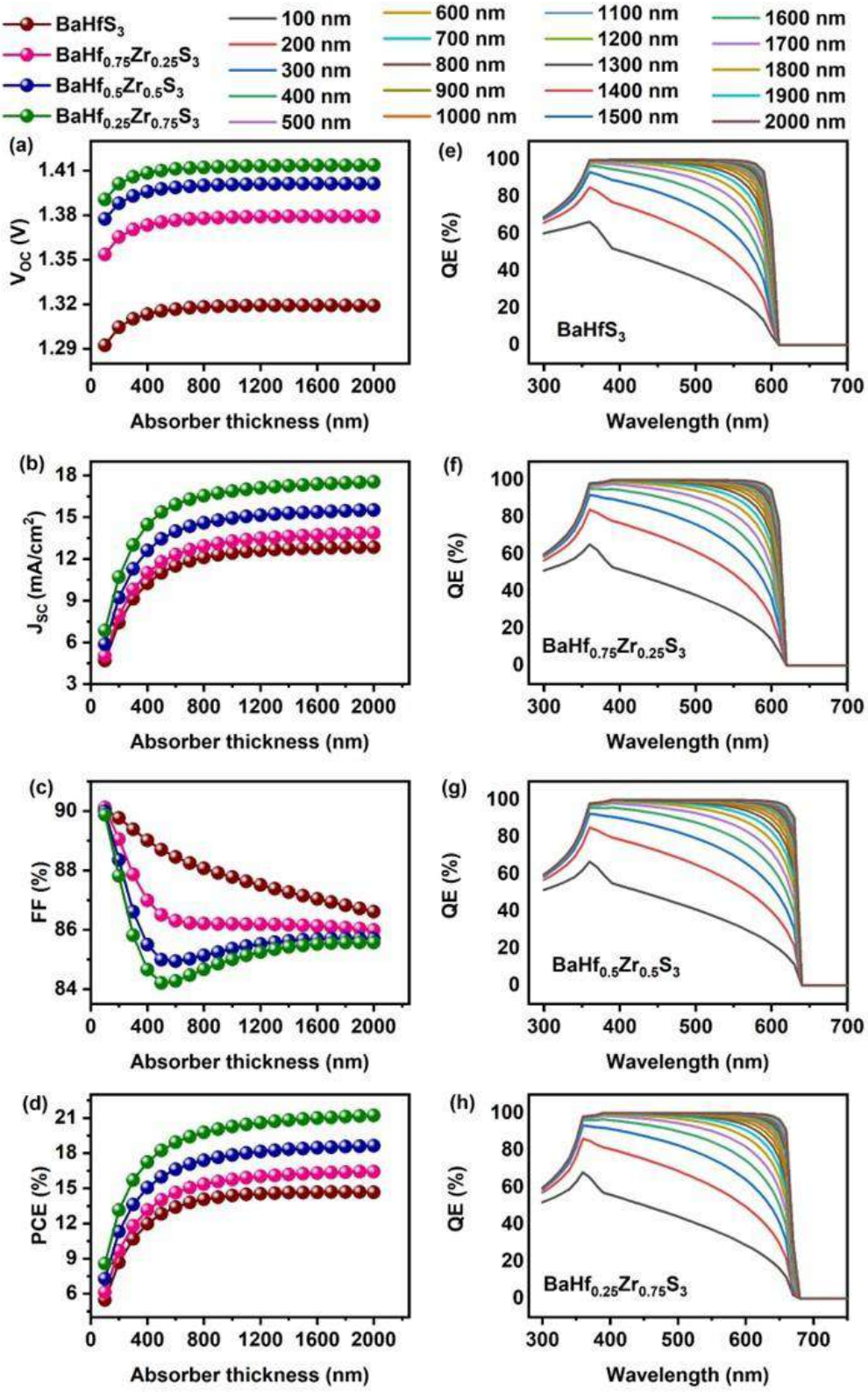

Fig. 49. Effect of absorber's thickness on (a-d) photovoltaic performance and (e-h) QE measurements [44].

6.3.6 Impact of NiO HTL's electron affinity and NiO HTL's acceptor density

The HTL's electron affinity is a primary aspect determining the VBO and CBO at the absorber/HTL interface. Enhancing the HTL's electron affinity is crucial in reducing energy barriers of charge carriers [114]. Consequently, we varied the electron affinity of NiO from 1.6 eV to 2.0 eV to determine the optimal value for enhanced hole transport. **Fig. 50**(a-d) illustrates the corresponding variations in PV parameters. PV parameters display an upward behavior with escalating affinity values. Generally, a high CBO and low VBO at the absorber/HTL interface are necessary, indicating a significant barrier for electrons and a lesser barrier for holes. The CBO and VBO for each affinity value are calculated using the following **Eqn (21)** and **(22)**, which restrict electron movement and promote hole transport through the HTL:

$$CBO = \chi_{\mathrm{ABS}} - \chi_{\mathrm{HTL}} \qquad (21)$$

$$VBO = \chi_{HTL} + E_{G,HTL} - (\chi_{ABS} + E_{G,ABS}) \qquad (22)$$

Where χ_{ABS} is the affinity of the absorber, χ_{HTL} is the affinity of HTL while $E_{G,ABS}$ and $E_{G,HTL}$ are the bandgaps of absorber and HTL, respectively. The CBO and VBO values for all devices, as calculated, are displayed in **Table 15**.

Examining the NiO/absorber interface, the VBO displays both positive and negative values, corresponding to variations in the absorber's electron affinity. A positive VBO creates a barrier at the NiO/absorber interface, impeding hole movement from the absorber to NiO. Conversely, a negative VBO creates a cliff-like obstacle that enhances hole accumulation at the back contact. However, a significant cliff increases hole concentration in NiO, leading to enhanced recombination at the rear contact, negatively impacting solar cell performance. Therefore, determining the optimal VBO and CBO values is crucial for improving solar cell performance [114]. If the affinity values drop below 2.0 eV, the efficiency of the solar cells for all absorbers is negatively impacted. Based on the findings in **Table 15**, the optimal VBO values for $BaHfS_3$, $BaHf_{0.75}Zr_{0.25}S_3$, $BaHf_{0.5}Zr_{0.5}S_3$, and $BaHf_{0.25}Zr_{0.75}S_3$-based solar cells are 1.0 eV, 1.1 eV, 1.2 eV, and 1.3 eV, respectively. Additionally, the optimum CBO values are 0.19 eV, 0.13 eV, 0.11 eV, and 0.1 eV for these same solar cell systems. As a result, we suggest selecting an affinity value of 2.0 eV for further research.

Table 15. The electron affinity of NiO, with corresponding CBO and VBO at absorber/HTL interface of various $BaHf_{1-x}Zr_xS_3$ absorbers. Optimum values are denoted in [bold] [44].

NiO affinity (eV)	$BaHfS_3$		$BaHf_{0.75}Zr_{0.25}S_3$		$BaHf_{0.5}Zr_{0.5}S_3$		$BaHf_{0.25}Zr_{0.75}S_3$	
	CBO (eV)	VBO (eV)	CBO (eV)	VBO (eV)	CBO (eV)	VBO (eV)	CBO (eV)	VBO (eV)
1.6	1.4	-0.21	1.5	-0.27	1.6	-0.29	1.7	-0.3
1.7	1.3	-0.11	1.4	-0.17	1.5	-0.19	1.6	-0.2
1.8	1.2	-0.01	1.3	-0.07	1.4	-0.09	1.5	-0.1
1.9	1.1	0.09	1.2	0.03	1.3	0.01	1.4	0
2.0	**1.0**	**0.19**	**1.1**	**0.13**	**1.2**	**0.11**	**1.3**	**0.1**

The role of acceptor density in the HTL significantly influences the interface characteristics between the absorber and the HTL [39]. To examine this parameter's effect on the performance of solar cells, we adjusted the acceptor density of the HTL to various levels, ranging from 10^{12} cm^{-3} to 10^{20} cm^{-3}, as illustrated in **Fig. 50**(e-h). The results indicate a minimal increase in V_{OC}, J_{SC}, and PCE, along with the escalation in acceptor density. In contrast, the FF remains constant up to a density of 10^{15} cm^{-3} and then increases significantly beyond that point. Generally, the enhancement in the electric field along the HTL region with increasing carrier concentration elevates the movement of holes from the absorber to the contact due to the intense electric field at the interface [219]. Furthermore, as the HTL carrier density rises, the V_B also increases, facilitating the collection and separation of charges. This reduces the recombination rate and enhances device performance. Increasing the HTL's carrier concentration can lower the barrier for holes and raise the barrier for electrons by shifting the respective bands upwards. The acceptor density of 10^{18} cm^{-3} in NiO is essential for achieving optimal solar cell performance, which is why it is maintained at this level for subsequent simulations.

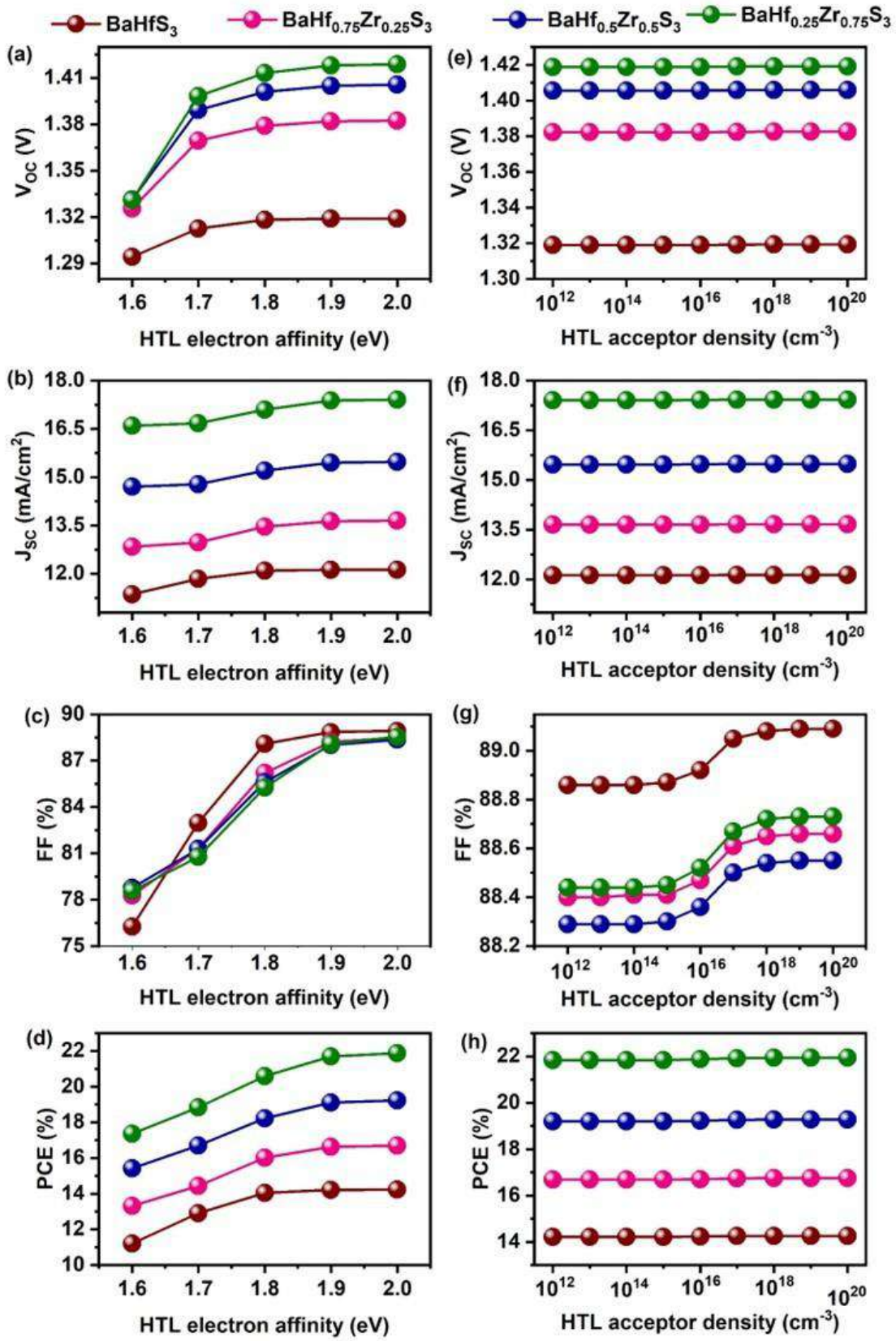

Fig. 50. The performance of HTL with all absorbers (a-d) electron affinity and **(**e-h) acceptor density [44].

6.3.7 Impact of back metal work function behaviors

The optimization of back contacts is critical in ensuring ohmic contact and effective hole transport, as well as enhancing the V_b in solar cells. Metals such as Cu/Mo, Ag, Fe, Cu-doped C, Au, W, Ni, Pd, and Pt, with work functions of 4.6 eV, 4.7 eV, 4.8 eV, 5.0 eV, 5.1 eV, 5.22 eV, 5.5 eV, 5.6 eV, and 5.7 eV, respectively, are employed in the proposed solar cell structure to identify the most suitable back metal contact [39]. The PV parameters of V_{OC}, J_{SC}, FF, and PCE are illustrated in **Fig. 51**(a-d) as functions of the metalwork function. It is evident that these parameters increase up to a metalwork function of 5.0 eV for all absorbers and then stabilize beyond this point. In general, when the work function is low, the metal's Fermi level is positioned near the interface of the HTL, leading to the significant barrier known as a Schottky barrier, which hinders hole flow from the HTL to the metal contact. Additionally, the low electron barrier facilitates rapid electron transfer between the HTL conduction band and the metal contact, leading to a high recombination rate in the solar cells. Conversely, with a higher work function, the Fermi level aligns closer to the valence band (E_V) of the HTL, reducing the hole barrier and enhancing hole transport to the metal contact [114]. The improved performance of solar cells with higher work functions can be attributed to the shift of the metal's Fermi level towards the HTL's valence band. The highest PCE values of 14.26%, 16.75%, 19.28%, and 21.94% for $BaHfS_3$, $BaHf_{0.75}Zr_{0.25}S_3$, $BaHf_{0.5}Zr_{0.5}S_3$, and $BaHf_{0.25}Zr_{0.75}S_3$-based solar cells are achieved using Cu-doped C, Au, W, Ni, Pd, and Pt work functions. These materials form ohmic contacts at the HTL/back metal interface, efficiently transporting holes while presenting a Schottky barrier to electrons. The saturation of PV parameters beyond a work function of 5.0 eV is due to increasing ohmic resistance at the HTL/back metal contact interface. Given Ni has a relatively lower material cost than other contacts, it is proposed as a suitable contact for future investigations.

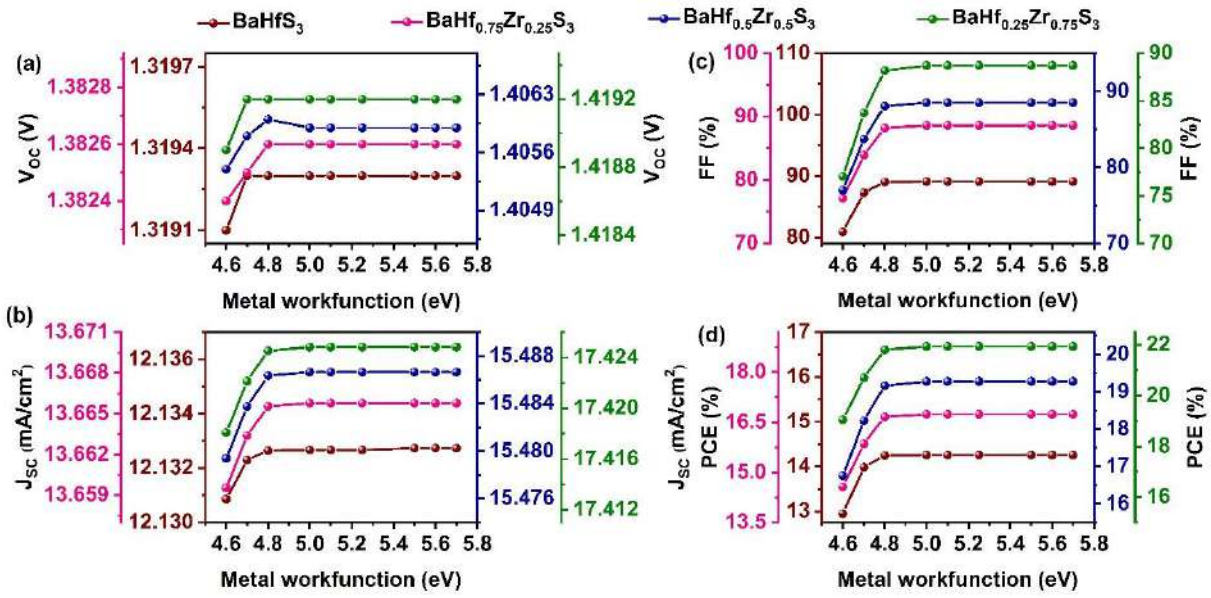

Fig. 51. The effect of back metal work function on (a) V_{OC} (V) (b) J_{SC} (mA/cm^2) (c) FF (%) and (d) PCE (%) [44].

6.3.8. Study of defect density at ETL/Absorbers and Absorbers/HTL interface

The fabrication of solar cells inevitably results in interface defects due to structural imperfections, which enhance charge carrier recombination at the interface and significantly affect solar cell performance [39]. Consequently, it is important to examine the impact of interface defects and determine the optimal defect density for experimental fabrication. In this work, a neutral interface defect density of 10^{12} cm^{-3} was employed at the ETL/absorber and absorber/HTL interfaces for all solar cells. To investigate the effects of interface defects on the PV characteristics, the defect density was altered from 10^{12} cm^{-3} to 10^{20} cm^{-3} at the ETL/absorber interface and from 10^{10} cm^{-3} to 10^{20} cm^{-3} at the absorber/HTL interface. As illustrated in **Fig. 52**(a-d), V_{OC} decreases significantly as the interface defects increase from 10^{12} cm^{-3} to 10^{20} cm^{-3}, while J_{SC} remains unchanged up to 10^{14} cm^{-3} and then decreases. However, the FF decreased abruptly from 89.09%, 88.65%, 88.54%, and 88.72% to 84.43%, 84.25%, 84.02%, and 83.95% for $BaHfS_3$, $BaHf_{0.75}Zr_{0.25}S_3$, $BaHf_{0.5}Zr_{0.5}S_3$, and $BaHf_{0.25}Zr_{0.75}S_3$-based solar cells, respectively. This results in a significant reduction in the PCE, indicating that the FF largely determines the overall solar cell performance at the ETL/absorber interface. The PCE degradation was observed to be approximately 2.94%, 3.94%, 3.75%, and 4.29% for $BaHfS_3$, $BaHf_{0.75}Zr_{0.25}S_3$, $BaHf_{0.5}Zr_{0.5}S_3$, and $BaHf_{0.25}Zr_{0.75}S_3$-based solar cells, respectively. This reduction is primarily attributed to the increased trap-assisted recombination at the ETL/absorber interface, which is a critical factor contributing to

the performance degradation [227]. Trap-assisted recombination occurs when charge carriers, such as electrons and holes, are captured by defect states, or traps, present at the interface [228]. These trapped carriers recombine before they can contribute to the photocurrent. The presence of these trap states enhances the recombination rate, significantly reducing the number of free charge carriers available for collection, which directly leads to a noticeable decrease in the PCE of the solar cells [229]. Minimizing these interface defects is, therefore, essential to improving the overall performance and efficiency of the devices. Therefore, an ideal defect density of 10^{12} cm^{-3} is recommended for superior performance in $BaHfS_3$, $BaHf_{0.75}Zr_{0.25}S_3$, $BaHf_{0.5}Zr_{0.5}S_3$, and $BaHf_{0.25}Zr_{0.75}S_3$-based solar cells. We examined the absorber/HTL interface defect density by varying it from 10^{10} to 10^{20} cm^{-3} as shown in **Fig. 52**(e-h). It was observed that V_{OC} and J_{SC} of $BaHfS_3$ are almost constant for the entire absorber/HTL defects, while Zr-substituted $BaHfS_3$ remained stable up to 10^{14} cm^{-3} with negligible reductions beyond that. The minimal change in V_{OC} is primarily due to its dependence on the quasi-Fermi levels of electrons and holes, where interface defects mainly cause local trapping and minor recombination rather than a significant loss of photogenerated carriers [196]. Similarly, the J_{SC} remains steady due to the unaffected photon absorption and carrier generation in the absorber respective to the absorber/HTL defects [230]. Considering FF, it remained unchanged up to 10^{14} cm^{-3} in $BaHfS_3$, with only a slight decrement thereafter. This minimal impact can be attributed to the near-optimal band alignment between $BaHfS_3$ and the HTL, which ensures a low energy barrier for carrier transport, making the devices less sensitive to interface defects [114]. Additionally, the high-quality interface between $BaHfS_3$ and the HTL facilitates efficient charge transfer, thereby reducing recombination losses, which may Pb to negligible changes of FF concerning the absorber/HTL interface. On the flip side, FF exhibited a significant decline from 10^{14} to 10^{16} cm^{-3} in Zr-substituted $BaHfS_3$, attributed to rapidly increasing recombination and charge transport issues at the HTL/absorber interface [231]. Beyond 10^{16} cm^{-3}, recombination effects saturate, and bulk absorber properties take precedence, leading to only insignificant changes in FF. This is evidenced in **Fig. 53,** where recombination rate as a function of absorber/HTL interface defects is extracted for all absorbers. It can be noted that the recombination rate is constant across all defect densities for $BaHfS_3$, leading to a negligible change in FF [232]. Contrarily, for Zr-alloyed $BaHfS_3$, the recombination rate is significantly elevated for the defect range of 10^{14} to 10^{16} cm^{-3}, resulting in considerable decrement in FF. While it is almost unaltered beyond 10^{16} cm^{-3} which has led to the saturated FF. On the whole, the PCE decreased from 14.26%, 16.75%, 19.28%, and 21.94% to 14.11%, 15.58%, 18.04%, and 20.50% for $BaHfS_3$, $BaHf_{0.75}Zr_{0.25}S_3$, $BaHf_{0.5}Zr_{0.5}S_3$, and $BaHf_{0.25}Zr_{0.75}S_3$-based solar cells, respectively.

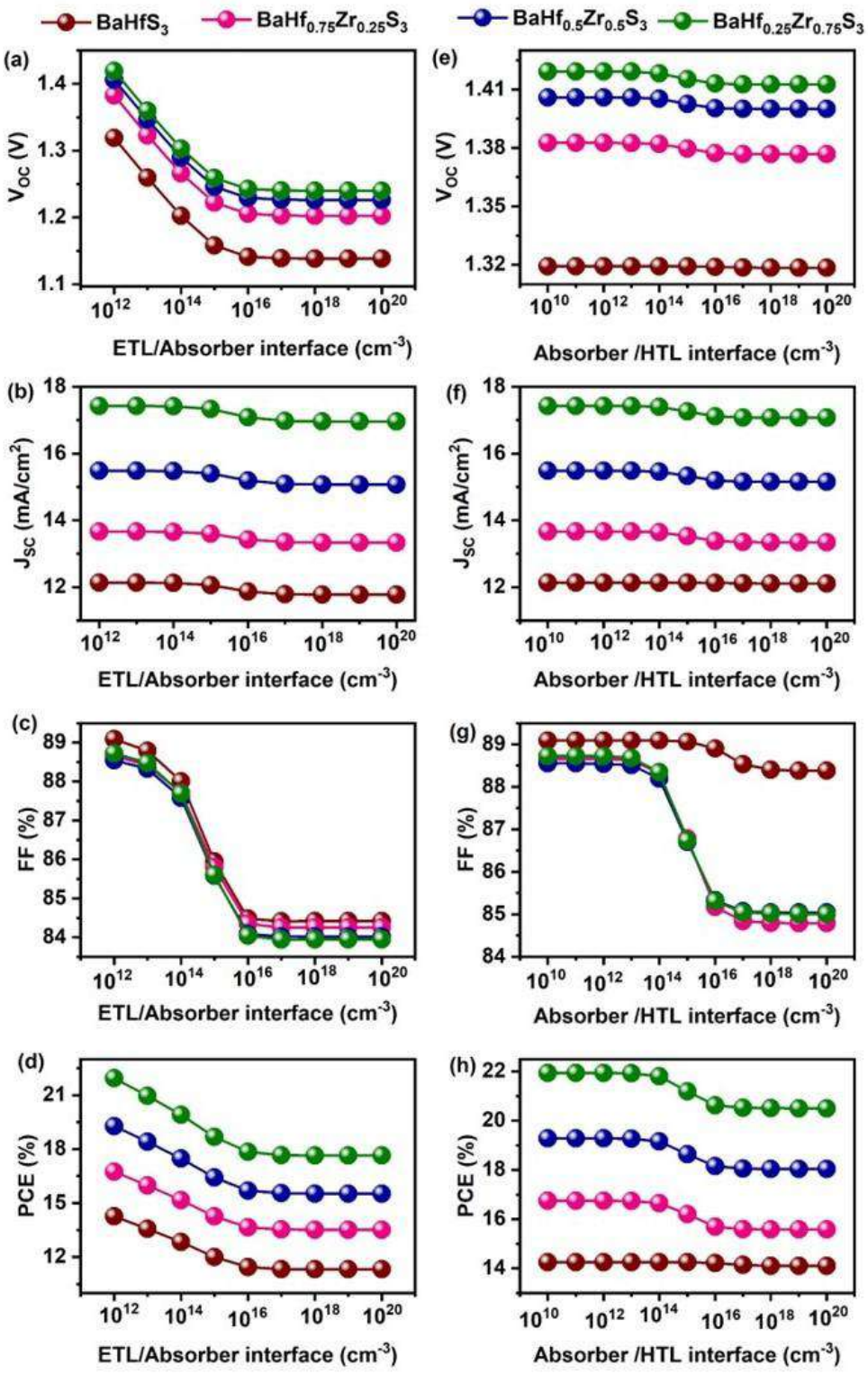

Fig. 52. Changes in photovoltaic performance relative to (a-d) ETL/ absorber interface defects and (e-h) Absorber/HTL interface defects for all solar cells [44].

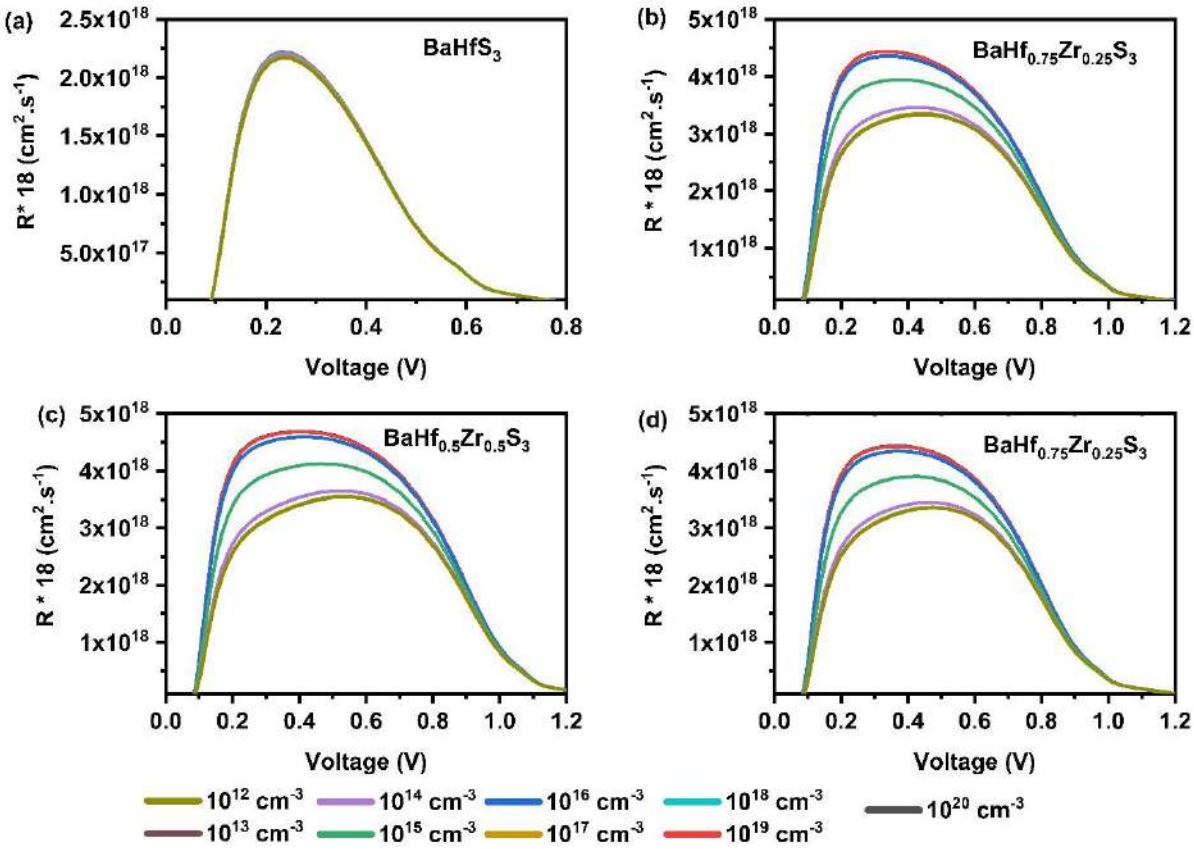

Fig. 53. Recombination rate of charge carriers as a function of absorber/HTL interface (a) $BaHfS_3$ (b) $BaHf_{0.75}Zr_{0.25}S_3$ (c) $BaHf_{0.5}Zr_{0.5}S_3$ and (d) $BaHf_{0.25}Zr_{0.75}S_3$ [44].

6.3.9 Study of R_S, R_{Sh}, and operating temperature

The efficiency of solar cells is significantly impacted by two primary factors: R_S and R_{Sh}. R_S refers to the resistance that occurs between metal contacts, transport layers, and the absorber's resistance outside the space charge region. Increasing R_S in solar cells can Pb to a higher power loss, which can result in a reduction in overall PCE. This occurs because a portion of the current is lost as heat rather than being converted into usable electrical energy. To examine the impact of R_S on $BaHfS_3$, $BaHf_{0.75}Zr_{0.25}S_3$, $BaHf_{0.5}Zr_{0.5}S_3$, and $BaHf_{0.25}Zr_{0.75}S_3$ based solar cells, we varied R_S from 1 to 10 Ω cm^2, as shown in **Fig. 54**(a-d). The results indicate that while V_{OC} and J_{SC} remain constant across the spectrum, FF decreases from 88.22%, 87.22%, 87.51%, and 87.57% for $BaHfS_3$, $BaHf_{0.75}Zr_{0.25}S_3$, $BaHf_{0.5}Zr_{0.5}S_3$ and $BaHf_{0.25}Zr_{0.75}S_3$ based solar cells, respectively, to 80.46%, 79.46%, 78.31% and 77.26%. This decline in FF is caused by the significant power loss (P_{loss}) that occurs within the solar cells for high RS values, as described by **Eqn** (23)

$$P_{loss} = I_{sc}^2 R_S \quad (23)$$

The relationship between P_{loss} and R_S is directly proportional, as indicated by the aforementioned equation [39]. As a result, an increase in R_S leads to a higher P_{loss}, which in turn reduces the PCE from 14.12% to 12.88%, 16.57% to 15.01%, 19.05% to 17.05% and 21.65% to 19.10% in $BaHfS_3$, $BaHf_{0.75}Zr_{0.25}S_3$, $BaHf_{0.5}Zr_{0.5}S_3$, and $BaHf_{0.25}Zr_{0.75}S_3$ based solar cells, respectively. To achieve efficient operation in solar cells, an ideal R_S of 1 Ω cm^2 is selected. On the other hand, R_{Sh} is primarily caused by factors such as interface barriers, charge-accumulating interlayers, metal-based electrodes, defects, or impurities, which effectively create reverse saturation current in solar cells [233]. Conversely, leakage channels, such as pinholes in the absorber and recombination losses, contribute to R_{Sh}. The Schockley equation, represented in **Eqn (24)** and **(25)**, describes the anticipated performance of a solar cell's J-V characteristics under optimal one-sun illumination conditions.

$$J_{SC} = J_{PH} - J_0 \left[\exp\left(\frac{q_e(V - JR_S)}{nkT_e}\right) - 1\right] - \frac{V - JR_S}{R_{Sh}} \quad (24)$$

$$V_{OC} = \left(\frac{nkT_e}{q_e}\right) \ln\left\{\frac{J_{PH}}{J_0}\left(1 - \frac{V_{OC}}{R_{Sh}J_{PH}}\right)\right\} \quad (25)$$

Where q_e, J_{PH}, J_0, R_S, R_{SH}, n, k, T_e represents the elementary charge, photocurrent density, density of the reverse bias saturation current, R_S, R_{Sh}, diode ideality factor, Boltzmann constant and ambient temperature, respectively. To examine the effect of R_{Sh} on the solar cell performance, it was altered from 500 to 5000 Ω cm^2. As depicted in **Fig. 54**(e-h), J_{SC} and V_{OC} remained constant, while FF and PCE exhibited improvements with an increase in R_{Sh}. Specifically, FF increased from 71.45% to 87.31%, 72.31% to 87.00%, 73.91% to 87.07%, and 75.56% to 87.40%, while PCE increased from 11.36% to 13.97%, 13.58% to 16.43%, 16.00% to 18.95%, and 18.59% to 21.60% for $BaHfS_3$, $BaHf_{0.75}Zr_{0.25}S_3$, $BaHf_{0.5}Zr_{0.5}S_3$ and $BaHf_{0.25}Zr_{0.75}S_3$ based solar cells, respectively. Consequently, elevated R_{Sh} values result in enhanced solar cell performance.

Solar cell performance often exhibits instability caused by layer deformation at high temperatures [234]. To explore the connection between temperature and PVparameters, we conducted experiments at temperatures ranging from 300 to 480K, as depicted in **Fig. 55**(a-d). Our results reveal that as the temperature, the V_{OC}, FF, and PCE decrease, while J_{SC} remains relatively constant. The decrease in V_{OC} values can be attributed to the increased vibration of thermally generated electrons at elevated temperatures [141]. This increased vibration renders the electrons less stable, making them more susceptible to recombination with holes, which, in

turn, increases the reverse saturation current (J_0). This inverse relationship between V_{OC} and J_0 is supported by **Eqn (26)** [114]**.**

$$V_{OC} = \frac{nKT}{q}\left(ln\left(1 + \frac{Jsc}{J_o}\right)\right) \quad (26)$$

Where $\frac{KT}{q}$ signifies the thermal voltage. In addition, a rise in temperature has a negative impact on the material characteristics, such as acceptor density, absorber bandgap, and mobility of charge carriers, consequently affecting the effectiveness of charge carrier transport and ultimately reducing the FF [39]. This decrease in both the V_{OC} and FF results in a decline in the PCE from 14.26% to 12.58%, 16.75% to 14.96%, 19.28% to 17.20%, and 21.94% to 19.40% in $BaHfS_3$, $BaHf_{0.75}Zr_{0.25}S_3$, $BaHf_{0.5}Zr_{0.5}S_3$ and $BaHf_{0.25}Zr_{0.75}S_3$-based solar cells, respectively.

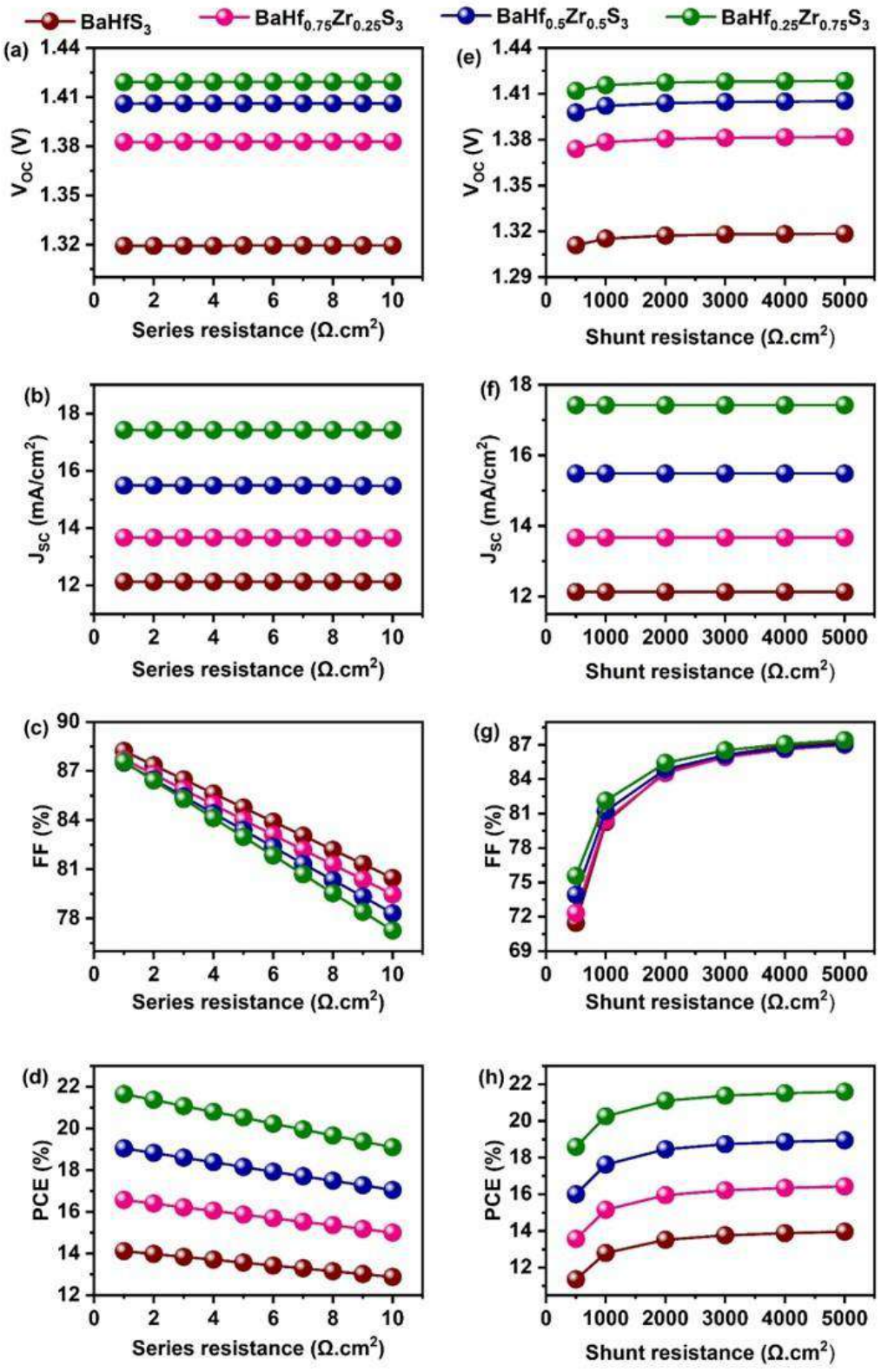

Fig. 54. (a-d) impact of series resistance for all absorbers and (e-h) impact of shunt resistance for all absorbers [44].

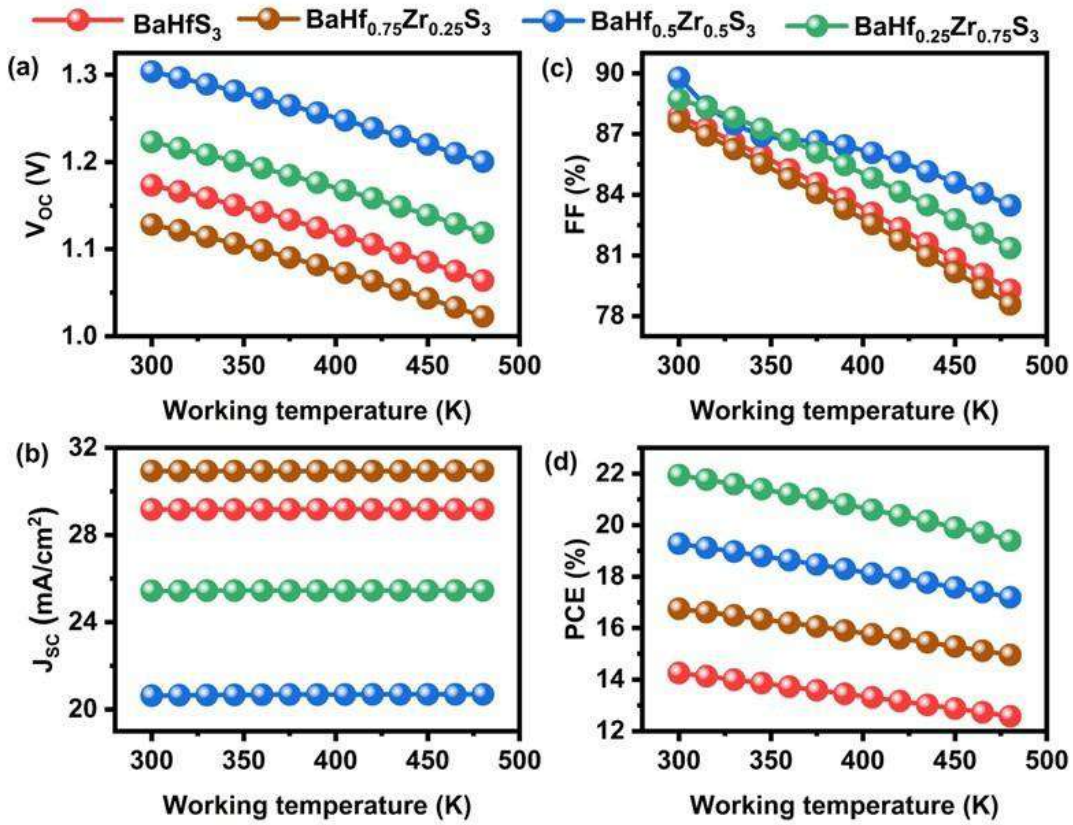

Fig. 55. (a-d) Impact of working temperature for all absorbers [44].

6.3.10. Comparison of base and optimized device

6.3.10.1. C-V characteristics and Mott-Schottky analysis

After optimization, solar cells show a significant increase in PCEs, from 3.42% to 14.26% for $BaHfS_3$, 4.31% to 16.75% for $BaHf_{0.75}Zr_{0.25}S_3$, 5.05% to 19.28% for $BaHf_{0.5}Zr_{0.5}S_3$, and 5.92% to 21.94% for $BaHf_{0.25}Zr_{0.75}S_3$ based solar cells, respectively. To understand this PCE enhancement, C-V measurements were performed on both base and optimized devices with various absorbers. Generally, when a solar cell is reverse-biased, a depletion region forms at the absorber/ETL junction. Since this region lacks mobile carriers, it does not respond to the applied AC field, resulting in very low capacitance, known as depletion capacitance (C_{dep}), which dominates at the reverse and low forward bias voltages [235]. However, as the reverse bias voltage decreases, the depletion region narrows, leading to a significant collection of charge carriers in the interface. Consequently, the capacitance rises exponentially with voltage, described as accumulation capacitance (C_{acc}) [235]. In our analysis, the C-V plots of both base and optimized devices reveal that capacitance remains constant or decreases at low voltages, indicating C_{dep}. Conversely, capacitance increases with higher voltages, resulting from the reduction of the depletion region, which leads to significant charge carrier accumulation at the

interface, termed C_{acc}. **Fig. 56**(a-d) shows that the C_{acc} for all base solar cells is considerably higher than the optimized solar cells, indicating a significant barrier at the ETL/absorber interface. This barrier requires more energy for photogenerated electrons to overcome, causing charge carriers to be collected at the absorber and recombined with holes, thus strengthening charge carrier accumulation in the interface. However, in optimized solar cells, a decrease in capacitance is observed due to significant dielectric dispersion and interface charges, failing to track the AC signal. This reduces the barrier, diminishing charge carrier accumulation at the interface, and facilitates rapid charge carrier collection without recombination, thereby enhancing the effectiveness of all optimized devices compared to the base device solar cells. Moreover, the C-V plots show that the voltage at which capacitance starts to rise shifts to a higher range for all optimized devices. This shift signifies reduced charge carrier trapping at the ETL/absorber interface, leading to improved charge carrier collection and an increase in the depletion width compared to the base device. To illustrate this, Mott-Schottky ($1/C^2$) plots for both the base and optimized devices of $BaHfS_3$, $BaHf_{0.75}Zr_{0.25}S_3$, $BaHf_{0.5}Zr_{0.5}S_3$ and $BaHf_{0.25}Zr_{0.75}S_3$ were obtained from their C-V data by using SCAPS-1D simulation software and the respective V_B were obtained from the intercept of these plots of Mott-Schottky as displayed in **Fig. 56**(e-h). These plots demonstrate the rise in V_B and depletion width (W). The V_B for the base devices is measured at 1.16V, 1.28 V, 1.29 V, and 1.29 V for $BaHfS_3$, $BaHf_{0.75}Zr_{0.25}S_3$, $BaHf_{0.5}Zr_{0.5}S_3$ and $BaHf_{0.25}Zr_{0.75}S_3$ **(Fig. 56**e-h**)**. The V_B for the base device is measured at 1.16 V, 1.28 V, 1.29 V, and 1.29 V for $BaHfS_3$, $BaHf_{0.75}Zr_{0.25}S_3$, $BaHf_{0.5}Zr_{0.5}S_3$ and $BaHf_{0.25}Zr_{0.75}S_3$, respectively. After optimizing key parameters of the ETL, absorber, and HTL, the potentials of the optimized devices are 1.47 V, 1.52 V, 1.46 V, and 1.57 V. Moreover, the increased V_B facilitates more effective transport of charge carriers to the contacts [108]. The corresponding W is derived from the formula in **Eqn 27** [114].

$$W=\sqrt[2]{\frac{2\varepsilon_0\varepsilon_S V_B}{qN_a}} \quad (27)$$

Where ε_0 is the dielectric permittivity of free space, ε_S is the dielectric constant, V_B is built-in potential, q is the elementary charge, and N_a is the acceptor density. The W for the base devices 0.037 µm, 0.0394 µm, 0.0396 µm, and 0.0396 µm for $BaHfS_3$, $BaHf_{0.75}Zr_{0.25}S_3$, $BaHf_{0.5}Zr_{0.5}S_3$, $BaHf_{0.25}Zr_{0.75}S_3$ respectively, while for the optimized devices it is 0.422 µm, 0.430 µm, 0.421 µm, and 0.437 µm. Thus, the increase in V_B and W in the optimized devices enhances the generation of charge carriers and improves their extraction in specific contacts. Overall, these findings underscore the pivotal role of optimization in enhancing solar cell performance.

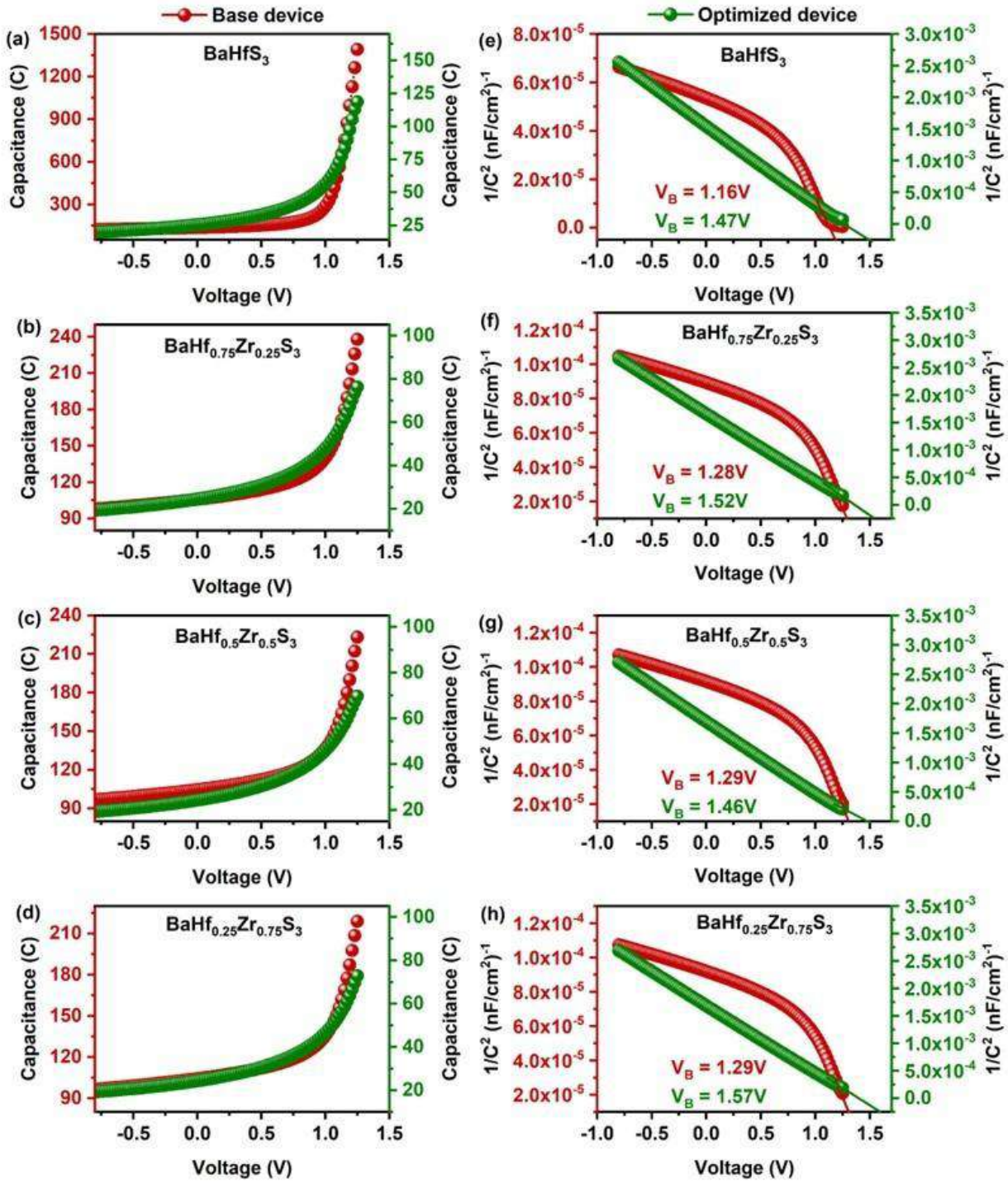

Fig. 56. (a-d) C-V characteristics for the base and optimized device and (e-h) Mott-Schottky analysis for the base and optimized device [44].

6.3.10.2. Nyquist Plot and QE measurements

Impedance spectroscopy has been utilized to characterize solar cells and understand the transport properties of charge carriers, providing insights into the working mechanisms of solar cells [236]. Consequently, Nyquist plots for both base and optimized solar cells made from

$BaHfS_3$, $BaHf_{0.75}Zr_{0.25}S_3$, $BaHf_{0.5}Zr_{0.5}S_3$, and $BaHf_{0.25}Zr_{0.75}S_3$ have been generated from C-F measurements in **Fig. 57**(a-d). All the solar cells display semi-circular plots, which strongly indicate the effectiveness of the depletion regions in these solar cells. Typically, the Nyquist plots of solar cells feature two semicircles in different frequency regions; the low-frequency semicircle relates with the recombination resistance (R_{rec}), while the high-frequency semicircle represents the charge transfer resistance (R_{CT}) [237]. In this work, a single semicircle was observed across the entire frequency range, indicating the R_{rec} of the solar cells. Additionally, the semicircle towards the optimized device is larger than the base device, indicating that R_{rec} is greater in the optimized solar cells. This larger R_{rec} suggests that photogenerated charge carriers in the optimized solar cells are more effectively extracted and accumulated at their respective contacts without recombination, contributing to superior PCE. Conversely, the smaller R_{rec} in the base device solar cells increases the recombination rate of charge carriers, resulting in poorer performance. QE measurements are essential for evaluating the performance of solar cells, as they provide insights into photon absorption, charge carrier generation, separation, and, afterward, the accumulation of photogenerated charge carriers at their specific contacts [137]. The QE for both base and optimized solar cells of $BaHfS_3$, $BaHf_{0.75}Zr_{0.25}S_3$, $BaHf_{0.5}Zr_{0.5}S_3$, and $BaHf_{0.25}Zr_{0.75}S_3$ is plotted in **Fig. 57**(e-h). In all four base device solar cells, absorption begins to decline at approximately 350 nm. However, a consistent spectral response up to around 650 nm is observed in the optimized solar cells $BaHfS_3$, $BaHf_{0.75}Zr_{0.25}S_3$, $BaHf_{0.5}Zr_{0.5}S_3$, and $BaHf_{0.25}Zr_{0.75}S_3$. This improved performance results from enhanced light absorption in the optimized solar cells, with overall absorption rates of 45.60%, 48.10%, 52.70%, and 57.80%, respectively, which are 2.66%, 2.82%, 3.1%, and 3.39% higher than those of the base devices. Additionally, it is noteworthy that the QE reaches 100% in the visible region (400-700 nm) for all optimized solar cells. This indicates that all four absorbers efficiently capture photons within this wavelength range, generating a substantial amount of charge carriers collected at the corresponding contacts. This efficiency is due to the proper alignment of energy bands in the optimized solar cells for all four absorbers. In contrast, the QE in the visible range is below 60% towards the base device solar cells of all four absorbers. This reduced efficiency is due to the poor band alignment of the base device solar cells and back contact, which results in high minority carrier recombination and, consequently, lower charge carrier generation. Therefore, the enhanced spectral response of all optimized solar cells is due to the expansion of the W along the absorber, as debated in the C-V measurements, thereby improving overall absorption within the solar cells.

6.3.10.3. Electric field and J-V characteristics

The electric field generated at the heterojunctions or homojunctions within a solar cell is vital for regulating its performance [114]. Consequently, the performance of solar cells using $BaHfS_3$, $BaHf_{0.75}Zr_{0.25}S_3$, $BaHf_{0.5}Zr_{0.5}S_3$, and $BaHf_{0.25}Zr_{0.75}S_3$ absorbers has been investigated, focusing on the electric field distribution within the cell layers as shown in **Fig. 58**(a-d). The optimized devices of these solar cells consistently exhibit a stronger electric field compared to their base device. This stronger electric field is crucial for the efficient separation of electron-hole pairs generated by photon absorption, significantly reducing the likelihood of recombination and ensuring that more photogenerated carriers contribute to the current [39]. Furthermore, the higher electric field enhances carrier mobility, allowing electrons and holes to travel more quickly through the semiconductor material toward the electrodes. This minimizes recombination losses and improves the FF. Additionally, the strong electric field helps maintain a greater separation between the quasi-Fermi levels, thereby increasing the V_{OC} and directly improving the PCE. Overall, these data demonstrate the optimized devices, with their higher electric fields, provide superior performance and effectiveness for solar cell applications. In summary, we investigated the solar cell performance of both base and optimized devices for $BaHfS_3$, $BaHf_{0.75}Zr_{0.25}S_3$, $BaHf_{0.5}Zr_{0.5}S_3$ and $BaHf_{0.25}Zr_{0.75}S_3$. Notably, the optimized devices achieved impressive PCEs of 14.46%, 16.75%, 19.28% and 21.94% for $BaHfS_3$, $BaHf_{0.75}Zr_{0.25}S_3$, $BaHf_{0.5}Zr_{0.5}S_3$, and $BaHf_{0.25}Zr_{0.75}S_3$ solar cells, respectively. This enhancement in PCE is primarily due to the improvement in the J_{SC}, as illustrated in **Fig. 58**(e-h). Additionally, a significant increase in V_{OC} from base to optimized device was observed, with values rising from 1.06 to 1.32 V, 1.22 to 1.38 V, 1.24 to 1.40 V, and 1.25 to 1.42 V for $BaHfS_3$, $BaHf_{0.75}Zr_{0.25}S_3$, $BaHf_{0.5}Zr_{0.5}S_3$ and $BaHf_{0.25}Zr_{0.75}S_3$ solar cells, respectively. This indicates a reduction in energy loss across all optimized solar cells. Remarkably, the optimized $BaHf_{0.25}Zr_{0.75}S_3$ device achieved a PCE exceeding 21%, which can be attributed to its elevated V_B, high recombination resistance, and enhanced light absorption properties compared to the other optimized devices. Our findings are expected to inspire material scientists to further explore the fabrication of efficient $BaHfS_3$, $BaHf_{0.75}Zr_{0.25}S_3$, $BaHf_{0.5}Zr_{0.5}S_3$, and $BaHf_{0.25}Zr_{0.75}S_3$ solar cell materials.

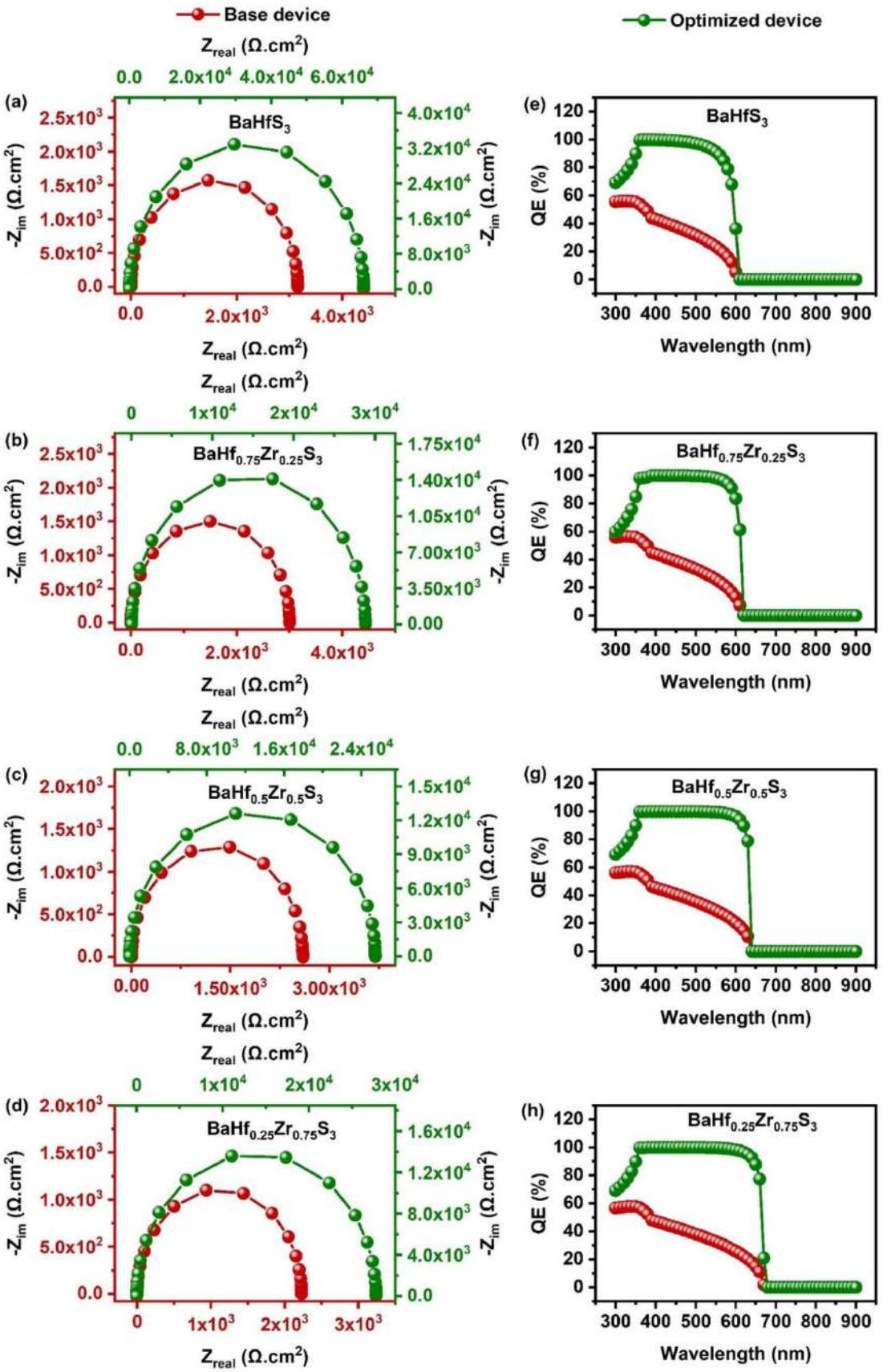

Fig. 57. (a-d) Nyquist plot for the base and optimized device and (e-h) QE measurements for the base and optimized device [44].

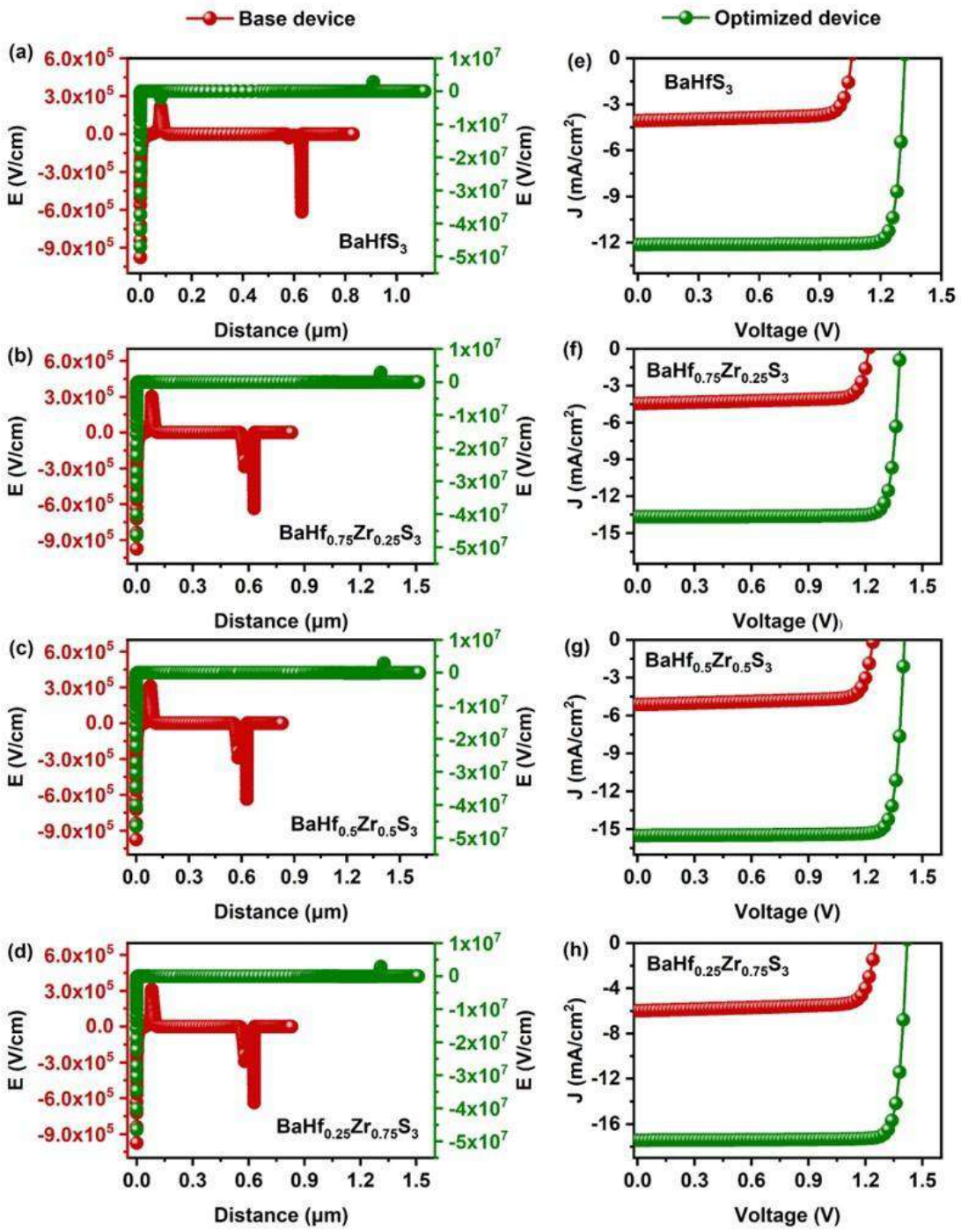

Fig. 58. (a-d) Electric field of the base and optimized device and (e-h) J-V measurements of the base and optimized device [44].

6.3.11. Comparison of SCAPS-1D outcomes with previous studies in the literature

Table 16 provides a comprehensive overview of theoretical studies on CPs solar cells simulated using SCAPS-1D software. Among the chalcogenide materials studied, $BaZrS_3$ has been extensively explored in theoretical research and has shown significant advancements in PV performance. The reported PCE of $BaZrS_3$ increased from an initial 12.12% to 28.17% through device architecture optimizations. Additionally, alloying $BaZrS_3$ with Ti further improved its performance, achieving a PCE of 32.58%. Beyond $BaZrS_3$, materials such as $SrZrS_3$, $CaZrS_3$, $MgHfS_3$, and $BaZrSe_3$ have also been investigated for their PV potential [48].

However, despite these advancements, research on other CPs materials, such as $BaHfS_3$ and its alloys $BaHf_{1-x}Zr_xS_3$, remains limited. Available studies mainly focus on density functional theory (DFT) calculations and synthesis optimization, with minimal attention to their solar cell performance using SCAPS-1D simulations, particularly for Zr-alloyed $BaHfS_3$. Our work addresses this gap by investigating the effects of Zr alloying on the optoelectronic properties and PV performance of $BaHfS_3$. This study marks the first development of solar cells incorporating Zr-alloyed $BaHfS_3$. We proposed and analyzed several compositions, including $BaHfS_3$, $BaHf_{0.75}Zr_{0.25}S_3$, $BaHf_{0.5}Zr_{0.5}S_3$ and $BaHf_{0.25}Zr_{0.75}S_3$, using TiO_2, NiO, and Au as the ETL, HTL, and metal contact, respectively. These materials exhibited PCEs of 14.26%, 16.75%, 19.28%, and 21.94%, respectively. This study provides the first insights into the application of Zr-alloyed $BaHfS_3$ in solar cell technology. We believe these findings will fill an existing gap in the literature and encourage future research into advanced CPs solar cells.

Table 16. Comparison of performance of CPs solar cells in the literature [44].

Device structure	**V_{OC} (V)**	**J_{SC} (mA/cm^2)**	**FF (%)**	**PCE (%)**	**Ref**
FTO/TiO_2 /$BaZrS_3$/Cu_2O/Au	1.16	12.24	87.13	12.42	[29]
FTO/TiO_2/$BaZrS_3$/Spiro-OMeTAD/Au	0.70	22.00	79.40	12.12	[147]
FTO/TiO_2/$BaZrS_3$/Spiro-OMeTAD/Au	1.08	16.80	88.60	16.07	[146]
AZO/i-ZnO/CdS/ $BaZrS_3$/a-Si	1.31	19.08	78.88	19.72	[137]
FTO/$BaZrS_3$/CuO/Au	0.79	40.5	85.2	27.30	[202]
FTO/ZrS_2/$BaZrS_3$/SnS/Pt	1.18	29.74	80.15	28.17	[39]
FTO/ZrS_2/$Ba(Zr_{0.96}Ti_{0.04})S_3$/SnS/ Pt	1.18	32.26	84.94	32.58	[39]
FTO/SnO_2/ $BaZr_{0.96}Ti_{0.04}S_3$/ZnPc/C	1.27	26.62	88.81	30.12	[193]
FTO/ZnO /$SrZrS_3$/NiO/Ni	1.18	26.13	84.29	25.97	[148]
FTO/SnO_2/$SrZrS_3$/Cu-MOF/Ni	1.17	29.54	88.40	30.60	[197]
Pt/CuO/$CaZrS_3$/ZnO/FTO	0.60	35.72	81.05	17.57	[238]
Pt/CuO/$CaZrS_3$/TiO_2/FTO	0.60	35.73	80.88	17.53	[238]
Pt/CuO/$CaZrS_3$/SnO_2/FTO	0.60	35.73	81.83	17.73	[238]
FTO/TiO_2/$MgHfS_3$/Cu_2O/Au	0.99	25.21	57.59	14.36	[239]
FTO/CdS/$BaZrSe_3$/SnSe/Au	0.88	46.14	79.30	32.20	[240]
FTO/TiO_2/$BaZrSe_3$/Spiro-OMeTAD/Au	0.72	46.65	77.32	25.84	[49]
FTO/TiO_2/$BaHfS_3$/NiO/Au	1.31	12.13	89.09	14.26	*
FTO/TiO_2/$BaHf_{0.75}Zr_{0.25}S_3$/NiO/Au	1.38	13.66	88.65	16.75	*
FTO/TiO_2/$BaHf_{0.5}Zr_{0.5}S_3$/NiO/Au	1.40	15.48	88.54	19.28	*
FTO/TiO_2/$BaHf_{0.25}Zr_{0.75}S_3$/NiO/Au	1.41	17.42	88.72	21.94	*
The * represents the findings of the present work					

6.3.12. Experimental suggestions to enhance solar cell performance in practice based on simulation results

SCAPS-1D is a commonly used tool for simulating PV devices, offering important insights into their electrical and optical behavior. The performed simulation provides a comprehensive theoretical investigation of the device engineering of Zr-based $BaHfS_3$ based solar cells. The highest PCEs, 14.26%, 16.75%, 19.28%, and 21.94%, were demonstrated for the Zr-based $BaHfS_3$ solar cell device. However, the software has certain limitations that could impact the current study. For instance, SCAPS-1D does not inherently account for reflection

losses at intermediate interfaces and lattice mismatches. Incorporating these effects would require inputs for the wavelength-dependent complex refractive index (n-k values) of each material of $BaHf_{1-x}Zr_xS_3$, which are critical for accurately modeling light absorption and propagation in multi-layer solar cells. Integrating these advanced mechanisms into SCAPS-1D would allow a more comprehensive evaluation of innovative materials and device architectures. In addition, since there are no reports available on the fabrication of these novel solar cells, it is indeed important to offer practical guidelines for experimentalists to attain the best PCEs practically. Therefore, we have proposed several strategies from the literature to prepare each layer by overcoming the experimental challenges and fabricating an efficient solar cell.

In the present work, TiO_2 has been employed as an ETL due to its low cost, high electron mobility, low trap density, and excellent thermal and chemical stability [114]. It can be synthesized using various methods, including the sol-gel method, hydrothermal synthesis, precipitation plasma chemical vapor deposition, chemical spray pyrolysis, and sputter deposition, among others [60]. The spray pyrolysis method is particularly popular for fabricating dense TiO_2 thin films with fewer defects, enabling better control of charge carrier transport properties. The surface passivation process in mesoporous TiO_2 is crucial for enhancing the interfacial properties between the ETL and the absorber layer in solar cells. By employing various strategies to modify the surface of TiO_2, researchers can significantly improve its performance in PV applications. One practical approach is the incorporation of Li and Co into the TiO_2 structure. This doping not only alters the electronic properties of TiO_2 but also plays a key role in mitigating surface defects that typically plague intrinsic TiO_2. Surface defects, such as O vacancies, can act as nonradiative recombination centers, which ultimately diminish the overall efficiency of solar cells by allowing charge carriers to recombine before contributing to the electrical current. Additionally, the introduction of Li salts during the synthesis of mesoporous TiO_2 has been shown to target and reduce these surface defects specifically. The Li ions can effectively fill in some of the O vacancies, thereby stabilizing the structure and enhancing the electron mobility within the material. Another promising modification involves treating mesoporous TiO_2 with ammonium sulfone compounds. This technique has demonstrated a significant capacity to passivate the surface of TiO_2, further suppressing nonradiative recombination processes and ensuring a more efficient extraction and collection of electrons. Overall, these surface passivation strategies are instrumental in developing high-performance mesoporous TiO_2 for solar cell applications, leading to improved

charge separation, enhanced electron collection efficiency, and, ultimately, a boost in the overall device performance. Additionally, the thickness of the TiO_2 layer deposited on FTO glass can be precisely controlled by adjusting the number of spray cycles, allowing for optimization of device performance.

Several methods have been developed for synthesizing $BaZrS_3$ and $BaHfS_3$. These include high-temperature sulfurization of oxide or carbonate precursors with CS_2 or H_2S at 700 -1100°C, the reaction of BaS and ZrS_2 with excess sulfur and $BaCl_2$ as a catalyst at 450 - 600°C (often resulting in contamination with ZrO_2 and, in some cases, BaS_3 and ZrS_3), the reaction of barium sulfide, zirconium, sulfur, and iodine at 600 - 1100°C for 60 hours, and solution phase synthesis using molecular precursors or metal hydrides of Zr and Hf dissolved in high boiling point solvents under air and water free conditions. Each method presents challenges, such as safety risks associated with toxic and flammable reagents like CS_2 and H_2S, contamination with byproducts that are difficult to remove, high synthesis temperatures requiring silica glass, costly and challenging-to-handle reactants, and the need for precise reaction control. Recently, Romagnoli et al. overcame some of these challenges by successfully synthesizing single-phase $BaHf_{1-x}Zr_xS_3$ for all alloying percentages using a simple approach at 500°C, as confirmed by XRD and Raman spectroscopy. Similarly, Zilevu et al. demonstrated successful control of Zr/Ti ratios in $Ba(Zr_{1-x}Ti_x)S_3$ materials through solution phase synthesis. Furthermore, Kong et al. synthesized $BaHf_{1-x}Ti_xS_3$ using a ball-milling technique, achieving precise tuning and control of the Hf/Ti ratio. These approaches have contributed to enhanced solar cell performance.

The Zr-alloyed $BaHfS_3$ was synthesized using the procedure described by Romagnoli et al. This involved mixing BaS, Zr/Hf, and S powders in a 1:1:3 molar ratio in an agate mortar for 20 mins in air. The mixture was then transferred into a 10 mL glass ampule pre-dried at 150^0C for 30 mins. The ampule was evacuated to a pressure of 3×10^{-1} mbar using a rotary vane pump while heated to ~80°C. After cooling to room temperature, the ampule was flame-sealed with a mini butane torch while still under vacuum. Once sealed, the ampule was placed in a 100 mL alumina crucible, which was heated in a muffle furnace preheated to 500^0C and held overnight at the same temperature. Afterward, the ampule was removed from the furnace, allowed to cool naturally to room temperature, and opened. The solid product was recovered using a stainless-steel spatula and ground in an agate mortar. If elemental sulfur contamination was present, the product was stirred in hot toluene (85^0C) for 1 hr at a ratio of 50 ml toluene per gram of solid. The suspension was filtered under suction, washed thrice with small amounts

of toluene, and dried for at least 1 hr. Characterization confirmed the formation of Zr-alloyed $BaHfS_3$ material. While these studies demonstrate successful synthesis using relatively straightforward methods, they have not explored stability tests. Therefore, stability challenges for these materials remain unaddressed. However, theoretical studies have provided insights into the stability of $BaHfS_3$ and Zr-substituted $BaHfS_3$ materials. For example, Sun et al. used DFT calculations to show that $BaHfS_3$ and similar CPs exhibit high stability. Likewise, Chami et al. examined $BaHf_{1-x}Zr_xS_3$ absorbers and reported good stability performance, though this has yet to be confirmed experimentally [241]. In our SCAPS simulation results revealed that the Zr-alloyed $BaHfS_3$ absorbers perform optimally at a thickness of 800 nm. This thickness can be achieved using techniques like vapor deposition, sputtering, and electrodeposition, which allow precise control over parameters such as thickness, composition, purity, and uniformity by varying deposition conditions (e.g., time, temperature, pressure). Film thickness can be increased by repeating deposition and annealing steps. The defect density of 10^{12} cm^{-3} in the absorber contributes to high PCE. Given that these materials are still in the early stages of development, no studies are related to defect density and carrier lifetime for $BaHfS_3$ and Zr-doped $BaHfS_3$. Interestingly, Meng et al. investigated the defect control in $BaZrS_3$, a largely explored CPs with similar material characteristics. They observed that S-rich/Zr-poor compositions suppress the formation energy of deep-level defects and maximize the charge carrier lifetime, revealing that adjusting the elemental composition during synthesis is crucial. This discloses that the low defect density and large carrier lifetime in $BaHfS_3$ and Zr-doped $BaHfS_3$ could also be achieved by controlling the composition of the constituent elements. Nevertheless, further studies focusing on the defect control of $BaHfS_3$ and its alloying is required to obtain a broader understanding of these materials. For high PCE, a defect density in the range of 10^{10}-10^{12} cm^{-3} is recommended. Accordingly, an optimal defect density of 10^{12} cm^{-3} has been selected for Zr-alloyed $BaHfS_3$ solar cells. Furthermore, Meng et al. reported that CPs films synthesized under S-rich/Zr-poor conditions exhibit strong p-type behavior with an optimal carrier concentration of 10^{15} cm^{-3}. In contrast, S-poor/Zr-rich films exhibit n-type behavior with a high carrier concentration (>10^{17} cm^{-3}), making them unsuitable as absorbers [115]. To achieve high PCE, a carrier concentration below 10^{17} cm^{-3} is recommended. Considering these factors, an optimal carrier concentration of 10^{16} cm^{-3} has been selected for Zr-alloyed $BaHfS_3$-based solar cells.

NiO stands out as a highly promising candidate for an efficient HTL due to its high optical transmittance, ease of processability, wide bandgap, excellent energy level alignment

with absorbers, and strong electron-blocking capability. It can be synthesized using various methods, including ultrasonic radiation, hydrothermal synthesis, the carbonyl method, laser chemical methods, pyrolysis by microwave, the sol-gel method, precipitation-calcination, and the microemulsion method, among others [242]. During reactive sputtering of Ni target, the oxygen partial pressure is crucial for controlling the carrier concentration of NiO, enabling the production of both n-type and p-type films [243,244]. Additionally, the oxygen stoichiometry of NiO films can be systematically tuned through thermal treatment in oxygen-rich (O-NiO) atmospheres. These processing conditions significantly influence the defect density and conductivity of NiO_x films, impacting surface recombination rates, PCE, and overall device stability [236].

In conclusion, the methods and strategies discussed have the potential to benefit the PV community significantly, paving the way for the fabrication of highly efficient Zr-alloyed $BaHfS_3$-based devices as the technology continues to advance.

6.4. Performance of $BaZrS_3$-based CPs Solar Cells with Delafossite and Spiro-OMeTAD HTLs

This section addresses **objectives 6** and **7**, presenting a full simulation-based optimization of $BaZrS_3$ solar cells using different HTLs. **Section 6.4.1** introduces the base device and its performance with $CuFeO_2$, $CuGaO_2$, $CuAlO_2$, and Spiro-OMeTAD HTLs. **Sections 6.4.2** to **6.4.5** analyze the effects of absorber and HTL properties acceptor density, defect density, and thickness on solar cell efficiency. **Section 6.4.6** evaluates the impact of interfacial defects at ETL/absorber and absorber/HTL junctions. **Section 6.4.7** compares baseline and optimized devices using Nyquist plots, QE, electric field, and J-V characteristics. **Section 6.4.8** benchmarks SCAPS-1D outcomes with literature data on $BaZrS_3$ CP solar cells. Finally, **Section 6.4.9** provides experimental recommendations for achieving high PCE using delafossite HTLs.

6.4.1. The primary performance of the device

The research employed a base PV device configured as FTO/TiO_2/$BaZrS_3$/HTL/Au, as shown in **Fig. 7**. Simulations using the parameters specified in **Table 6** and **Table 7** were conducted to assess the performance of the baseline device. **Table 17** presents the PV metrics for $BaZrS_3$ solar cells, comparing various delafossite HTLs with the Spiro-OMeTAD HTL. Specifically, the base device achieved PCEs of 8.25%, 10.35%, 7.42%, and 9.86% for $CuFeO_2$,

$CuGaO_2$, $CuAlO_2$, and Spiro-OMeTAD-based HTLs, respectively. To further enhance device performance, extensive optimization of absorber and HTL material parameters was performed. A detailed discussion of these optimization procedures is provided in the following sections.

Table 17. Base device performance of PV parameters with different HTLs [260].

Base device configuration	V_{OC} (V)	J_{SC} (mA/cm^2)	FF (%)	PCE (%)
FTO/TiO_2/$BaZrS_3$/$CuFeO_2$/Au	1.17	9.72	71.89	8.25
FTO/TiO_2/$BaZrS_3$/ $CuGaO_2$/Au	1.38	9.92	75.44	10.35
FTO/TiO_2/$BaZrS_3$/ $CuAlO_2$/Au	1.07	9.63	71.27	7.42
FTO/TiO_2/$BaZrS_3$/Spiro-OMeTAD/Au	1.36	9.87	73.20	9.86

6.4.2. Performance of $BaZrS_3$ absorber's acceptor density with different HTLs

The concentration of charge carriers within the absorber layer of solar cells is crucial for their performance, as it greatly affects both the efficiency of light absorption and the transport of charges [29]. Thus, identifying the optimum acceptor density is vital for achieving exceptional performance. In this investigation, the acceptor density of $BaZrS_3$ was varied from 10^{12} cm^{-3} to 10^{18} cm^{-3}, and the subsequent effects on PV metrics are illustrated in **Fig. 59**(a-d). It was noted that both V_{OC} and FF remained consistent up to a concentration of 10^{14} cm^{-3}, but exhibited a notable increase beyond this threshold. Notably, as the acceptor density escalated from 10^{12} cm^{-3} to 10^{18} cm^{-3}, V_{OC} rose from 0.81 V, 0.13 V, 0.72 V, and 1.03 V to 0.90 V, 1.23 V, 0.80 V, and 1.12 V, respectively. Similarly, FF improved from 50.28%, 53.17%, 47.60%, and 54.81% to 60.12%, 62.09%, 58.92%, and 61.54%. Consequently, the PCE increased from 7.27%, 10.86%, 5.95%, and 10.25% to 9.11%, 13.28%, 7.82%, and 11.87% for solar cells with $CuFeO_2$, $CuGaO_2$, $CuAlO_2$, and Spiro-OMeTAD, respectively. This enhancement is attributed to improved intrinsic properties that enable effective charge collection and buildup at the contacts without recombination losses [39,245]. A higher density of acceptor states affects the arrangement of energy levels, resulting in an increased separation of carrier quasi-levels. This ultimately improves the V_{OC} and enhances the device's efficiency. SCAPS-1D was employed to generate energy band diagrams for acceptor concentrations ranging from 10^{12} cm^{-3} to 10^{18} cm^{-3}, as shown in **Fig. 59**(e-h), to examine these effects. As an acceptor concentration rises, the energy levels of each layer rise, causing the absorber's valence band to align more closely with the hole quasi-Fermi level, thereby improving the V_{OC} [215]. Furthermore, the enhanced electric field at the interface of $BaZrS_3$/HTL facilitated the transfer of holes from the absorber to the HTL, effectively blocking electron flow and enhancing hole collection at the rear contact [246]. In contrast, J_{SC} remained unchanged until 10^{14} cm^{-3} but declined sharply at higher

acceptor densities [246]. This drop is due to the depletion region extending toward the ETL, reducing light absorption in the solar cells while contracting within the absorber [110]. **Fig. 60**(a-d) illustrates this effect with QE measurements across 10^{12} cm^{-3} to 10^{18} cm^{-3}, showing a slight absorption reduction of 22.11%, 22.64%, 21.37%, and 22.50% for solar cells based on $CuFeO_2$, $CuGaO_2$, $CuAlO_2$, and Spiro-OMeTAD, respectively. As a result, the rate at which charge carriers were generated declined, causing a decrease in J_{SC}. Additionally, as the depletion width in the absorber shrinks, charge carriers generated in the quasi-neutral region face diffusion challenges, with shorter diffusion lengths or lifetimes increasing recombination rates, further reducing J_{SC} [39]. However, the enhancement in solar cell performance primarily arises from the increase in V_{OC} and FF, while remaining independent of J_{SC} reductions. The results clearly indicate that increasing $BaZrS_3$'s carrier concentration adjusts the position of the energy bands and enhances splitting of the quasi-Fermi level, accelerating PCE. As illustrated in **Fig. 60**(e-h), when acceptor densities surpass 10^{17} cm^{-3}, recombination processes are expedited, resulting in a decline in PCE beyond this point. Based on these findings of PCE improvement, an acceptor density of 10^{16} cm^{-3} is identified as the optimum value for further simulations.

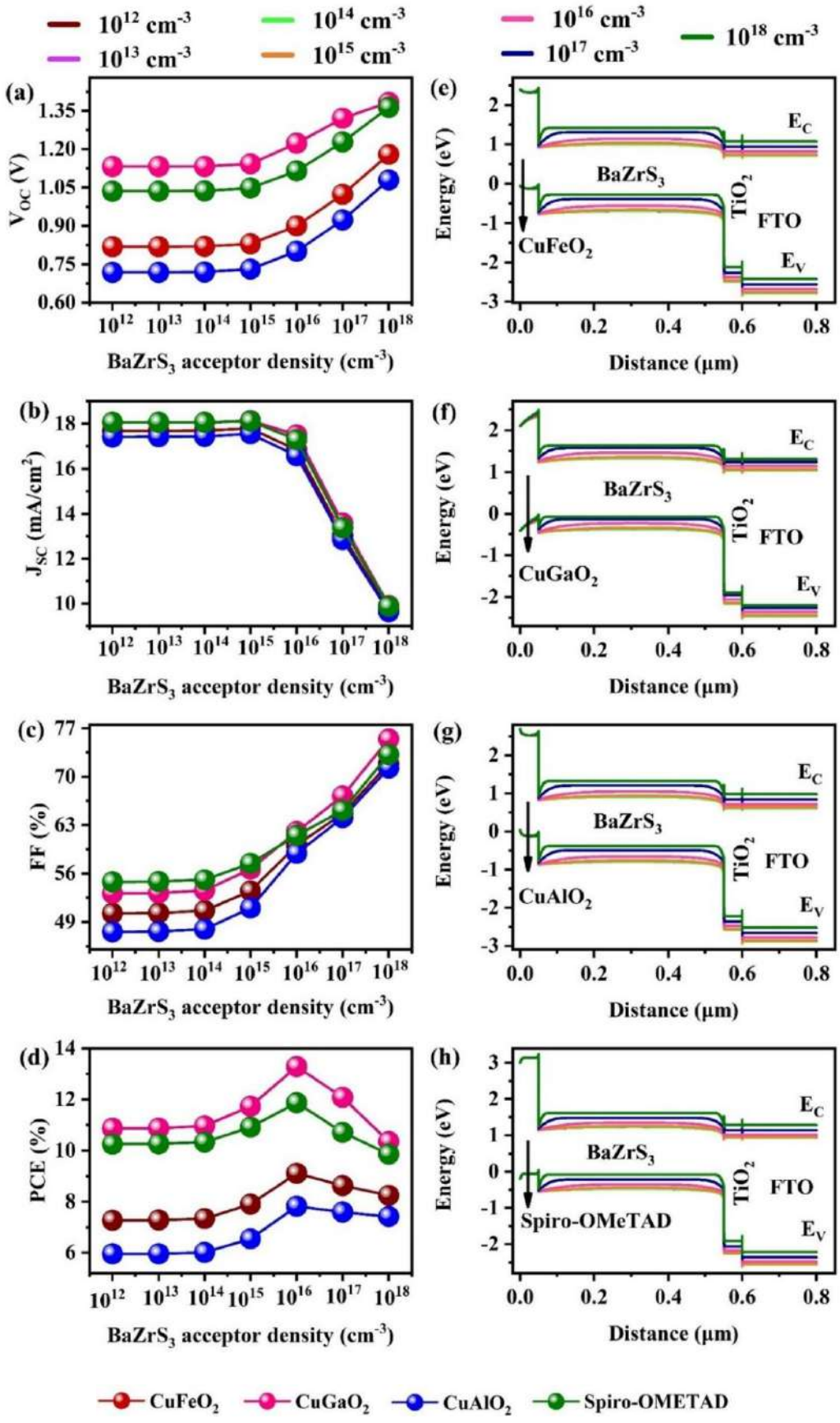

Fig. 59. Performance of $BaZrS_3$ acceptor density (a-d), photovoltaic parameters variations (e-h), energy band alignment behaviours [260].

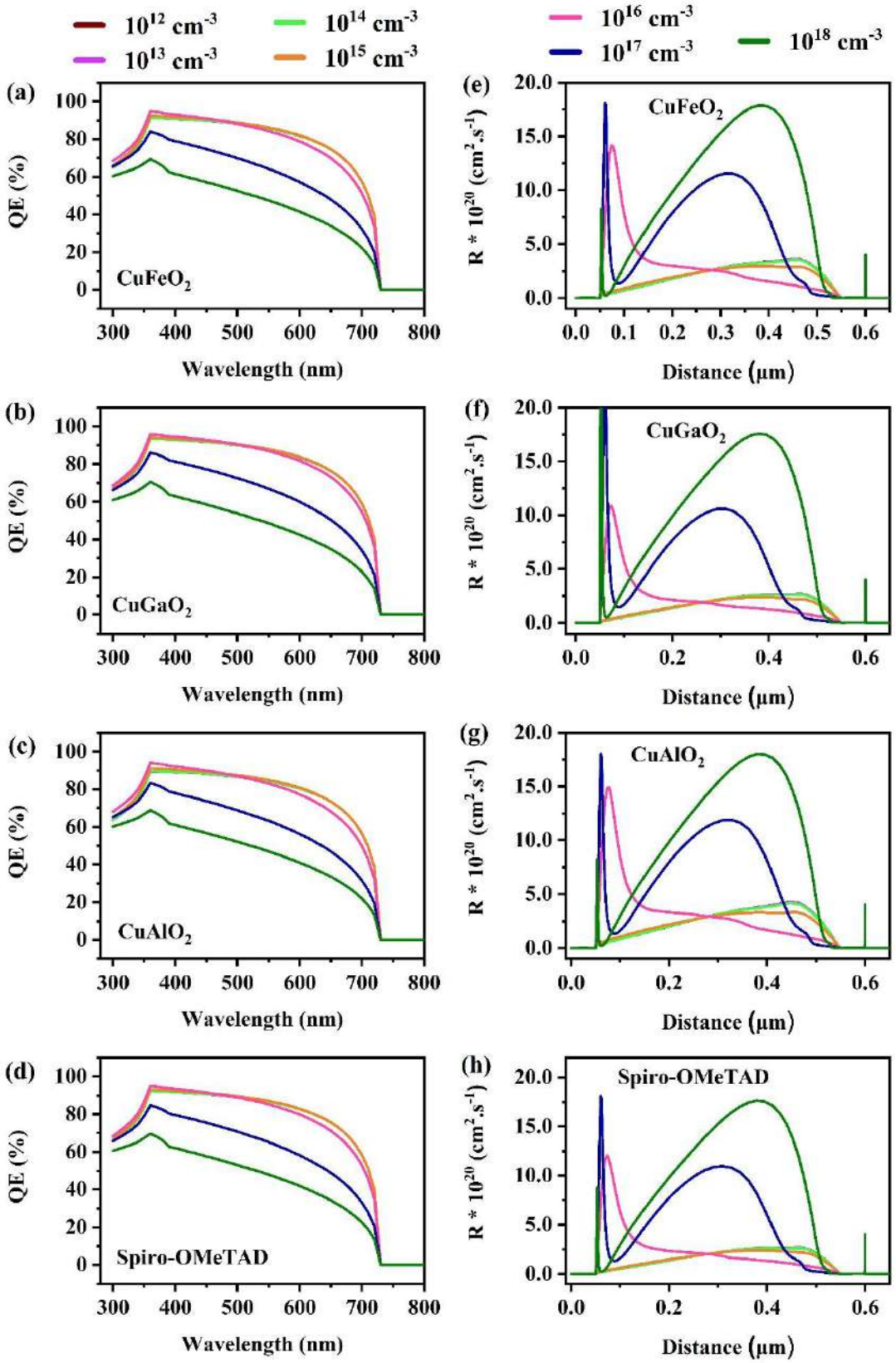

Fig. 60. Performance of $BaZrS_3$ acceptor concentration (a-d), QE measurement (e-h) recombination rate [260].

6.4.3. Performance of $BaZrS_3$ absorber's defect density with different HTLs

The presence of defects in the active layer is pivotal in affecting the efficiency of PV cells [111]. Furthermore, the absorber's performance is further compromised by bulk defects, including vacancies, interstitial defects, Schottky defects, and Frenkel defects [247]. Therefore, effectively controlling defects in the active layer is essential for optimizing the efficiency of PV devices. In this research, we meticulously adjusted the defect concentrations in $BaZrS_3$ from 10^{10} cm^{-3} to 10^{20} cm^{-3} to comprehensively evaluate their impact. **Fig. 61**(a-d) shows the relationship between PV performance and varying $BaZrS_3$ defect densities. The results reveal that all performance parameters decline significantly with increasing $BaZrS_3$ defects. In particular, as the defect concentration in $BaZrS_3$ increases from 10^{12} cm^{-3} to 10^{20} cm^{-3}, PCE of $CuFeO_2$-based cells significantly declines, dropping from 12.76% to 0.07%, from 18.15% to 0.12% for $CuGaO_2$-based cells, from 11.18% to 0.06% for $CuAlO_2$-based cells, and from 16.02% to 0.11% for Spiro-OMeTAD-based cells. This decline is attributed to elevated recombination centers that trap generated charge carriers, leading to shorter lifetimes and diffusion lengths [199]. **Eqn (28)** is used to determine the minority carrier lifetime (τ) [200]:

$$\tau = \frac{1}{\sigma v_{th} N_t} \quad (28)$$

where σ is the charge carrier capture cross-section, V_{th} is the thermal velocity, and N_t represents the defects.

The diffusion length (L) is expressed as **Eqn (29):**

$$L = \sqrt{D\tau} \quad (29)$$

where D is the diffusion coefficient. SCAPS-1D simulation is used to determine L and τ for $BaZrS_3$ defects while maintaining a fixed $BaZrS_3$ thickness of 500 nm, as illustrated in **Fig. 62**(a-d). As $BaZrS_3$ defect level increased between 10^{12} cm^{-3} to 10^{20} cm^{-3}, τ decreased dramatically from 1×10^{5} ns to 1×10^{-3} ns, while L decreased from 3.0 μm to 3.0×10^{-4} μm. At a $BaZrS_3$ defect concentration of 10^{12} cm^{-3}, L (3.0 μm) exceeds $BaZrS_3$ thickness, leaving the PCE unaffected. However, at 10^{13} cm^{-3}, L reduces to 0.53 μm, less than the absorber thickness, which increases recombination rates. As L continues to decrease, solar cell functionality deteriorates. This confirms that when L falls below the absorber thickness, solar cell performance is significantly impacted. As illustrated in **Fig. 62**(i-l), decreases in L and τ Pb directly to increased recombination rates. Increased defect density intensifies recombination within the absorber, diminishing the concentration of light-induced carriers and degrading solar

cell efficiency [98]. This study demonstrates that rising defect density adversely affects L and τ, increasing recombination rates and reducing the performance of the PV device. The findings indicate that a defect level of 10^{12} cm^{-3} is the ideal value for $BaZrS_3$ across each PV device.

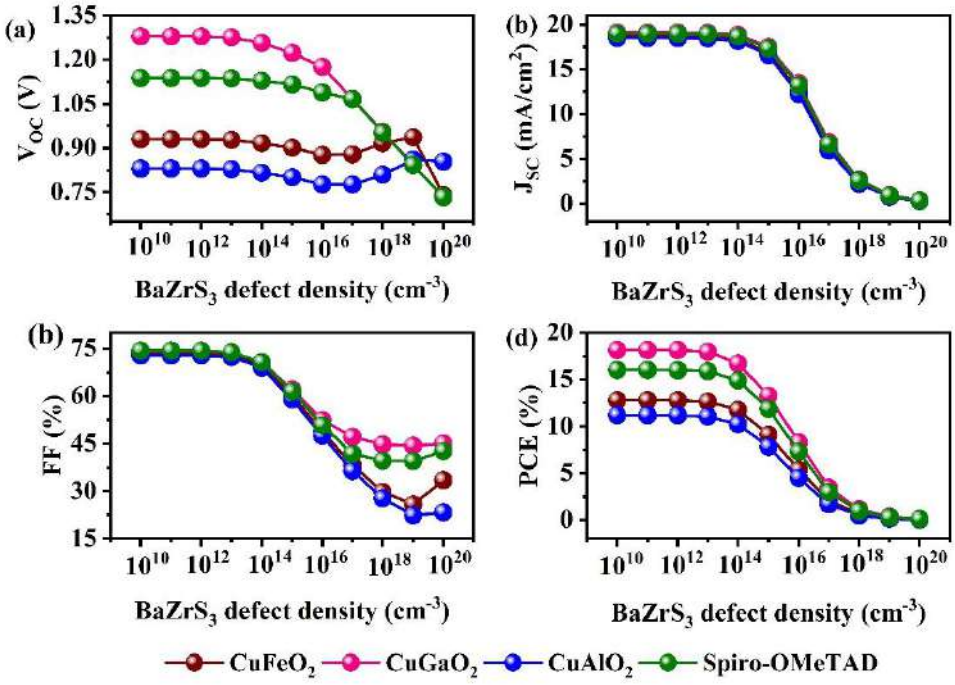

Fig. 61. Performance of $BaZrS_3$ defect density (a-d) solar cell parameters variation [260].

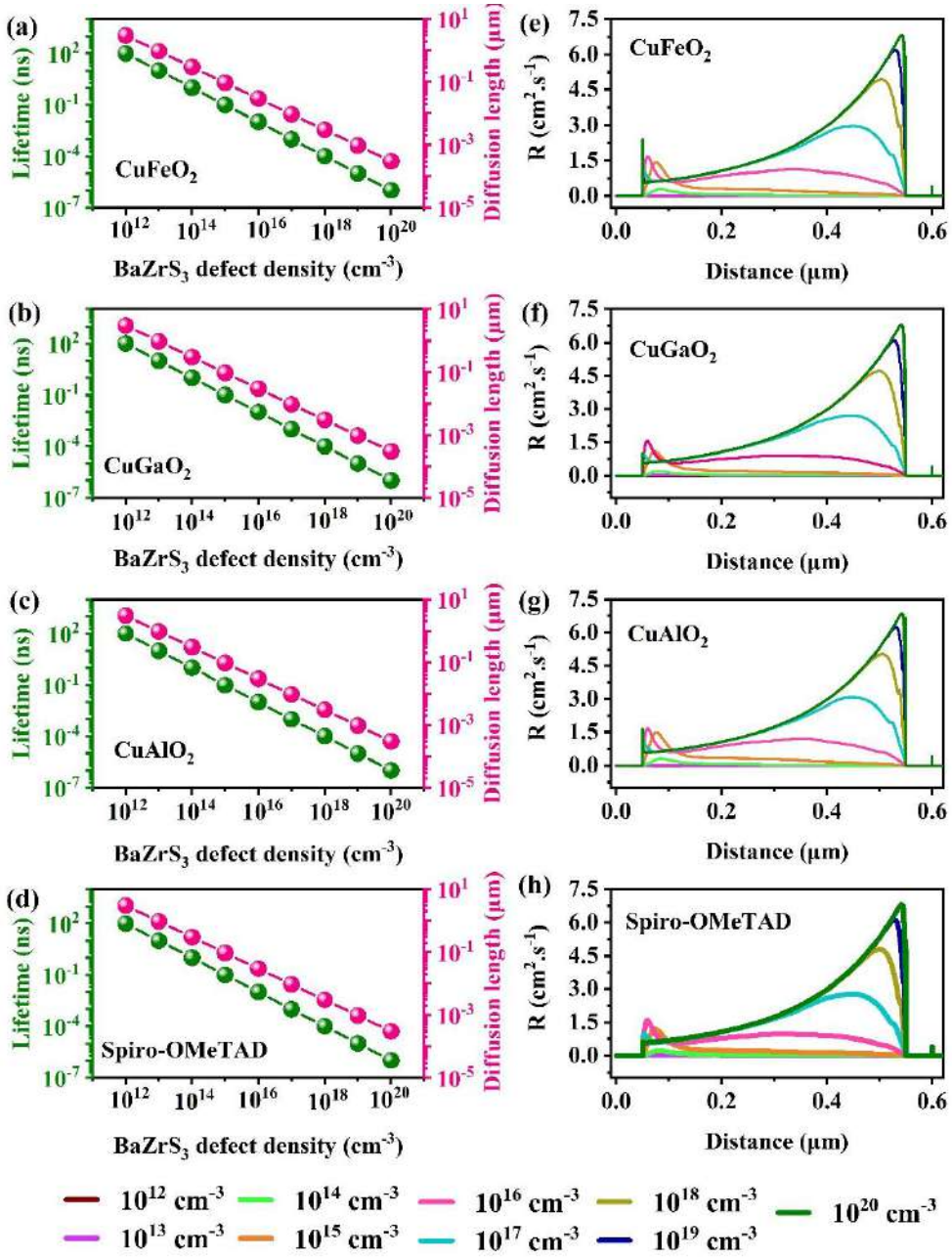

Fig. 62. Performance of $BaZrS_3$ defect density (a-d) diffusion length and lifetime behaviours, and (e-h) recombination rate [260].

6.4.4. Performance of $BaZrS_3$ absorber's thickness with different HTLs

The active layer thickness is a key factor in enhancing solar cell performance [248]. It must be carefully selected to maximize current density while avoiding excessive thickness to reduce reverse saturation current. A thinner active layer fails to capture sufficient photons, allowing most light to pass through and minimizing the production of carrier formation [249]. On the other hand, increasing active layer thickness may negatively impact performance because charge carriers have a restricted movement range, limiting their effective transport and

collection [118]. Thus, it is crucial to optimize the thickness of the absorber to attain the highest possible PCE. In the study of $BaZrS_3$-based solar cells, the thickness of the $BaZrS_3$ layer was varied between 100 nm and 2000 nm to determine the optimal value. **Fig. 63**(a-d) shows the impact on PV parameters as the thickness of BaZrS3 is altered. As the thickness of $BaZrS_3$ increases from 100 nm to 2000 nm, there is a notable enhancement in V_{OC}, J_{SC}, and FF, leading to an increase in PCE from 10.22%, 11.75%, 9.13%, and 11.53% to 24.78%, 27.81%, 22.81%, and 27.68% for solar cells based on $CuFeO_2$, $CuGaO_2$, $CuAlO_2$, and Spiro-OMeTAD, respectively. When the thickness is increased from 100 nm to 800 nm, there is a marked improvement in PCE, achieving values of 11.35%, 15.44%, 12.95%, and 15.44% for each of the PV devices, respectively. Nevertheless, when the thickness of $BaZrS_3$ is increased from 800 nm to 2000 nm, the PCE sees only a minor enhancement of approximately 1.32%. Excessive thickness causes the photogenerated carriers to traverse longer distances to reach the electrodes, leading to increased recombination due to the mismatch between diffusion length and absorber thickness [39]. This limits further performance gains. This behavior is also reflected in the QE measurements shown in **Fig. 64**(a-d). Absorption is enhanced by approximately 31.58% with an absorber thickness range of 100 nm to 800 nm, while further extending it to 2000 nm results in a minimal gain of about 2.38%. Additionally, V_{OC} rises slightly up to 800 nm before declining at higher thicknesses. The early rise in V_{OC} occurs due to increased separation of quasi-Fermi levels, driven by a higher concentration of generated carriers, as illustrated in **Fig. 64**(e-h), while the decline results from higher recombination rates and increased dark saturation current. Similarly, FF increases up to 800 nm and then stabilizes, likely due to the rising series resistance in thicker absorbers. Considering material usage, cost, and overall performance, an absorber thickness of 800 nm is determined to be optimal for $BaZrS_3$-based solar cells in this simulation.

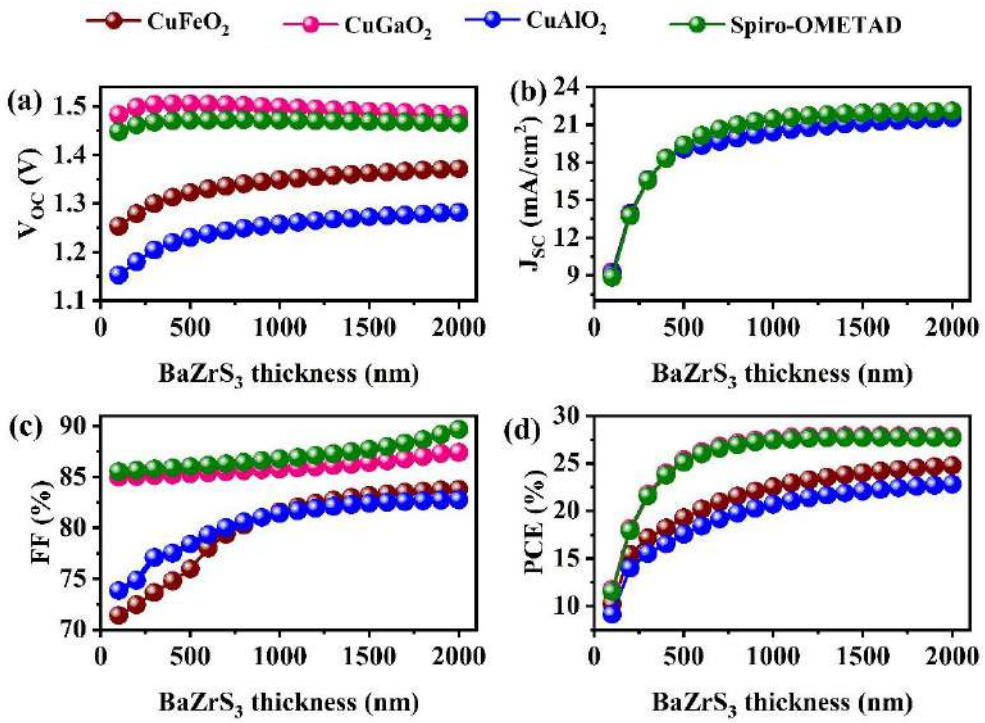

Fig. 63. Performance of $BaZrS_3$ thickness (a-d) solar cell parameters variation (e-h) QE analysis, (i-l) generation rate [260].

6.4.5. Performance of different HTL acceptor density with $BaZrS_3$ absorber

The level of acceptor states in the HTL plays a crucial role in influencing the interfacial characteristics between the active layer and HTL, which affects PV performance [121]. The impact on device performance was evaluated by tuning the HTL acceptor concentration from 10^{12} cm^{-3} to 10^{20} cm^{-3}, while keeping the active layer's acceptor density constant at 10^{16} cm^{-3}, as illustrated in **Fig. 65**(a-d). The results indicate that the V_{OC} remains relatively stable across all solar cells until the HTL acceptor density reaches 10^{16} cm^{-3}. Once this limit is surpassed, a significant rise in V_{OC} is detected, which can be linked to the improved separation of quasi-Fermi levels. This effect arises from the greater electrochemical potential difference between charge carriers in the respective layers of the solar cell. Additionally, significant improvements in both the FF and PCE occur when the HTL acceptor concentration surpasses 10^{16} cm^{-3}. The increase in acceptor concentration of HTL lowers the energy barrier at the HTL/active layer junction, improving electrical conductivity and the internal voltage of the PV performance [39]. These factors together enhance the overall efficiency of the devices. To achieve optimal PCE, an HTL acceptor density of 10^{20} cm^{-3} is recommended for $CuFeO_2$, $CuGaO_2$, $CuAlO_2$, and Spiro-OMeTAD-based solar cells.

The concentration of acceptors in the HTL plays a crucial role in affecting the distortion of energy levels at the junctions with the absorber in solar cells [250]. To investigate these impacts, SCAPS-1D was utilized to produce energy band representations which are illustrated in **Fig. 65**(e-h). The diagrams illustrate the interplay between the HTL's acceptor density and the resulting band bending, along with the E_C and E_V. The results indicate that when the HTL's acceptor density is lower than that of the absorber, the band alignment remains unchanged, leading to consistent solar cell performance up to a density of 10^{16} cm^{-3}. Under these conditions, a significant barrier for hole transport exists at the $BaZrS_3$/HTL junction. When the concentration of acceptors in the HTL exceeds that in the active layer, the energy levels shift downward, reducing the interface barrier and enhancing the transport of charge carriers. In particular, when the concentration of acceptors in the HTL is lower than that in the $BaZrS_3$, holes are likely to gather at the energy states at the interface of the absorber and HTL junction. These states serve as centers for carrier recombination, hindering their movement toward the contacts [125]. In contrast, when the HTL's acceptor density surpasses that of the absorber, the majority of charge carriers occupy states with lower density at the absorber/HTL interface. This shift enhances the carrier transfer potential, lowers the energy bands, and minimizes barriers at the interface [251]. Consequently, the solar cells exhibit improved conductivity. Thus, the acceptor density in the HTL is a critical parameter for determining band bending in $CuFeO_2$, $CuGaO_2$, $CuAlO_2$, and Spiro-OMeTAD-based solar cells, ultimately enabling optimal performance.

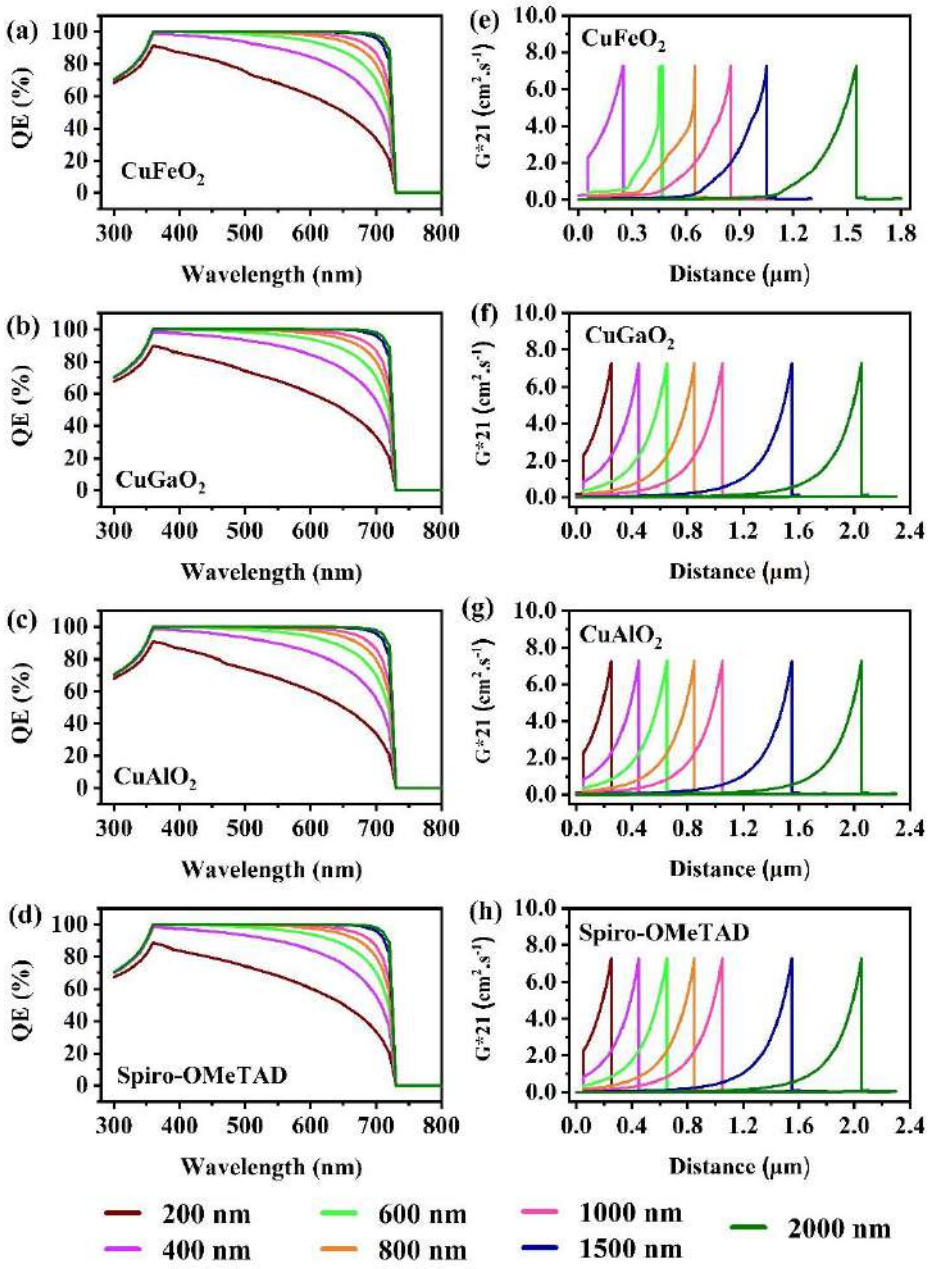

Fig. 64. Performance of $BaZrS_3$ thickness (a-d) QE analysis and (e-h) generation rate [260].

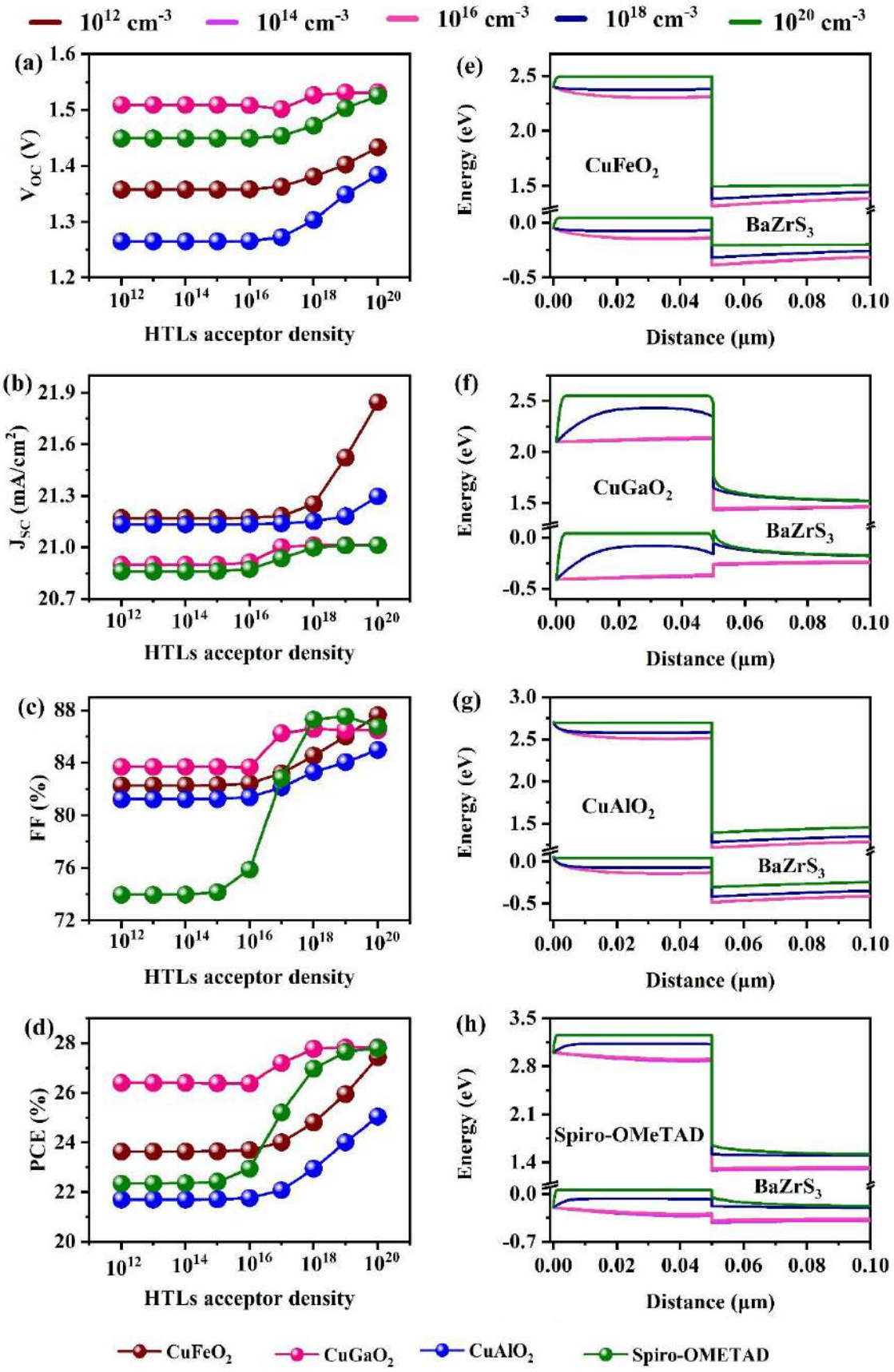

Fig. 65. Performance of different HTL acceptor concentrations (a-d) solar cell parameters variation (e-h) energy level behaviours [260].

Impedance spectroscopy is a highly effective technique for assessing PVefficiency and analyzing the dynamics of charge transport, thereby offering critical insights into their operational processes [136]. Nyquist plots depicting the HTL acceptor concentrations of 10^{12} cm^{-3} and 10^{20} cm^{-3} for $CuFeO_2$, $CuGaO_2$, $CuAlO_2$, and Spiro-OMeTAD-based solar cells, as shown in **Fig. 66**(a-d). Nyquist plots, which were generated using capacitance-frequency (C-F) analysis in SCAPS-1D. The data obtained from these measurements were exported, and the real (x-axis) and imaginary (y-axis) components were used to construct the Nyquist plot graph, representing the impedance behavior of the devices. Each PV devices demonstrate semicircular Nyquist curves, signifying the proficiency of their depletion zones. In the impedance spectra of PV devices, two distinct arcs are typically observed, each corresponding to different frequency domains. The arc present at lower frequencies is indicative of recombination resistance (R_{rec}), whereas the arc at higher frequencies pertains to charge transfer resistance (R_{CT}) [237,252]. In this research, a solitary arc appeared over the entire frequency spectrum, signifying the R_{rec} of the PV device. The results show that the semicircle for the 10^{20} cm^{-3} HTL acceptor density is significantly larger than that for the 10^{12} cm^{-3} density. This indicates an enhanced Rrec in solar cells with a 10^{20} cm^{-3} HTL acceptor density, suggesting that photogenerated charge carriers are effectively collected and retained at their respective interfaces with minimal recombination loss. This enhances a better PCE. On the other hand, the lower R_{rec} found in solar cells with a 10^{12} cm^{-3} HTL acceptor density results in an increased rate of charge carrier recombination, which diminishes performance.

In addition, **Fig. 66**(e-h) illustrates the extraction of built-in potential. This was obtained through the SCAPS-1D simulation by first performing a capacitance-voltage (C-V) analysis on the devices. Using the resulting data, we constructed a Mott-Schottky plot ($1/C^2$ vs. voltage), where the built-in potential was determined from the slope of the linear region. It demonstrates a notable enhancement in the built-in potential as a result of optimizing the HTL acceptor density. For solar cells utilizing $CuFeO_2$, $CuGaO_2$, $CuAlO_2$, and Spiro-OMeTAD, the V_{OC} demonstrated an increase from 1.24 V to 1.38 V, 1.52 V to 1.55 V, 1.61 V to 1.79 V, and 1.54 V to 1.83 V, respectively. Enhancing the built-in potential leads to more effective separation of charge carriers and optimizes their collection at the respective interfaces [108]. As a result, the optimized HTL acceptor density of 10^{20} cm^{-3} leads to PCEs of 27.43%, 27.83%, 25.04%, and 27.80% for solar cells based on $CuFeO_2$, $CuGaO_2$, $CuAlO_2$, and Spiro-OMeTAD, respectively. This research highlights the crucial role of HTL acceptor density in boosting PV performance.

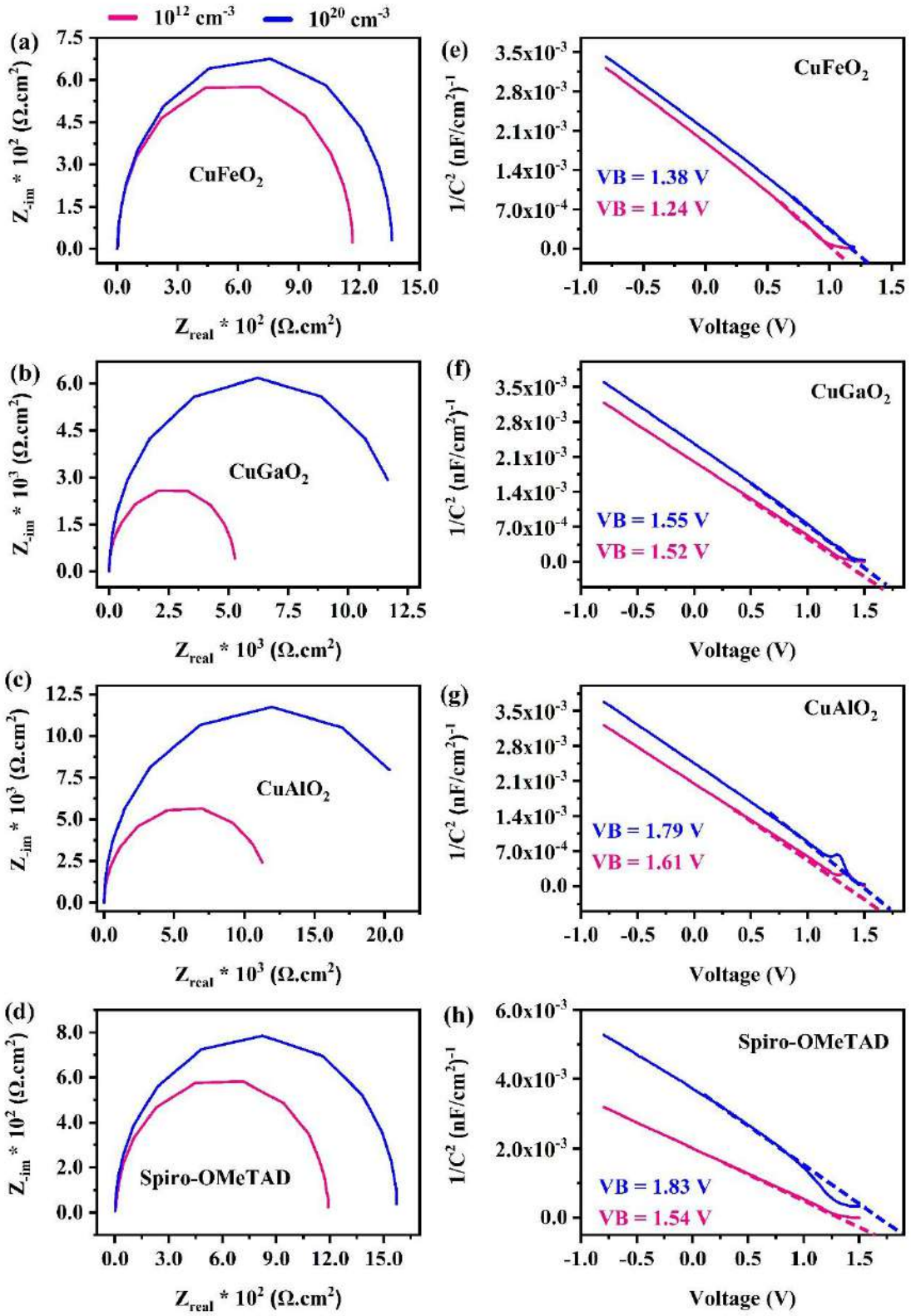

Fig. 66. Performance of acceptor concentration of different HTL's (a-d) Nyquist plot (e-h) Mott-Schottky [260].

6.4.6. Performance of ETL/$BaZrS_3$ and $BaZrS_3$/HTL interface defects properties

During the manufacturing of PV devices, structural flaws inevitably Pb to the formation of interfacial defects. These defects enhance charge carrier recombination at the junctions, thereby significantly reducing the devices' overall efficiency [248,253]. Therefore, it is essential to evaluate the effects of interfacial defects and determine an appropriate defect concentration for efficient production. In this research, a balanced interfacial defect concentration of 10^{12} cm^{-3} was applied at the ETL/$BaZrS_3$ and $BaZrS_3$/HTL junctions for entire PV devices. To examine the impact of interfacial defects on solar cell efficiency, the defect concentration was adjusted between 10^{12} cm^{-3} and 10^{20} cm^{-3} at both junctions. **Fig. 67**(a-d) demonstrates that as the defect concentration increases from 10^{12} cm^{-3} to 10^{20} cm^{-3}, there is a marked reduction in the V_{OC}. In contrast, the J_{SC} remains unchanged until the defect concentration reaches 10^{15} cm^{-3}, at which point it starts to diminish. Similarly, FF exhibits a significant decline, decreasing from 88.28%, 89.40%, 85.05%, and 89.36% to 85.54%, 86.47%, 83.52%, and 86.73% for solar cells based on $CuFeO_2$, $CuGaO_2$, $CuAlO_2$, and Spiro-OMeTAD, respectively. As a result, there is a significant decline in PCE, mainly caused by the degradation of FF at the ETL/absorber junction. Notably, the PCE dropped by approximately 3.28%, 3.61%, 1.97% and 3.59% for $CuFeO_2$, $CuGaO_2$, $CuAlO_2$, and Spiro-OMeTAD-integrated PV devices, respectively. This decline results from increased defect-mediated recombination at the ETL/absorber junction, impeding charge transport toward the front electrode [209,254,255]. The impact of defect concentration at the $BaZrS_3$/HTL junction was examined by adjusting it between 10^{12} cm^{-3} and 10^{20} cm^{-3}, as illustrated in **Fig. 67**(e-h). The PV performance metrics experienced significant decline until the defect concentration reached 10^{17} cm^{-3}, at which point they stabilized. Specifically, PCE declined from 28.34%, 27.83%, 25.05%, and 27.80% to 26.65%, 26.72%, 24.47%, and 24.62% for $CuFeO_2$, $CuGaO_2$, $CuAlO_2$, and Spiro-OMeTAD-integrated PV devices, respectively. This reduction is due to a higher probability of hole trapping at the $BaZrS_3$/HTL junction as the defect concentration increases [116,256,257]. To provide a comprehensive understanding of interface defects, we conducted impedance spectroscopy and recombination studies at both ETL/$BaZrS_3$ and $BaZrS_3$/HTL interfaces**. Fig. 68**(a-h) present the impedance spectra for devices incorporating $CuFeO_2$, $CuGaO_2$, $CuAlO_2$, and Spiro-OMeTAD, comparing high efficiency interface defect of 10^{12} cm^{-3} and low efficiency interface defect of 10^{20} cm^{-3} devices. All PV devices exhibit semicircular Nyquist plots, indicating well-defined depletion zones and effective charge separation. Typically, the impedance spectra show two distinct arcs, each corresponding to different

frequency ranges [192,197]. The arc at lower frequencies reflects higher recombination resistance, suggesting reduced carrier recombination. In contrast, the arc at higher frequencies is associated with lower recombination resistance, implying increased recombination activity. As shown in **Fig. 69**(a-h), devices with a higher interface defects of 10^{20} cm^{-3} exhibit increased recombination, as evidenced by the smaller semicircular arcs. Conversely, the larger semicircles observed for 10^{12} cm^{-3} lower interface defect indicate significantly lower recombination losses. These results underscore the importance of minimizing interface defects, particularly maintaining them around 10^{12} cm^{-3} interface defect at both the ETL/$BaZrS_3$ and $BaZrS_3$/HTL interfaces to enhance PV performance and achieve higher device efficiency.

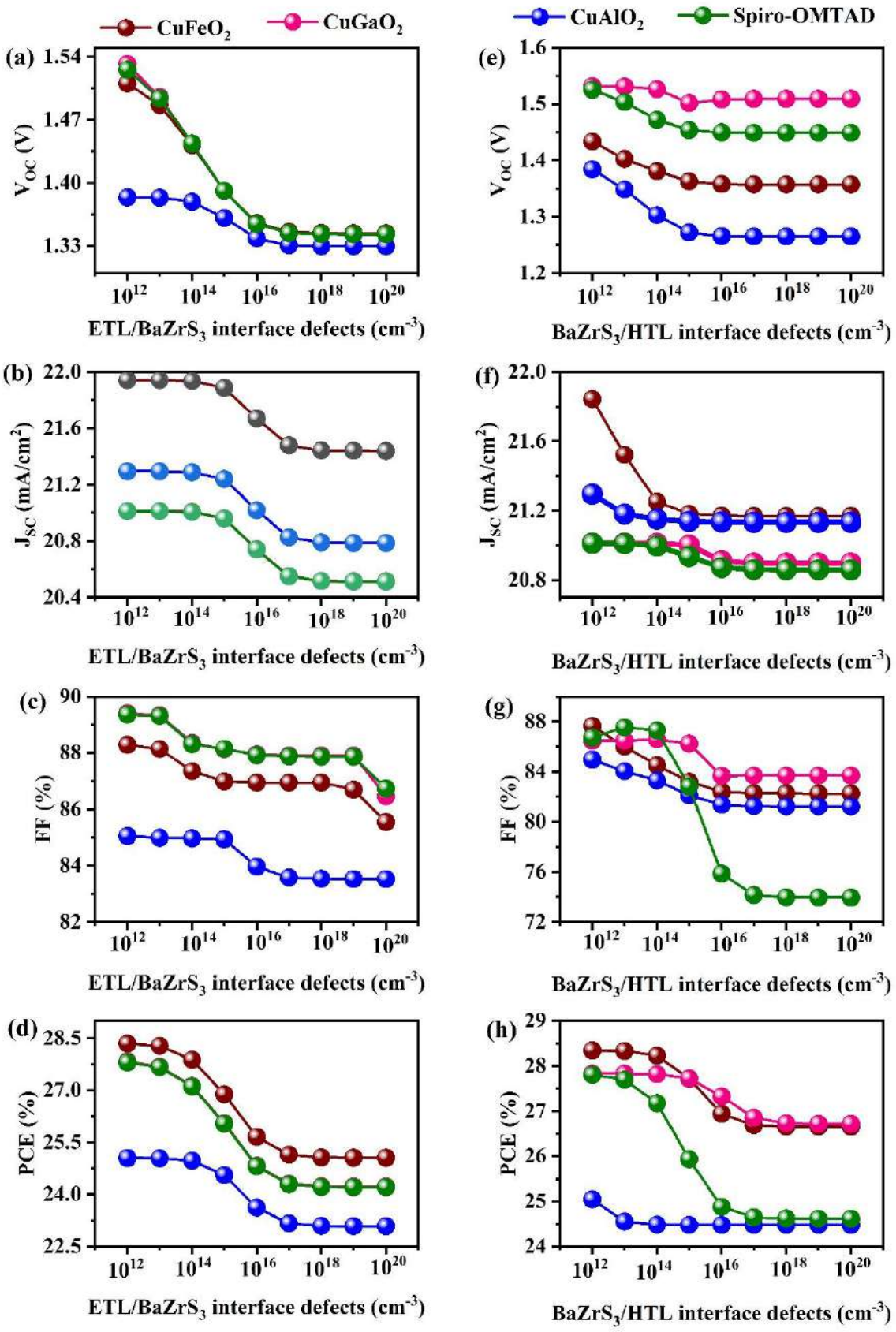

Fig. 67. Performance of interface defects for photovoltaic performance (a-d) ETL/$BaZrS_3$ (e-h) $BaZrS_3$/HTL [260].

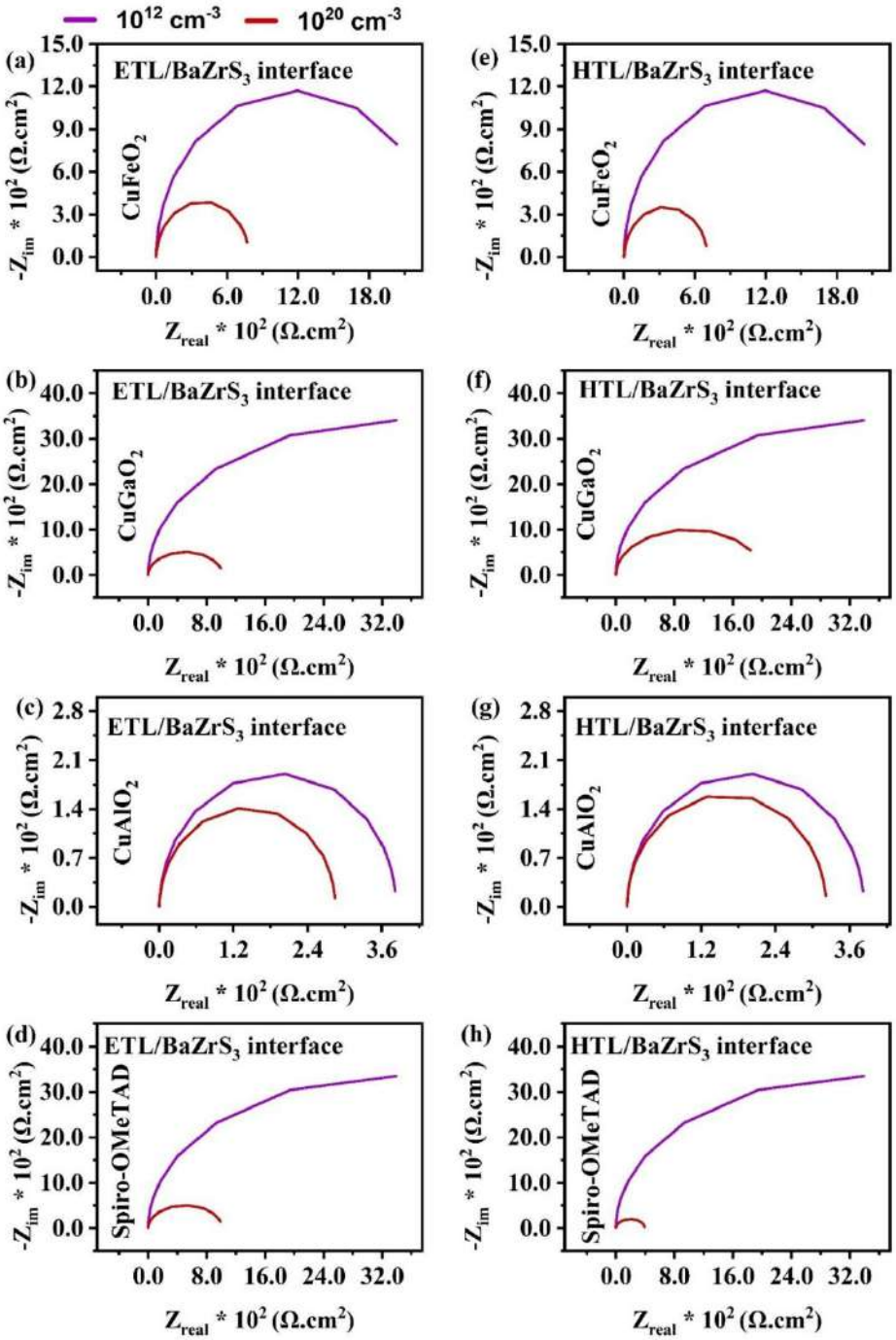

Fig. 68. Performance of impedance spectroscopy relation in interface defects for photovoltaic performance (a-d) ETL/$BaZrS_3$ interface defects (e-h) $BaZrS_3$/HTL interface defects [260].

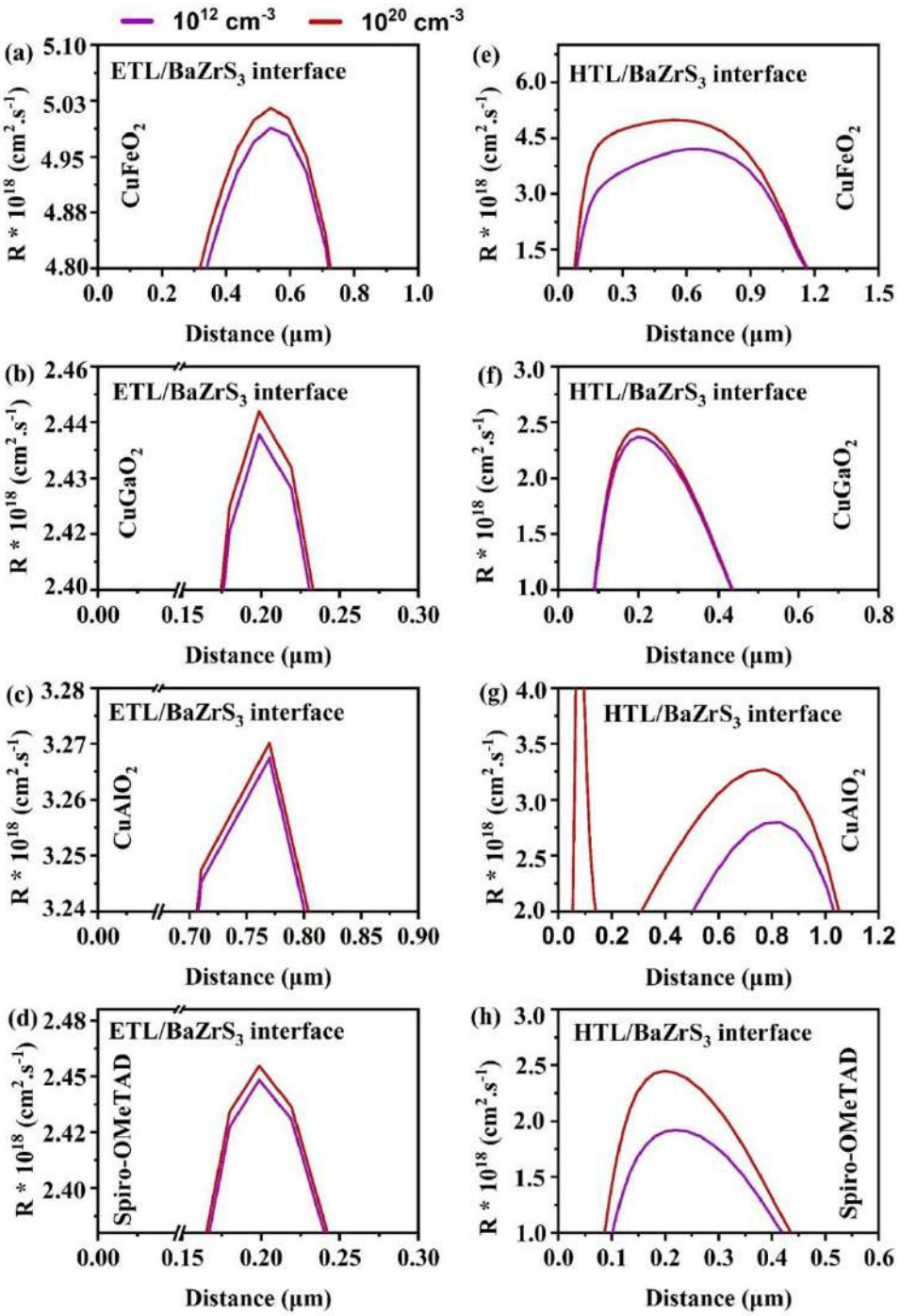

Fig. 69. Performance of recombination mechanism relation in interface defects for photovoltaic performance (a-d) ETL/$BaZrS_3$ interface defects (e-h) $BaZrS_3$/HTL interface defects [260].

6.4.7. Comparison between base device and optimized device

6.4.7.1. Nyquist Plot and Recombination mechanisms

Fig. 70(a-d) illustrates the impedance spectra obtained from (C-F) analysis for both the baseline and optimized PV cells, which incorporate $CuFeO_2$, $CuGaO_2$, $CuAlO_2$, and Spiro-OMeTAD. The plots illustrate a semi-circular configuration, underscoring the significance of

charge-depleted zones in optimizing the functionality of PV devices. The impedance spectra of PV devices typically exhibit two distinct arcs, each associated with unique frequency domains. The weak-frequency arc is indicative of recombination resistance (R_{rec}), whereas the high-frequency are corresponding to charge transfer resistance (R_{CT}) [114,197]. In this research, the presence of a singular arc spanning the entire frequency spectrum was noted, highlighting the significant impact of R_{rec} on the PV devices being studied. Notably, the arc in the impedance spectra of the optimized devices is larger compared to their base devices, indicating a higher R_{rec} in the enhanced PV devices. The increase in R_{rec} signifies an improved collection and retention of photogenerated carriers at the respective electrodes, resulting in reduced charge loss and thereby enhancing PCE. On the other hand, the baseline devices exhibit a lower R_{rec} in charge carrier recombination, resulting in reduced efficiency, as illustrated in **Fig. 70**(e-h).

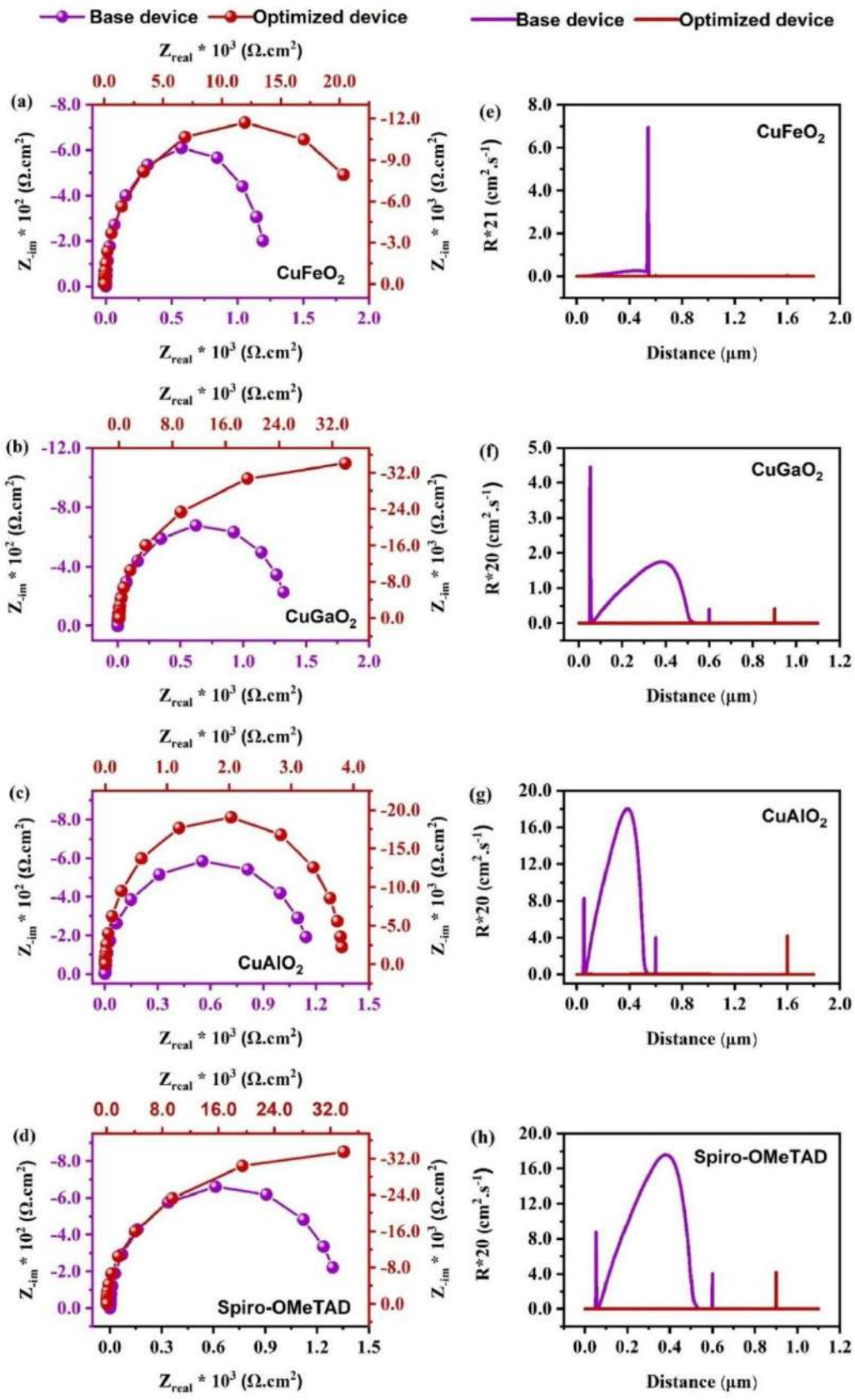

Fig. 70. Performance of baseline and optimized device (a-d) Nyquist plot (e-h) Recombination rate [260].

6.4.7.2. QE measurements and Generation rate

Analyzing QE is essential for assessing the performance of solar cells, as it offers valuable insights into the processes of light absorption, the excitation and dissociation of charge carriers, and the subsequent collection of these photoinduced carriers at their respective electrodes [39]. **Fig. 71**(a-d) presents the QE of both baseline and optimized PV devices incorporating $CuFeO_2$, $CuGaO_2$, $CuAlO_2$, and Spiro-OMeTAD. In the initial configuration, the absorption of light starts to diminish at roughly 300 nm, whereas the improved devices exhibit a stable optical response that extends up to approximately 600 nm. This enhancement in the optimized PV device is attributed to improved light absorption, with overall absorption rates of 67.72%, 65.66%, 67.79%, and 65.66% for $CuFeO_2$, $CuGaO_2$, $CuAlO_2$, and Spiro-OMeTAD, respectively. These values represent increases of 1.97%, 1.87%, 1.99%, and 1.90% compared to the base devices. Notably, all optimized solar cells achieve QE values approaching 100% within the visible wavelength range (400–700 nm), indicating efficient photon capture and substantial charge carrier generation at their contacts evidenced in **Fig. 71**(e-h). This superior efficiency arises from the proper energy band alignment in the optimized devices for all four absorbers. Conversely, the base solar cells exhibit QE values below 60% within the same range due to poor band alignment and suboptimal back-contact properties, which Pb to increased nonradiative recombination and lower production of charge carriers. The improved optical response observed in the optimized PV device is attributed to the expanded depletion region within the absorber, as corroborated by capacitance-voltage measurements [51]. This expansion facilitates greater light absorption and significantly improves the overall efficiency of PV devices.

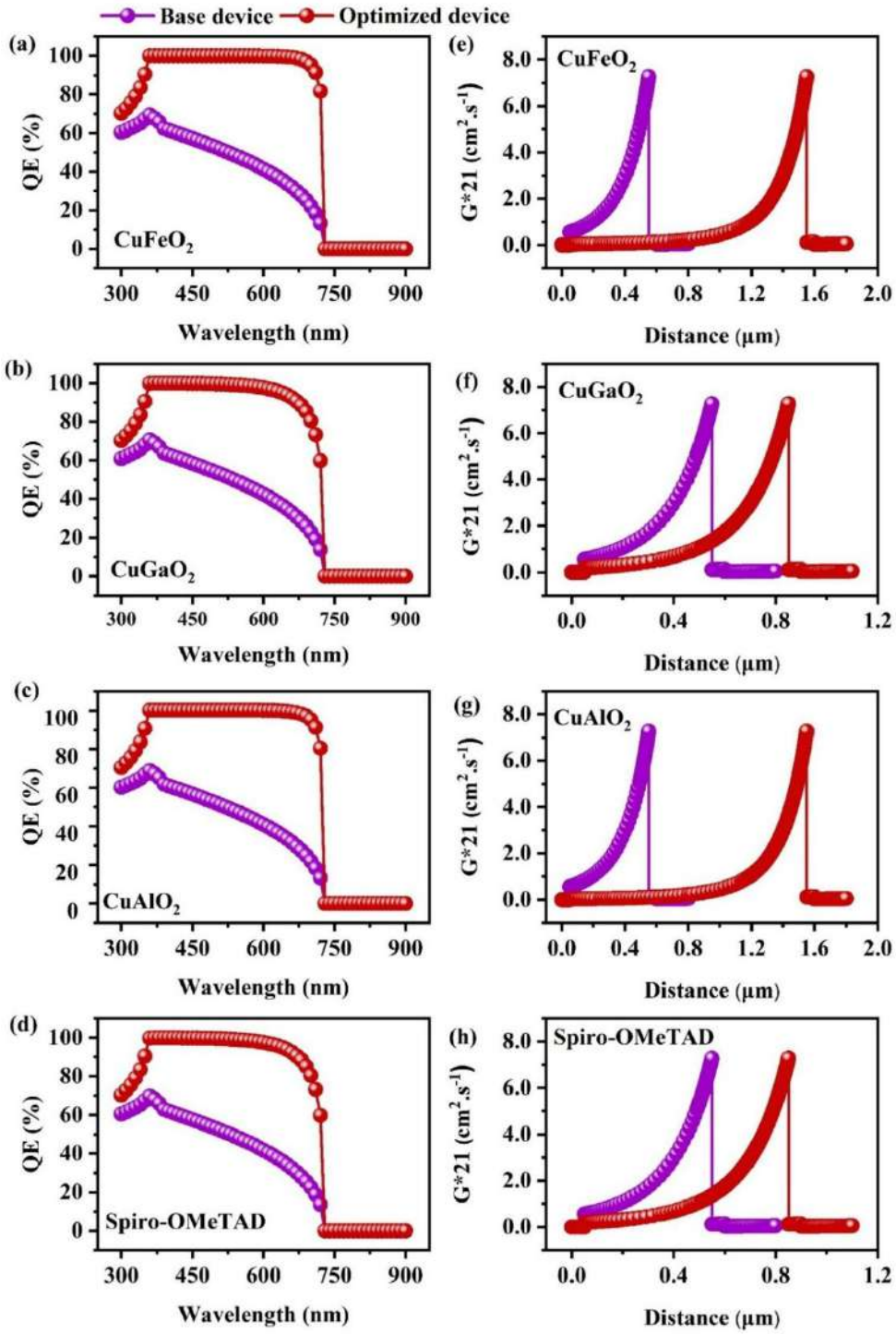

Fig. 71. Performance of baseline and optimized device (a-d) Analysis of QE (e-h) generation rate [260].

6.4.7.3. Electric field and J-V characteristics

The intrinsic electric field established at heterojunctions or homojunctions within a PV device is essential for modulating its performance [51]. To evaluate this aspect, the distribution of the electric field across the layers in PV devices incorporating $CuFeO_2$, $CuGaO_2$, $CuAlO_2$,

and Spiro-OMeTAD absorbers was analyzed, as depicted in **Fig. 72**(a-d). The findings show that optimized devices consistently demonstrate enhanced electric field strength relative to the baseline device. The enhanced internal field is pivotal in the efficient dissociation of charge carrier pairs generated through light absorption, thereby reducing carrier losses and improving the flow of photo-induced charges within the device. Moreover, the enhanced internal field facilitates charge transport, enabling negatively and positively charged carriers to traverse the semiconductor layers more efficiently toward the contacts [39]. This minimizes carrier recombination, improves the FF, and enhances PCE. Moreover, the intensified internal field maintains a wider gap between the quasi-Fermi levels, leading to a higher V_{OC}. Collectively, these factors ensure superior performance and efficiency in the optimized devices. The comparative analysis of base and optimized devices revealed significant improvements in solar cell performance for $CuFeO_2$, $CuGaO_2$, $CuAlO_2$, and Spiro-OMeTAD. The optimized solar cells achieved remarkable PCEs of 28.35%, 27.83%, 25.05%, and 27.80%, respectively, primarily driven by enhancements in the J_{SC}, as shown in **Fig. 72**(e-h). Furthermore, notable increases in V_{OC} were recorded, showing an upward trend from 1.17 V to 1.51 V, 1.38 V to 1.53 V, 1.07 V to 1.38 V, and 1.36 V to 1.52 V for $CuFeO_2$, $CuGaO_2$, $CuAlO_2$, and Spiro-OMeTAD, respectively. These advancements suggest minimized energy losses and emphasize the impact of the optimized device's increased built-in potential, strong resistance to carrier recombination, and enhanced ability to capture light [192]. Our findings underscore the impressive performance of optimized devices, with PCEs exceeding >25% for all solar cell configurations. These results provide valuable insights into the design of PCE of $CuFeO_2$, $CuGaO_2$, $CuAlO_2$, and Spiro-OMeTAD solar cells, offering a foundation for further advancements in solar cell technology.

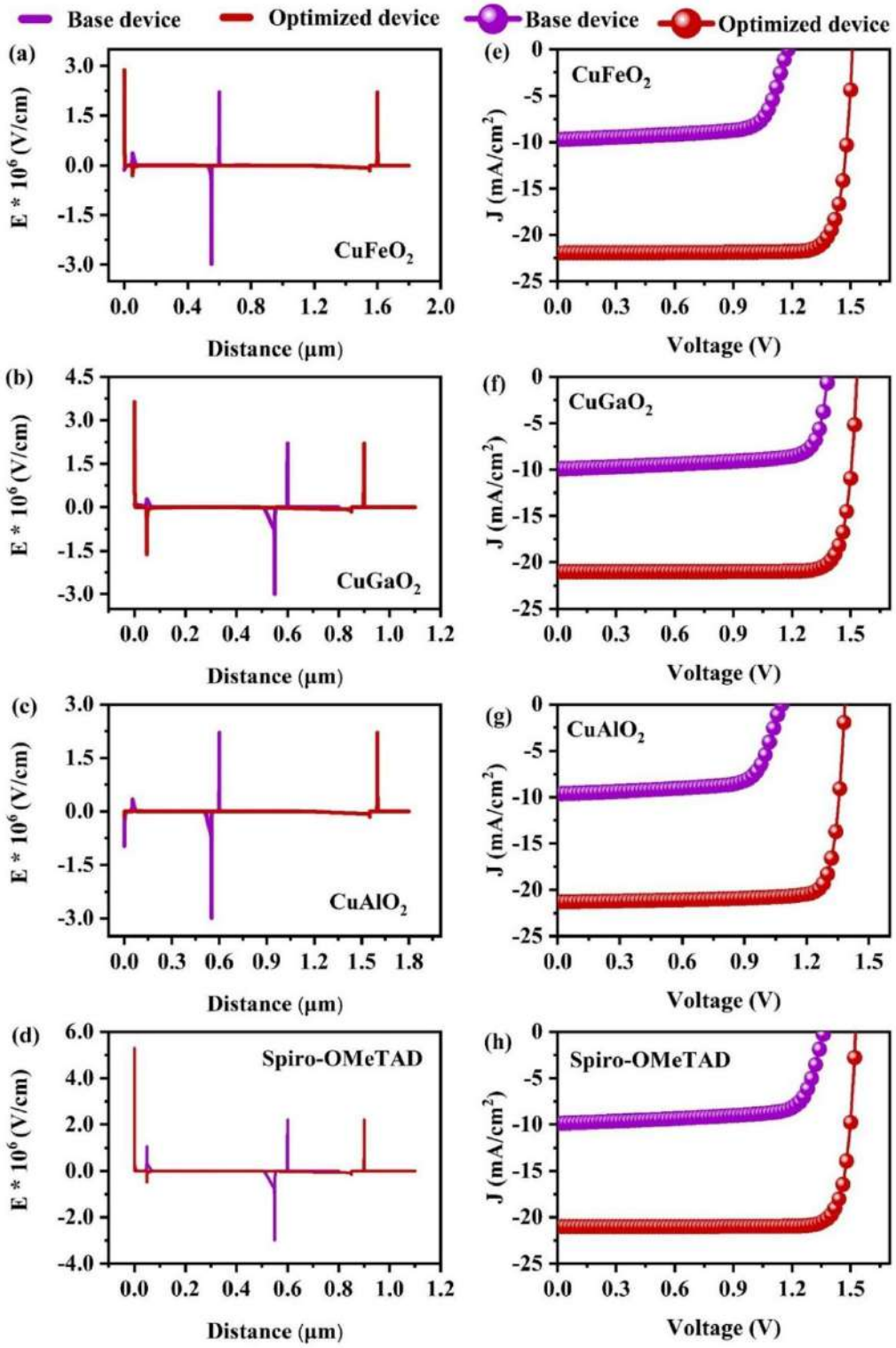

Fig. 72. Performance of baseline and optimized device (a-d) electric field (e-h) JV measurements [260].

6.4.8. Evaluation of SCAPS-1D outcomes in relation to $BaZrS_3$ CPs devices found in existing studies.

Table 18 provides a detailed summary of computational studies on PV devices based on CPs, modeled using the SCAPS-1D software. $BaZrS_3$, one of the CPs compounds studied, has garnered significant interest. Early research indicated a PCE of 12.12% for this compound. However, subsequent advancements in device architecture have significantly improved this efficiency, with the highest reported PCE reaching 28.17%. These advancements emphasize the importance of refining device architecture to improve PV efficiency. Despite these advancements, the literature primarily focuses on dioxide and disulfide variants of CPs, leaving a notable research gap for further exploration. Recently, inorganic ternary metal oxides have gained considerable attention due to their versatile oxidation states, which allow precise tuning of their electrical and optical properties. A comparison of our findings reveals that inorganic delafossite HTLs such as $CuFeO_2$, $CuGaO_2$, and $CuAlO_2$ achieve higher PCEs compared to Spiro-OMeTAD and other HTLs. This improvement is likely due to superior charge transport properties or better energy band alignment with $BaZrS_3$. Notably, the performance of the FTO/TiO_2/$BaZrS_3$/$CuFeO_2$/Au device highlights the potential of $CuFeO_2$ as an exceptional HTL. Its integration leads to significant enhancements in the efficiency of $BaZrS_3$-based solar cells, establishing it as a promising candidate for further performance improvements in CPs PVs.

Table 18. Comparison between SCAPS-1D results of $BaZrS_3$ CP solar cell.

Device structure	V_{OC} (V)	J_{SC} (mA/cm^2)	FF (%)	PCE (%)	Ref
FTO/TiO_2/$BaZrS_3$/Spiro-OMeTAD/Au	0.70	22.00	79.40	12.12	[147]
FTO/TiO_2 /$BaZrS_3$/Cu_2O /Au	1.16	12.24	87.13	12.42	[29]
FTO/TiO_2/$BaZrS_3$/Spiro-OMeTAD/Au	1.21	16.54	86.26	17.29	[146]
AZO/i-ZnO/CdS/ $BaZrS_3$/ a-Si	1.31	19.08	78.88	19.72	[137]
FTO/ZrS_2/$BaZrS_3$/SnS/Pt	1.18	29.74	80.15	28.17	[39]
FTO/TiO_2/$BaZrS_3$/Pt	0.39	0.71	63.00	0.17	[92]
FTO/TiO_2/$BaZrS_3$/$CuFeO_2$/Au	1.51	21.94	85.54	28.35	*
FTO/TiO_2/$BaZrS_3$/ $CuGaO_2$/Au	1.53	21.01	86.47	27.83	*
FTO/TiO_2/$BaZrS_3$/ $CuAIO_2$/Au	1.38	21.29	84.97	25.05	*
FTO/TiO_2/$BaZrS_3$/Spiro-OMeTAD/Au	1.52	21.01	86.74	27.80	*
*** Indicates the results of the present work.**					

6.4.9. Experimental suggestions to achieve the highest PCE of $BaZrS_3$ absorber with delafossite HTLs.

The simulations conducted in this work provide a thorough theoretical exploration of device engineering for solar cells based on $CuFeO_2$, $CuGaO_2$, $CuAlO_2$, and Spiro-OMeTAD. The highest PCE of 28.35% was achieved with the FTO/TiO_2/$BaZrS_3$/$CuFeO_2$/Au configuration, showcasing its significant potential in solar cell design. Given the lack of experimental reports on fabricating $BaZrS_3$-based solar cells, this study aims to provide valuable guidelines for researchers to achieve optimal PCEs in practical applications. To address the challenges associated with experimental fabrication, several strategies have been proposed based on insights from existing literature, ensuring a pathway for creating high-efficiency solar cells. The $BaZrS_3$ absorber layer can be produced through several techniques, such as solid-state synthesis, layered metal sulfides, hybrid colloidal inks, and selenium flux. Our SCAPS simulation results reveal that $BaZrS_3$ absorbers perform optimally when their thickness reaches 800 nm. To ensure $BaZrS_3$ absorbers reach the desired thickness, methods such as vapor deposition and sputtering can be utilized to precisely adjust the thickness of the film. In environments with high sulfur and low zirconium levels, $BaZrS_3$ demonstrates significant P-type characteristics, featuring an optimal acceptor concentration of 10^{16} cm^{-3}. By incorporating this composition, the density of defects is diminished, as the substantial energy needed to create deep-level defects leads to a decrease in their occurrence [258]. $CuFeO_2$ can be produced through several techniques, such as the solid-state reaction, glycine-nitrate process (GNP), sol-gel method, and hydrothermal technique. Additionally, the acceptor density in $CuFeO_2$ can be enhanced by doping with elements like Mg or Ni to improve p-type conductivity [259]. To achieve effective defect control, stoichiometry is optimized, and annealing is conducted in oxygen-rich conditions, which ensures excellent performance as an HTL [207]. To conclude, the discussed approaches and techniques provide significant promise for advancing PVs, facilitating the development of efficient $BaZrS_3$-driven devices as the field progresses.

7. Conclusion

In this thesis, we systematically investigated the photovoltaic potential of novel CPs semiconductors as lead-free alternatives to conventional perovskite absorbers. We began our work by examining the performance of $SrHfSe_3$ solar cells using 41 different 41 HTLs, which included inorganic semiconductors, polymers, and MXenes, as well as 9 different metal contacts. Next, we tailored the absorber properties of $ABSe_3$ (A = Ca, Ba; B = Zr, Hf; X = Se)

and Zr-alloyed $BaHfS_3$ solar cells. We also evaluated the suitability of delafossite HTLs as alternatives to Spiro-OMeTAD in $BaZrS_3$ solar cells. Throughout these studies, we investigated device performance by optimizing parameters related to the ETL, absorber, and HTL layer, including thickness, carrier concentration, and defect density. Additionally, we examined the influence of interface properties, series and shunt resistance, and operating temperature. As a result, we designed a total of 3,043 configurations and conducted comprehensive investigations using various characterization techniques, including C-V, Mott-Schottky analysis, impedance spectroscopy, quantum efficiency, recombination resistance, generation rate, and band alignment. The research outcomes are detailed below.

1. The first study demonstrated the potential of $SrHfSe_3$ in solar cell applications. The initial device structure, which consisted of SLG/FTO/$BaSnO_3$/$SrHfSe_3$/MoS_2/Au, achieved a PCE of 11.42%. This efficiency increased to 15.25% after optimizing the absorber thickness to 700 nm and the carrier density to 10^{18} cm^{-3}, enhancing both photon absorption (45%) and the built-in potential (1.04V). Further increasing the MoS_2 carrier concentration to 10^{20} cm^{-3} resulted in 1.17 times boost in PCE, due to upward shifts in the energy band. By replacing the back contact with Ni, an ohmic contact was achieved, resulting in an efficiency increase of 26.21%. Additionally, experiments with 40 alternative HTLs and simulations of 1,627 configurations yielded maximum PCEs of 27.87% (SnS), 27.39% (CPE-K), and 26.30% (Ti_2CO_2). These improvements were primarily attributed to favorable band alignment, higher recombination resistance, and stronger near-infrared absorption of 58.22%, 56.67%, and 60.48% in SnS, CPE-K, and Ti_2CO_2 based solar cells, respectively.

2. The second study focused on evaluating the absorbers $CaZrSe_3$, $BaZrSe_3$, $CaHfSe_3$, and $BaHfSe_3$. By optimizing the absorber thickness and carrier concentration, light absorption improved by 5.83%, 4.77%, 7.3%, and 11.93%, respectively. These changes also enhanced conductivity and built-in potential, facilitating more efficient charge transport. Further optimizing the HTL thickness, carrier concentration, and defect density increased PCEs by about 5.1% across all devices, owing to the formation of stronger electric fields at the absorber/HTL interface. After these optimizations, the PCE increased from 9.94% to 30.08%, 10.14% to 30.58%, 8.20% to 22.74% and 13.04% to 27.60% for $CaZrSe_3$, $BaZrSe_3$, $CaHfSe_3$, and $BaHfSe_3$. This increase in efficiency was driven by enhanced absorption of 57.78%, 61.10%, 43.94%, and 51.57% and by the highest generation rates of 1.22×10^{22} $cm^{-3}s^{-1}$, 1.35×10^{22} $cm^{-3}s^{-1}$, 7.77×10^{21} $cm^{-3}s^{-1}$, and 1.02×10^{22} $cm^{-3}s^{-1}$ at the absorber/ETL interface respectively. Notably, both $CaZrSe_3$ and $BaZrSe_3$ achieved a PCE >30%, which can be

attributed to their narrow bandgaps, enhanced absorption, and higher charge carrier generation rates.

3. The third study examined the PV potential of $BaHfS_3$ and Zr-alloyed $BaHfS_3$ absorbers. The initial efficiencies were 4.35%, 5.37%, 6.28%, and 7.35% for $BaHfS_3$, $BaHf_{0.75}Zr_{0.25}S_3$, $BaHf_{0.5}Zr_{0.5}S_3$, and $BaHf_{0.25}Zr_{0.75}S_3$, respectively. Following careful optimization of the absorber and HTL properties, these efficiencies improved substantially, reaching 14.67%, 16.43%, 18.62%, and 20.59%, respectively. These gains were largely attributed to enhanced light absorption, with overall absorption rates of 45.60%, 48.10%, 52.70%, and 57.80%. There was a notable rise in V_{OC}, which rose from 1.06 to 1.32 V for $BaHfS_3$, from 1.22 to 1.38 V for $BaHf_{0.75}Zr_{0.25}S_3$, from 1.24 to 1.40 V for $BaHf_{0.5}Zr_{0.5}S_3$, and from 1.25 to 1.42 V for $BaHf_{0.25}Zr_{0.75}S_3$. These improvements indicate a reduction in energy loss, elevated valence band positions, favorable band shifts in the band structure, and stronger electric fields at the absorber/HTL interface, which collectively minimize charge carrier barriers. Among the various compositions studied, $BaHf_{0.25}Zr_{0.75}S_3$ emerged as the most promising, achieving a PCE above 20%. This superior performance is attributed to decreased accumulation capacitance, reduced recombination, and improved band alignment.

4. The fourth study evaluated the PV performance of solar cells using $BaZrS_3$ as the absorber and various delafossite HTLs as an alternative to the conventional Spiro-OMeTAD. At the optimized acceptor density of $BaZrS_3$, set at 10^{16} cm^{-3}, the maximum PCEs recorded were 9.11%, 13.28%, 7.82%, and 11.87% for $CuFeO_2$, $CuGaO_2$, $CuAlO_2$, and Spiro-OMeTAD, respectively. These efficiencies were attributed to a higher V_{OC} and enhanced intrinsic material properties, which reduced recombination losses. Further optimization involved fixing the absorber thickness at 800 nm, which resulted in a PCE increase of approximately 15.3%. This enhancement was driven by extended carrier lifetimes of 1×10^5 ns and longer diffusion lengths of about 3 μm. Modifying the HTL acceptor density helped minimize band offsets, improve carrier transfer, and reduce recombination resistance. Consequently, maximum efficiencies of 28.35%, 27.83%, 23.05%, and 27.80% were achieved using $CuFeO_2$, $CuGaO_2$, $CuAlO_2$, and Spiro-OMeTAD, respectively. These remarkable outcomes stem from the combined effects of a higher built-in potential, strong absorption, enhanced carrier generation, and reduced energy losses.

This thesis highlights the significant potential of CP semiconductor as a stable, non-toxic, and high-performing absorber layer for thin-film photovoltaics. By integrating various HTLs and

metal contacts and by carefully adjusting the properties of the absorbers, this research establishes valuable guidelines for enhancing device performance. The insights gained from SCAPS-1D simulations not only emphasize the remarkable promise of CPs but also lay a solid foundation for future experimental validation and the practical development of environmentally friendly, high-efficiency solar cells.

8. References

[1] T.-Z. Ang, M. Salem, M. Kamarol, H.S. Das, M.A. Nazari, N. Prabaharan, A comprehensive study of renewable energy sources: Classifications, challenges and suggestions, Energy Strategy Reviews 43 (2022) 100939. **https://doi.org/10.1016/j.esr.2022.100939**.

[2] J. Tian, S.A. Culley, H.R. Maier, A.C. Zecchin, Is renewable energy sustainable? Potential relationships between renewable energy production and the Sustainable Development Goals, Npj Climate Action 3 (2024) 35. **https://doi.org/10.1038/s44168-024-00120-6**.

[3] H.H. Pourasl, R.V. Barenji, V.M. Khojastehnezhad, Solar energy status in the world: A comprehensive review, Energy Reports 10 (2023) 3474–3493. **https://doi.org/10.1016/j.egyr.2023.10.022**.

[4] F.J.M.M. Nijsse, J.-F. Mercure, N. Ameli, F. Larosa, S. Kothari, J. Rickman, P. Vercoulen, H. Pollitt, The momentum of the solar energy transition, Nat Commun 14 (2023) 6542. **https://doi.org/10.1038/s41467-023-41971-7**.

[5] J. Gómez-Catasús, M.B. Morales, D. Giralt, D.G. del Portillo, R. Manzano-Rubio, L. Solé-Bujalance, F. Sardà-Palomera, J. Traba, G. Bota, Solar photovoltaic energy development and biodiversity conservation: Current knowledge and research gaps, Conserv Lett 17 (2024). **https://doi.org/10.1111/conl.13025**.

[6] G.T. Chala, S.M. Al Alshaikh, Solar Photovoltaic Energy as a Promising Enhanced Share of Clean Energy Sources in the Future—A Comprehensive Review, Energies (Basel) 16 (2023) 7919. **https://doi.org/10.3390/en16247919**.

[7] D. Thakur, S.H. Chang, Material properties and optoelectronic applications of lead halide perovskite thin films, Synth Met 301 (2024) 117535. **https://doi.org/10.1016/j.synthmet.2023.117535**.

[8] V. Hazra, A. Mandal, S. Bhattacharyya, Optoelectronic insights of lead-free layered halide perovskites, Chem Sci 15 (2024) 7374–7393. **https://doi.org/10.1039/D4SC01429D**.

[9] J. Liang, Y. Wang, Y. Zhang, X. Liu, J. Lin, Construction of perovskite homojunction for highly efficient perovskite solar cells by SCAPS-1D, Materials Science and Engineering: B 301 (2024) 117196. **https://doi.org/10.1016/j.mseb.2024.117196**.

[10] Z. Zhang, Y. Liu, Q. Sun, H. Ban, Z. Liu, H. Yu, X. Li, L. Dai, W. Yang, Y. Shen, M. Wang, The importance of elemental lead to perovskites photovoltaics, Chemistry of Inorganic Materials 1 (2023) 100017. **https://doi.org/10.1016/j.cinorg.2023.100017**.

[11] C.R. Kalaiselvi, N. Muthukumarasamy, D. Velauthapillai, M. Kang, T.S. Senthil, Importance of halide perovskites for next generation solar cells – A review, Mater Lett 219 (2018) 198–200. **https://doi.org/10.1016/j.matlet.2018.02.089**.

[12] S.F. Hoefler, G. Trimmel, T. Rath, Progress on lead-free metal halide perovskites for photovoltaic applications: a review, Monatshefte Für Chemie - Chemical Monthly 148 (2017) 795–826. **https://doi.org/10.1007/s00706-017-1933-9**.

[13] S. Nair, S.B. Patel, J. V. Gohel, Recent trends in efficiency-stability improvement in perovskite solar cells, Mater Today Energy 17 (2020) 100449. **https://doi.org/10.1016/j.mtener.2020.100449**.

[14] B. Kazaishvili, NREL Best Research-Cell PV Efficiency Chart, 1976.

[15] M. Li, S. Johnson, L. Gil-Escrig, M. Sohmer, C.A. Figueroa Morales, H. Kim, S. Sidhik, A. Mohite, X. Gong, L. Etgar, H.J. Bolink, A. Palmstrom, M.D. McGehee, N. Rolston, Strategies to improve the mechanical robustness of metal halide perovskite solar cells, Energy Advances 3 (2024) 273–280. **https://doi.org/10.1039/D3YA00377A**.

[16] D.B. Khadka, Y. Shirai, M. Yanagida, K. Miyano, Insights into Accelerated Degradation of Perovskite Solar Cells under Continuous Illumination Driven by Thermal Stress and Interfacial Junction, ACS Appl Energy Mater 4 (2021) 11121–11132. **https://doi.org/10.1021/acsaem.1c02037**.

[17] M.T. Mbumba, D.M. Malouangou, J.M. Tsiba, L. Bai, Y. Yang, M. Guli, Degradation mechanism and addressing techniques of thermal instability in halide perovskite solar

cells, Solar Energy 230 (2021) 954–978. **https://doi.org/10.1016/j.solener.2021.10.070**.

[18] Z. Dai, N.P. Padture, Challenges and opportunities for the mechanical reliability of metal halide perovskites and photovoltaics, Nat Energy 8 (2023) 1319–1327. **https://doi.org/10.1038/s41560-023-01378-6**.

[19] A.D. Khan, M. Mustajab, S. Moeen, M. Imran, M. Ikram, Q. Khan, M. Khan, Advancements in the stability, protection and lead-free strategies of perovskite solar cells: a critical review, Environmental Science: Advances 3 (2024) 1004–1029. **https://doi.org/10.1039/D3VA00401E**.

[20] H. Tang, Y. Xu, X. Hu, Q. Hu, T. Chen, W. Jiang, L. Wang, W. Jiang, Lead-Free Halide Double Perovskite Nanocrystals for Light-Emitting Applications: Strategies for Boosting Efficiency and Stability, Advanced Science 8 (2021). **https://doi.org/10.1002/advs.202004118**.

[21] V. Deswal, S. Kaushik, R. Kundara, S. Baghel, Numerical simulation of highly efficient Cs2AgInBr6-based double perovskite solar cell using SCAPS 1-D, Materials Science and Engineering: B 299 (2024) 117041. **https://doi.org/10.1016/j.mseb.2023.117041**.

[22] Md. Ferdous Rahman, Md. Naim Hasan Toki, A. Kuddus, M.K.A. Mohammed, Md. Rasidul Islam, S. Bhattarai, J. Madan, R. Pandey, R. Marzouki, M. Jemmali, Boosting efficiency above 30 % of novel inorganic Ba_3SbI_3 perovskite solar cells with potential ZnS electron transport layer (ETL), Materials Science and Engineering: B 300 (2024) 117073. **https://doi.org/10.1016/j.mseb.2023.117073**.

[23] R. Kundara, S. Baghel, Predictive design of $KSnI_3$-based perovskite solar cells using SCAPS and machine learning model, Materials Science and Engineering: B 307 (2024) 117536. **https://doi.org/10.1016/j.mseb.2024.117536**.

[24] Md.A.F. Siddique, A.S.Md. Sayem Rahman, The SCAPS-1D simulation of non-toxic $KGeCl_3$ perovskite from DFT derived properties, Materials Science and Engineering: B 303 (2024) 117268. **https://doi.org/10.1016/j.mseb.2024.117268**.

[25] B. Ghosh, S. Chakraborty, H. Wei, C. Guet, S. Li, S. Mhaisalkar, N. Mathews, Poor Photovoltaic Performance of $Cs_3Bi_2I_9$: An Insight through First-Principles Calculations,

The Journal of Physical Chemistry C 121 (2017) 17062–17067. **https://doi.org/10.1021/acs.jpcc.7b03501**.

[26] J. Yang, C. Bao, W. Ning, B. Wu, F. Ji, Z. Yan, Y. Tao, J. Liu, T.C. Sum, S. Bai, J. Wang, W. Huang, W. Zhang, F. Gao, Stable, High-Sensitivity and Fast-Response Photodetectors Based on Lead-Free $Cs_2AgBiBr_6$ Double Perovskite Films, Adv Opt Mater 7 (2019). **https://doi.org/10.1002/adom.201801732**.

[27] Z. Jin, Z. Zhang, J. Xiu, H. Song, T. Gatti, Z. He, A critical review on bismuth and antimony halide-based perovskites and their derivatives for photovoltaic applications: recent advances and challenges, J Mater Chem A Mater 8 (2020) 16166–16188. **https://doi.org/10.1039/D0TA05433J**.

[28] N. Thakur, K.A. Aly, M. Mohery, M.M. Ebrahium, P. Kumar, P. Sharma, Recent advances in $BaZrS_3$ perovskites: Synthesis, properties, and future trends, J Alloys Compd 957 (2023) 170457. **https://doi.org/10.1016/j.jallcom.2023.170457**.

[29] S. Karthick, S. Velumani, J. Bouclé, Chalcogenide $BaZrS_3$ perovskite solar cells: A numerical simulation and analysis using SCAPS-1D, Opt Mater (Amst) 126 (2022) 112250. **https://doi.org/10.1016/j.optmat.2022.112250**.

[30] A.A. Pradhan, S. Agarwal, K.C. Vincent, D.C. Hayes, J.M. Peterson, J.W. Turnley, R.M. Spilker, M.C. Uible, S.C. Bart, L. Huang, K. Kisslinger, R. Agrawal, Emergence of Ruddlesden–Popper phases and other pitfalls for moderate temperature solution deposited chalcogenide perovskites, Mater Chem Front 8 (2024) 3358–3372. **https://doi.org/10.1039/D4QM00441H**.

[31] R. Bystrický, S.K. Tiwari, P. Hutár, M. Sýkora, Thermal Stability of Chalcogenide Perovskites, Inorg Chem 63 (2024) 12826–12838. **https://doi.org/10.1021/acs.inorgchem.4c01308**.

[32] S. Agarwal, K.C. Vincent, R. Agrawal, Quantitative Scales for Haliphilicity of Metals: Tailoring the Halide Affinity of Alkaline Earth Metals to Synthesize Chalcogenide Perovskite $BaMS_3$ (M = Zr, and Hf) and Cu_2BaSnS_4 Compounds, ACS Appl Energy Mater 7 (2024) 10584–10595. **https://doi.org/10.1021/acsaem.4c02205**.

[33] S. Agarwal, K.C. Vincent, J.W. Turnley, D.C. Hayes, M.C. Uible, I. Durán, A.S.M. Canizales, S. Khandelwal, I. Panicker, Z. Andoh, R.M. Spilker, Q. Ma, L. Huang, S.

Hwang, K. Kisslinger, S. Svatek, E. Antolin, S.C. Bart, R. Agrawal, Breaking Barriers in Chalcogenide Perovskite Synthesis: A Generalized Framework for Fabrication of $BaMS_3$ (M═Ti, Zr, Hf) Materials, Adv Funct Mater 34 (2024). **https://doi.org/10.1002/adfm.202405416**.

[34] C. Comparotto, P. Ström, O. Donzel-Gargand, T. Kubart, J.J.S. Scragg, Synthesis of $BaZrS_3$ Perovskite Thin Films at a Moderate Temperature on Conductive Substrates, ACS Appl Energy Mater 5 (2022) 6335–6343. **https://doi.org/10.1021/acsaem.2c00704**.

[35] R. Yang, A.D. Jess, C. Fai, C.J. Hages, Low-Temperature, Solution-Based Synthesis of Luminescent Chalcogenide Perovskite $BaZrS_3$ Nanoparticles, J Am Chem Soc 144 (2022) 15928–15931. **https://doi.org/10.1021/jacs.2c06168**.

[36] K.C. Vincent, S. Agarwal, J.W. Turnley, R. Agrawal, Liquid Flux–Assisted Mechanism for Modest Temperature Synthesis of Large-Grain $BaZrS_3$ and $BaHfS_3$ Chalcogenide Perovskites, Advanced Energy and Sustainability Research 4 (2023). **https://doi.org/10.1002/aesr.202300010**.

[37] D. Tiwari, O.S. Hutter, G. Longo, Chalcogenide perovskites for photovoltaics: current status and prospects, Journal of Physics: Energy 3 (2021) 034010. **https://doi.org/10.1088/2515-7655/abf41c**.

[38] D. Liu, H. Zeng, H. Peng, R. Sa, Computational study of the fundamental properties of Zr-based chalcogenide perovskites for optoelectronics, Physical Chemistry Chemical Physics 25 (2023) 13755–13765. **https://doi.org/10.1039/D3CP01522J**.

[39] E.N. Vincent Mercy, D. Srinivasan, L. Marasamy, Emerging $BaZrS_3$ and $Ba(Zr,Ti)S_3$ Chalcogenide Perovskite Solar Cells: A Numerical Approach Toward Device Engineering and Unlocking Efficiency, ACS Omega 9 (2024) 4359–4376. **https://doi.org/10.1021/acsomega.3c06627**.

[40] A.A. Pradhan, M.C. Uible, S. Agarwal, J.W. Turnley, S. Khandelwal, J.M. Peterson, D.D. Blach, R.N. Swope, L. Huang, S.C. Bart, R. Agrawal, Synthesis of $BaZrS_3$ and $BaHfS_3$ Chalcogenide Perovskite Films Using Single-Phase Molecular Precursors at Moderate Temperatures, Angewandte Chemie International Edition 62 (2023). **https://doi.org/10.1002/anie.202301049**.

[41] L. Romagnoli, A. Ciccioli, P.J. Dale, H.A. Yetkin, R. Panetta, A. Latini, A simple synthetic approach to $BaZrS_3$, $BaHfS_3$, and their solid solutions, Journal of the American Ceramic Society 107 (2024) 698–703. **https://doi.org/10.1111/jace.19506**.

[42] S. Kong, H. Dong, Z. Yu, J. Guo, K. Cao, K. Chen, X. Ke, C. Zhou, J. Deng, S. Yang, Y. Zhang, Ti–S antibonding coupling enables enhanced bandgap tuning in Ti-substituted $BaHfS_3$ perovskite, Ceram Int 50 (2024) 10889–10896. **https://doi.org/10.1016/j.ceramint.2023.12.405**.

[43] R. Chami, A. Lekdadri, L.H. Omari, E.K. Hlil, M. Chafi, Investigation of the photovoltaic properties of $BaHf_{1-x}Zr_xS_3$ chalcogenide perovskites using first principles calculations, Mater Today Energy 20 (2021) 100689. **https://doi.org/10.1016/j.mtener.2021.100689**.

[44] D. Srinivasan, A.-D. Rasu Chettiar, L. Marasamy, Engineering $BaHfS_3$ with Zr alloying to improve solar cell performance: Insights from SCAPS-1D simulations, Materials Science and Engineering: B 315 (2025) 118126. **https://doi.org/10.1016/j.mseb.2025.118126**.

[45] G.G. Njema, J.K. Kibet, A review of chalcogenide-based perovskites as the next novel materials: Solar cell and optoelectronic applications, catalysis and future perspectives, Next Nanotechnology 7 (2025) 100102. **https://doi.org/10.1016/j.nxnano.2024.100102.**

[46] K. Ye, I. Sadeghi, M. Xu, J. Van Sambeek, T. Cai, J. Dong, R. Kothari, J.M. LeBeau, R. Jaramillo, A Processing Route to Chalcogenide Perovskites Alloys with Tunable Band Gap via Anion Exchange, Adv Funct Mater 34 (2024). **https://doi.org/10.1002/adfm.202405135**.

[47] D. Srinivasan, A.-D. Rasu Chettiar, E.N. Vincent Mercy, L. Marasamy, Scrutinizing the untapped potential of emerging $ABSe_3$ (A = Ca, Ba; B = Zr, Hf) chalcogenide perovskites solar cells, Sci Rep 15 (2025) 3454. **https://doi.org/10.1038/s41598-024-80473-4.**

[48] K.A. Aly, N. Thakur, P. Kumar, Y. Saddeek, T. Shater, Y.A.M. Ismail, P. Sharma, Optimizing solar cell performance with chalcogenide Perovskites: A numerical study of $BaZrSe_3$ absorber layers, Solar Energy 282 (2024) 112961. **https://doi.org/10.1016/j.solener.2024.112961**.

[49] N. Thakur, P. Kumar, P. Sharma, Simulation study of chalcogenide perovskite ($BaZrSe_3$) solar cell by SCAPS-1D, Mater Today Proc (2023). **https://doi.org/10.1016/j.matpr.2023.01.012**.

[50] E. Osei-Agyemang, C. Enninful Adu, G. Balasubramanian, Doping and Anisotropy–Dependent Electronic Transport in Chalcogenide Perovskite $CaZrSe_3$ for High Thermoelectric Efficiency, Adv Theory Simul 2 (2019). **https://doi.org/10.1002/adts.201900060**.

[51] E.N. Vincent Mercy, A. Rasu Chettiar, D. Srinivasan, L. Marasamy, Unlocking the Potential of Emerging $SrZrSe_3$ Solar Cells with Diverse Inorganic Metal Sulfide Hole Transport Layers, Energy Technology 13 (2025). **https://doi.org/10.1002/ente.202401459**.

[52] D. Srinivasan, A.-D. Rasu Chettiar, K.T. Arockiadoss, L. Marasamy, A new class of $SrHfSe_3$ chalcogenide perovskite solar cells with diverse HTMs: Theoretical modelling towards efficiency enhancement, Solar Energy Materials and Solar Cells 290 (2025) 113727. **https://doi.org/10.1016/j.solmat.2025.113727**.

[53] R. Ghosh, A. Singh, P. Agarwal, Study on effect of different HTL and ETL materials on the perovskite solar cell performance with TCAD simulator, Mater Today Proc (2023). **https://doi.org/10.1016/j.matpr.2023.06.161**.

[54] M.K. Hossain, G.F.I. Toki, A. Kuddus, M.H.K. Rubel, M.M. Hossain, H. Bencherif, Md.F. Rahman, Md.R. Islam, M. Mushtaq, An extensive study on multiple ETL and HTL layers to design and simulation of high-performance lead-free $CsSnCl_3$-based perovskite solar cells, Sci Rep 13 (2023) 2521. **https://doi.org/10.1038/s41598-023-28506-2.**

[55] J. Hakami, A comprehensive study to optimize organic/inorganic ETL and HTL materials on double perovskite layer $Cs_2AgBiBr_6$ solar cells with SCAPS 1D simulator, Results in Engineering 25 (2025) 104044. **https://doi.org/10.1016/j.rineng.2025.104044**.

[56] M. Kohan, T. Mahmoudi, Y. Wang, Y.H. Im, Y.-B. Hahn, $SnO_2/BaSnO_3$ electron transport materials for stable and efficient perovskite solar cells, Appl Surf Sci 613 (2023) 156068. **https://doi.org/10.1016/j.apsusc.2022.156068**.

[57] C.W. Myung, G. Lee, K.S. Kim, La-doped $BaSnO_3$ electron transport layer for perovskite solar cells, J Mater Chem A Mater 6 (2018) 23071–23077. **https://doi.org/10.1039/C8TA08764D**.

[58] L. Zhu, J. Ye, X. Zhang, H. Zheng, G. Liu, X. Pan, S. Dai, Performance enhancement of perovskite solar cells using a La-doped $BaSnO_3$ electron transport layer, J Mater Chem A Mater 5 (2017) 3675–3682. **https://doi.org/10.1039/C6TA09689A.**

[59] M.M. Tavakoli, P. Yadav, R. Tavakoli, J. Kong, Surface Engineering of TiO_2 ETL for Highly Efficient and Hysteresis-Less Planar Perovskite Solar Cell (21.4%) with Enhanced Open-Circuit Voltage and Stability, Adv Energy Mater 8 (2018). **https://doi.org/10.1002/aenm.201800794**.

[60] M.R. Mohammadi, F. Saremi, Enhancing perovskite solar cells with nanostructured $TiO_2/BaTiO_3$ electron transport bilayers: Materials design and performance, Materials Science and Engineering: B 320 (2025) 118454. **https://doi.org/10.1016/j.mseb.2025.118454**.

[61] S. Mohammadi, S. Akbari Nia, D. Abbaszadeh, Reduction of recombination at the interface of perovskite and electron transport layer with graded pt quantum dot doping in ambient air-processed perovskite solar cell, Sci Rep 14 (2024) 24254. **https://doi.org/10.1038/s41598-024-75495-x**.

[62] C. Li, D. Ye, J. Tan, Zinc-Doped Delafossite $CuGaO_2$: An Innovative Candidate for Stable Hole Transport Layers in Tin-Perovskite Solar Cell Architectures, Surfaces and Interfaces (2025) 106915. **https://doi.org/10.1016/j.surfin.2025.106915**.

[63] J. Shi, T.F.T. Cerqueira, W. Cui, F. Nogueira, S. Botti, M.A.L. Marques, High-throughput search of ternary chalcogenides for p-type transparent electrodes, Sci Rep 7 (2017) 43179. **https://doi.org/10.1038/srep43179**.

[64] A. Bouich, J.C. Torres, H. Chfii, J. Marí-Guaita, Y.H. Khattak, F. Baig, B.M. Soucase, P. Palacios, Delafossite as hole transport layer a new pathway for efficient perovskite-based solar sells: Insight from experimental, DFT and numerical analysis, Solar Energy 250 (2023) 18–32. **https://doi.org/10.1016/j.solener.2022.12.022.**

[65] W. Hou, Y. Xiao, G. Han, J.-Y. Lin, The Applications of Polymers in Solar Cells: A Review, Polymers (Basel) 11 (2019) 143. **https://doi.org/10.3390/polym11010143**.

[66] X. Zhang, H. Zhang, Y. Li, S. Zafar, S. Yang, J. Chen, H. Zhou, Y. Zhang, Recent Progress in Hole-Transporting Layers of Conventional Organic Solar Cells with p–i–n Structure, Adv Funct Mater 32 (2022). **https://doi.org/10.1002/adfm.202205398**.

[67] S.K. Azadi, S. Asgharizadeh, Comparative performance analysis of HTLs in MXene-assisted perovskite solar cells, Opt Commun 529 (2023) 129104. **https://doi.org/10.1016/j.optcom.2022.129104**.

[68] P.K. Kanti, D.J. K., J. Swapnalin, V. Vicki Wanatasanappan, Advancements and prospects of MXenes in emerging solar cell technologies, Solar Energy Materials and Solar Cells 285 (2025) 113540. **https://doi.org/10.1016/j.solmat.2025.113540**.

[69] D. Huang, H. Xiang, R. Ran, W. Wang, W. Zhou, Z. Shao, Recent Advances in Nanostructured Inorganic Hole-Transporting Materials for Perovskite Solar Cells, Nanomaterials 12 (2022) 2592. **https://doi.org/10.3390/nano12152592**.

[70] Q. Wang, Z. Lin, J. Su, Z. Hu, J. Chang, Y. Hao, Recent progress of inorganic hole transport materials for efficient and stable perovskite solar cells, Nano Select 2 (2021) 1055–1080. **https://doi.org/10.1002/nano.202000238**.

[71] S. Karthick, J. Bouclé, S. Velumani, Effect of bismuth interfacial layer with different HTL's in FAPI based perovskite solar cell – SCAPS – 1D study, Solar Energy 218 (2021) 157–168. **https://doi.org/10.1016/j.solener.2021.02.041**.

[72] K. Sekar, L. Marasamy, S. Mayarambakam, P. Selvarajan, J. Bouclé, Highly efficient lead-free silver bismuth iodide (Ag_3BiI_6) rudorffite solar cells with novel device architecture: A numerical study, Mater Today Commun 38 (2024) 108347. **https://doi.org/10.1016/j.mtcomm.2024.108347**.

[73] S. Rabhi, K. Sekar, K. Kalna, Y.I. Bouderbala, N. Bouri, N. Oueldna, N. Belbachir, K. Dadda, M.S. Aida, N. Attaf, Experimental findings and SCAPS-1D simulations for high-efficiency $MAPbI_3$ perovskite solar cells beyond 31%, Opt Quantum Electron 56 (2024) 1372. **https://doi.org/10.1007/s11082-024-07282-x**.

[74] S. Karthick, S. Velumani, J. Bouclé, Experimental and SCAPS simulated formamidinium perovskite solar cells: A comparison of device performance, Solar Energy 205 (2020) 349–357. **https://doi.org/10.1016/j.solener.2020.05.041**.

[75] A. Goetzberger, J. Luther, G. Willeke, Solar cells: past, present, future, Solar Energy Materials and Solar Cells 74 (2002) 1–11. **https://doi.org/10.1016/S0927-0248(02)00042-9.**

[76] P. Sharma, R.K. Mishra, Comprehensive study on photovoltaic cell's generation and factors affecting its performance: A Review, Mater Renew Sustain Energy 14 (2025) 21. **https://doi.org/10.1007/s40243-024-00292-5**.

[77] H. Latif, J. Liu, D. Mo, R. Wang, J. Zeng, P.F. Zhai, A. Sattar, Effect of Target Morphology on Morphological, Optical and Electrical Properties of FTO Thin Film Deposited by Pulsed Laser Deposition for $MAPbBr_3$ Perovskite Solar Cell, Surfaces and Interfaces 24 (2021) 101117. **https://doi.org/10.1016/j.surfin.2021.101117.**

[78] P. Holzhey, M. Prettl, S. Collavini, C. Mortan, M. Saliba, Understanding the impact of surface roughness: changing from FTO to ITO to PEN/ITO for flexible perovskite solar cells, Sci Rep 13 (2023) 6375. **https://doi.org/10.1038/s41598-023-33147-6.**

[79] S.A. Abubaker, M.Z. Pakhuruddin, An Overview of Electron Transport Layer Materials and Structures for Efficient Organic Photovoltaic Cells, Energy Technology 12 (2024). **https://doi.org/10.1002/ente.202400285.**

[80] A. Kumar, D. Kumar, N. Jain, M. Kumar, G. Ghodake, S. Kumar, R.K. Sharma, J. Holovsky, V.S. Saji, S.K. Sharma, Enhanced efficiency and stability of electron transport layer in perovskite tandem solar cells: Challenges and future perspectives, Solar Energy 266 (2023) 112185. **https://doi.org/10.1016/j.solener.2023.112185**.

[81] S. Foo, M. Thambidurai, P. Senthil Kumar, R. Yuvakkumar, Y. Huang, C. Dang, Recent review on electron transport layers in perovskite solar cells, Int J Energy Res 46 (2022) 21441–21451. **https://doi.org/10.1002/er.7958**.

[82] P. Kumar, S. You, A. Vomiero, Recent Progress in Materials and Device Design for Semi-transparent Photovoltaic Technologies, Adv Energy Mater 13 (2023). **https://doi.org/10.1002/aenm.202301555.**

[83] M. Maoz, Z. Abbas, S.A.B. Shah, V. Lughi, Recent Advances in Flexible Solar Cells; Materials, Fabrication, and Commercialization, Sustainability 17 (2025) 1820. **https://doi.org/10.3390/su17051820**.

[84] P. Baraneedharan, S. Sekar, S. Murugesan, D. Ahamada, S.A.B. Mohamed, Y. Lee, S. Lee, Recent Advances and Remaining Challenges in Perovskite Solar Cell Components for Innovative Photovoltaics, Nanomaterials 14 (2024) 1867. **https://doi.org/10.3390/nano14231867**.

[85] M.A. Deshmukh, S.-J. Park, B.S. Hedau, T.-J. Ha, Recent progress in solar cells based on carbon nanomaterials, Solar Energy 220 (2021) 953–990. **https://doi.org/10.1016/j.solener.2021.04.001**.

[86] S. Liu, V.P. Biju, Y. Qi, W. Chen, Z. Liu, Recent progress in the development of high-efficiency inverted perovskite solar cells, NPG Asia Mater 15 (2023) 27. **https://doi.org/10.1038/s41427-023-00474-z**.

[87] Y.-Y. Sun, M.L. Agiorgousis, P. Zhang, S. Zhang, Chalcogenide Perovskites for Photovoltaics, Nano Lett 15 (2015) 581–585**. https://doi.org/10.1021/nl504046x**.

[88] Z. Yu, H. Hui, D. West, H. Zhang, Y. Sun, S. Kong, Y. Zhang, C. Deng, S. Yang, S. Zhang, H. Zeng, Chalcogenide Perovskite Thin Films with Controlled Phases for Optoelectronics, Adv Funct Mater 34 (2024). **https://doi.org/10.1002/adfm.202309514**.

[89] C. Comparotto, P. Ström, O. Donzel-Gargand, T. Kubart, J.J.S. Scragg, Synthesis of $BaZrS_3$ Perovskite Thin Films at a Moderate Temperature on Conductive Substrates, ACS Appl Energy Mater 5 (2022) 6335–6343. **https://doi.org/10.1021/acsaem.2c00704**.

[90] Z. Yu, X. Wei, Y. Zheng, H. Hui, M. Bian, S. Dhole, J.-H. Seo, Y.-Y. Sun, Q. Jia, S. Zhang, S. Yang, H. Zeng, Chalcogenide perovskite $BaZrS_3$ thin-film electronic and optoelectronic devices by low temperature processing, Nano Energy 85 (2021) 105959. **https://doi.org/10.1016/j.nanoen.2021.105959**.

[91] D. Zilevu, O.O. Parks, S.E. Creutz, Solution-phase synthesis of the chalcogenide perovskite barium zirconium sulfide as colloidal nanomaterials, Chemical Communications 58 (2022) 10512–10515. **https://doi.org/10.1039/D2CC03494H**.

[92] P. Dallas, K. Gkini, A. Kaltzoglou, L. Givalou, M. Konstantakou, S. Orfanoudakis, N. Boukos, E. Sakellis, P. Tsipas, A. Kalafatis, A.G. Karydas, A. Lagogiannis, P. Falaras, V. Psycharis, T. Stergiopoulos, Exploring the potential of powder-to-film processing for

proof-of-concept $BaZrS_3$ perovskite solar cells, Mater Today Commun 39 (2024) 108608. **https://doi.org/10.1016/j.mtcomm.2024.108608**.

[93] S.M. Park, M. Wei, N. Lempesis, W. Yu, T. Hossain, L. Agosta, V. Carnevali, H.R. Atapattu, P. Serles, F.T. Eickemeyer, H. Shin, M. Vafaie, D. Choi, K. Darabi, E.D. Jung, Y. Yang, D. Bin Kim, S.M. Zakeeruddin, B. Chen, A. Amassian, T. Filleter, M.G. Kanatzidis, K.R. Graham, L. Xiao, U. Rothlisberger, M. Grätzel, E.H. Sargent, Low-loss contacts on textured substrates for inverted perovskite solar cells, Nature 624 (2023) 289–294. **https://doi.org/10.1038/s41586-023-06745-7**.

[94] E. Van Kerschaver, G. Beaucarne, Back-contact solar cells: a review, Progress in Photovoltaics: Research and Applications 14 (2006) 107–123. **https://doi.org/10.1002/pip.657**.

[95] T. Ji, R.S. Delima, D.J. Dvorak, Y. Cao, S. Ren, T.D. Morrissey, X. Lu, C.P. Berlinguette, High-Efficiency Perovskite Solar Cells with Sputtered Metal Contacts, ACS Appl Mater Interfaces 14 (2022) 50731–50738. **https://doi.org/10.1021/acsami.2c10204**.

[96] M.K. Hossain, A.K. Datta, M.S. Uddin, A. Kumar, A. Agrawal, R.A. Alshgari, V.K. Mishra, Numerical modeling and performance evaluation of non-toxic Cs_2TiF_6 based perovskite solar cells: A SCAPS-1D simulation study, Journal of Physics and Chemistry of Solids 203 (2025) 112734. **https://doi.org/10.1016/j.jpcs.2025.112734**.

[97] S. Bhattarai, R. Pandey, J. Madan, S. Tayeng, P.K. Kalita, M.Z. Ansari, L. Ben Farhat, M. Amami, M.K. Hossain, Comparative study of distinct halide composites for highly efficient perovskite solar cells using a SCAPS-1D simulator, RSC Adv 13 (2023) 26851–26860. **https://doi.org/10.1039/D3RA04134D**.

[98] T.M. Khan, M.A. Shams, M.M. Khatun, J.H. Chowdhury, M.S. Uddin, T.A. Emon, M.M. Shakil, S.R. Al Ahmed, Predictive modeling and optimization of WS_2 thin-film solar cells: A comprehensive study integrating machine learning, deep learning and SCAPS-1D approaches, Renew Energy 252 (2025) 123519. **https://doi.org/10.1016/j.renene.2025.123519**.

[99] H. Li, J. Cheng, L. Tu, H. Wang, X. Liu, J. Zhang, Y. Zhu, L. Huang, Device design and simulation of wide band-gap $CsPbBr_3$ based ETL-free perovskite solar cell, Renew Energy 245 (2025) 122765. **https://doi.org/10.1016/j.renene.2025.122765**.

[100] A. Chauhan, M. Alla, A. Oudhia, A.K. Shrivastav, F. Elfatouaki, M. Alla, B. Fares, B. Narayana, A.K. Sinha, Complete study to boosting the power conversion efficiency of inorganic double perovskite Cs_2SnI6 non-toxic and stable with efficiency ~23 %, Renew Energy 242 (2025) 122425. **https://doi.org/10.1016/j.renene.2025.122425**.

[101] S. Çetinkaya, S. Yildirimcan, Design and optimization study of all inorganic based double-absorption- layer $CsPbI_3/MoS_2$ heterojunction perovskite solar cells by SCAPS-1D, Journal of Physics and Chemistry of Solids 195 (2024) 112274. **https://doi.org/10.1016/j.jpcs.2024.112274**.

[102] Md.F. Rahman, Md.A. Monnaf, M. Amami, L. Ben Farhat, Md.A. Rahman, Improving the efficiency above 35 % of MoS_2-based solar cells by through optimization of various wide-bandgap S-chalcogenides ETL, Journal of Physics and Chemistry of Solids 194 (2024) 112216. **https://doi.org/10.1016/j.jpcs.2024.112216**.

[103] R. Ranjan, N. Anand, M.N. Tripathi, N. Srivastava, A.K. Sharma, M. Yoshimura, L. Chang, R.N. Tiwari, SCAPS study on the effect of various hole transport layer on highly efficient 31.86% eco-friendly CZTS based solar cell, Sci Rep 13 (2023) 18411. **https://doi.org/10.1038/s41598-023-44845-6**.

[104] J.C. Zepeda Medina, E. Rosendo Andrés, C. Morales Ruíz, E. Camacho Espinosa, L. Treviño Yarce, R. Galeazzi Isasmendi, R. Romano Trujillo, G. García Salgado, A. Coyopol Solis, F.G. Nieto Caballero, A.C. Carranza Sanchez, Performance simulation of solar cell based on AZO/CdTe heterostructure by SCAPS 1D software, Heliyon 9 (2023) e14547. **https://doi.org/10.1016/j.heliyon.2023.e14547**.

[105] S. Kong, H. Dong, Z. Yu, J. Guo, K. Cao, K. Chen, X. Ke, C. Zhou, J. Deng, S. Yang, Y. Zhang, Ti–S antibonding coupling enables enhanced bandgap tuning in Ti-substituted BaHfS3 perovskite, Ceram Int 50 (2024) 10889–10896. **https://doi.org/10.1016/j.ceramint.2023.12.405**.

[106] N.N. Som, V. Sharma, V. Mankad, M.L.C. Attygalle, P.K. Jha, Role of $CuAlO_2$ as an absorber layer for solar energy converter, Solar Energy 193 (2019) 799–805. **https://doi.org/10.1016/j.solener.2019.09.098**.

[107] S. Bhattarai, M.K.A. Mohammed, J. Madan, R. Pandey, H. Abdelkader, L. Ben Farhat, M. Amami, M.K. Hossain, Comparative Study of Different Perovskite Active Layers for

Attaining Higher Efficiency Solar Cells: Numerical Simulation Approach, Sustainability 15 (2023) 12805**. https://doi.org/10.3390/su151712805**.

[108] L. Marasamy, R. Aruna-Devi, O. Iván Domínguez Robledo, J. Álvaro Chávez Carvayar, N. Enrique Vázquez Barragán, J. Santos-Cruz, S. Andrea Mayén-Hernández, G. Contreras-Puente, M. de la Luz Olvera, F. de Moure Flores, Probing the significance of RF magnetron sputtering conditions on the physical properties of CdS thin films for ultra-thin CdTe photovoltaic applications, Appl Surf Sci 574 (2022) 151640. **https://doi.org/10.1016/j.apsusc.2021.151640**.

[109] A. Sunny, S.R. Al Ahmed, Numerical Simulation and Performance Evaluation of Highly Efficient Sb_2Se_3 Solar Cell with Tin Sulfide as Hole Transport Layer, Physica Status Solidi (b) 258 (2021). **https://doi.org/10.1002/pssb.202000630**.

[110] J. V. Li, X. Li, D.S. Albin, D.H. Levi, A method to measure resistivity, mobility, and absorber thickness in thin-film solar cells with application to CdTe devices, Solar Energy Materials and Solar Cells 94 (2010) 2073–2077. **https://doi.org/10.1016/j.solmat.2010.06.018**.

[111] Y. Chen, Y. Wang, R. Wang, X. Hu, J. Tao, G.-E. Weng, C. Zhao, S. Chen, Z. Zhu, J. Chu, H. Akiyama, Importance of Interfacial Passivation in the High Efficiency of Sb_2Se_3 Thin-Film Solar Cells: Numerical Evidence, ACS Appl Energy Mater 3 (2020) 10415–10422. **https://doi.org/10.1021/acsaem.0c01203**.

[112] T. Hossain, M.K. Sobayel, F.T. Munna, S. Islam, H.I. Alkhammash, K. Althubeiti, S.M. Jahangir Alam, K. Techato, Md. Akhtaruzzaman, M.J. Rashid, Tuning the bandgap of Cd_1-ZnS (x = 0~1) buffer layer and CIGS absorber layer for obtaining high efficiency, Superlattices Microstruct 161 (2022) 107100. **https://doi.org/10.1016/j.spmi.2021.107100**.

[113] M.T. Islam, A.K. Thakur, Two stage modelling of solar photovoltaic cells based on Sb_2S_3 absorber with three distinct buffer combinations, Solar Energy 202 (2020) 304–315. **https://doi.org/10.1016/j.solener.2020.03.058**.

[114] K.T. Arockiya-Dass, K. Sekar, L. Marasamy, Theoretical Insights of Degenerate ZrS_2 as a New Buffer for Highly Efficient Emerging Thin-Film Solar Cells, Energy Technology 11 (2023). **https://doi.org/10.1002/ente.202300333**.

[115] W. Meng, B. Saparov, F. Hong, J. Wang, D.B. Mitzi, Y. Yan, Alloying and Defect Control within Chalcogenide Perovskites for Optimized Photovoltaic Application, Chemistry of Materials 28 (2016) 821–829. **https://doi.org/10.1021/acs.chemmater.5b04213**.

[116] S.K. Hwang, J. Park, K.B. Cheon, S.W. Seo, J.E. Song, I.J. Park, S.G. Ji, M. Park, J.Y. Kim, Improved interfacial properties of electrodeposited $Cu_2ZnSn(S,Se)_4$ thin-film solar cells by a facile post-heat treatment process, Progress in Photovoltaics: Research and Applications 28 (2020) 1345–1354. **https://doi.org/10.1002/pip.3332**.

[117] Y. Lv, Y. Shi, X. Song, J. Liu, M. Wang, S. Wang, Y. Feng, S. Jin, C. Hao, Bromine Doping as an Efficient Strategy to Reduce the Interfacial Defects in Hybrid Two-Dimensional/Three-Dimensional Stacking Perovskite Solar Cells, ACS Appl Mater Interfaces 10 (2018) 31755–31764**. https://doi.org/10.1021/acsami.8b09461**.

[118] H.-J. Du, W.-C. Wang, J.-Z. Zhu, Device simulation of lead-free $CH_3NH_3SnI_3$ perovskite solar cells with high efficiency, Chinese Physics B 25 (2016) 108802. **https://doi.org/10.1088/1674-1056/25/10/108802**.

[119] S. Abdelaziz, A. Zekry, A. Shaker, M. Abouelatta, Investigating the performance of formamidinium tin-based perovskite solar cell by SCAPS device simulation, Opt Mater (Amst) 101 (2020) 109738. **https://doi.org/10.1016/j.optmat.2020.109738**.

[120] Y. Nishigaki, T. Nagai, M. Nishiwaki, T. Aizawa, M. Kozawa, K. Hanzawa, Y. Kato, H. Sai, H. Hiramatsu, H. Hosono, H. Fujiwara, Extraordinary Strong Band-Edge Absorption in Distorted Chalcogenide Perovskites, Solar RRL 4 (2020). **https://doi.org/10.1002/solr.201900555**.

[121] A. Swarnkar, W.J. Mir, R. Chakraborty, M. Jagadeeswararao, T. Sheikh, A. Nag, Are Chalcogenide Perovskites an Emerging Class of Semiconductors for Optoelectronic Properties and Solar Cell?, Chemistry of Materials 31 (2019) 565–575. **https://doi.org/10.1021/acs.chemmater.8b04178**.

[122] G. Pindolia, S.M. Shinde, P.K. Jha, Optimization of an inorganic lead free $RbGeI_3$ based perovskite solar cell by SCAPS-1D simulation, Solar Energy 236 (2022) 802–821. **https://doi.org/10.1016/j.solener.2022.03.053.**

[123] C. Walkons, R. Murshed, S. Bansal, Numerical Analysis of Pb-Free Perovskite Absorber Materials: Prospects and Challenges, Solar RRL 4 (2020). **https://doi.org/10.1002/solr.202000299**.

[124] K. Sekar, L. Marasamy, S. Mayarambakam, H. Hawashin, M. Nour, J. Bouclé, Lead-free, formamidinium germanium-antimony halide ($FA_4GeSbCl_{12}$) double perovskite solar cells: the effects of band offsets, RSC Adv 13 (2023) 25483–25496. **https://doi.org/10.1039/D3RA03102K**.

[125] Most.R. Sultana, B. Islam, S.R. Al Ahmed, Modeling and Performance Analysis of Highly Efficient Copper Indium Gallium Selenide Solar Cell with Cu_2O Hole Transport Layer Using Solar Cell Capacitance Simulator in One Dimension, Physica Status Solidi (a) 219 (2022). **https://doi.org/10.1002/pssa.202100512**.

[126] M.K. Hossain, S. Bhattarai, A.A. Arnab, M.K.A. Mohammed, R. Pandey, M.H. Ali, Md.F. Rahman, Md.R. Islam, D.P. Samajdar, J. Madan, H. Bencherif, D.K. Dwivedi, M. Amami, Harnessing the potential of $CsPbBr_3$ -based perovskite solar cells using efficient charge transport materials and global optimization, RSC Adv 13 (2023) 21044–21062. **https://doi.org/10.1039/D3RA02485G**.

[127] A. Ait Abdelkadir, E. Oublal, M. Sahal, A. Gibaud, Numerical simulation and optimization of n-Al-ZnO/n-CdS/p-CZTSe/p-NiO(HTL)/Mo solar cell system using SCAPS-1D, Results in Optics 8 (2022) 100257. **https://doi.org/10.1016/j.rio.2022.100257**.

[128] Md.M.A. Moon, Md.H. Ali, Md.F. Rahman, J. Hossain, A.B.Md. Ismail, Design and Simulation of $FeSi_2$ -Based Novel Heterojunction Solar Cells for Harnessing Visible and Near-Infrared Light, Physica Status Solidi (a) 217 (2020). **https://doi.org/10.1002/pssa.201900921**.

[129] L. Lin, L. Jiang, P. Li, B. Fan, Y. Qiu, A modeled perovskite solar cell structure with a Cu_2O hole-transporting layer enabling over 20% efficiency by low-cost low-temperature processing, Journal of Physics and Chemistry of Solids 124 (2019) 205–211. **https://doi.org/10.1016/j.jpcs.2018.09.024**.

[130] F. Behrouznejad, S. Shahbazi, N. Taghavinia, H.-P. Wu, E. Wei-Guang Diau, A study on utilizing different metals as the back contact of $CH_3NH_3PbI_3$ perovskite solar cells, J Mater Chem A Mater 4 (2016) 13488–13498. **https://doi.org/10.1039/C6TA05938D**.

[131] D. Jayan K., V. Sebastian, Comparative Study on the Performance of Different Lead-Based and Lead-Free Perovskite Solar Cells, Adv Theory Simul 4 (2021). **https://doi.org/10.1002/adts.202100027**.

[132] J.P. Correa Baena, L. Steier, W. Tress, M. Saliba, S. Neutzner, T. Matsui, F. Giordano, T.J. Jacobsson, A.R. Srimath Kandada, S.M. Zakeeruddin, A. Petrozza, A. Abate, M.K. Nazeeruddin, M. Grätzel, A. Hagfeldt, Highly efficient planar perovskite solar cells through band alignment engineering, Energy Environ Sci 8 (2015) 2928–2934. **https://doi.org/10.1039/C5EE02608C**.

[133] N. Mozaffari, D. Walter, T.P. White, A.D. Bui, G.D. Tabi, K. Weber, K.R. Catchpole, Unraveling the Role of Energy Band Alignment and Mobile Ions on Interfacial Recombination in Perovskite Solar Cells, Solar RRL 6 (2022). **https://doi.org/10.1002/solr.202101087**.

[134] T. Minemoto, J. Julayhi, Buffer-less Cu(In,Ga)Se_2 solar cells by band offset control using novel transparent electrode, Current Applied Physics 13 (2013) 103–106. **https://doi.org/10.1016/j.cap.2012.06.019**.

[135] M.T. Khan, M. Salado, A. Almohammedi, S. Kazim, S. Ahmad, Elucidating the Impact of Charge Selective Contact in Halide Perovskite through Impedance Spectroscopy, Adv Mater Interfaces 6 (2019). **https://doi.org/10.1002/admi.201901193**.

[136] M. Haider, C. Zhen, T. Wu, G. Liu, H.-M. Cheng, Boosting efficiency and stability of perovskite solar cells with nickel phthalocyanine as a low-cost hole transporting layer material, J Mater Sci Technol 34 (2018) 1474–1480. **https://doi.org/10.1016/j.jmst.2018.03.005**.

[137] B. Barman, S. Ingole, Analysis of Si Back-Contact for Chalcogenide Perovskite Solar Cells Based on $BaZrS_3$ Using SCAPS-1D, Adv Theory Simul 6 (2023). **https://doi.org/10.1002/adts.202200820**.

[138] P. Singh, N.M. Ravindra, Analysis of series and shunt resistance in silicon solar cells using single and double exponential models, Emerging Materials Research 1 (2012) 33–38. **https://doi.org/10.1680/emr.11.00008**.

[139] D. Jayan K, High-Efficiency Non-Toxic 2-Terminal and 4-Terminal Perovskite-Transition Metal Dichalcogenide Tandem Solar Cells, Adv Theory Simul 5 (2022). **https://doi.org/10.1002/adts.202100611**.

[140] A. Raj, M. Kumar, A. Kumar, A. Laref, A. Anshul, Investigating the potential of lead-free double perovskite $Cs_2AgBiBr_6$ material for solar cell applications: A theoretical study, Int J Energy Res 46 (2022) 13801–13819. **https://doi.org/10.1002/er.8099.**

[141] K. Chakraborty, M.G. Choudhury, S. Paul, Numerical study of Cs_2TiX_6 ($X = Br^-$, I^-, F^- and Cl^-) based perovskite solar cell using SCAPS-1D device simulation, Solar Energy 194 (2019) 886–892. **https://doi.org/10.1016/j.solener.2019.11.005**.

[142] V. Nadenau, U. Rau, A. Jasenek, H.W. Schock, Electronic properties of $CuGaSe_2$-based heterojunction solar cells. Part I. Transport analysis, J Appl Phys 87 (2000) 584–593. **https://doi.org/10.1063/1.371903**.

[143] I. Gharibshahian, A.A. Orouji, S. Sharbati, Efficient $Sb_2(S,Se)_3$/Zn(O,S) solar cells with high open-circuit voltage by controlling sulfur content in the absorber-buffer layers, Solar Energy 227 (2021) 606–615. **https://doi.org/10.1016/j.solener.2021.09.039**.

[144] K. Sekar, S. Mayarambakam, Effect of Annealed and Non-Annealed Inorganic MnS Hole-Transport Layer for Efficient $Sb_2(S,Se)_3$ Solar Cells: A Theoretical Justification, Physica Status Solidi (b) 260 (2023). **https://doi.org/10.1002/pssb.202300087**.

[145] H. Elanzeery, F. Babbe, M. Melchiorre, F. Werner, S. Siebentritt, High-performance low bandgap thin film solar cells for tandem applications, Progress in Photovoltaics: Research and Applications 26 (2018) 437–442. **https://doi.org/10.1002/pip.3026**.

[146] N. Chawki, M. Rouchdi, B. Fares, Numerical Study of $BaZrS_3$ Based Chalcogenide Perovskite Solar Cell Using SCAPS-1D Device Simulation, (2022). **https://doi.org/10.21203/rs.3.rs-1251663/v1**.

[147] N. Thakur, P. Kumar, R. Neffati, P. Sharma, Design and simulation of chalcogenide perovskite $BaZr(S,Se)_3$ compositions for photovoltaic applications, Phys Scr 98 (2023) 065921. **https://doi.org/10.1088/1402-4896/accfc6**.

[148] N. Chawki, M. Rouchdi, M. Alla, B. Fares, Simulation and analysis of high-performance hole transport material $SrZrS_3$-based perovskite solar cells with a theoretical efficiency

approaching 26%, Solar Energy 262 (2023) 111913. **https://doi.org/10.1016/j.solener.2023.111913**.

[149] J. John, V.P. Mahadevan Pillai, A.R. Thomas, R. Philip, J. Joseph, S. Muthunatesan, V. Ragavendran, R. Prabhu, Synthesis, Structural and Morphological Property of $BaSnO_3$ Nano powder Prepared by Solid State Ceramic Method, IOP Conf Ser Mater Sci Eng 195 (2017) 012007. **https://doi.org/10.1088/1757-899X/195/1/012007**.

[150] J. Shi, H. Lu, X. Kang, L. Hou, F. Chen, Y. Zhang, K. Chen, X. Wang, X. Guan, L. Ma, Accelerating electron transport in Eosin Y by bidentately bridging on $BaSnO_3$ for noble-metal-free photocatalytic H2 production, Energy Storage and Saving 2 (2023) 328–335. **https://doi.org/10.1016/j.enss.2022.10.003**.

[151] J. Li, Z. Ma, R. Sa, K. Wu, Improved thermoelectric power factor and conversion efficiency of perovskite barium stannate, RSC Adv 7 (2017) 32703–32709. **https://doi.org/10.1039/C7RA05193J**.

[152] C. Huang, X. Wang, X. Liu, M. Tian, T. Zhang, Extensive analysis of the formation mechanism of $BaSnO_3$ by solid-state reaction between $BaCO_3$ and SnO_2, J Eur Ceram Soc 36 (2016) 583–592. **https://doi.org/10.1016/j.jeurceramsoc.2015.11.001**.

[153] Y.H. Ochoa Muñoz, M. Ponce, J.E. Rodríguez Páez, Comparative study of two wet chemical methods of $BaSnO_3$ synthesis: Mechanism of formation of mixed oxide, Powder Technol 279 (2015) 86–95. **https://doi.org/10.1016/j.powtec.2015.03.049**.

[154] C. Huang, X. Wang, Q. Shi, X. Liu, Y. Zhang, F. Huang, T. Zhang, A Facile Peroxo-Precursor Synthesis Method and Structure Evolution of Large Specific Surface Area Mesoporous $BaSnO_3$, Inorg Chem 54 (2015) 4002–4010. **https://doi.org/10.1021/acs.inorgchem.5b00269**.

[155] R. Kurre, S. Bajpai, P.K. Bajpai, Synthesis, Characterization, Optical and Transport Properties of $BaSnO_3$; Synthesized by Wet Chemical Route, Materials Sciences and Applications 09 (2018) 92–110. **https://doi.org/10.4236/msa.2018.91007**.

[156] J. Cerdà, J. Arbiol, R. Diaz, G. Dezanneau, J.R. Morante, Synthesis of perovskite-type BaSnO3 particles obtained by a new simple wet chemical route based on a sol–gel process, Mater Lett 56 (2002) 131–136. **https://doi.org/10.1016/S0167-577X(02)00428-7.**

[157] A. Tiwari, M.-S. Wong, Substrate temperature effect on structure and properties of sputtered polycrystalline transparent conducting oxide films of La-doped $BaSnO_3$, Thin Solid Films 715 (2020) 138427. **https://doi.org/10.1016/j.tsf.2020.138427**.

[158] H. Paik, Z. Chen, E. Lochocki, A. Seidner H., A. Verma, N. Tanen, J. Park, M. Uchida, S. Shang, B.-C. Zhou, M. Brützam, R. Uecker, Z.-K. Liu, D. Jena, K.M. Shen, D.A. Muller, D.G. Schlom, Adsorption-controlled growth of La-doped BaSnO3 by molecular-beam epitaxy, APL Mater 5 (2017). **https://doi.org/10.1063/1.5001839**.

[159] M. Wu, S. Yu, L. He, L. Yang, W. Zhang, High quality transparent conductive Ag-based barium stannate multilayer flexible thin films, Sci Rep 7 (2017) 103. **https://doi.org/10.1038/s41598-017-00178-9.**

[160] K. Ganguly, P. Ambwani, P. Xu, J.S. Jeong, K.A. Mkhoyan, C. Leighton, B. Jalan, Structure and transport in high pressure oxygen sputter-deposited $BaSnO_{3-\delta}$, APL Mater 3 (2015) 062509. **https://doi.org/10.1063/1.4919969**.

[161] J. Kang, J.H. Lee, H.-K. Lee, K.-T. Kim, J.H. Kim, M.-J. Maeng, J.-A. Hong, Y. Park, K.H. Kim, Effect of Threading Dislocations on the Electronic Structure of La-Doped $BaSnO_3$ Thin Films, Materials 15 (2022) 2417. **https://doi.org/10.3390/ma15072417**.

[162] P. Rajasekaran, M. Arivanandhan, Y. Kumaki, R. Jayavel, Y. Hayakawa, M. Shimomura, Facile synthesis of morphology-controlled La:$BaSnO_3$ for the enhancement of thermoelectric power factor, CrystEngComm 22 (2020) 5363–5374. **https://doi.org/10.1039/D0CE00702A**.

[163] H.J. Cho, T. Onozato, M. Wei, A. Sanchela, H. Ohta, Effects of vacuum annealing on the electron mobility of epitaxial La-doped $BaSnO_3$ films, APL Mater 7 (2019). **https://doi.org/10.1063/1.5054154**.

[164] Q. Liu, F. Jin, G. Gao, B. Li, Y. Zhang, Q. Liu, Transparent and conductive Ta doped BaSnO3 films epitaxially grown on MgO substrate, J Alloys Compd 684 (2016) 125–131. **https://doi.org/10.1016/j.jallcom.2016.05.157**.

[165] U.S. Alaan, P. Shafer, A.T. N'Diaye, E. Arenholz, Y. Suzuki, Gd-doped $BaSnO_3$: A transparent conducting oxide with localized magnetic moments, Appl Phys Lett 108 (2016). **https://doi.org/10.1063/1.4939686**.

[166] H.F. Wang, Q.Z. Liu, F. Chen, G.Y. Gao, W. Wu, X.H. Chen, Transparent and conductive oxide films with the perovskite structure: La- and Sb-doped $BaSnO_3$, J Appl Phys 101 (2007). **https://doi.org/10.1063/1.2736629**.

[167] R. Zhang, X. Li, J. Bi, S. Zhang, S. Peng, Y. Song, Q. Zhang, L. Gu, J. Duan, Y. Cao, One-step epitaxy of high-mobility La-doped $BaSnO_3$ films by high-pressure magnetron sputtering, APL Mater 9 (2021). **https://doi.org/10.1063/5.0046639**.

[168] Y. He, R. Wei, C. Zhou, W. Cheng, X. Ding, C. Shao, L. Hu, W. Song, X. Zhu, Y. Sun, Microstructural Engineering of Solution-Processed Epitaxial La-Doped $BaSnO_3$ Transparent Conducting Films, Cryst Growth Des 21 (2021) 5800–5806. **https://doi.org/10.1021/acs.cgd.1c00698**.

[169] S.P. Ramanandan, A. Giunto, E.Z. Stutz, B. Reynier, I.T.F.M. Lefevre, M. Rusu, S. Schorr, T. Unold, A. Fontcuberta I Morral, J.A. Márquez, M. Dimitrievska, Understanding the growth mechanism of $BaZrS_3$ chalcogenide perovskite thin films from sulfurized oxide precursors, Journal of Physics: Energy 5 (2023) 014013. https://doi.org/10.1088/2515-7655/aca9fe.

[170] K.C. Vincent, S. Agarwal, J.W. Turnley, R. Agrawal, Liquid Flux–Assisted Mechanism for Modest Temperature Synthesis of Large-Grain $BaZrS_3$ and $BaHfS_3$ Chalcogenide Perovskites, Advanced Energy and Sustainability Research 4 (2023). **https://doi.org/10.1002/aesr.202300010**.

[171] C. Comparotto, P. Ström, O. Donzel-Gargand, T. Kubart, J.J.S. Scragg, Synthesis of $BaZrS_3$ Perovskite Thin Films at a Moderate Temperature on Conductive Substrates, ACS Appl Energy Mater 5 (2022) 6335–6343. **https://doi.org/10.1021/acsaem.2c00704**.

[172] Z. Yu, X. Wei, Y. Zheng, H. Hui, M. Bian, S. Dhole, J.-H. Seo, Y.-Y. Sun, Q. Jia, S. Zhang, S. Yang, H. Zeng, Chalcogenide perovskite $BaZrS_3$ thin-film electronic and optoelectronic devices by low temperature processing, Nano Energy 85 (2021) 105959. **https://doi.org/10.1016/j.nanoen.2021.105959**.

[173] R. Yang, A.D. Jess, C. Fai, C.J. Hages, Low-Temperature, Solution-Based Synthesis of Luminescent Chalcogenide Perovskite $BaZrS_3$ Nanoparticles, J Am Chem Soc 144 (2022) 15928–15931. **https://doi.org/10.1021/jacs.2c06168**.

[174] C. Devi, R. Mehra, Device simulation of lead-free $MASnI_3$ solar cell with $CuSbS_2$ (copper antimony sulfide), J Mater Sci 54 (2019) 5615–5624. **https://doi.org/10.1007/s10853-018-03265-y**.

[175] N. Spalatu, J. Hiie, R. Kaupmees, O. Volobujeva, J. Krustok, I. Oja Acik, M. Krunks, Postdeposition Processing of SnS Thin Films and Solar Cells: Prospective Strategy To Obtain Large, Sintered, and Doped SnS Grains by Recrystallization in the Presence of a Metal Halide Flux, ACS Appl Mater Interfaces 11 (2019) 17539–17554. **https://doi.org/10.1021/acsami.9b03213**.

[176] C. Rana, S. Saha, Growth and study of tin sulfide nanocrystals by precipitation technique using triethylamine, Mater Today Proc 11 (2019) 667–672. **https://doi.org/10.1016/j.matpr.2019.03.025**.

[177] P.K. Dutta, S. Mitra, Quick Synthesis of SnS Nanoparticles, Mater Today Proc 5 (2018) 23321–23325. **https://doi.org/10.1016/j.matpr.2018.11.067**.

[178] M. Wu, S. Yu, L. He, L. Yang, W. Zhang, High quality transparent conductive Ag-based barium stannate multilayer flexible thin films, Sci Rep 7 (2017) 103. **https://doi.org/10.1038/s41598-017-00178-9**.

[179] Y. Wu, T. Wei, X. An, L.-M. Liu, Colloidal synthesis of SnS nanocrystals with dimension-dependent photoelectrochemical properties, New Journal of Chemistry 43 (2019) 7457–7462. **https://doi.org/10.1039/C9NJ00506D**.

[180] S. Sohila, R. Ramesh, S. Ramya, S. Ponnusamy, C. Muthamizhchelvan, Synthesis and characterization of SnS/ZnO nanocomposite by chemical method, Journal of Materials Science: Materials in Electronics 24 (2013) 4807–4811**.** **https://doi.org/10.1007/s10854-013-1479-5.**

[181] H. Choi, C.-K. Mai, H.-B. Kim, J. Jeong, S. Song, G.C. Bazan, J.Y. Kim, A.J. Heeger, Conjugated polyelectrolyte hole transport layer for inverted-type perovskite solar cells, Nat Commun 6 (2015) 7348. **https://doi.org/10.1038/ncomms8348**.

[182] J. Cameron, P.J. Skabara, The damaging effects of the acidity in PEDOT:PSS on semiconductor device performance and solutions based on non-acidic alternatives, Mater Horiz 7 (2020) 1759–1772. **https://doi.org/10.1039/C9MH01978B**.

[183] L. Zhang, X. Zhou, X. Zhong, C. Cheng, Y. Tian, B. Xu, Hole-transporting layer based on a conjugated polyelectrolyte with organic cations enables efficient inverted perovskite solar cells, Nano Energy 57 (2019) 248–255. **https://doi.org/10.1016/j.nanoen.2018.12.033**.

[184] H. Jian, H. Chen, L. He, C. Zhao, J. Chen, T. Jiu, G.-H. Tao, Conjugated Polyelectrolyte Combined with Ionic Liquid as the Hole Transport Layer for Efficient Inverted Perovskite Solar Cells, J Electrochem Soc 168 (2021) 036503. **https://doi.org/10.1149/1945-7111/abe8ee.**

[185] M. Xu, S. Lei, J. Qi, Q. Dou, L. Liu, Y. Lu, Q. Huang, S. Shi, X. Yan, Opening Magnesium Storage Capability of Two-Dimensional MXene by Intercalation of Cationic Surfactant, ACS Nano 12 (2018) 3733–3740. **https://doi.org/10.1021/acsnano.8b00959**.

[186] M. Khazaei, A. Ranjbar, M. Arai, T. Sasaki, S. Yunoki, Electronic properties and applications of MXenes: a theoretical review, J Mater Chem C Mater 5 (2017) 2488–2503. **https://doi.org/10.1039/C7TC00140A**.

[187] M. Shi, P. Xiao, J. Lang, C. Yan, X. Yan, Porous g-C_3N_4 and MXene Dual-Confined FeOOH Quantum Dots for Superior Energy Storage in an Ionic Liquid, Advanced Science 7 (2020). **https://doi.org/10.1002/advs.201901975**.

[188] S. Lai, J. Jeon, S.K. Jang, J. Xu, Y.J. Choi, J.-H. Park, E. Hwang, S. Lee, Surface group modification and carrier transport properties of layered transition metal carbides (Ti_2CT_x, T: $^{-}$OH, $^{-}$F and $^{-}$O), Nanoscale 7 (2015) 19390–19396. **https://doi.org/10.1039/C5NR06513E**.

[189] L. Yin, Y. Li, X. Yao, Y. Wang, L. Jia, Q. Liu, J. Li, Y. Li, D. He, MXenes for Solar Cells, Nanomicro Lett 13 (2021) 78. **https://doi.org/10.1007/s40820-021-00604-8**.

[190] A. Iqbal, F. Shahzad, K. Hantanasirisakul, M.-K. Kim, J. Kwon, J. Hong, H. Kim, D. Kim, Y. Gogotsi, C.M. Koo, Anomalous absorption of electromagnetic waves by 2D transition metal carbonitride Ti_3CNT_x (MXene), Science (1979) 369 (2020) 446–450. **https://doi.org/10.1126/science.aba7977**.

[191] Md.S. Rana, Md.M. Islam, M. Julkarnain, Enhancement in efficiency of CZTS solar cell by using CZTSe BSF layer, Solar Energy 226 (2021) 272–287. **https://doi.org/10.1016/j.solener.2021.08.035**.

[192] K.T. Arockiya Dass, M.K. Hossain, L. Marasamy, Highly efficient emerging $Ag_2BaTiSe_4$ solar cells using a new class of alkaline earth metal-based chalcogenide buffers alternative to CdS, Sci Rep 14 (2024) 1473. **https://doi.org/10.1038/s41598-024-51711-6.**

[193] E. Linda, A.-D. Rasu Chettiar, L. Marasamy, Theoretical insights into high-efficiency $BaZr_{0.96}Ti_{0.04}S_3$ chalcogenide perovskite solar cells using phthalocyanine HTLs, Mater Lett 375 (2024) 137203. **https://doi.org/10.1016/j.matlet.2024.137203**.

[194] D.N. Qasim Agha, Q.T. Algwari, The influence of the interface layer between the electron transport layer and absorber on the performance of perovskite solar cells, IOP Conf Ser Mater Sci Eng 1152 (2021) 012033. **https://doi.org/10.1088/1757-899X/1152/1/012033.**

[195] M. Córdoba, K. Taretto, Insight into the Dependence of Photovoltaic Performance on Interfacial Energy Alignment in Solar Cells with Mobile Ions, Solar RRL 8 (2024). **https://doi.org/10.1002/solr.202300742**.

[196] M. Saadat, O. Amiri, P.H. Mahmood, Potential efficiency improvement of $CuSb(S_{1-x},Se_x)_2$ thin film solar cells by the Zn(O,S) buffer layer optimization, Solar Energy 225 (2021) 875–881**. https://doi.org/10.1016/j.solener.2021.08.013.**

[197] E. Linda, A.-D. Rasu Chettiar, L. Marasamy, Emerging class of $SrZrS_3$ chalcogenide perovskite solar cells: Conductive MOFs as HTLs - A game changer?, Solar Energy Materials and Solar Cells 278 (2024) 113204. **https://doi.org/10.1016/j.solmat.2024.113204**.

[198] H. Dixit, N.K. Bansal, S. Porwal, D. Kumar, T. Singh, Performance assessment of earth-abundant Kesterite and lead-free chalcogenide-based perovskite solar cells using SCAPS-1D, Optik (Stuttg) 295 (2023) 171474. **https://doi.org/10.1016/j.ijleo.2023.171474**.

[199] H. Duan, W. Yang, B. Bob, C. Hsu, B. Lei, Y. Yang, The Role of Sulfur in Solution-Processed $Cu_2ZnSn(S,Se)_4$ and its Effect on Defect Properties, Adv Funct Mater 23 (2013) 1466–1471. **https://doi.org/10.1002/adfm.201201732**.

[200] S.Z. Haider, H. Anwar, M. Wang, Theoretical Device Engineering for High-Performance Perovskite Solar Cells Using CuSCN as Hole Transport Material Boost the Efficiency Above 25%, Physica Status Solidi (a) 216 (2019). **https://doi.org/10.1002/pssa.201900102**.

[201] R.T. Mouchou, T.C. Jen, O.T. Laseinde, K.O. Ukoba, Numerical simulation and optimization of p-NiO/n-TiO_2 solar cell system using SCAPS, Mater Today Proc 38 (2021) 835–841. **https://doi.org/10.1016/j.matpr.2020.04.880**.

[202] A.A. El-Naggar, L.A. Lotfy, A.A. Felfela, W. Ismail, M. Abdelfatah, S.W. Sharshir, A. El-Shaer, Numerical simulation-based performance enhancement approach for an inorganic $BaZrS_3$/CuO heterojunction solar cell, Sci Rep 14 (2024) 7614. **https://doi.org/10.1038/s41598-024-57636-4.**

[203] M. Shasti, A. Mortezaali, Numerical Study of Cu_2O, $SrCu_2O_2$, and $CuAlO_2$ as Hole-Transport Materials for Application in Perovskite Solar Cells, Physica Status Solidi (a) 216 (2019). **https://doi.org/10.1002/pssa.201900337**.

[204] A.K. Sharma, D.K. Kaushik, Numerical simulation of $MASnI_3$ /CuI heterojunction based perovskite solar cell, J Phys Conf Ser 2267 (2022) 012148. **https://doi.org/10.1088/1742-6596/2267/1/012148**.

[205] Y. Yuan, G. Yan, C. Dreessen, T. Rudolph, M. Hülsbeck, B. Klingebiel, J. Ye, U. Rau, T. Kirchartz, Shallow defects and variable photoluminescence decay times up to 280 µs in triple-cation perovskites, Nat Mater 23 (2024) 391–397. **https://doi.org/10.1038/s41563-023-01771-2.**

[206] M. Saadat, O. Amiri, Fine adjusting of charge carriers transport in absorber/HTL interface in $Sb_2(S,Se)_3$ solar cells, Solar Energy 243 (2022) 163–173. **https://doi.org/10.1016/j.solener.2022.07.047.**

[207] C. Baiano, E. Schiavo, C. Gerbaldi, F. Bella, G. Meligrana, G. Talarico, P. Maddalena, M. Pavone, A.B. Muñoz-García, Role of surface defects in CO2 adsorption and

activation on $CuFeO_2$ delafossite oxide, Molecular Catalysis 496 (2020) 111181. **https://doi.org/10.1016/j.mcat.2020.111181**.

[208] T.M. Khan, S.R. Al Ahmed, Investigating the Performance of $FASnI_3$ -Based Perovskite Solar Cells with Various Electron and Hole Transport Layers: Machine Learning Approach and SCAPS-1D Analysis, Adv Theory Simul 7 (2024). **https://doi.org/10.1002/adts.202400353**.

[209] A. Hosen, Md.S. Mian, S.R. Al Ahmed, Improving the Performance of Lead-Free $FASnI_3$ -Based Perovskite Solar Cell with Nb_2O_5 as an Electron Transport Layer, Adv Theory Simul 6 (2023). **https://doi.org/10.1002/adts.202200652**.

[210] X. Wang, X. Shi, F. Zhang, F. Zhou, P. Zeng, J. Song, J. Qu, Chemical etching induced surface modification and gentle gradient bandgap for highly efficient $Sb_2(S,Se)_3$ solar cell, Appl Surf Sci 579 (2022) 152193. **https://doi.org/10.1016/j.apsusc.2021.152193**.

[211] A. Raj, M. Kumar, A. Kumar, A. Laref, A. Anshul, Investigating the potential of lead-free double perovskite $Cs_2AgBiBr_6$ material for solar cell applications: A theoretical study, Int J Energy Res 46 (2022) 13801–13819. **https://doi.org/10.1002/er.8099**.

[212] N. Rono, C.C. Ahia, E.L. Meyer, A numerical simulation and analysis of chalcogenide $BaZrS_3$-based perovskite solar cells utilizing different hole transport materials, Results Phys 61 (2024) 107722. **https://doi.org/10.1016/j.rinp.2024.107722**.

[213] N. Chawki, R. Essajai, M. Rouchdi, M. Braiche, M. Al-Hattab, B. Fares, Efficacy analysis of $BaZrS_3$ -based perovskite solar cells: investigated through a numerical simulation, Advances in Materials and Processing Technologies 11 (2025) 389–402. **https://doi.org/10.1080/2374068X.2024.2307093**.

[214] R. Gutzler, W. Witte, A. Kanevce, D. Hariskos, S. Paetel, V_{OC} -losses across the band gap: Insights from a high-throughput inline process for CIGS solar cells, Progress in Photovoltaics: Research and Applications 31 (2023) 1023–1031. **https://doi.org/10.1002/pip.3707**.

[215] P.K. Patel, Device simulation of highly efficient eco-friendly $CH_3NH_3SnI_3$ perovskite solar cell, Sci Rep 11 (2021) 3082. **https://doi.org/10.1038/s41598-021-82817-w**.

[216] M.K. Hossain, A.A. Arnab, R.C. Das, K.M. Hossain, M.H.K. Rubel, Md.F. Rahman, H. Bencherif, M.E. Emetere, M.K.A. Mohammed, R. Pandey, Combined DFT, SCAPS-1D,

and wxAMPS frameworks for design optimization of efficient Cs_2BiAgI_6 -based perovskite solar cells with different charge transport layers, RSC Adv 12 (2022) 34850–34873. **https://doi.org/10.1039/D2RA06734J**.

[217] N. Wu, Y. Wu, D. Walter, H. Shen, T. Duong, D. Grant, C. Barugkin, X. Fu, J. Peng, T. White, K. Catchpole, K. Weber, Identifying the Cause of Voltage and Fill Factor Losses in Perovskite Solar Cells by Using Luminescence Measurements, Energy Technology 5 (2017) 1827–1835. https://doi.org/10.1002/ente.201700374.

[218] H. Baig, H. Kanda, A.M. Asiri, M.K. Nazeeruddin, T. Mallick, Increasing efficiency of perovskite solar cells using low concentrating photovoltaic systems, Sustain Energy Fuels 4 (2020) 528–537. **https://doi.org/10.1039/C9SE00550A**.

[219] A.W. Welch, L.L. Baranowski, H. Peng, H. Hempel, R. Eichberger, T. Unold, S. Lany, C. Wolden, A. Zakutayev, Trade-Offs in Thin Film Solar Cells with Layered Chalcostibite Photovoltaic Absorbers, Adv Energy Mater 7 (2017). **https://doi.org/10.1002/aenm.201601935**.

[220] M.K. Hossain, M.S. Uddin, G.F.I. Toki, M.K.A. Mohammed, R. Pandey, J. Madan, Md.F. Rahman, Md.R. Islam, S. Bhattarai, H. Bencherif, D.P. Samajdar, M. Amami, D.K. Dwivedi, Achieving above 24% efficiency with non-toxic $CsSnI_3$ perovskite solar cells by harnessing the potential of the absorber and charge transport layers, RSC Adv 13 (2023) 23514–23537. **https://doi.org/10.1039/D3RA02910G**.

[221] M. Leng, M. Luo, C. Chen, S. Qin, J. Chen, J. Zhong, J. Tang, Selenization of Sb_2Se_3 absorber layer: An efficient step to improve device performance of CdS/Sb_2Se_3 solar cells, Appl Phys Lett 105 (2014). **https://doi.org/10.1063/1.4894170**.

[222] M.A. Ashraf, I. Alam, Numerical simulation of CIGS, CISSe and CZTS-based solar cells with In_2S_3 as buffer layer and Au as back contact using SCAPS 1D, Engineering Research Express 2 (2020) 035015**. https://doi.org/10.1088/2631-8695/abade6**.

[223] C.W. Hong, S.W. Shin, M.P. Suryawanshi, M.G. Gang, J. Heo, J.H. Kim, Chemically Deposited CdS Buffer/Kesterite Cu_2ZnSnS_4 Solar Cells: Relationship between CdS Thickness and Device Performance, ACS Appl Mater Interfaces 9 (2017) 36733–36744. **https://doi.org/10.1021/acsami.7b09266**.

[224] G. Kartopu, B.L. Williams, V. Zardetto, A.K. Gürlek, A.J. Clayton, S. Jones, W.M.M. Kessels, M. Creatore, S.J.C. Irvine, Enhancement of the photocurrent and efficiency of CdTe solar cells suppressing the front contact reflection using a highly-resistive ZnO buffer layer, Solar Energy Materials and Solar Cells 191 (2019) 78–82. **https://doi.org/10.1016/j.solmat.2018.11.002**.

[225] K. Sarkar, Effects of very thin CdS window layer on CdTe solar cell, JOURNAL OF MECHANICS OF CONTINUA AND MATHEMATICAL SCIENCES 14 (2019) 14–29. **https://doi.org/10.26782/jmcms.2019.06.00002**.

[226] D.K. Shah, D. KC, M. Muddassir, M.S. Akhtar, C.Y. Kim, O.-B. Yang, A simulation approach for investigating the performances of cadmium telluride solar cells using doping concentrations, carrier lifetimes, thickness of layers, and band gaps, Solar Energy 216 (2021) 259–265. **https://doi.org/10.1016/j.solener.2020.12.070**.

[227] T.S. Sherkar, C. Momblona, L. Gil-Escrig, J. Ávila, M. Sessolo, H.J. Bolink, L.J.A. Koster, Recombination in Perovskite Solar Cells: Significance of Grain Boundaries, Interface Traps, and Defect Ions, ACS Energy Lett 2 (2017) 1214–1222. **https://doi.org/10.1021/acsenergylett.7b00236**.

[228] X. Ma, R.A.J. Janssen, G.H. Gelinck, Trap-Assisted Charge Generation and Recombination in State-of-the-Art Organic Photodetectors, Adv Mater Technol 8 (2023). **https://doi.org/10.1002/admt.202300234**.

[229] V. Sarritzu, N. Sestu, D. Marongiu, X. Chang, S. Masi, A. Rizzo, S. Colella, F. Quochi, M. Saba, A. Mura, G. Bongiovanni, Optical determination of Shockley-Read-Hall and interface recombination currents in hybrid perovskites, Sci Rep 7 (2017) 44629. **https://doi.org/10.1038/srep44629**.

[230] Md.F. Wahid, Md.S. Rahman, N. Ahmed, A. Al Mamun, Md.N. Howlader, T. Paul, Md.M.R. Tareq, Md.S. Rahman, Md.M. Rahman, Performance Enhancement of Lead-Free $CsSnI_3$ Perovskite Solar Cell: Design and Simulation with Different Electron Transport Layers, IEEE Access 12 (2024) 8296–8312. **https://doi.org/10.1109/ACCESS.2024.3352444**.

[231] D. Wang, Y. Li, Y. Yang, S. Hayase, H. Wu, R. Wang, C. Ding, Q. Shen, How to minimize voltage and fill factor losses to achieve over 20% efficiency lead chalcogenide quantum

dot solar cells: Strategies expected through numerical simulation, Appl Energy 341 (2023) 121124. **https://doi.org/10.1016/j.apenergy.2023.121124**.

[232] A. Uzum, Device simulations of electron-transfer-layer-free perovskite solar cells focused on absorber/hole transfer-layer interface, Semicond Sci Technol 36 (2021) 075026. **https://doi.org/10.1088/1361-6641/ac01fd**.

[233] A. Srivastava, S.K. Tripathy, T.R. Lenka, V. Goyal, Numerical simulations of novel quaternary chalcogenide $Ag_2MgSn(S/Se)_4$ based thin film solar cells using SCAPS 1-D, Solar Energy 239 (2022) 337–349. **https://doi.org/10.1016/j.solener.2022.05.014**.

[234] M.K. Hossain, D.P. Samajdar, R.C. Das, A.A. Arnab, Md.F. Rahman, M.H.K. Rubel, Md.R. Islam, H. Bencherif, R. Pandey, J. Madan, M.K.A. Mohammed, Design and Simulation of Cs_2BiAgI_6 Double Perovskite Solar Cells with Different Electron Transport Layers for Efficiency Enhancement, Energy & Fuels 37 (2023) 3957–3979. **https://doi.org/10.1021/acs.energyfuels.3c00181.**

[235] T. Kirchartz, W. Gong, S.A. Hawks, T. Agostinelli, R.C.I. MacKenzie, Y. Yang, J. Nelson, Sensitivity of the Mott–Schottky Analysis in Organic Solar Cells, The Journal of Physical Chemistry C 116 (2012) 7672–7680. **https://doi.org/10.1021/jp300397f**.

[236] M.I. Haider, A. Fakharuddin, S. Ahmed, M. Sultan, L. Schmidt-Mende, Modulating defect density of NiO hole transport layer via tuning interfacial oxygen stoichiometry in perovskite solar cells, Solar Energy 233 (2022) 326–336. **https://doi.org/10.1016/j.solener.2022.01.023**.

[237] M. Salado, M. Andresini, P. Huang, M.T. Khan, F. Ciriaco, S. Kazim, S. Ahmad, Interface Engineering by Thiazolium Iodide Passivation Towards Reduced Thermal Diffusion and Performance Improvement in Perovskite Solar Cells, Adv Funct Mater 30 (2020). **https://doi.org/10.1002/adfm.201910561**.

[238] N. Chawki, M. Rouchdi, M. Alla, B. Fares, Numerical modeling of a novel solar cell system consisting of electron Transport material (ETM)/$CaZrS_3$-based chalcogenide perovskites using SCAPS-1D software, Solar Energy 274 (2024) 112592. **https://doi.org/10.1016/j.solener.2024.112592**.

[239] A.D. Adewoyin, A.M. Feika, M.A. Olopade, Performance Optimization of $MgHfS_3$ Chalcogenide Perovskite Solar Cells Using SCAPS-1D, East European Journal of Physics (2024) 456–464. **https://doi.org/10.26565/2312-4334-2024-3-55**.

[240] M. Masum Mia, Md. Faruk Hossain, M. Rahman, N. Badi, A. Irfan, Md. Ferdous Rahman, Unveiling the impact of Se based HTM on $BaZrSe_3$ perovskites solar cell and improving the theoretical efficiency above 32%, Materials Science and Engineering: B 311 (2025) 117817. **https://doi.org/10.1016/j.mseb.2024.117817**.

[241] R. Chami, A. Lekdadri, L.H. Omari, E.K. Hlil, M. Chafi, Investigation of the photovoltaic properties of $BaHf_{1-x}Zr_xS_3$ chalcogenide perovskites using first principles calculations, Mater Today Energy 20 (2021) 100689. **https://doi.org/10.1016/j.mtener.2021.100689**.

[242] N.N.M. Zorkipli, N.H.M. Kaus, A.A. Mohamad, Synthesis of NiO Nanoparticles through Sol-gel Method, Procedia Chem 19 (2016) 626–631. **https://doi.org/10.1016/j.proche.2016.03.062**.

[243] A. Al Mamun, T.T. Ava, T.M. Abdel-Fattah, H.J. Jeong, M.S. Jeong, S. Han, H. Yoon, G. Namkoong, Effect of hot-casted NiO hole transport layer on the performance of perovskite solar cells, Solar Energy 188 (2019) 609–618. **https://doi.org/10.1016/j.solener.2019.06.040**.

[244] M.I. Pintor-Monroy, B.L. Murillo-Borjas, M. Catalano, M.A. Quevedo-Lopez, Controlling Carrier Type and Concentration in NiO Films To Enable in Situ PN Homojunctions, ACS Appl Mater Interfaces 11 (2019) 27048–27056. **https://doi.org/10.1021/acsami.9b04380**.

[245] V. Deswal, S. Baghel, Designing and optimization of a highly efficient and new lead-free Cs_2RbGaI_6 based double perovskite solar cell through SCAPS-1D and machine learning, Inorg Chem Commun 176 (2025) 114316. **https://doi.org/10.1016/j.inoche.2025.114316**.

[246] A. Ghosh, M.R. Hasan, M. Moumita, K.U. Apu, S. Begum, A. Rahman, M.A. Bappy, S. Ahmed, Y.A. Kumar, A.A. Hassan, H.A. Alrafai, Discovering the relationship between sulfide and selenide-based HTLs and cubic Ba_3SbI_3 solar cells with SCAPS-1D and machine learning modelling, Inorg Chem Commun 173 (2025) 113782. **https://doi.org/10.1016/j.inoche.2024.113782**.

[247] B.N.M. Ghadhab, A. Bahrami, A comprehensive study on $ZnSnN_2$-based solar cells with different Cu-based delafossite as buffer layers: A numerical analysis using SCAPS-1D, Solar Energy Materials and Solar Cells 289 (2025) 113675. **https://doi.org/10.1016/j.solmat.2025.113675**.

[248] A. Mavlonov, T. Negami, H. Mori, N. Krobkrong, M. Yamanishi, T. Hara, Y. Hishikawa, Y. Kawano, A. Hayakawa, T. Minemoto, Insights into structural and morphological properties of flexible perovskite solar modules with different barrier film under damp-heat test, Renew Energy 250 (2025) 123349. **https://doi.org/10.1016/j.renene.2025.123349**.

[249] A.H. Hassan Khan, Y.-C. Wang, Tailoring transporters for all-inorganic tin-based perovskite solar cells with efficiency exceeding 22% using SCAPS-1D simulator, Inorg Chem Commun 179 (2025) 114707. **https://doi.org/10.1016/j.inoche.2025.114707**.

[250] M. Guo, S. Kang, H. Liang, X. Liu, J. Zhang, Y. Zhu, L. Huang, Device simulation of chalcogenide perovskite $BaZrS_3$ solar cells with different structures, Mater Today Commun 46 (2025) 112686. **https://doi.org/10.1016/j.mtcomm.2025.112686**.

[251] S. Ganesan, T. Kokulnathan, A. Palaniappan, MoS_2 /Tungsten Carbide Nanocomposite as Disposable Electrochemical Strips for the Detection of Hazardous 4-Nitroaniline, ACS Appl Nano Mater 8 (2025) 7004–7014. **https://doi.org/10.1021/acsanm.5c00148**.

[252] A. Mortadi, E.M. El Hafidi, Hamid. Nasrellah, M. Monkade, R. El Moznine, Investigation of bandgap grading on performances of perovskite solar cell using SCAPS-1D and impedance spectroscopy, Solar Energy Advances 4 (2024) 100056. **https://doi.org/10.1016/j.seja.2024.100056**.

[253] Md.N.H. Riyad, A. Sunny, Most.M. Khatun, S. Rahman, S.R. Al Ahmed, Performance evaluation of WS_2 as buffer and Sb_2S_3 as hole transport layer in CZTS solar cell by numerical simulation, Engineering Reports 5 (2023). **https://doi.org/10.1002/eng2.12600**.

[254] M.E. Erkan, V. Chawla, M.A. Scarpulla, Reduced defect density at the CZTSSe/CdS interface by atomic layer deposition of Al_2O_3, J Appl Phys 119 (2016). **https://doi.org/10.1063/1.4948947**.

[255] M. Kauk-Kuusik, K. Timmo, K. Muska, M. Pilvet, J. Krustok, R. Josepson, G. Brammertz, B. Vermang, M. Danilson, M. Grossberg, Detailed Insight into the CZTS/CdS Interface Modification by Air Annealing in Monograin Layer Solar Cells, ACS Appl Energy Mater 4 (2021) 12374–12382. **https://doi.org/10.1021/acsaem.1c02186**.

[256] K. Jeganath, S.D. George, M.S. Murari, Y. Raviprakash, Probing the depth inhomogeneity of spray pyrolyzed CZTS thin films via chemical etching, Inorg Chem Commun 145 (2022) 109952. **https://doi.org/10.1016/j.inoche.2022.109952**.

[257] S. Rijal, D. Li, R.A. Awni, C. Xiao, S.S. Bista, M.K. Jamarkattel, M.J. Heben, C. Jiang, M. Al-Jassim, Z. Song, Y. Yan, Templated Growth and Passivation of Vertically Oriented Antimony Selenide Thin Films for High-Efficiency Solar Cells in Substrate Configuration, Adv Funct Mater 32 (2022). **https://doi.org/10.1002/adfm.202110032**.

[258] P. Basera, S. Bhattacharya, Chalcogenide Perovskites (ABS_3; A = Ba, Ca, Sr; B = Hf, Sn): An Emerging Class of Semiconductors for Optoelectronics, J Phys Chem Lett 13 (2022) 6439–6446. **https://doi.org/10.1021/acs.jpclett.2c01337**.

[259] T. Jiang, Y. Zhao, M. Liu, Y. Chen, Z. Xia, H. Xue, Enhancing the Lifetime of Photoinduced Charge Carriers in $CuFeO_2$ Nanoplates by Hydrothermal Doping of Mg for Photoelectrochemical Water Reduction, Physica Status Solidi (a) 215 (2018). **https://doi.org/10.1002/pssa.201800056**.

[260] D. Srinivasan, A.-D. Rasu Chettiar, S. Rajendran, H. Bencherif, P. Sasikumar, J. Ramanujam, L. Marasamy, Boosting the efficiency of $BaZrS_3$ solar cells with inorganic delafossite HTLs: A promising alternative to Spiro-OMeTAD, Inorganic Chemistry Communications 180 (2025) 114997. **https://doi.org/10.1016/j.mseb.2025.118126.**